THE UNIVERSITY *of* EDINBURGH

The Synthesis and Study of Frustrated Oxide and Mixed Anion Materials

Lucy Clark

Doctor of Philosophy
The University of Edinburgh
July 2013

Lay Summary of Thesis

The study and understanding of magnetism is a central feature of solid state and materials sciences. As early as the 2nd century A.D. the appreciation of the magnetic properties of materials, such as naturally occurring iron oxides, led to the very first applications of magnetic materials as navigational tools or compasses. However, it was not until the beginning of the 20th century and the development of quantum mechanics before we had an understanding of magnetism on a microscopic level. It is thanks to this detailed understanding that we are now able to design materials that exploit the useful properties of magnets. As a result, magnetic materials have become ubiquitous within modern day life with a wide range of important applications, including magnetic imaging techniques in medicine and memory storage devices in information technology. On a more fundamental level, magnetic materials are of interest as they can be used as model systems to experimentally test and explore many scientific concepts or theories. The microscopic magnetic moments that give rise to magnetism in a material behave in a similar manner to the atoms or molecules in a gas. At sufficiently high temperatures they are weakly interacting and free to move or fluctuate in a random fashion. However, as a gas is cooled the atoms or molecules begin to slow down and ultimately arrange in a regular pattern to form a solid. In analogy, the magnetic moments in a magnet will also tend to interact with each other at lower temperatures and eventually align to give magnetic order. There are, however, certain situations in which this conventional magnetic ordering is not observed. This unusual behaviour is not entirely understood and may give rise to exotic physical phenomena. One particularly important class of magnetic materials that support such behaviour are known as geometrically frustrated magnets. In a geometrically frustrated magnet, the arrangement or geometry of the magnetic moments with respect to each other prevents them from ordering at low temperatures. Instead, they can adopt novel magnetic phases that display unusual and often difficult to predict glassy or liquid-like behaviours. Within this

Thesis the unconventional magnetic properties of several geometrically frustrated magnets are discussed through a range of experimental studies.

Abstract

Mixed anion systems, such as oxynitrides and oxyfluorides, are an emerging class of interesting materials. The lower stability of mixed anion systems in comparison to oxide materials has had the consequence that this area of materials research is relatively less well explored. However, the development of new synthesis techniques has resulted in the preparation of many new mixed anion systems and so a detailed understanding of their structure and how this relates to their electronic and magnetic properties is necessary. Within this Thesis, several oxide, oxynitride and oxyfluoride systems are investigated with a particular focus on the magnetic behaviour of materials based on geometrically frustrated pyrochlore and kagome lattices.

The $Lu_2Mo_2O_7$ pyrochlore contains a geometrically frustrated network of vertex sharing Mo^{4+} (d^2 $S = 1$) tetrahedra. Here, the solid state synthesis of $Lu_2Mo_2O_{7-x}$ is reported along with a discussion of the coexistence of two cubic pyrochlore phases that has been discovered in samples synthesised at 1600 °C. Powder neutron diffraction and thermogravimetric analysis have revealed that this two-phase behaviour originates from a miscibility gap between stoichiometric $Lu_2Mo_2O_7$ and oxygen deficient $Lu_2Mo_2O_{6.6}$. Magnetic susceptibility and muon spin relaxation measurements support the formation of a geometrically frustrated spin glass ground state in $Lu_2Mo_2O_7$ with a spin freezing temperature $T_f \sim 16$ K. Low temperature neutron diffraction has confirmed the absence of long range magnetic order and magnetic diffuse neutron scattering data have indicated the presence of competing nearest and next nearest neighbour antiferromagnetic exchange interactions in the spin glass state. The magnetic heat capacity of $Lu_2Mo_2O_7$ follows a T^2-dependence at the low temperatures, indicating that $Lu_2Mo_2O_7$ is another rare example of an unconventional, topological spin glass, which is stable in the absence of significant chemical disorder. The magnetic properties of the oxygen deficient pyrochlore phase $Lu_2Mo_2O_{6.6}$ are qualitatively

similar to those of $Lu_2Mo_2O_7$, but an increase in the spin freezing temperature $T_f \sim 20$ K suggests that oxygen-vacancy disorder in $Lu_2Mo_2O_{6.6}$ favours the onset of a glassy state at higher temperatures and enhances the degree of frustration.

Oxynitride pyrochlores with the ideal composition $R_2Mo_2O_5N_2$ (R = rare earth) contain Mo^{5+} d^1 $S = \frac{1}{2}$ cations on the frustrated pyrochlore lattice and are thus ideal candidates to support exotic magnetic ground states. Here, the synthesis of oxynitride pyrochlores of the $Lu_2Mo_2O_7$ system by thermal ammonolysis is discussed alongside powder neutron diffraction and susceptibility data that show no evidence for long range magnetic order and an absence of spin freezing down to at least 2 K despite the persistence of strong antiferromagnetic exchange ($\theta = -120$ K). A comparison of the magnetic diffuse neutron scattering between the spin glass state of $Lu_2Mo_2O_7$ and the oxynitride is given, which suggests that the majority of the magnetic scattering in the oxynitride system is inelastic. In addition, low temperature magnetic heat capacity shows an absence of magnetic phase transitions and a continuous density of states through a T-linear dependence down to 500 mK.

$[NH_4]_2[C_7H_{14}N][V_7O_6F_{18}]$, diammonium quinuclidinium vanadium(III,IV) oxyfluoride or DQVOF, is a kagome bilayer system with a geometrically frustrated two-dimensional kagome network of V^{4+} d^1 $S = \frac{1}{2}$ cations and V^{3+} d^2 $S = 1$ cations between the kagome layers. Here, low temperature magnetisation and heat capacity data are presented, which demonstrate that the interplane V^{3+} d^2 cations are well decoupled from the kagome layers at low temperatures such that DQVOF is a good experimental realisation of a $S = \frac{1}{2}$ kagome antiferromagnet. Despite significant antiferromagnetic exchange ($\theta = -60$ K) within the kagome planes, muon spin relaxation data have confirmed the absence of spin freezing and the persistence of internal field fluctuations that are intrinsic to the kagome layers down to temperatures of 40 mK. The low temperature heat capacity of the V^{4+} kagome network follows T-linear behaviour down to the 300 mK, highlighting the absence of a spin gap in the low energy excitation spectrum of DQVOF. The low temperature magnetic study of DQVOF presented here thus strongly supports the formation of a gapless quantum spin liquid phase.

In the final results chapter, a discussion of the anion ordering principles in oxynitride systems is given. A high temperature, high resolution neutron diffraction study of the oxynitride perovskite $SrTaO_2N$ has revealed that the partial anion order that results in segregated Ta-N zig-zag chains is stable up to 1100 °C. Furthermore, these anion ordering principles are extended to the d^1

perovskite oxynitrides $R\mathrm{VO}_{2-x}\mathrm{N}_{1+x}$ (R = La, Nd, Pr) in a variable temperature neutron diffraction study, which confirms that the anion chain ordering discovered in d^0 $\mathrm{SrTaO_2N}$ is robust to electron doping. The R = La analogue also provides an interesting example of a rhombohedral oxynitride perovskite phase which coexists with an orthorhombic phase over the $4-300$ K temperature range of the neutron diffraction study.

Declaration

I declare that this thesis was composed by myself, that the work contained herein is my own except where explicitly stated otherwise in the text, and that this work has not been submitted for any other degree or professional qualification except as specified.

(*Lucy Clark, July 2013*)

Acknowledgements

First of all, I would like to thank my supervisors Prof Paul Attfield and Prof Andrew Harrison for an extremely enjoyable and rewarding Ph.D. experience and for giving me the opportunity to work on such interesting research projects. I feel very grateful to have been given the freedom to carry out my work with the confidence that their guidance, support and expertise were available whenever I was unsure. I want to thank Paul for giving up so much of his time to help me over the past three years and for everything that he has taught me. I want to thank Andrew for always taking the time to meet me whenever our paths crossed and for his positive encouragement throughout my Ph.D. At this point, I should also thank the Science and Technology Facilities Council and the University of Edinburgh Principal's Career Development Scholarship programme for funding.

I am very happy to acknowledge my colleagues and friends that I have had the pleasure to work with during my time at the University of Edinburgh. Most importantly, I have to thank Dr Ángel Arévalo López who has helped me so much, from my very first day in Edinburgh and along every step of the way towards my Ph.D. Thank you so much for all of your patience, enthusiasm, encouragement and friendship. Thank you to all of the Attfield group members, past and present, but in particular Alex Sinclair, and to all of the CSEC Open Plan Office residents, especially Gino Abdul Jabbar and Michal Kepa, for a friendly and helpful working environment. Thanks also to Dr Konstanin Kamenev and his group, Dr Matthew Jacobsen and Dr Martin Misek for their help in the Mag Lab with SQUID and PPMS measurements. I am extremely grateful to Dr Mark de Vries for his help with experiments, many useful scientific discussions, and in particular his support with the DQVOF project. Thanks also must go to Dr Chris Stock for his advice on neutron scattering results. I have had such a wonderful time working in CSEC over the past three years and I want to thank everybody there for many happy memories.

I am very fortunate to have had the opportunity to work and collaborate with many scientists from a number of different universities and central facilities during my time at Edinburgh. I am extremely grateful to Prof Phil Lighfoot, Prof Russell Morris and Dr Farida Aidoudi from the University of St Andrews for giving me the great opportunity to work on the DQVOF compound. I would also like to thank my former supervisors at St Andrews, Dr Sharon Ashbrook, Dr Karen

Johnston and Prof Paul Wright for giving me the confidence and enthusiasm to embark upon a Ph.D.

Also involved with the DQVOF project were Prof Philippe Mendels, Dr Fabrice Bert and their student Jean-Christophe Orain from Université Paris-Sud, Orsay. I cannot stress enough how thankful I am for their expertise and dedication to the project. I learnt so much through our collaboration, especially on the subjects of μSR and kagome physics, for which I am extremely grateful.

I am very thankful to have been able to participate in the oxynitride perovskite project in collaboration with Prof Amparo Fuertes and her group from the Institut de Ciència de Materials de Barcelona. In particular, thanks to Dr Judith Oró-Solé for all her hard work in preparing many samples and joining me on several neutron diffraction experiments.

I want to thank the many talented and friendly people that I met during my visit to McMaster University in Summer 2012. I have to thank Prof Bruce Gaulin for the interest that he has taken in my work, for his helpful discussion of results and his encouragement. In addition, thanks to Prof John Greedan for the time that he took to share his experience in the synthesis of the molybdate pyrochlores and his work on $Y_2Mo_2O_7$. Thanks also to Andrew for encouraging me to go and spend time there, I feel very lucky to be starting my post-doctoral career at McMaster and hope to make my time there a success.

I have had the privilege of performing many experiments at central facilities during my Ph.D. and I must thank all of the instrument scientists for their hard work and assistance, who have always ensured that my experiments were successful and as such have made this Ph.D. Thesis possible. From ISIS, I would like to thank Dr Kevin Knight for several enjoyable experiments on HRPD and Dr Ross Stewart for many useful discussions about my work on $Lu_2Mo_2O_7$ and for sharing his expertise on the neutron polarisation analysis technique and the D7 instrument. I would also like to thank Dr James Lord, Dr Mark Telling and the ISIS Muon Group for their assistance with my various experiments there and for their helpful discussions regarding data analysis. Thank you to Dr Alex Amato and Christopher Baines from PSI for their assistance with the μSR experiments on DQVOF. I would like to acknowledge the scientists that I have worked with at the ILL, Dr Clemens Ritter, for always making our D2B experiments run so smoothly, Dr Hannu Mutka for useful discussions regarding inelastic neutron scattering, and especially Prof Andrew Wildes and Dr Gøran Nilsen for their help with the diffuse scattering pyrochlore work, the D7 experiments were my favourite!

Finally, I would like to say thank you to my family, my brother Ross and my amazing mother Elinor, for their encouragement, friendship, and for always making me happy. Especially thanks to you, Mum, for your life-long support (moral, financial and otherwise!), none of this would have been possible without you.

Contents

List of Figures

List of Tables

Chapter 1

Magnetism and Magnetic Frustration

1.1 Introduction

The study of magnetism is one of the oldest subjects in science and continues to be a hugely important and popular topic in the fields of solid state chemistry, condensed matter physics and materials science [1]. In addition to being of great technological importance, magnetic materials provide model systems with which to test the often complicated theories of many body interacting systems [2]. The interactions between the magnetic moments that build up within a magnetic solid upon cooling often result in long range magnetic order, giving rise to magnetic ground states such as ferromagnets, the oldest known class of magnets, and antiferromagnets. When these magnetic interactions are frustrated, their competing nature means that they cannot be satisfied simultaneously. As such, materials that are magnetically frustrated give rise to a rich variety of novel magnetic ground states that can display complex physical phenomena. The aim of the Thesis is to seek and study magnetic materials that support these frustrated magnetic ground states. In particular, this study is focussed on mixed anion transition metal systems, such as oxynitrides and oxyfluorides, which are an emerging class of interesting materials that are relatively less well explored in comparison with their oxide counterparts. The following Chapter aims to describe to origin of magnetism in solids before going on to discuss the phenomenon of magnetic frustration in detail.

The study and understanding of the intricate behaviour demonstrated by highly frustrated magnets is often complicated and requires a concerted theoretical and experimental approach. As an experimentalist, the field of frustrated magnetism is an exciting one to work within. One important task is the design and synthesis of new materials that can support exotic frustrated ground states in order to compare with theory. Furthermore, the arsenal of tools required to characterise their behaviour allows one to become practised in a wide variety of experimental techniques. Chapter 2, therefore, outlines the synthetic methods used within this Thesis and the important principles of experimental techniques that were employed, including neutron scattering, muon spectroscopy, magnetisation and thermodynamic measurements.

Chapters 3 - 6 contain the main body of work that was performed for this Thesis. Chapter 3 gives a detailed experimental description of the frustrated spin glass ground state in the rare earth molybdate pyrochlore $Lu_2Mo_2O_7$. Chapter 4 discusses the suppression of the spin freezing transition in $Lu_2Mo_2O_7$ upon nitridation by thermal ammonlysis and the possibility of a spin liquid ground state in the oxynitride pyrochlore $Lu_2Mo_2O_{4.8}N_{1.7}$. In Chapter 6, a low temperature magnetic study of the first V^{4+} d^1 $S = \frac{1}{2}$ kagome antiferromagnet, $[NH_4]_2[C_7H_{14}N][V_7O_6F_{18}]$, is presented. Finally, Chapter 6 gives a discussion of the anion ordering principles in mixed anion oxynitride systems, which can play an important role in governing the properties that such materials display. A summary of the main scientific conclusions drawn from this work can be found in Chapter 7.

1.2 The Origin of Magnetism in Solids

The Magnetic Moment

The orbital motion of an electron about the nucleus of an atom gives rise to an orbital angular momentum, $\mathbf{L}$, which is associated with a magnetic moment $\boldsymbol{\mu}$ [3]. The magnetic moment lies in the same direction as the orbital angular momentum and is proportional to it,

$$\boldsymbol{\mu} = \gamma \mathbf{L} \tag{1.1}$$

where the constant of proportionality, γ, is known as the gyromagnetic ratio. The orbital angular momentum of an electron is quantised in units of $\hbar$,

$$\mathbf{L}^2 = l(l+1)\hbar^2 \tag{1.2}$$

where l is the orbital angular momentum quantum number, which can take values of $l = 0, 1, 2, \cdots, n$ where n is the principal quantum number. The magnitude of the orbital angular momentum is given by,

$$|\mathbf{L}| = \sqrt{l(l+1)}\hbar \tag{1.3}$$

and since $\mathbf{L}$ is a vector quantity, its direction as well as its magnitude is quantised such that a component of its direction projected along a given axis (conventionally the z-axis) is,

$$L_z = m_l\hbar \tag{1.4}$$

m_l is the magnetic quantum number, which takes $2l + 1$ values between $+l$ and $-l$. A convenient unit for describing the magnitude of atomic magnetic moments is the Bohr magneton, μ_B, which is defined by,

$$\mu_B = \frac{e\hbar}{2m_e} = 9.274{\times}10^{-24}\ \mathrm{Am}^2 \tag{1.5}$$

The component of the magnetic moment associated with the orbital angular momentum projected along the z-axis is thus,

$$\mu_z = \gamma L_z = \gamma m_l\hbar = -m_l\mu_B \tag{1.6}$$

and its magnitude is,

$$|\boldsymbol{\mu}| = \sqrt{l(l+1)}\mu_B \tag{1.7}$$

The energy of a magnetic moment in an applied magnetic field $\mathbf{B}$ is given by the

scalar product,

$$E = \boldsymbol{\mu}\cdot\mathbf{B} = -\mu B\cos\theta \tag{1.8}$$

where θ is the angle between the magnetic moment and the applied field. The energy of a magnetic moment is thus minimised when it lies along the direction of the applied field. The presence of a magnetic field will also cause the direction of a magnetic moment to precess about the the direction of the field with a characteristic frequency known as the Larmor precession frequency, $\omega_L = \gamma B$, as shown in Figure 1.1.

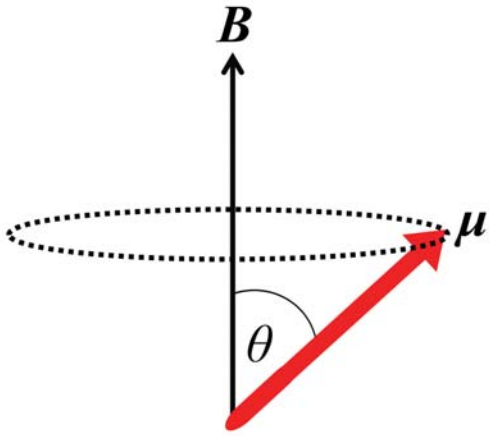

Figure 1.1 *A magnetic moment $\boldsymbol{\mu}$ at an angle θ to an applied magnetic field $\mathbf{B}$, which causes the direction of the magnetic moment to precess about the field with an angular frequency ω_L.*

In addition to the magnetic moment associated with the orbital angular momentum of an electron there is also a magnetic moment associated with the intrinsic angular momentum or spin of an electron [3]. The spin angular momentum can be treated in a similar manner to the orbital angular momentum, it is quantised in units of $\hbar$ by the spin quantum number, s, which takes a value of $\frac{1}{2}$. The magnitude of the spin angular momentum, $\mathbf{S}$, is given by,

$$|\mathbf{S}| = \sqrt{s(s+1)}\hbar \tag{1.9}$$

and its direction projected along a given axis is quantised by the spin magnetic quantum number m_s, which can take $2s+1$ values of $m_s = \pm\frac{1}{2}$. The component of the spin angular momentum along a particular axis is then given by $m_s\hbar$ according to Equation 2.4, which gives rise to values of $\frac{+\hbar}{2}$ and $\frac{-\hbar}{2}$, known as the

spin-up $|\uparrow\rangle$ and the spin-down $|\downarrow\rangle$ spin states, respectively. The component of the magnetic moment projected along the z-axis that is associated with the spin orbital angular momentum is,

$$\mu_z = -g\mu_B m_s \tag{1.10}$$

and the magnitude of the magnetic moment associated with this intrinsic angular momentum is given by,

$$|\boldsymbol{\mu}| = \sqrt{s(s+1)}g\mu_B \tag{1.11}$$

where g is a constant known as the g-factor, which for spin orbital angular momentum takes a value of 2. In an applied magnetic field $\mathbf{B}$, the energy of an electron is given by,

$$E = g\mu_B m_s B \tag{1.12}$$

and the interaction of the electron with this external field results in a splitting of the m_s levels as shown in Figure 1.2, which is known as the Zeeman interaction.

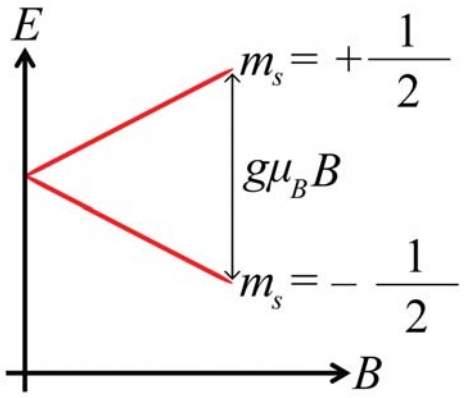

Figure 1.2 *The Zeeman energy splitting of the m_s levels of the spin angular momentum of an electron upon the application of a magnetic field of strength B.*

For an electron in an atom, there may be both orbital and spin angular momenta such that the value of g and the total magnetic moment will depend on the relative contributions of each. The effective magnetic moment of an atom or ion

is given by,

$$\mu_{eff} = g_J\sqrt{J(J+1)}\mu_B \tag{1.13}$$

where J is the total angular momentum quantum number, which results from the coupling of the total orbital, L, and total spin, S, angular momentum quantum numbers. g_J is the Landé g-factor, which is calculated according to,

$$g_J = \frac{3}{2} + \frac{S(S+1) - L(L+1)}{2J(J+1)} \tag{1.14}$$

The orbital and spin angular momenta can couple in a total of $(2L+1)(2S+1)$ different ways to give a values of J between $|L-S|$ and $|L+S|$. Each value of J obtained in this way is simply a multiplet of the $(2L+1)(2S+1)$ states. The situation is complicated further by the fact that the spin and orbital angular momenta are not independent of each other and can, in fact, interact via the spin orbit coupling interaction, $\lambda\mathbf{L}\cdot\mathbf{S}$, where λ is the spin orbit coupling constant. When the spin-orbit coupling interaction is considered, the $(2L+1)(2S+1)$ levels split into their fine structure levels, which are labelled by J. Furthermore, each of these fine structure levels has a degeneracy of $2J+1$ that can be split into their individual m_J states upon the application of a magnetic field [3]. The magnetic ground state of an atom of ion can be estimated using Hund's Rules and is typically expressed as a term symbol of the form,

$$^{(2S+1)}L_J \tag{1.15}$$

where L is a letter associated with the total orbital angular momentum according to the sequence given in Table 1.1. The definition of the effective magnetic moment given in Equation 1.13 holds well for the $4f$ ions of the lanthanide series. First row transition metal ions, on the other hand, have $3d$ orbitals that are far more spatially extended than the $4f$ orbitals of the lanthanide ions, which are held beneath the filled $5s$ and $5p$ shells. As a consequence, the $3d$ electrons of the first row transition metal elements interact strongly with their surrounding crystal field, which can outweigh the effect of the coupling between the spin and orbital angular momenta. A discussion of crystal field theory [4] and its effect on the magnetic properties of the early transition metals is given in Figures 1.3

Table 1.1 *Term symbols associated with the total orbital angular momentum L.*

L	0	1	2	3	4	5	6	$\cdots$
Label	S	P	D	F	G	H	I	$\cdots$

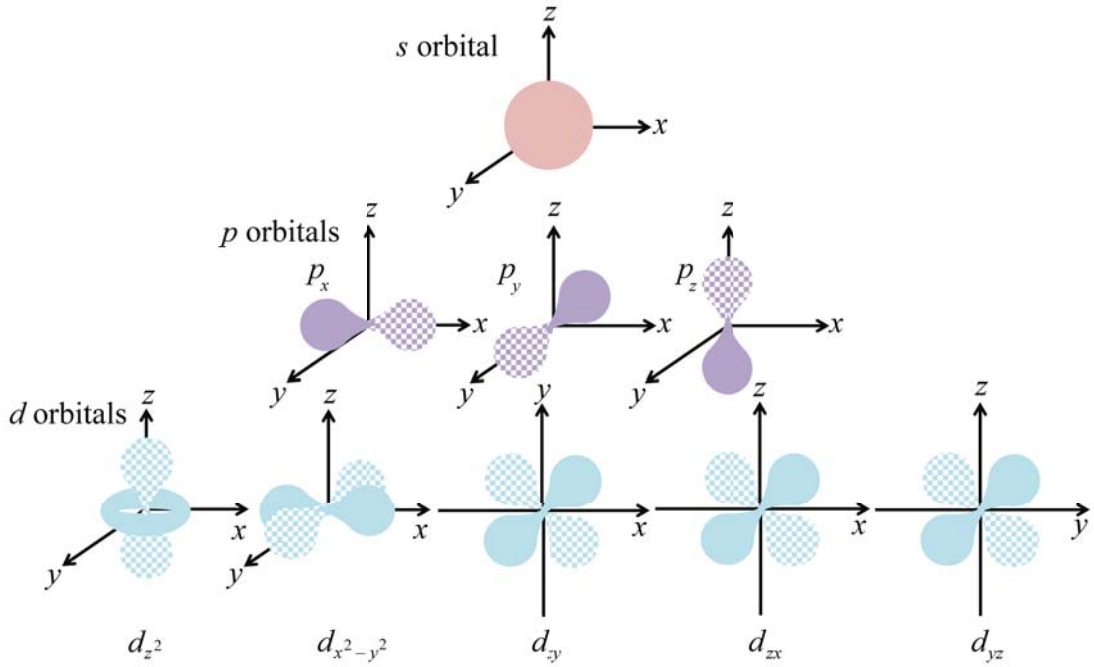

Figure 1.3 *For 3rd row transition metal cations, Hund's rules fail to describe the magnetic ground state of the ion because the strength of the crystal field interaction is greater than the spin-orbit interaction. As such, it is important to consider the shape and symmetry of the d-orbitals of the metal cations and the s- and p-orbitals of the anions that can surround them in a crystal structure, depicted here, which generate the electrostatic crystal field.*

- 1.5. Under these circumstances, the orbital angular momentum is said to be quenched such that $L = 0$, $J = S$, $g_J = 2$ and the effective magnetic moment can be calculated using the spin-only formula,

$$\mu_{so} = 2\sqrt{S(S+1)}\mu_B \tag{1.16}$$

Magnetisation and Susceptibility

A magnetic solid is made up of an extremely large number of atoms or ions with magnetic moment. The magnetic moment per unit volume of such a material is

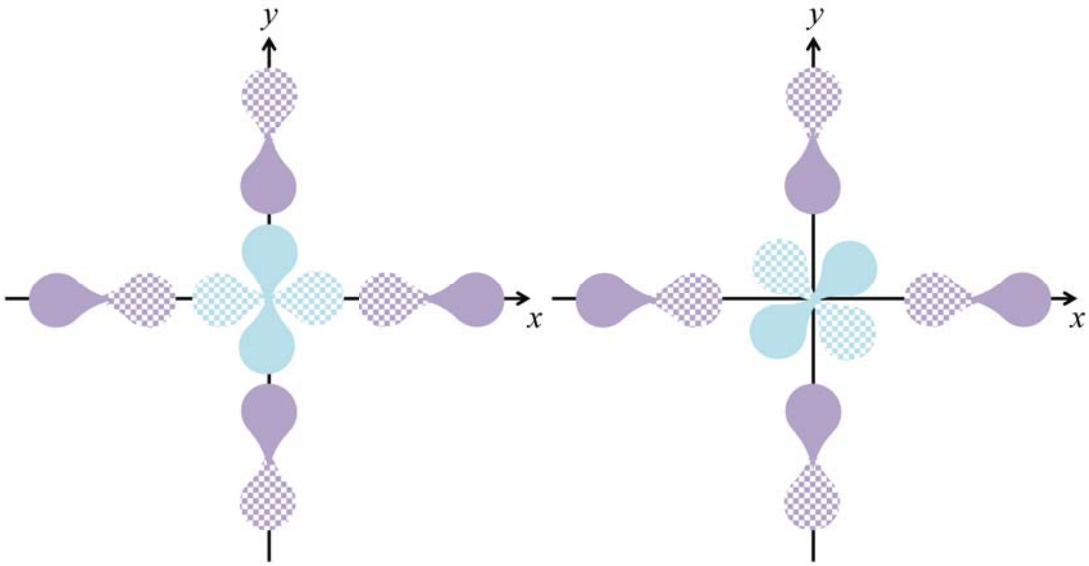

Figure 1.4 *Crystal field theory states that the d-orbitals of a metal cation centre that point directly towards the orbitals of the surrounding anions (left) are higher in energy than the metal orbitals that point between the surrounding anions (right) due to the unfavourable electrostatic repulsion of the electrons in the anion orbitals.*

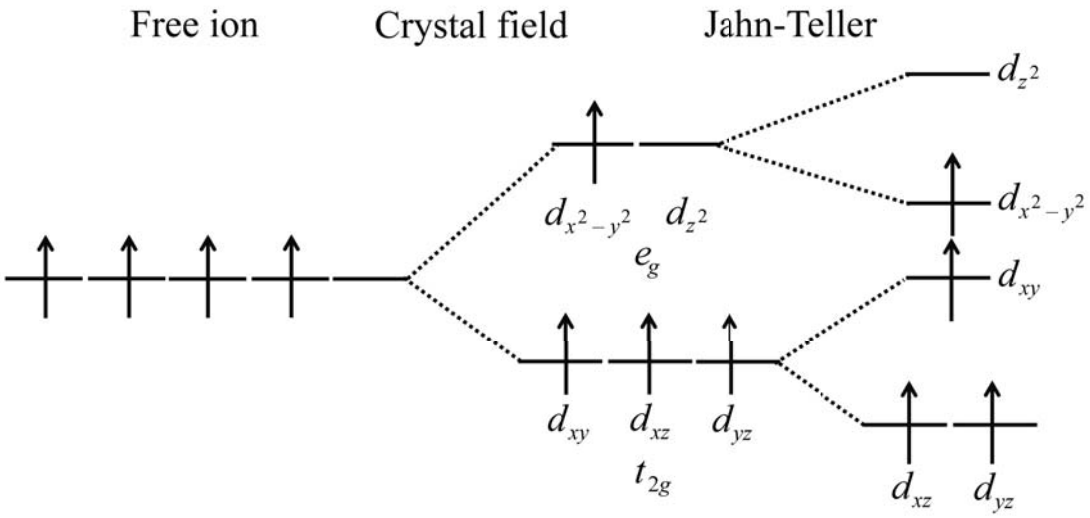

Figure 1.5 *The interaction with the crystal field thus spilts the metal cation d-orbitals into two groups, in the octahedral case shown here, the lower energy t_{2g} set and the higher energy e_g set. Depending on the electronic configuration of the the metal cation, these levels can be split further by, for example, the Jahn-Teller effect, which is acting here to remove the orbital degeneracy of this high spin d^4 cation resulting in a distortion of the crystal field.*

known as its magnetisation, $\mathbf{M}$ [5]. Magnetisation is a smooth vector field, which is continuous everywhere within a magnetic solid except at its edges. Within a vacuum there is no magnetisation and so a magnetic field can be described by two linearly proportional vectors,

$$\mathbf{B} = \mu_0 \mathbf{H} \tag{1.17}$$

where $\mathbf{B}$ is referred to a the magnetic flux density (in units T) $\mathbf{H}$ is the magnetic field strength (in units Am^{-1}) and μ_0 is the vacuum permeability. The relationship between $\mathbf{B}$ and $\mathbf{H}$ in a magnetic solid, however, is given by,

$$\mathbf{B} = \mu_0(\mathbf{H} + \mathbf{M}) \tag{1.18}$$

The magnetic susceptibility of a material, χ, is a dimensionless quantity that linearly relates magnetisation and an applied external field,

$$\mathbf{M} = \chi \mathbf{H} \tag{1.19}$$

such that Equation 1.18 becomes,

$$\mathbf{B} = \mu_0(1 + \chi)\mathbf{H} = \mu_0 \mu_r \mathbf{H} \tag{1.20}$$

where $\mu_r = 1 + \chi$ is the relative permeability of a material. The magnetic susceptibility, χ, therefore, represents the magnetic moment induced in a magnetic solid by an external magnetic field per unit volume.

Diamagnetism and Paramagnetism

Magnetic susceptibility is a measure of the response of a material in an applied magnetic field [5]. A diamagnetic material is repelled by an external field, where as a paramagnetic substance is attracted by an external field. Diamagnetism is important in systems of paired electrons and a diamagnet is defined as a substance in which the density of magnetic field lines of force is reduced when it is placed into an external magnetic field. Diamagnetic molar susceptibilities are negative, relatively small ($\sim 10^{-6}$ emu mol^{-1}) and temperature independent [5].

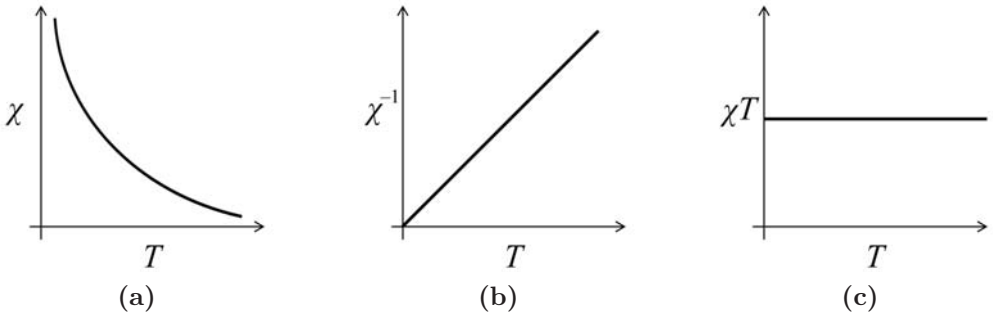

Figure 1.6 *The Curie law states that (a) magnetic susceptibility, χ, is inversely proportional to temperature, T, resulting in a straight line graph (b) when plotting χ^{-1} against T with gradient C and (c) constant χT against T.*

Paramagnetism is displayed in materials with unpaired electrons and is defined by a concentration of of magnetic lines of force within a substance when it is placed within an external field. Paramagnetic susceptibilities are temperature dependent, and to a first approximation at high temperatures, the magnetic susceptibility is inversely proportional to temperature as shown in Figure 1.6,

$$\chi = \frac{C}{T} \tag{1.21}$$

Equation 1.21 is known as the Curie Law, where C the Curie constant. This behaviour can be understood from a classical treatment of paramagnetism [3], such that one takes the total angular momentum quantum number $J = \infty$ and allows the magnetic moments within a system to point in any direction. Any magnetic moments lying between angles of θ and $\theta + \mathrm{d}\theta$ to an applied magnetic field $\mathbf{B}$, as shown in Figure 1.7, will have an energy of $-\mu B\cos\theta$ according to Equation 1.8 and a moment of $\mu\cos\theta$ in the direction of the applied field. The fraction of magnetic moments that will point between these two angles is given by $\frac{1}{2}\sin\theta\mathrm{d}\theta$ and the probability of a magnetic moment pointing in this direction at a given temperature, T, is given by the product of this fraction and the Boltzmann factor [3],

$$P(T) = \frac{1}{2}\sin\theta\mathrm{d}\theta exp\left(\frac{\mu B\cos\theta}{k_B T}\right) \tag{1.22}$$

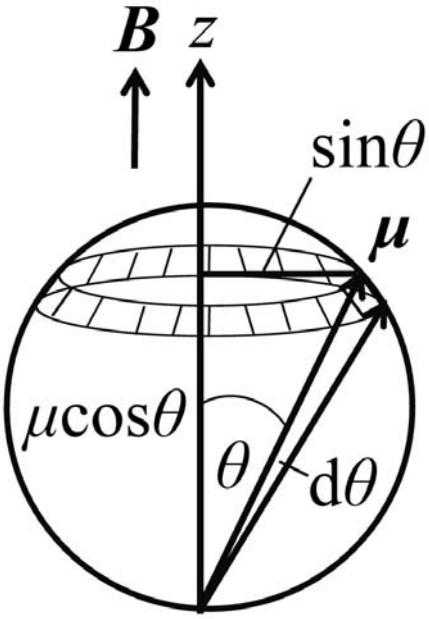

Figure 1.7 *The fraction of classical magnetic moments, $\boldsymbol{\mu}$, that lie between angles of θ and $\theta + \mathrm{d}\theta$ to an applied magnetic field* **B** *is given by $\frac{1}{2}\sin\theta \mathrm{d}\theta$, which corresponds to the shaded annulus shown here on a unit sphere of surface area 4π.*

The average magnetic moment along the direction of the field is then given by,

$$\langle \mu_{field} \rangle = \frac{\int_0^\infty \mu \cos\theta exp(\mu_B \cos\theta / k_B T) \frac{1}{2} \sin\theta \mathrm{d}\theta}{\int_0^\infty exp(\mu_B \cos\theta / k_B T) \frac{1}{2} \sin\theta \mathrm{d}\theta} = \mu \frac{\int_{-1}^1 x exp(xy) \mathrm{d}x}{\int_{-1}^1 exp(xy) \mathrm{d}x} \tag{1.23}$$

where $y = \mu / k_B T$ and $x = \cos\theta$ such that,

$$\frac{\langle \mu_{field} \rangle}{\mu} = \mathrm{coth}y - \frac{1}{y} \tag{1.24}$$

which is known as the Langevin function, $L(y)$, shown in Figure 1.8. For small values of y (*i.e.* in small applied fields or at high temperatures) coth$y$ can be approximated by the series expansion,

$$\mathrm{coth}y = \frac{1}{y} + \frac{y}{3} + O(y^3) \tag{1.25}$$

such that the Langevin function becomes,

$$L(y) = \frac{y}{3} + O(y^3) \tag{1.26}$$

The saturation magnetisation, M_{sat}, is the magnetisation obtained when all of the magnetic moments within the system are aligned,

$$M_{sat} = n\mu \tag{1.27}$$

where n is the number of magnetic moments within the system per unit volume. The ratio between the observed magnetisation, $M = n\mu_{field}$, and the saturated magnetization is given by,

$$\frac{M}{M_{sat}} = \frac{\langle \mu_{field} \rangle}{\mu} \simeq \frac{y}{3} = \frac{\mu B}{3k_B T} \tag{1.28}$$

In small applied fields one can approximate the susceptibility according to,

$$\chi = \frac{M}{H} \simeq \frac{\mu_0 M}{B} \tag{1.29}$$

and by substituting this expression for the susceptibility into Equation 1.28 one obtains the Curie Law for a paramagnetic system of classical magnetic moments,

$$\chi = \frac{n\mu_0\mu^2}{3k_B T} = \frac{C}{T} \tag{1.30}$$

where,

$$C = \frac{n\mu_0\mu^2}{3k_B T} \tag{1.31}$$

is the Curie constant. In the more general case, however, J can take any integer or half integer value and the component of the of the magnetic moment along the field is quantised by m_J which takes $2J+1$ values between $+J$ and $-J$. The

saturation magnetisation in this case is given by,

$$M_{sat} = ng_J\mu_B J \tag{1.32}$$

and,

$$\frac{M}{M_{sat}} = B_J(y) \tag{1.33}$$

where $B_J(y)$ is known as the Brillouin function,

$$B(y) = \frac{2J+1}{J}\coth\left(y\frac{2J+1}{2J}\right) - \frac{1}{2J}\coth\left(\frac{y}{2J}\right) \tag{1.34}$$

and,

$$y = \frac{g_J\mu_B JB}{k_B T} \tag{1.35}$$

In the classical limit ($J \to \infty$), the Brillouin function becomes the Langevin function given in Equation 1.24. In the quantum limit ($J = \frac{1}{2}$), it reduces to,

$$B_{\frac{1}{2}}(y) = \tanh(y) \tag{1.36}$$

as shown in Figure 1.8. Once again, for small y in small magnetic fields, Equation 1.34 can be approximated by the series expansion,

$$B_J(y) = y\frac{J+1}{3J} + O(y^3) \tag{1.37}$$

and the susceptibility is given by,

$$\chi = \frac{n\mu_0{\mu_{eff}}^2}{3k_B T} \tag{1.38}$$

The Curie Law can, therefore, be used to relate the bulk property χ to the effective magnetic moment given in Equation 1.13 of the atoms or ions in a paramagnetic

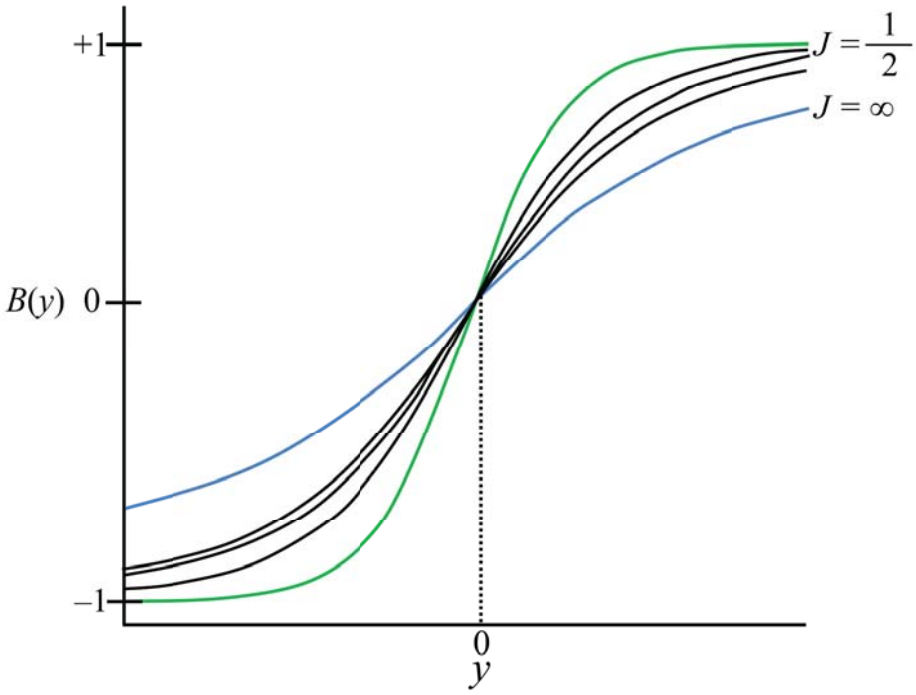

Figure 1.8 *The Brillouin function for paramagnetic moments for several J from* $\tanh(y)$ *function for* $J = \frac{1}{2}$ *in green to the Langevin function of the classical* $J = \infty$ *limit in blue.*

system,

$$\mu_{eff} = \sqrt{\frac{3k_B\chi T}{n\mu_0}} \tag{1.39}$$

In analogy with an ideal gas, an increase in temperature will cause the magnetic moments in a Curie paramagnet to randomise or disorder. On the other hand, the application of a stronger external field will tend the magnetic moments to align and order. When the temperature applied to the system is on the order of the energy of the magnetic moments in the applied field (*i.e.* $k_BT \sim \mu B$) it is possible to excite transitions from the magnetic ground state, which gives rise to a characteristic broad feature in the magnetic heat capacity, known as a Schottky anomaly [3].

1.3 Long Range Magnetic Order

As the magnetic analogue of the ideal gas law, there are circumstances in which the magnetic moments in a system do not obey Curie's law due magnetic interactions between the magnetic atoms or ions [3], [5]. The simplest description for this behaviour is given by the Curie-Weiss law, a modified version of the Curie law,

$$\chi = \frac{C}{T - \theta} \tag{1.40}$$

where C is once again the Curie constant and θ is known as the Weiss constant. Due to the interactions between the atoms or ions in a magnetically ordered state, a sharp transition can be observed in the magnetic susceptibility upon cooling as the material transforms from a paramagnetic state of randomly orientated magnetic moments and adopts magnetic order. Low temperature magnetically ordered states are typically ferromagnetic, antiferromagnetic or ferrimagnetic, which are depicted in Figure 1.9. A ferromagnet has a spontaneous magnetisation below a transition temperature known as the Curie temperature, T_C, as shown in Figure 1.10, at which point the magnetic moments on neighbouring ions align parallel to one another. As a result, the magnetisation is no longer directly proportional to the applied external field as is the case for a paramagnet. The magnitude of the spontaneous molar magnetisation of a ferromagnet in the absence of an external field at low temperatures is given by,

$$M_{sat} = N_A \mu_{sat} \tag{1.41}$$

where N_A is Avogadro's number and μ_{sat} is the saturated moment per ion,

$$\mu_{sat} = 2S \tag{1.42}$$

in the spin-only case. In an antiferromagnet, neighbouring magnetic moments align antiparallel with respect to each other below a transition temperature known as the Néel temperature, T_N, as shown in Figures 1.9 and 1.10. This gives rise to two sublattices of magnetic moments $\mu_{sat} = 2S$, which results in a total magnetisation on each that exactly cancel out, such that there is no net

magnetisation. In a ferrimagnetic system, neighbouring magnetic moments align antiparallel below T_C but the magnitude of the magnetisation on one sublattice is larger than on the other such that there is an overall net magnetisation the material will behave as a ferromagnet. The Weiss constant, θ, takes a positive value for a ferromagnet and is negative for an antiferromagnet. The magnitude of θ gives an indication of the energy scale of the magnetic interactions within a system and, therefore, the temperature at which one might expect them to take effect.

The underlying mechanism for long range magnetic order is known as magnetic exchange. The Hamiltonian for the spins of two interacting magnetic moments, $\mathbf{S}_1$ and $\mathbf{S}_2$, is given by,

$$\hat{\mathcal{H}} = -2J\mathbf{S}_1 \cdot \mathbf{S}_2 \tag{1.43}$$

where J is the exchange constant,

$$J = \frac{E_S - E_T}{2} \tag{1.44}$$

Here, E_S and E_T are the energies of the spin singlet ($S = 0$, $|\uparrow\downarrow - \downarrow\uparrow\rangle/\sqrt{2}$) and triplet ($S = 1$, $|\uparrow\uparrow\rangle$, $|\uparrow\downarrow + \downarrow\uparrow\rangle/\sqrt{2}$ and $|\downarrow\downarrow\rangle$) states, respectively. If J is positive, $E_S > E_T$ such that the triplet state is energetically favoured and spins align parallel. If J is negative, $E_S < E_T$ such that the singlet state is energetically favoured and spins align antiparallel. An estimate of the exchange energy can be determined from the Weiss constant θ using the mean field approximation [6],

$$\theta = \frac{2S(S+1)}{3k_B} \sum_n z_n J_n \tag{1.45}$$

where n is the nth nearest neighbour of a magnetic moment and J_n is the corresponding exchange energy. For a many body system, the spin Hamiltonian given in Equation 1.43 is generalised to give the Heisenberg Hamiltonian,

$$\hat{\mathcal{H}} = -\sum_{ij} J_{ij} \mathbf{S}_i \cdot \mathbf{S}_j \tag{1.46}$$

where J_{ij} is the exchange constant for the interaction between the ith and jth

(a) *Paramagnetism.*

(b) *Ferromagnetism.*

(c) *Antiferromagnetism.*

(d) *Ferrimagnetism.*

Figure 1.9 *A representation of the arrangement of magnetic moments of magnetically ordered states (b), (c) and (d) that can result from the interaction of moments in a paramagnetic state (a).*

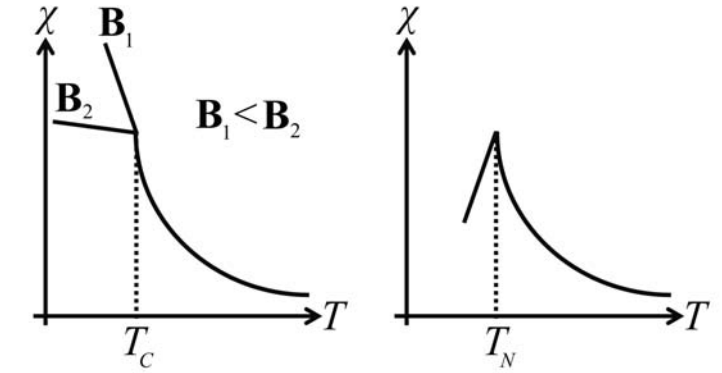

(a) *Susceptibility.* **(b)** *Susceptibility.*

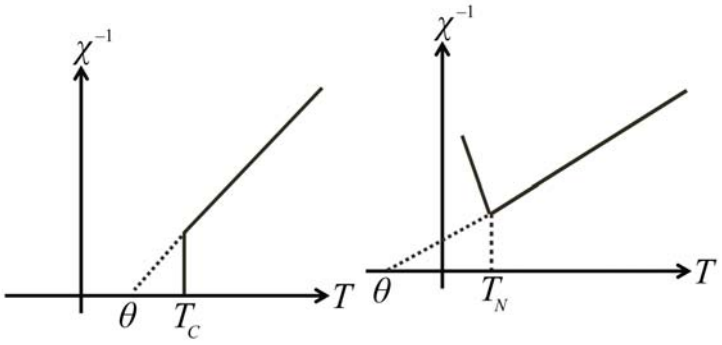

(c) *Inverse susceptibility.* **(d)** *Inverse susceptibility.*

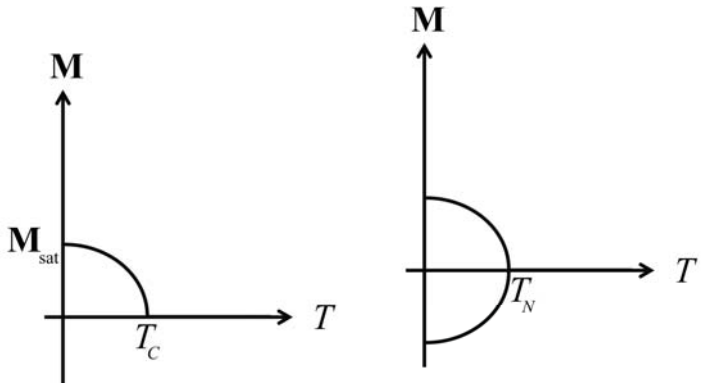

(e) *Magnetisation.* **(f)** *Magnetisation.*

Figure 1.10 *A critical magnetic phase transition can be observed in the (a),(b) magnetic and (c),(d) inverse susceptibilities at the critical Curie or Néel temperatures for a ferromagnet and antiferromagnet, respectively. In the ferromagnetic case these leads to the (e) onset of a spontaneous saturated magnetisation* $\mathbf{M}_{sat}$ *and in the (f) antiferromagnetic case, a spontaneous magnetisation of equal magnitude on each spin sublattice.*

spins. If magnetic exchange occurs directly between two neighbouring atoms or ions, then the interaction is known as direct exchange. However, it is unlikely that direct exchange is primarily responsible for the magnetic properties of a solid due to the insufficient overlap of the orbitals of nearest neighbours [3].

Superexchange is an indirect exchange mechanism that couples the magnetic ions in an ionic solid via a non-magnetic intermediate ion, see Figure 1.11. The superexchange mechanism depends strongly upon the angle and degree of orbital overlap. An antiferromagnetic interaction is favoured when orbitals of the magnetic ions overlap well with the same intermediate orbital with a 180 ° bonding angle. Ferromagnetic superexchange is less common, but can result from a weaker 90 ° orbital overlap. In metal oxides with mixed valence metal cations, for example $La_{0.7}Sr_{0.3}MnO_3$ which contains Mn^{3+} $3d^4$ and Mn^{4+} $3d^3$ cations [7], it is also possible to observe a ferromagnetic ground state via the double exchange mechanism, which is shown in Figure 1.12.

1.4 Magnetic Frustration

A consequence common to all magnetically ordered phases is that of broken symmetry. A high temperature paramagnetic state is highly symmetrical, each magnetic moment can point in any direction such that the system is invariant to translational and rotational symmetry operations. Below a critical Curie or Néel temperature, the magnetic moments align along a unique direction and the total invariant symmetry is broken. In the case of long range magnetically ordered states the parameter driving this symmetry breaking transition is temperature and the fact that at high temperatures, thermodynamics favours a high entropy state. The order parameter, which characterises a magnetically ordered state, is its magnetization $\mathbf{M}$, which is zero above the critical temperature and finite below [8]. There are, however, certain magnetic systems, namely low dimensional magnets and frustrated magnets, in which no such symmetry breaking magnetic transitions are observed. This can give rise to unusual glass or liquid like magnetic behaviour at low temperature. In the most extreme cases, magnetic fluctuations can persist down to $T = 0$ in a quantum spin liquid phase. The remainder of this chapter is devoted to giving an understanding of some of the most important concepts in the field of frustrated magnetism, including a discussion of some of the most widely studied experimental realisations of highly frustrated magnets that have helped to build our knowledge of the complex magnetic behaviour that

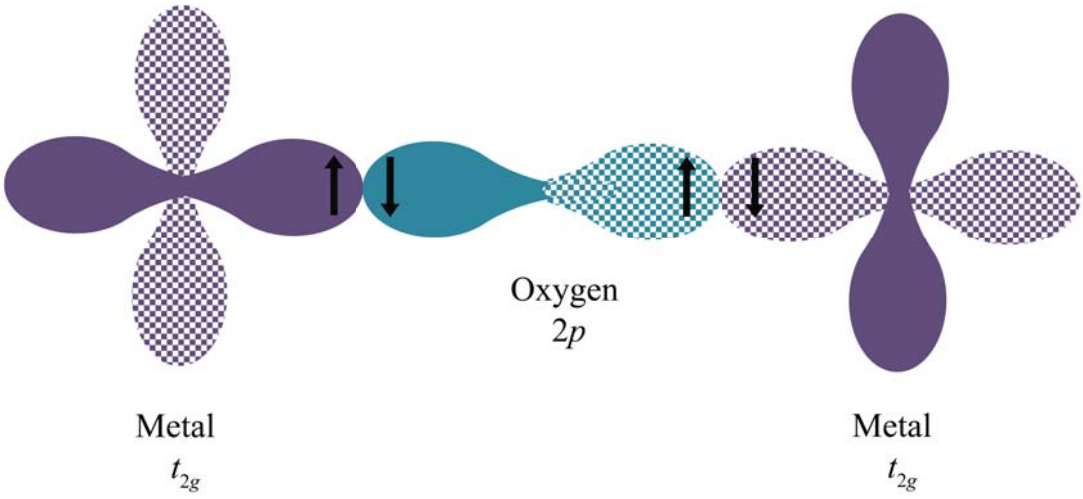

(a) 180 ° *superexchange interaction leads to antiferromagnetic ordering of magnetic moments on neighbouring magnetic metal ions.*

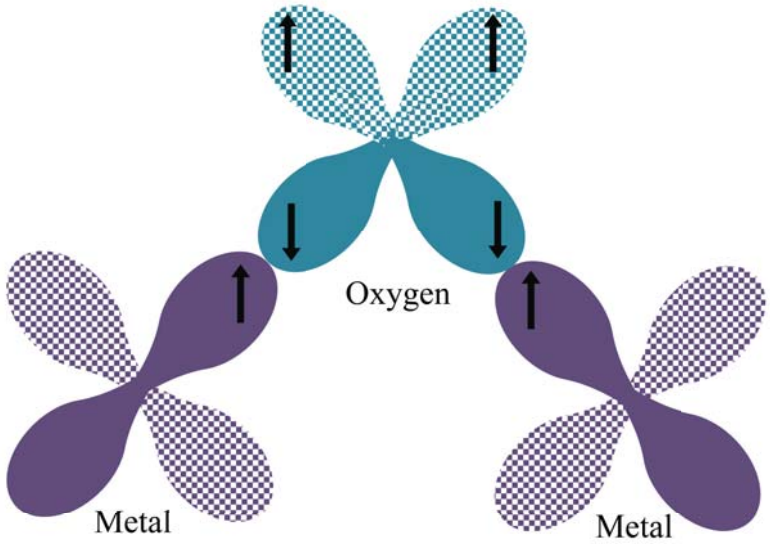

(b) 90 ° *superexchange interaction results in a ferromagnetic ordering of magnetic moments on neighbouring magnetic metal ions.*

Figure 1.11 *Superexchange mechanism between two magnetic metal ions with an* e_g^1 *configuration and intermediate non-magnetic centres such as the oxide anion.*

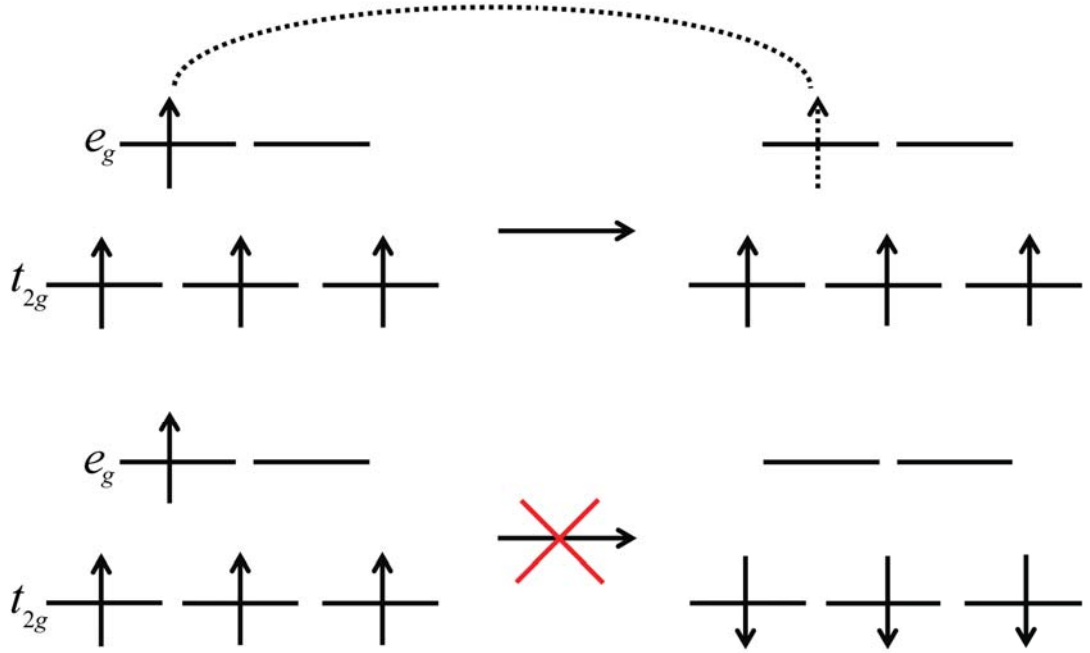

Figure 1.12 *The double exchange mechanism results in the ferromagnetic ordering (top) of localised t_{2g} electrons on neighbouring sites since antiferromagnetic ordering (bottom) would prevent the energetically favourable hopping of localised e_g electrons.*

they display.

1.4.1 Competition, Degeneracy and Underconstraint

Frustration is a phenomenon common to systems of competing interactions. It is frequently associated with magnetic materials in which it is not possible to simultaneously satisfy each pairwise magnetic exchange interaction [6], [9], [10]. Magnetic frustration was first used in the context of spin glasses, such as the magnetically dilute metal alloys $Cu_{1-x}Mn_x$ and $Au_{1-x}Fe_x$ [10]. Here the competition between different exchange interactions arises from site disorder, the magnetic ions are randomly distributed throughout the non-magnetic matrix, and the oscillatory nature of the Ruderman-Kittel-Kasuya-Yosida (RKKY) interaction through which the magnetic ions couple indirectly resulting in frustrated ferro- and antiferromagnetic exchange interactions [11], [12], [13]. This competition, or frustration, means that there is no single or unique magnetic ground state and the energy landscape consists of a large number of degenerate ground states between which the system can fluctuate.

An experimental result of this macroscopic degeneracy is that one observes a lowering in the ordering temperature of a frustrated spin system with respect to a non-frustrated system as it is able to resonate between its manifold of potential ground states [14]. A quantitative measure of magnetic frustration can, therefore, be given by the frustration index, f [15],

$$f = \frac{|\theta|}{T_c} \tag{1.47}$$

which compares the energy scale of magnetic interactions, $|\theta|$, with a critical magnetic ordering temperature, T_c. For antiferromagnetic order in the absence of frustration $|\theta|$ is on the order of the Néel temperature, T_N, as shown in Figure 1.13 [16]. For a frustrated magnet, in which long range order is inhibited, $|\theta| >> T_N$ and so in the extreme case $f \rightarrow \infty$. A value of $f > 10$ is taken as an indication for strong frustration of the spin order of a magnetic material. It should be noted, however, that a high frustration index is not unique to strongly frustrated magnets and can also be observed in systems of low dimensionality. In one-dimension, entropy effects can prohibit long range order such that T_N is suppressed and should not be confused as a result of magnetic frustration [17].

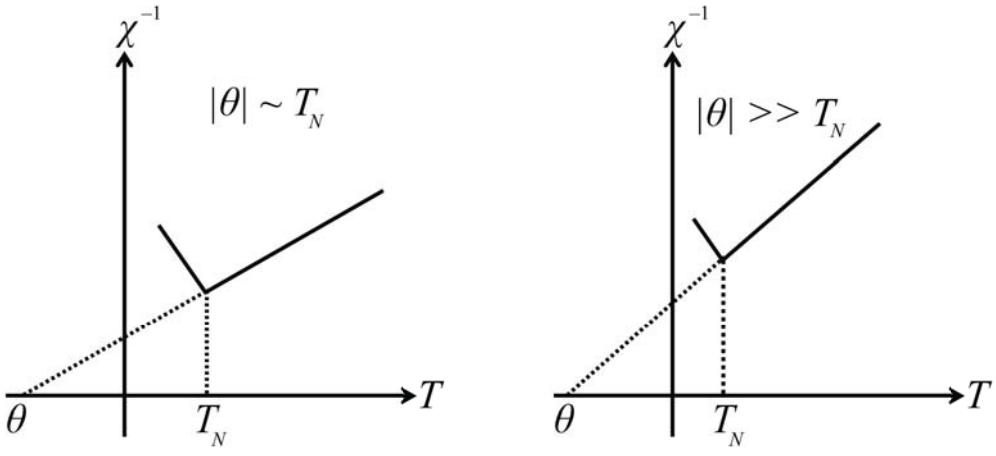

(a) *Non-frustrated* **(b)** *Frustrated.*

Figure 1.13 *For (a) antiferromagnetism in the absence of frustration, $|\theta|$ is on the order of the Néel temperature, T_N. The presence of frustration in (b) lowers T_N with respect to $|\theta|$.*

Another important concept used to quantify magnetic frustration is that of underconstraint. The ground state degeneracy, D, of a system can be estimated

by [18],

$$D = F - K \tag{1.48}$$

where F is the degeneracy of the entire system and K is the number of constraints required to keep that system in its ground state. For a magnetic lattice built of N units or plaquettes of q sites that are common to b of the plaquettes, and are occupied by spins which individually have n dimensions or degrees of freedom (see Table 1.2), the degrees of freedom per plaquette, D/N, is given by,

$$\frac{D}{N} = \frac{q(n-1)}{b} - n \tag{1.49}$$

A system where $D/N<0$ is referred to as over-constrained since it has more constraints, K, than total degrees of freedom, D, and therefore, will not possess macroscopic ground state degeneracy. A system in which $D/N>0$, on the other hand, is under-constrained since it has fewer constraints than total degrees of freedom and so will possess macroscopic degeneracy in its ground state. Under-constrained ($D/N\geq 0$) frustrated magnets are, therefore, most likely to show interesting and unusual physics.

1.4.2 Geometric Frustration

It is also possible for magnetic frustration to arise in the absence of magnetic site or bond disorder, in systems where the magnetic moments are located on a regular lattice and couple through uniform magnetic exchange interactions. Here, the frustration arises as a result of the lattice topology or geometry, which prevents all pair-wise exchange interactions from being satisfied at once [9], [6], [10]. This kind of geometric frustration was first discussed in the context of magnetism

Table 1.2 *Spin degrees of freedom or dimensionality, n, as required in Equation* 1.49.

	Spin degrees of freedom, n
Ising	1
XY	2
Heisenberg	3

with a model of antiferromagnetic Ising spins on a triangular plaquette shown in Figure 1.14, where one can easily observe that the lattice geometry prevents the simultaneous satisfaction of each pair-wise antiferromagnetic interaction [19], [20]. The three-dimensional analogue of the antiferromagnetic triangular plaquette is a tetrahedron of antiferromagnetically interacting spins (Figure 1.14). Again, one can see that it is not possible to satisfy each pair-wise exchange interaction simultaneously as a result of the tetrahedral geometry. The geometrically frustrated triangular and tetrahedral plaquettes can be extended to form infinite lattices in two dimensions, the triangular and kagome lattices, and in three-dimensions, the face centred cubic (FCC) and pyrochlore lattices shown in Figure 1.15. The degeneracy of these infinite lattices depends on the way in which they are connected and the number of degrees of freedom per spin and in certain cases can be macroscopic [14]. The design and synthesis of magnetic materials built of these frustrated lattices is, therefore, of interest since their macroscopic ground state degeneracy leads unusual glass or liquid like magnetic behaviour and has been shown to induce many novel, exotic phenomena [18].

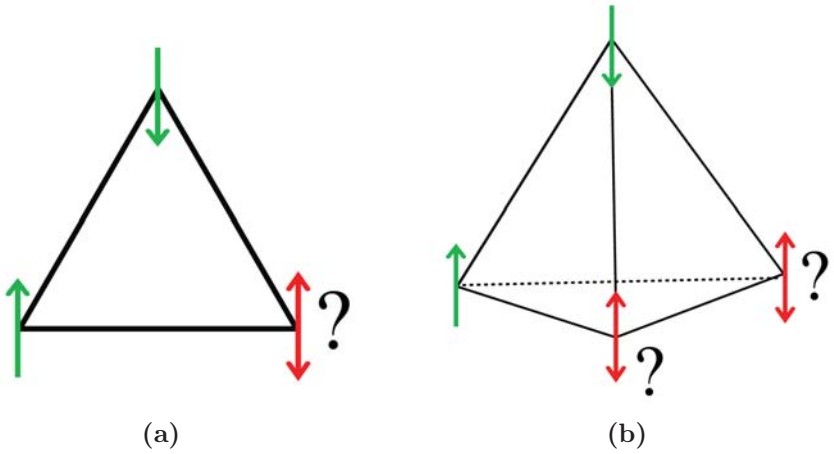

Figure 1.14 *The geometrically frustrated (a) triangular and (b) tetrahedral plaquettes of anitferromagnetically interacting spins.*

1.4.3 Geometrically Frustrated Magnetic Ground States

Non-Collinear Grounds States

Frustrated systems in which it is possible to undergo a transition to a ground state of long-range order do so by adopting non-collinear or compromise spin configurations [6], [21]. Non-collinear spin configurations are achieved when the

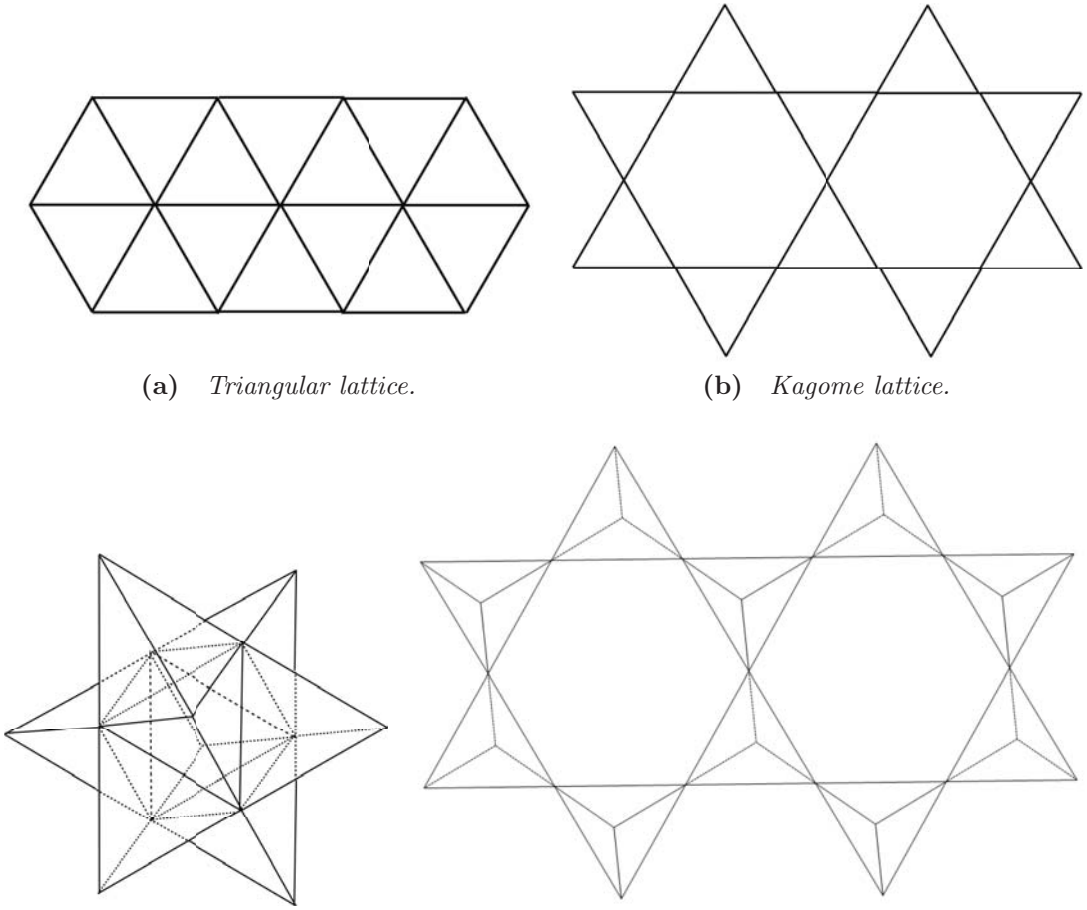

(a) *Triangular lattice.* **(b)** *Kagome lattice.*

(c) *FCC lattice.* **(d)** *Pyrochlore lattice.*

Figure 1.15 *The geometrically frustrated lattice that can be built up from (a,b) triangular and (c,d) tetrahedral plaquettes.*

spins on the triangular antiferromagnetic plaquette align at an angle of 120 °, resulting in a vector sum of the spins that is equal to zero, and hence satisfying the antiferromagnetic constraint. A similar result can be obtained when the spins on the tetrahedral antiferromagnetic plaquette align at an angle of 109 ° as shown in Figure 1.16. The ability of a system to adopt the 120 ° and 109 ° structures depends upon the dimensionality of the spins involved and can be achieved with XY and Heisenberg spins which have more than one degree of freedom. In these cases, degeneracy is introduced as there is more than one way to adopt the compromise spin configurations. Ising spins, however, which only have one degree of freedom cannot adopt a non-collinear spin configuration.

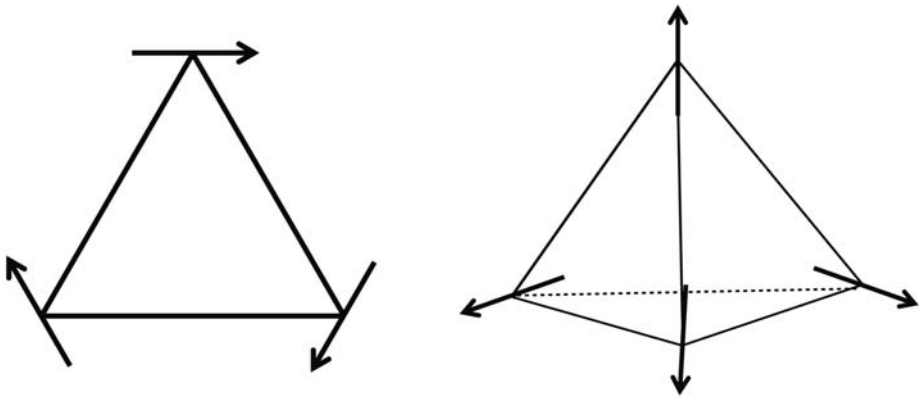

(a) **(b)**

Figure 1.16 *The (a)* 120 ° *and (b)* 109 ° *compromise spin configurations on the triangular and tetrahedral plaquettes, respectively.*

Spin Glasses

A spin glass is a magnetic system which exhibits a distinct freezing temperature, T_f, upon cooling from its paramagnetic state. At this well defined transition temperature a spin glass undergoes a cooperative freezing process to a highly irreversible glass like state of randomly orientated spins, which lacks the usual long range order of a conventional ferromagnetic or antiferromagnetic phase transition [13], [22], [23]. A spin glass has many experimental signatures, including the divergence of field cooled (FC) and zero field cooled (ZFC) DC magnetic susceptibility below T_f, the strong frequency dependence of the AC magnetic susceptibility, the linear temperature dependence of magnetic heat capacity below T_f and the absence of long range magnetic order in neutron diffraction experiments. An important difference between a conventional glass material *i.e.* an amorphous, non-crystalline solid, and a spin glass is that the latter undergoes a true thermodynamic phase transition to its spin glass ground state. The key experiment to observe this defining feature of a static spin glass state is that of non-linear susceptibility, which is defined by [13],

$$\chi_{nl} = 1 - \frac{M}{\chi_0 H} \tag{1.50}$$

where χ_0 is the linear susceptibility. Magnetisation, M, can be expanded in odd

powers of the field, H, according to,

$$M = \chi_0 H - a_3(\chi_0 H)^3 + a_5(\chi_0 H)^5 - \cdots \tag{1.51}$$

Spin glass theory predicts that the linear susceptibility should remain non-singular at T_f but that the other a_n-coefficients should diverge according to the critical exponents,

$$a_3 = (T - T_f)^{-\gamma} \tag{1.52}$$

$$a_5 = (T - T_f)^{-(2\gamma+\beta)} \tag{1.53}$$

etc. An important example of such a non-linear susceptibility measurement was performed on the spin glass pyrochlore $Y_2Mo_2O_7$, where is was shown that the system adheres to the critical exponents expected for a canonical spin glass that has undergone a true thermodynamic phase transition [24].

As mentioned above, the first spin glasses to be studied were the magnetically dilute metal alloys, in which small concentrations of a magnetic metal are placed into a non-magnetic metallic matrix. It was long perceived that the necessary ingredients for a spin glass were randomness, either through site disorder or the sign of neighbouring exchange interactions, and frustration, which could arise from competing exchange interactions or geometrically. In the case of the metallic alloys, both of these requirements are satisfied given their random site occupancy and the oscillatory nature of the aforementioned RKKY interaction in which the exchange interaction between two spins, J, as a function of their separation, r, is given by [13],

$$J(r) \propto \frac{\sin(2k_f r)}{(2k_F r)^4} - \frac{\cos(2k_F r)}{(2k_F r)^3} \tag{1.54}$$

were k_F is the Fermi momentum. This oscillatory behaviour in the exchange interaction J changes the sign of the interaction between the magnetic impurities within the non-magnetic matrix depending on their separation and, therefore, produces the required frustration or competition between ferromagnetic and antiferromagnetic interactions.

More recently, the formation of a spin glass state in the absence of site or bond disorder has become an important concept in highly frustrated magnetism. Two widely studied examples of these so called topological spin glasses are the jarosites [25], for example $(H_2)_6Fe_3(SO_4)_2OH_6$, which contain a kagome network of Fe^{3+} $S = \frac{5}{2}$ cations and the Heisenberg pyrochlore antiferromagnets, such as $Y_2Mo_2O_7$, which is composed of a vertex-sharing tetrahedral framework of Mo^{4+} $S = 1$ cations [26]. In both cases, the frustration arises from the geometrically frustrated corner-sharing lattices, but the source of disorder and whether it is truly required for the formation of a spin glass remains an open question.

Spin Ice

Another widely studied and important class of frustrated magnets is that of the spin ice materials [27]. The first reported example of a spin ice was the rare earth pyrochlore $Ho_2Ti_2O_7$, which has magnetic Ho^{3+} cations occupying the corners of the tetrahedra in the geometrically frustrated pyrochlore lattice. The nearest neighbour exchange interaction in $Ho_2Ti_2O_7$ is ferromagnetic, with a positive Weiss constant $\theta = +1.9$ K, however, the initial study of the system showed no evidence for long range magnetic order down at least to 50 mK [28]. It is perhaps not immediately obvious why a ferromagnetic pyrochlore should display behaviour characteristic of strong magnetic frustration. For instance, a pyrochlore lattice composed of ferromagnetically interacting Ising spins on a tetrahedral plaquette, shown in Figure 1.17, is not frustrated and will undergo a conventional magnetic phase transition to a long range ordered ground state at $T_C \sim \theta$. On the other hand, a tetrahedral plaquette of antiferromagnetically interacting Ising spins is considered as the canonical example of geometrical frustration in three-dimensions. In the cubic pyrochlore system, however, this uniaxial Ising spin anisotropy is unphysical since there is no reason that the spins should be constrained to lie along one particular crystallographic axis over the other two when all three are symmetrically equivalent. In fact, the local crystal field at the Ho^{3+} site splits its ${}^5I_8$ free ion ground state such that its lowest crystal field level is composed of the $m_J = +8$ and $m_J = -8$ free ion states, which results in a strong easy-axis anisotropy that is compatible with the overall cubic symmetry of the pyrochlore structure [29]. As such, the Ho^{3+} spins align along the crystallographic 111-axis, which points towards the centre of each tetrahedron. In the presence of antiferromagnetic exchange, this gives rise to a unique ground state and thus long range magnetic order. For ferromagnetic exchange, two spins point in

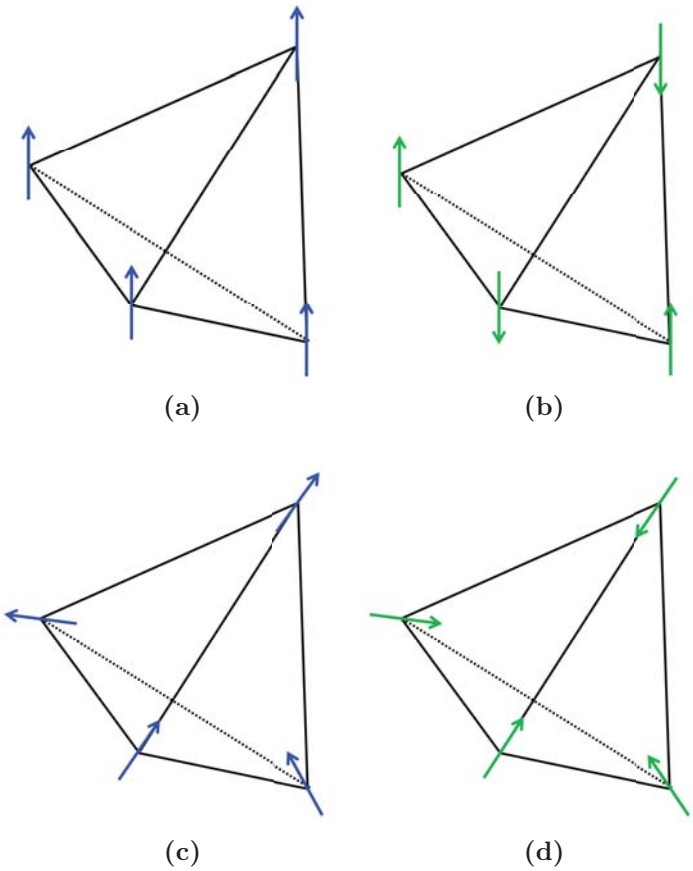

Figure 1.17 *(a) Ferromagnetically and (b) antiferromagnetically interacting uniaxial Ising spins on a tetrahedral lattice have long range ordered and geometrically frustrated ground states, respectively. The introduction of* 111 *easy axis anisotropy effectively swaps the nature of the ground states such that the (c) ferromagnetic state is frustrated and the (d) antiferromagnetic state is a unique non-collinear ground state.*

towards and two spins point out from the centre of each tetrahedron. The infinite number of ways to arrange these two-in two-out spin tetrahedra on a real lattice results in a macroscopically degenerate, disordered ground state that evades long range order down to the lowest temperatures. The magnetic anisotropy in $Ho_2Ti_2O_7$, therefore, effectively swaps the nature of the antiferromagnetic and ferromagnetic ground states on the pyrochlore lattice such that the ferromagnetic system becomes frustrated as shown in Figure 1.17 [30].

The spin directions of $Ho_2Ti_2O_7$ map directly onto the proton positions of crystalline water ice as shown in Figure 1.18, hence the name for this family of materials, spin ice [27]. The crystalline structure of water ice can be considered as the first frustrated system to be investigated. In water ice, proton disorder

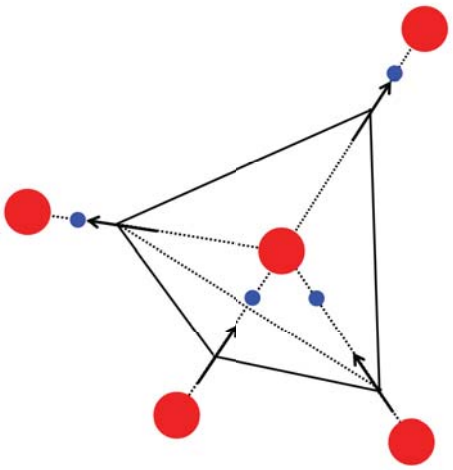

Figure 1.18 *In crystalline water ice each oxygen atom (red) has two short bonds and two long bonds to hydrogen atoms (blue), which corresponds to the spin directions (arrows) on a tetrahedron within the pyrochlore structure of spin ice.*

results in macroscopic degeneracy and frozen-in disorder, which leads to a residual or zero-point entropy at low temperatures. The proton disorder, to which the spin directions in spin ice correspond, obey the so-called "ice rules" that require each oxygen atom to possess two short bond and two long bonds to hydrogen atoms in a tetrahedral arrangement with the oxygen atom located at the centre of each tetrahedron [31]. The ground state degeneracy expected for such a structure, which has since been validated by neutron diffraction [32], was of great interest thermodynamically. Pauling famously predicted the residual zero-point entropy of water ice as $\frac{1}{2}Rln(\frac{3}{2})$ per H atom [33], which was later confirmed by experiment [34]. This led Ramirez *et al.* to determine the entropy of the spin ice $Dy_2Ti_2O_7$ through the measurement of heat capacity ($S = \int C/TdT$). The benefit of spin ice here was that it is stable over a far greater energy range than water ice such that the progression of the system towards its degenerate ground state could be studied [35]. The experimentally determined values of the spin entropies of $Dy_2Ti_2O_7$ and water ice differed by less than 6 %, which demonstrates beautifully how magnetic systems such as spin ice can be used as models for other physical phenomena.

Perhaps the best example of this can be given by the excitations that emerge from the spin ice ground state. The separation and transport of electrically charged particles such as electrons and ions is widely exploited in modern technology. However, no magnetic analogue of particles with a net magnetic

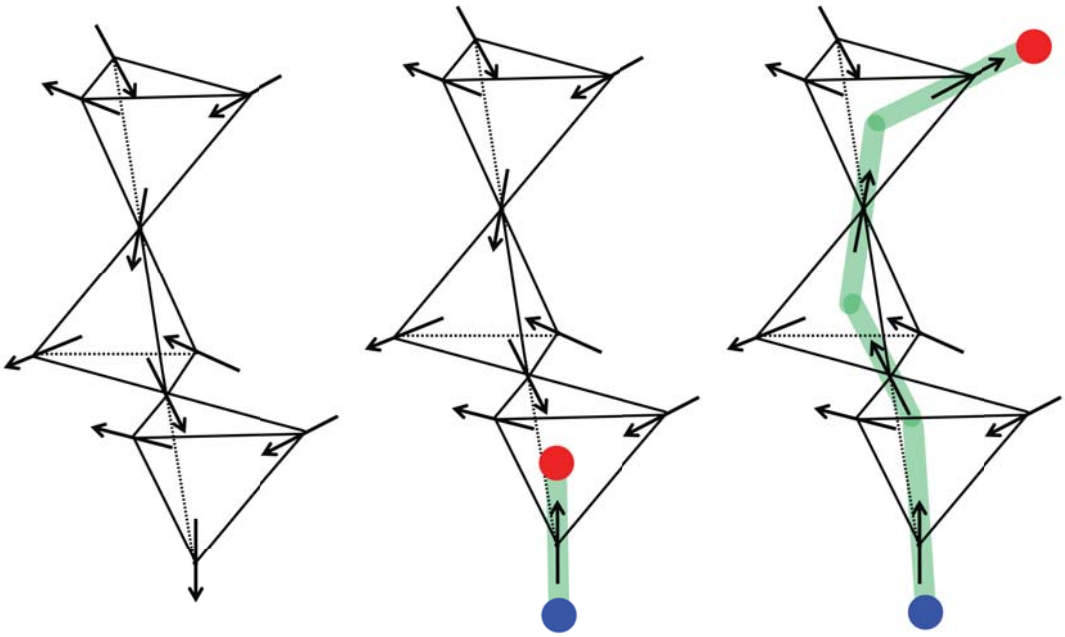

Figure 1.19 *In (a) spin ice the magnetic rare earth ions obey the ice rules such that two spins point towards and two spins point away from the centre of each tetrahedron. An excitation from the spin ice ground state in the form of (b) a spin flip on a tetrahedron creates a monopole (blue) and antimonopole (red) pair. These fractionalized magnetic particles can then (c) separate throughout the lattice through a series of spin flips with a Dirac string (green) carrying the magnetic flux between the magnetic monopoles.*

charge, a magnetic monopole, had ever been observed. In spin ice, however, local violations of the ice rules generated by flipping a single spin, create a magnetic source and magnetic sink on two neighbouring tetrahedra [36]. These defects can move apart from each other throughout the spin ice structure as an oppositely charged monopole-antimonopole pair connected by a Dirac string of flipped spins, see Figure 1.19 [37], [38]. The experimental and theoretical study of spin ice continues to be a important field of solid-state sciences. Current research involves the characterisation of the magnetic coulomb phase and the magnetic monopoles that spin ice supports, how their charge and current can be measured directly [39], [40], [41], [42] and the synthesis of novel spin ice phases through different synthetic methods, such as the high pressure high temperature technique [43].

1.4.4 Quantum Frustrated Spin Systems

The geometrically frustrated spin systems discussed above possess a large ground state degeneracy which allows spins to fluctuate down to a certain temperature at which point they will either order and adopt a non-colinear ground state, or freeze, as in the spin glass or spin ice systems. This is due to the fact that in these cases, the spin fluctuations are thermally driven and at increasingly lower temperatures, there is no longer sufficient energy to allow these spin fluctuations to persist. However, in frustrated spin systems with low spin magnetic ions ($S = \frac{1}{2}$) strong quantum effects and the cooperative tunnelling of spins means that there is no such energy barrier to prevent spins from fluctuating and evading long range order even in the thermodynamic limit of $T = 0$ [44], [45], [46]. This so called quantum spin liquid state was initially proposed by P. W. Anderson in 1973, who argued that a long range ordered Néel state was not the only possible ground state for a quantum frustrated antiferromagnet. Anderson put forward the concept of a resonating valence bond (RVB) state as a form of spin liquid that is built up from a linear superposition of $S = 0$ spin singlet pairs or valence bonds that cover the frustrated lattice [47]. In the 1980s, a possible link between the RVB state and superconductivity led to a surge in interest in spin liquid theory [48]. Since then, the study of this unusual state of matter has been a major theme in both theoretical and experimental solid state research in an attempt to understand its typically unpredictable behaviour and to find real materials that support its existence.

It is important at this point to give the necessary features that positively define a true quantum spin liquid. It is perhaps a common misconception that the spin liquid is simply defined by what it is not; its spins do not order nor do they freeze. However, the quantum spin liquid is, in fact, an entirely new phase of matter with many non-trivial properties. It is a non-magnetic ground state that is built up of well defined, localised magnetic moments, which allows for the emergence of unusual fractionalised quasi-particles as excitations from the ground state. The first key definition of a quantum spin liquid is that is does not develop any long range order in any local order parameter at any temperature down to $T = 0$. By pairing into spin singlet valence bonds, the spin symmetry in a spin liquid phase is rotationally invariant and the continuous spin symmetry is not broken [49], [50]. If these valence bond pairs cover the spin lattice in a periodic fashion such that there is long range order in the valence bond configuration and translational symmetry is broken, the system is known as a valence bond

crystal or solid (VBS). The distinction between the valence bond solid and a true RVB-liquid has an important consequence on the nature of their excitations. In a VBS, the elemetary excitations are confined to take integer spin values. In a RVB-type ground state these excitations can form deconfined $S = \frac{1}{2}$ entities known as spinons. This fractionalisation is the second key definition of a true quantum spin liquid. Most elementary excitations are either electron-like, with spin $S = \frac{1}{2}$ and charge $e = \pm 1$, or magnon like, with spin $S = 1$ and charge neutral [49]. The spinon can, therefore, be considered as a "fraction of an electron" given its $S = \frac{1}{2}$ and charge-0 state [44].

The fundamental building block in both the VBS and the RVB-liquid is the valence bond, which minimises the antiferromagnetic exchange interaction between two spins. A valence bond configuration is given by the product of all the valence bonds covering the spin lattice such the total spin of the configuration, $\mathbf{S}^2_{tot} = S_{tot}(S_{tot} + 1) = 0$, is non-magnetic. In certain systems, such as the $S = \frac{1}{2}$ Heisenberg kagome and pyrochlore lattices this type of valence bond ground state is energetically favourable such that it wins out over classical Néel order [44]. In any valence bond configuration, the energy of each spin singlet pair is minimised which acts to relieve the competing interactions that arise due to the geometrically frustrated lattice topology. It is however, very unlikely that one single valence bond configuration can exactly describe the ground state of a frustrated spin system and, therefore, the fluctuations between different valence bond coverings becomes very important in determining the true nature of a system.

Valence Bond Solids

An ordered or periodic arrangement of valence bond coverings acts to break some discrete lattice symmetry to form a VBS, see Figure 1.20. The dominant valence bond configuration in such a system can be unique, or there may be several degenerate configurations that are related by symmetry. In the case where there is a dominant configuration, local fluctuations can act to lower the energy of the system and drive it towards its true ground state, an example of the mechanism known as order by disorder [16]. The magnetic excitations in a VBC are gapped, integer spin $\Delta S = 1$ transitions that appear as a sharp feature in an inelastic neutron scattering spectrum [45]. In a VBS it is energetically unfavourable to liberate two free $S = \frac{1}{2}$ quasi-particles from the integer spin excitation as this would require a disruption in the valence bond order and create a string of

misaligned spin singlet pairs. The energy cost of this spinon separation process grows with the length of the string such that there is a strong force that acts to keep the two $S = \frac{1}{2}$ entities confined together. Deconfined spinons, a key feature of a true spin liquid phase, are thus not observed in a VBS as shown in Figure 1.20.

Quantum Spin Liquids

In a RVB-liquid the broad distribution of valence bond configurations or partitionings covering the lattice means that there is no preferred ordering of the spin singlet pairs. As a result, it becomes energetically favourable to resonate between the many different valence bond configurations, which gives rise to a fully resonant superposition ground state, shown in Figure 1.21, where no spatial symmetry is broken at all. The lack of an ordered valence bond configuration means that there is no mechanism to prevent the deconfinement of spinons. In a neutron scattering experiment, spinons are created in pairs due to the $\Delta S^z_{tot} = \pm 1$ selection rule, but can then propagate independently throughout the fluctuating "sea" of valence bond pairs. Spinon excitations are well understood in one-dimensional systems, such as a $S = \frac{1}{2}$ Heisenberg chain, where a spin flip excitation creates two spinons. The important property of such a fractionalised system is that these two fractional entities can separate to an infinite distance with only a finite energy cost. Neutron scattering experiments on such low-dimensional systems provides a proof of principal that such fractional excitations are observable [51]. An important feature that emerges alongside fractionalised spinons is the gauge field, which contains the path information between deconfined spinons [44].

It is now understood that not all quantum spin liquids are alike and that there are several different flavours of this exotic ground state. In the most general terms these can be classified into two main groups depending on the nature of their low energy excitation spectrum, which can either be gapped or gapless. Gapped quantum spin liquids are the simplest and best understood class, which are well described by the original, short range RVB ground state model of Anderson [47]. In modern terminology, gapped spin liquids are known as the Z_2 spin liquids, which possess a finite energy gap required to promote the non-magnetic singlet ground state to the excited triplet state with deconfined spinons. In addition, the Z_2 spin liquid has non-magnetic excitations, known as visons, which are

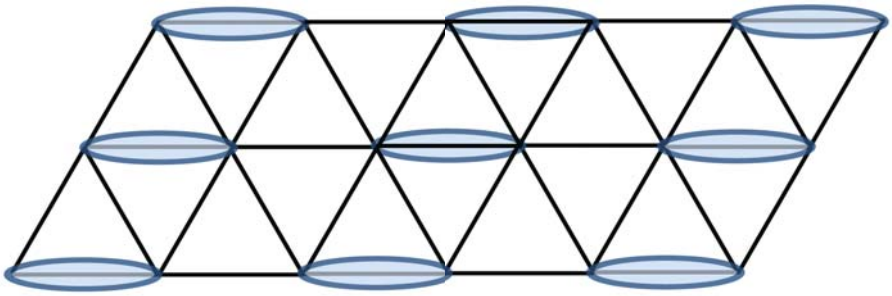

(a) *A valence bond crystal has an ordered configuration of valence bond partionings, shown here covering a triangular lattice. This configuration can be unique or dressed by local perturbations about a dominant configuration.*

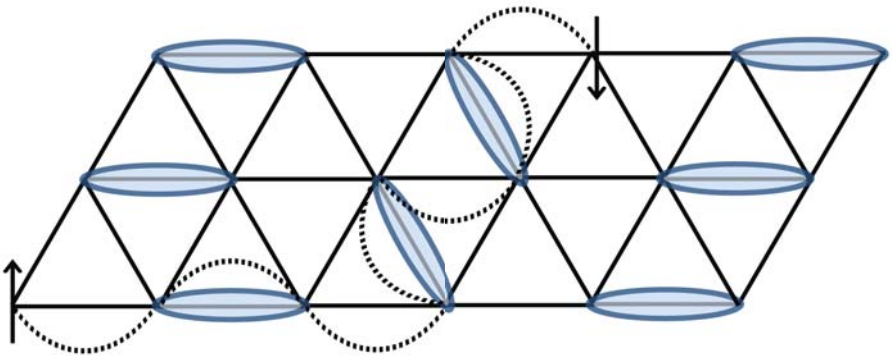

(b) *Due to the existence of an energetically favourable arrangement of valence bonds, two spinons experience a confinement potential that grows with the length of their separation path shown by the black dotted line.*

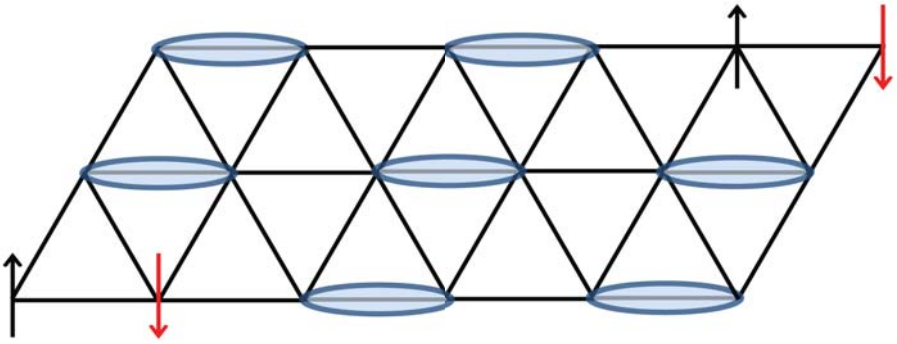

(c) *Due to this unfavourable misalignement of valence bonds, deconfined spinons are not observed as an excitation from the VBS ground state and instead one observes integer spin $\Delta S = 1$ transitions.*

Figure 1.20 *The valence bond solid ground state and its excitations.*

excitations from the Z_2 gauge field that arises as a result of fractionalisation and spinon deconfinement. Gapless spin liquids, known as long range RVB or algebraic

spin liquids, have a gapless spinon excitation spectrum. Unlike the Z_2 spin liquid ground state, in which spin-spin correlations decay exponentially with distance, gapless spin liquids have an algebraically decaying spin correlation function. Algebraic spin liquids are, therefore, sometime referred to as a critical phase as this algebraic decay is characteristic of a system close to a phase transition where correlations diverge before a long range ordered state is adopted [8].

The exact ground state of several important lattice spin models are still not very well understood and so the synthesis and experimental study of candidate materials and their comparison with the theoretical models remains an important task. For instance, the most recent predictions from density matrix renormalization group algorithms are that the ground state of a $S = \frac{1}{2}$ kagome antiferromagnet is a fully gapped, topologically ordered [52], [53] Z_2 spin liquid, with an estimated spin gap of 0.13(1) J [54], [55]. However, other theories expect a gapless spin liquid ground state [56], [57], [58], [59] and the best experimental candidate to date, the $S = \frac{1}{2}$ KAFM herbertsmithite, ($ZnCu_3(OH)_6Cl_2$), appears to be a gapless critical QSL [60], [61]. In the case of the $S = \frac{1}{2}$ pyrochlore antiferromagnet there is some uncertainty too as to whether the system should adopt a VBS ground state at low temperatures or a true RVB liquid state [62], [63], [64]. An experimental realisation of a quantum spin liquid should display an absence of long range order upon cooling in magnetic susceptibility and diffraction experiments. The absence of spin freezing and the persistence of incoherent spin fluctuations down to temperatures on the order of the energy scale of the spin gap in a gapped spin liquid, or $T = 0$ in the gapless case, can be observed by local probes such as nuclear magnetic resonance or muon spectroscopies. The experimental signature of deconfined spinons is energy continuum in the dynamical structure factor probed by inelastic magnetic neutron scattering [65], as opposed to a sharp mode of a conventional magnon excitation. Thermodynamic measurements, such as heat capacity, are also important for revealing the spectrum of low energy states [44].

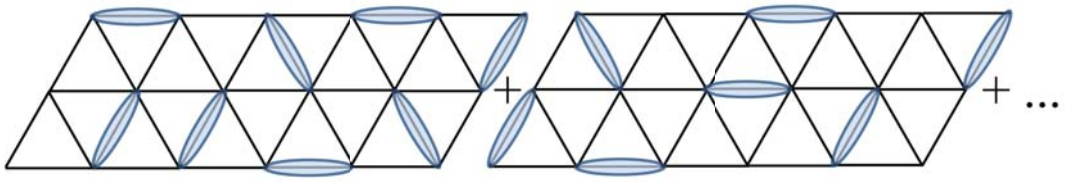

(a) *Short range RVB.*

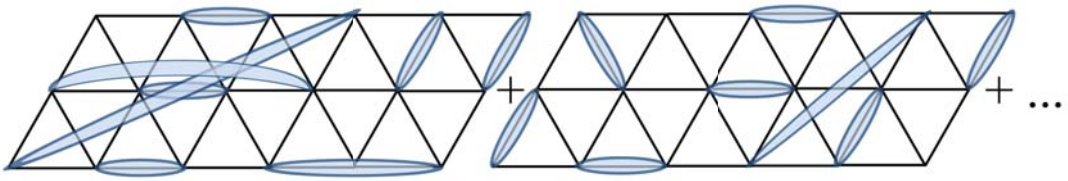

(b) *Long range RVB.*

Figure 1.21 *In a true quantum spin liquid ground state there is no preferred valence bond configuration and the ground state is fully resonant between many different valence bond configurations. The valence bond partitionings can be short range in nature or long range, leading to highly entangled spin singlet pairs that stretch across the spin lattice.*

Chapter 2

Experimental Methods

2.1 Solid State Synthesis and Sample Characterisation

Polycrystalline metal oxides are most commonly prepared by solid state ceramic synthesis [66]. Typically, stoichiometric amounts of the necessary precursors are ground together and pressed into a pellet before heating. The ceramic method usually requires high temperatures (up to 2000 °C) and small reactant particle size to allow for ionic diffusion and sample homogeneity. The time, temperature and heating profile of a particular reaction can each be varied in order to affect the final product. Samples can be heat treated in air in a box furnace or under a specific atmosphere in a tube furnace. For instance, if one wants to change the oxidation state of a transition metal in one of the precursor materials involved in the reaction, an oxidising (O_2) or reducing (H_2) environment could be used. If one wants to control or maintain a certain oxidation state an inert atmosphere of argon or nitrogen gases could be chosen, or the reaction could be carried inside a sealed ampoule. Within this Thesis the oxide pyrochlore $Lu_2Mo_2O_7$ was prepared by the solid state ceramic method.

The direct synthesis of nitrides and oxynitrides is limited by their lower stability in comparison with oxide materials [67]. The free energy of formation is lower for nitrides due to the higher bond enthalpy of nitrogen compared with oxygen and a more energetically costly electron affinity. The thermal ammonolysis of an oxide precursor in ammonia gas, however, allows for the formation of oxynitrides

at moderate temperatures (up to 1000 °C). During an ammonolysis reaction, ammonia gas acts as a nitriding agent whilst inducing a change in the oxidation state of the transition metals involved in order to charge balance the incorporation of the higher charge of the N^{3-} nitride anion into the oxide framework [68]. By varying the time, temperature, ammonia gas flow rate and sample surface area of an ammonolysis reaction it is possible to control the O : N ratio in the resulting oxynitride product. The thermal ammonolysis technique was employed to prepare samples of the oxynitride pyrochlore $Lu_2Mo_2O_{4.8}N_{1.7}$ presented in Chapter 4 along with the oxynitride perovskites presented in Chapter 6.

Another common preparative route in solid state chemistry is that of solvothermal synthesis [66]. This is most often used in the synthesis of microporous framework solids, such aluminosilicates and aluminophosphates, and metal organic framework (MOF) solids [69]. In these cases, the aluminate and silicate or phosphate sources are mixed together into a homogeneous gel along with a solvent, usually water, and heated in a Teflon-lined steel autoclave to temperatures around 250 °C. When water is used as a solvent, the process is known as hydrothermal synthesis. There are many parameters that can be varied during a synthesis: the relative ratio of reagents present in the gel, the solvent, the reaction pH and the reaction time and temperature, all of which can affect the final structure of the framework material that is formed. Organic template molecules, often amines, can also be added to the reaction system in order to direct the synthesis towards a particular structure. Ionothermal synthesis [70] makes use of ionic liquids, which act as both the solvent and the structure directing agent during a reaction. An ionic liquid is defined as a salt which consists of only ionic species with a melting point of less than 100 °C [71]. In recent years, there has been significant progress in synthetic chemistry through the development of the ionothermal technique [72], [73], [74]. Most importantly for this work, it was responsible for the discovery of a novel $S = \frac{1}{2}$ kagome antiferromagnet diammonium quinuclidinium vanadium (III,IV) oxyfluoride, $[NH_4]_2[C_7H_{14}N][V_7O_6F_{18}]$, or DQVOF, the study of which is presented in Chapter 5 [75].

Once a sample has been prepared, it is initially characterised by powder X-ray diffraction to ensure that the desired phase has been synthesised and that the reaction is complete. X-rays are a form of electromagnetic radiation with a wavelength on the order of the inter-atomic spacings within crystalline solids. As such, the diffraction of X-rays by their interaction with the electrons of an atom or ion can be used to yield structural information about a crystalline material.

X-rays for laboratory diffraction experiments are generated by bombarding a metal target, in this case copper, with electrons produced by a heated filament. The incident electrons ionise electrons from the $1s$ K shell of the target, which results in the emission of X-rays as the vacancies in the K shell are filled by higher electrons from the $2p$ L or $3s$ M shells. These are known as K_α and K_β radiation, respectively. Within this Thesis powder X-ray diffraction data were collected on a Bruker D8 powder X-ray diffractometer with monochromated Cu $K_{\alpha 1}$ $\lambda = 1.5406$ Å radiation. Further information on diffraction theory and the differences between neutron and X-ray scattering are given within § 2.2 of this Chapter. Thermogravimetric analysis, which involves taking a known mass of sample and oxidising it completely in air or oxygen and measuring the change in weight is also carried out so that one can determine the oxide content within the sample and hence, the oxidation state of the transition metal cations that it contains [76]. The nitrogen content of oxynitride samples was measured by elemental analysis on a Carlo Erba CHNS analyser through the EaSTChem Elemental Analysis Service at the School of Chemistry, University of St Andrews. The combination of elemental and thermogravimetric analyses, therefore, allows the total anion content of an oxynitride system to be accounted for [77]. Once suitable, well characterised samples were prepared their structural and magnetic properties that are of prime interest within this work were investigated through a combination of techniques, including neutron scattering studies, muon spin relaxation, magnetisation and heat capacity measurements. The rest of this chapter is dedicated to explaining the fundamental principals of these techniques and aims to describe how they have been of use in the study of the materials presented within the results chapters of this Thesis.

2.2 Neutron Scattering

There are several important properties of the neutron what make it a useful probe in the study of materials. For instance, the de Broglie wavelength of the neutron, $\lambda = h/mv$, is typically on the order of the inter-atomic spacings within crystalline solids ($\sim$ 1 - 2 Å) and, therefore, is an ideal tool with which to investigate the structure of crystals by diffraction methods. Furthermore, the energy of a neutron of wavevector $\mathbf{k}$, $E = \hbar^2 k^2/2m \sim$ meV is of the same energy scale of certain lattice and spin excitations that are of interest within condensed matter systems. The neutron is a charge neutral particle, which means that it

interacts very weakly with matter and penetrates deeply into a target where is it scattered by its interaction potential with the target nuclei. In addition to this nuclear interaction, the neutron possesses a magnetic moment such that it is also scattered by its interaction with the unpaired electrons within a magnetic sample [78], [79].

During a neutron scattering experiment, the neutron can undergo a change in wavevector, from an initial wavevector state $|\mathbf{k}\rangle$ to a final state wavevector state $|\mathbf{k}'\rangle$. This momentum transfer is denoted $\hbar\mathbf{Q}$, where $\mathbf{Q}$ is the scattering vector shown in Figure 2.1,

$$\mathbf{Q} = \mathbf{k} - \mathbf{k}' \tag{2.1}$$

The wavevector $\mathbf{k}$ indicates the direction of propagation of the wave associated with a neutron and its magnitude, the wavenumber is given by,

$$|\mathbf{k}| = k = \frac{2\pi}{\lambda} \tag{2.2}$$

If the energy of the incident neutron, E, remains unchanged during its interaction with the sample, such that $k = k'$, the scattering process is known as *elastic*. Upon inspection of the elastic scattering process depicted in Figure 2.1, it can be shown that the magnitude of the scattering vector $\mathbf{Q}$ is given by,

$$|\mathbf{Q}| = Q = \frac{4\pi \sin\theta}{\lambda} \tag{2.3}$$

If the incident neutron, with initial energy E, loses or gains energy by an energy transfer with the sample to give a final energy, E', then the scattering is *inelastic* and the energy transfer is given by,

$$\hbar\omega = E - E' \tag{2.4}$$

In a typical neutron scattering experiment, one would like to observe the proportion of incident neutrons that emerge from a scattering system with a given energy and momentum transfer. This information is contained within a four-dimensional function or scattering law commonly referred to as $S(\mathbf{Q}, \omega)$. When the scattering process is elastic and $\omega = 0$, this collapses to a three-dimensional

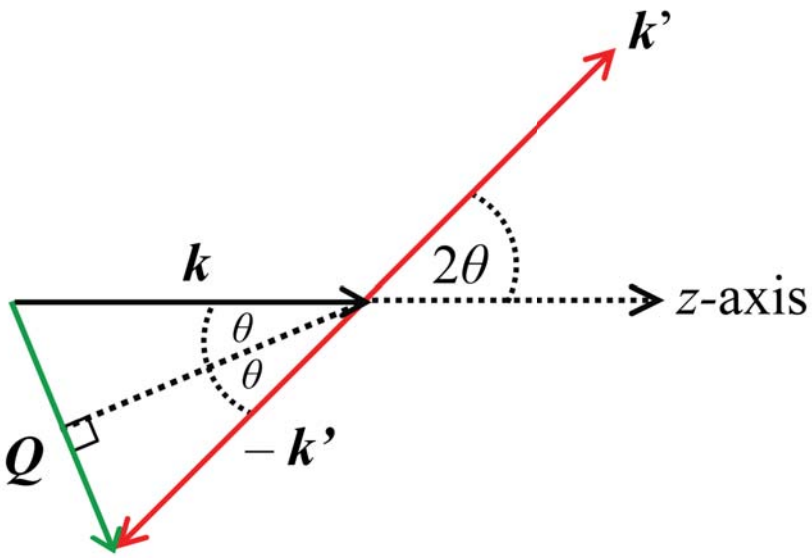

(a) *Elastic scattering.*

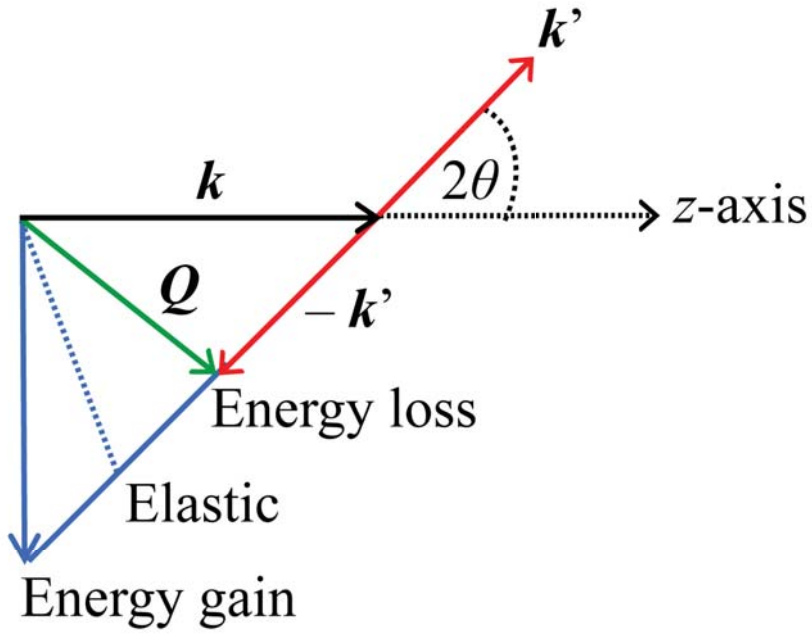

(b) *Inelastic scattering.*

Figure 2.1 *The scattering vector* **Q** *for (a) an elastic scattering experiment in which* $|\mathbf{k}| = |\mathbf{k}'|$ *and (b) an inelastic scattering experiment in which* $|\mathbf{k}| \neq |\mathbf{k}'|$ *due to an energy transfer between the incident neutron and the sample.*

scattering law known as $S(\mathbf{Q})$ [80]. Figure 2.2 shows the general geometry of such a neutron scattering experiment. The quantity that is measured during a

neutron scattering experiment is the partial differential cross section [78],

$$\frac{d^2\sigma}{d\Omega dE'} = \textit{the number of neutrons of energy } E \textit{ scattered into a solid angle } d\Omega \textit{ with a final energy between } E' \textit{ and } E' + dE'/\Phi d\Omega dE' \tag{2.5}$$

where Φ is the flux of the incident neutrons. If only the elastic scattering is of interest and the final energy of the scattered neutron is not analysed, then the differential cross section is observed [78],

$$\frac{d\sigma}{d\Omega} = \textit{the number of neutrons scattered into a solid angle } d\Omega/\Phi d\Omega \tag{2.6}$$

The total scattering cross section, σ_{tot}, gives the number of neutrons scattered in all directions per second.

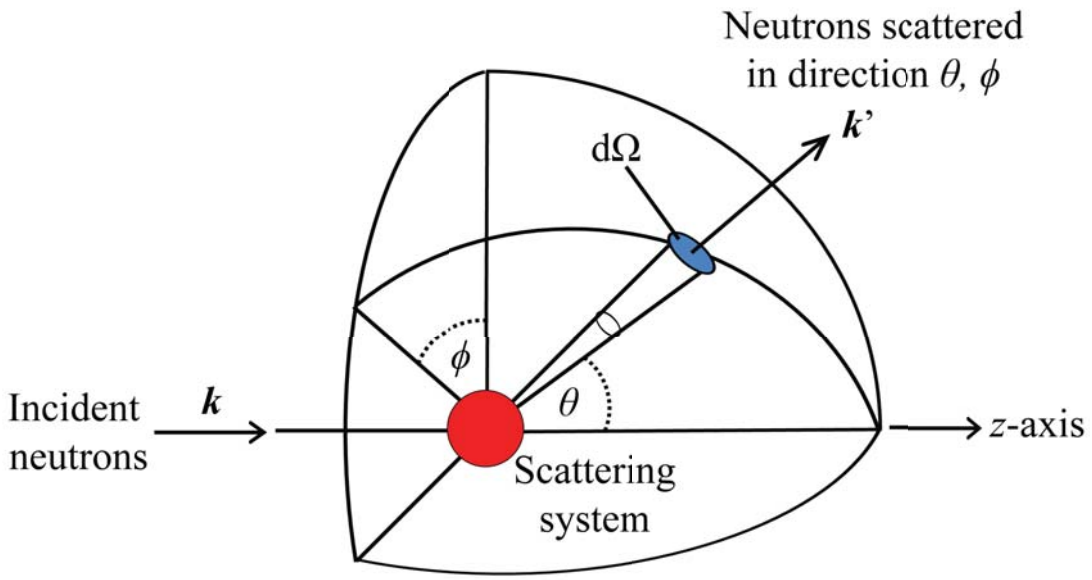

Figure 2.2 *The geometry of a scattering experiment in which incident neutrons with wave vector* $\mathbf{k}$ *are scattered into a solid angle* $d\Omega$ *with a final wave vector* $\mathbf{k}'$.

2.2.1 Nuclear Neutron Scattering

When a neutron interacts with a single fixed nucleus, the nucleus acts as a point scatterer *i.e.* the length scale of the nuclear forces that the neutron experiences ($\sim 10^{-15}$ m) is several orders of magnitude smaller than incident neutron wavelength ($\sim 10^{-10}$ m). As a result, the scattered neutron takes the form of a spherically symmetrical wave [80]. If one takes the position of the scattering nucleus to be at the origin and the direction of the incident neutron wave vector $\mathbf{k}$ aligned along the z-axis, then the wavefunction of the incoming neutron plane wave is given by,

$$\psi_{inc} = \exp(ikz) \tag{2.7}$$

The wavefunction of the spherically symmetric scattered wave, shown in Figure 2.3, at a distance r from the nucleus is denoted,

$$\psi_{sc} = -\frac{b}{r}\exp(ikr) \tag{2.8}$$

where b is known as the neutron scattering length. The scattering interaction between the neutron and the nucleus is a resonance phenomenon that results in the formation of a compound nucleus of the neutron and scattering nucleus. The behaviour of this compound state and, hence, the value of b depends on particular details of a specific nuclide and on the spin state of the compound nucleus, which can take values of $I + \frac{1}{2}$ or $I - \frac{1}{2}$ for a system of non-zero nuclear spin, $I \neq 0$. $I = 0$ nuclei only have one value of b and the spin state on the compound nucleus is $\frac{1}{2}$. The total scattering cross section, σ_{tot}, is then dependent on the nuclear scattering length according to [80],

$$\sigma_{tot} = 4\pi b^2 \tag{2.9}$$

A typical scattering system, however, will contain a very large number of nuclei and for each element present within the system, the scattering length b can vary from nucleus to nucleus due to the formation of different neutron-nucleus spin states or the presence of difference nuclear isotopes. This gives rise to the incoherent scattering of neutrons (spin incoherent and isotope incoherent

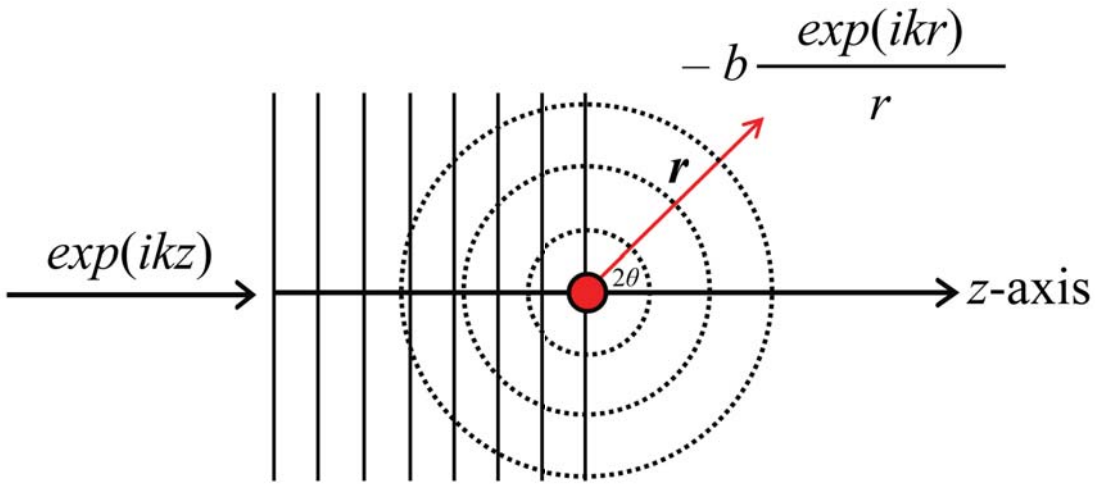

Figure 2.3 *An incident beam of neutron plane waves are scattered isotropically and elastically as spherical waves by their interaction with a single fixed nucleus.*

scattering, respectively.) The coherent scattering cross section,

$$\sigma_{coh} = 4\pi(\bar{b})^2 \tag{2.10}$$

reflects the scattering from the mean scattering length of the system, $\bar{b}$, which gives rise to interference effects between the scattered neutron wave functions, and hence, diffraction if the scattering system is a crystalline solid. The incoherent scattering cross section,

$$\sigma_{inc} = 4\pi(\bar{b^2} - (\bar{b})^2) \tag{2.11}$$

then reflects the random deviation of the scattering lengths from their mean value values. This incoherent scattering does not give rise to interference effects but rather leads to diffuse scattering of neutrons that adds to the background of a diffraction profile.

In order to obtain an expression for the nuclear differential scattering cross section that one measures during an elastic neutron scattering experiment, it is necessary to make use of a standard result in quantum mechanics, Fermi's Golden Rule [78], [79]. By considering the definition of the differential scattering cross section given

in Equation 2.6, one can write,

$$\frac{d\sigma}{d\Omega} = \frac{1}{\Phi}\frac{1}{d\Omega}\sum_{\mathbf{k}'} W_{\mathbf{k}\to\mathbf{k}'} \tag{2.12}$$

where $W_{\mathbf{k}\to\mathbf{k}'}$ is the number of transitions per second from the incident wavevector state $|\mathbf{k}\rangle$ to the final wavevector state $|\mathbf{k}'\rangle$. This determines the probability of the incident neutron undergoing a transition from its initial plane wave state to its final wave state, which according to Fermi's golden rule, is formally given by [78],

$$W_{\mathbf{k}\to\mathbf{k}'} = \frac{2\pi}{\hbar}|\langle\mathbf{k}'|V(\mathbf{Q})|\mathbf{k}\rangle|^2\rho_{\mathbf{k}'} \tag{2.13}$$

where $V(\mathbf{Q})$ is the interaction potential through which the transition from the $|\mathbf{k}\rangle$ state to the $|\mathbf{k}'\rangle$ state occurs and $\rho_{\mathbf{k}'}$ is the density of final $|\mathbf{k}'\rangle$ states. In scattering theory, Fermi's golden rule is equivalent to the Born approximation, which implicitly assumes that the scattering interaction between the neutron and the nucleus is weak and that the scattered neutron has a negligible effect on the incident beam [79], [80]. By evaluating the density of final states $\rho_{\mathbf{k}'}$ [78], one arrives at the following expression for the differential cross section,

$$\frac{d\sigma}{d\Omega} = \left(\frac{m}{2\pi\hbar^2}\right)^2 |\langle\mathbf{k}'|V|\mathbf{k}\rangle|^2 \tag{2.14}$$

where m is the mass of the neutron. If the scattering potential of the neutron for the jth nucleus with position vector $\mathbf{R}_j$ in the scattering system has the form $V_j(\mathbf{r}-\mathbf{R}_j)$, then the scattering potential for the entire scattering system is given by,

$$V = \sum_j V_j(\mathbf{r}-\mathbf{R}_j) = \sum_j V_j(\mathbf{x}_j) \tag{2.15}$$

where $\mathbf{r}$ is the neutron coordinate and $\mathbf{x}_j = \mathbf{r}-\mathbf{R}_j$.

Evaluating the matrix element in Equation 2.14 gives,

$$\langle \mathbf{k}' | V | \mathbf{k} \rangle = \sum_j V_j(\mathbf{Q}) \exp(i\mathbf{Q}\cdot\mathbf{R}_j) \tag{2.16}$$

where,

$$V_j(\mathbf{Q}) = \int V_j(\mathbf{x}_j) \exp(i\mathbf{Q}\cdot\mathbf{x}_j) d\mathbf{x}_j \tag{2.17}$$

is the Fourier transform of the scattering potential for the jth nucleus. In order to evaluate the expression given in Equation 2.17 further, it is necessary to find a function that describes this scattering potential. Since the nuclear interaction between the neutron and the nuclei within the scattering system is known to be very short-ranged, the potential can take the form of a three-dimensional δ-function [81],

$$V(\mathbf{x}_j) = \frac{2\pi\hbar^2}{m} b\delta(\mathbf{x}_j) \tag{2.18}$$

which as a function of the scattering vector $\mathbf{Q}$ is given by,

$$V_j(\mathbf{Q}) = \int \frac{2\pi\hbar^2}{m} \delta(\mathbf{x}_j) \exp(i\mathbf{Q}\cdot\mathbf{x}_j) d\mathbf{x}_j = \frac{2\pi\hbar^2}{m} b_j \tag{2.19}$$

Inserting this into Equation 2.14, along with the evaluated matrix element given in Equation 2.16, one obtains a general expression for the differential cross section for nuclear elastic neutron scattering,

$$\frac{d\sigma}{d\Omega} = |\sum_j \exp(i\mathbf{Q}\cdot\mathbf{R}_j)|^2 \tag{2.20}$$

For inelastic neutron scattering, one must consider the energy transfer, $\hbar\omega$, between the neutron and the scattering system, which undergoes a transition from an initial state $|\lambda\rangle$ to its final state $|\lambda'\rangle$. The energy distribution of the scattered neutrons takes the form of delta function, so the inelastic scattering

cross section can be written as [78],

$$\frac{d^2\sigma}{d\Omega dE'} = \frac{k'}{k}\left(\frac{m}{2\pi\hbar}\right)^2 |\langle \mathbf{k}'\lambda'|V|\mathbf{k}\lambda\rangle|^2 \delta(E_\lambda - E_{\lambda'} + \hbar\omega) \tag{2.21}$$

By summing over all final $|\lambda'\rangle$ states and averaging with respect to $|\lambda\rangle$ one obtains the general expression for the partial differential cross section, which becomes [78],

$$\frac{d^2\sigma}{d\Omega dE'} = \frac{k'}{k}\frac{1}{2\pi\hbar}\sum_{jj'}\int_{-\infty}^{\infty} \langle \exp(-i\mathbf{Q}\cdot\mathbf{R}_j(0))\exp(i\mathbf{Q}\cdot\mathbf{R}_j(t))\rangle \exp(-i\omega t)dt \tag{2.22}$$

Nuclear Scattering by Crystalline Materials

A crystalline material is a highly ordered phase of matter with a periodic structure that gives rise to the diffraction of radiation, such as neutrons and X-rays. A crystal can be described in terms of a lattice, a periodic array of points, onto which a chemical entity, such as an atom or ion can be superimposed [80], [82]. These lattice points are displaced from the origin by the lattice vector,

$$\mathbf{l} = n_1\mathbf{a} + n_2\mathbf{b} + n_2\mathbf{c} \tag{2.23}$$

where n_1, n_2 and n_3 are any set of integers such that any point in the lattice can be translated to an equivalent one by integer multiples of **a**, **b** and **c**. The crystal lattice, therefore, reflects the underlying periodicity of a structure and the translational symmetry that is a special property of crystalline solids. The vectors **a**, **b** and **c** form a parallelepiped that defines the unit cell of the crystal structure shown in Figure 2.4. This is smallest repeat unit in a crystalline solid, which is extended in all directions to give a three-dimensional periodic structure. The magnitudes of the unit cell vectors, (a, b, c), and the angles between them, (α, β, γ) are known as the lattice constants.

The differential cross section for elastic scattering by a crystal of n nuclei is given

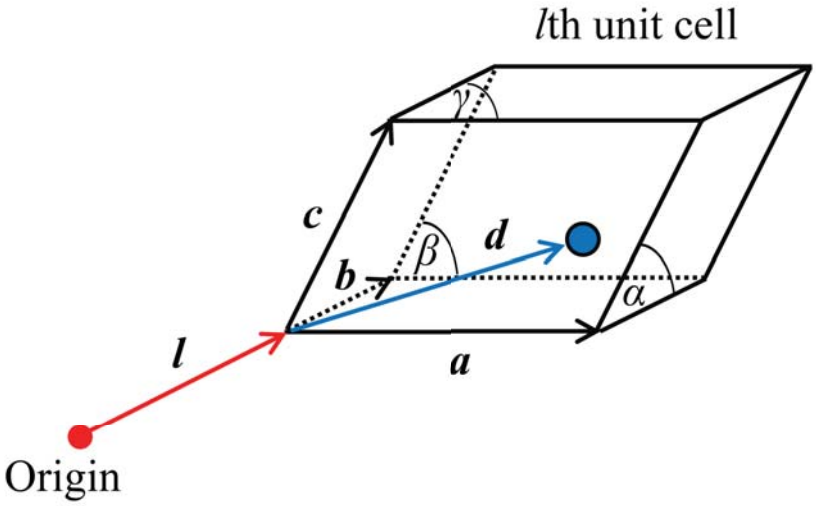

Figure 2.4 *A unit cell defined by three vectors* **a**, **b** *and* **c** *which is displaced from the origin by the lattice vector* **l**. *The position of a particular nucleus contained within this unit cell is given in terms of its fractional coordinates* (x_d, y_d, z_d) *by the position vector* **d**.

by,

$$\frac{d\sigma}{d\Omega} = |\sum_n b_n \exp(i\mathbf{Q}\cdot\mathbf{r}_n)|^2 \tag{2.24}$$

where the position vector of a particular nucleus, $\mathbf{r}_n$, is given by,

$$\mathbf{r}_n = \mathbf{l} + \mathbf{d} \tag{2.25}$$

The differential cross section can thus be re-written as,

$$\frac{d\sigma}{d\Omega} = |\sum_l \exp(i\mathbf{Q}\cdot\mathbf{l}) \sum_d b_d \exp(i\mathbf{Q}\cdot\mathbf{d})|^2 \tag{2.26}$$

where **l** and **d** are the vectors shown in Figure 2.4. The summation over **l**, the lattice vector, will cancel out to zero unless all of the terms in the sum are equal such that,

$$\exp(i\mathbf{Q}\cdot\mathbf{l}) = 1 \tag{2.27}$$

for all **l**. This gives rise to non-zero scattering at well-defined points in **Q**. This

situation is satisfied when the scattering vector, $\mathbf{Q}$, is equal to the reciprocal lattice, $\boldsymbol{\tau}$, given by [83],

$$\boldsymbol{\tau} = h\mathbf{a}^* + k\mathbf{b}^* + l\mathbf{c}^* \tag{2.28}$$

where,

$$\mathbf{a}^* = \frac{2\pi \mathbf{b}\times\mathbf{c}}{\mathbf{a}\cdot(\mathbf{b}\times\mathbf{c})} \tag{2.29}$$

$$\mathbf{b}^* = \frac{2\pi \mathbf{c}\times\mathbf{a}}{\mathbf{a}\cdot(\mathbf{b}\times\mathbf{c})} \tag{2.30}$$

and

$$\mathbf{c}^* = \frac{2\pi \mathbf{a}\times\mathbf{b}}{\mathbf{a}\cdot(\mathbf{b}\times\mathbf{c})} \tag{2.31}$$

are the reciprocal lattice vectors. An example of the relationship between a real space lattice and its reciprocal lattice is shown in Figure 2.5. The indices h, k and l are known as the Miller indices, which describe how parallel planes of lattice points cut the axes of a unit cell at fractional parts, given by the reciprocals of their intercepts with the a, b and c unit cell axes, respectively (see Figure 2.5). The spacing between these parallel planes is denoted d_{hkl}. The reciprocal lattice has two important properties. Firstly, its direction is normal to a particular hkl plane and secondly, its magnitude is given by [82],

$$|\boldsymbol{\tau}_{hkl}| = \frac{2\pi}{d_{hkl}} \tag{2.32}$$

The condition for strong elastic scattering of neutrons from a crystalline solid is known as the Laue condition, from which it is possible to derive the fundamental law of scattering theory,

$$|\mathbf{Q}| = |\boldsymbol{\tau}_{hkl}| \tag{2.33}$$

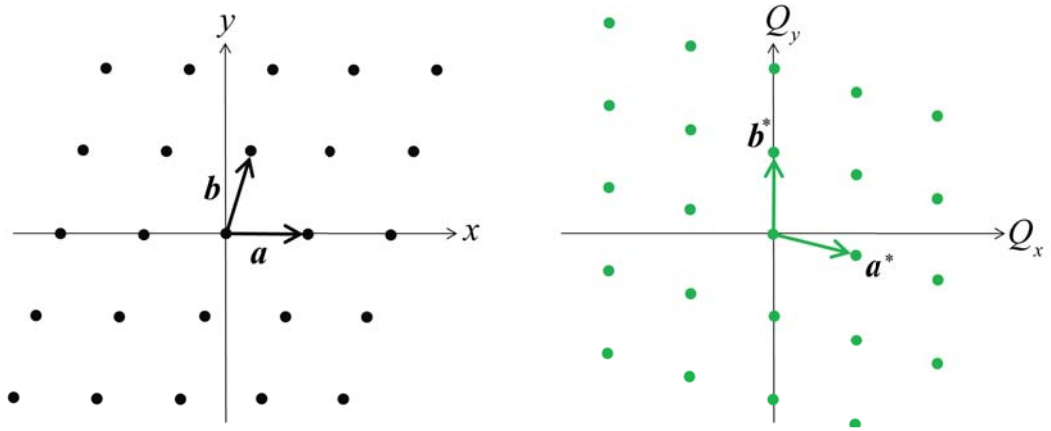

(a) *Real space lattice.* **(b)** *Reciprocal lattice.*

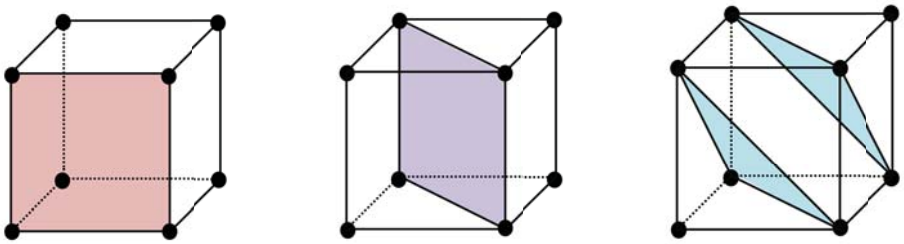

(c) 100 *plane.* **(d)** 110 *plane.* **(e)** 111 *plane.*

Figure 2.5 *The (a) two-dimensional crystal lattice with lattice vectors* **a** *and* **b** *has a (b) reciprocal lattice with reciprocal lattice vectors* $\mathbf{a}^*$ *and* $\mathbf{b}^*$ *such that* $\mathbf{a}\perp\mathbf{b}^*$ *and* $\mathbf{b}\perp\mathbf{a}^*$ *and* $|\mathbf{a}|/|\mathbf{b}| = |\mathbf{b}^*|/|\mathbf{a}^*|$. *The Miller indices describe parallel planes of atoms within a crystal structure where h, k and l denote the reciprocals of the intercepts of the particular plane with unit cell axes. Shown here are the (c)* 100*, (d)* 110 *and (e)* 111 *Miller planes for a primitive cubic unit cell.*

$$Q = \tau_{hkl} \tag{2.34}$$

$$\frac{4\pi \sin\theta_{hkl}}{\lambda} = \frac{2\pi}{d_{hkl}} \tag{2.35}$$

Bragg's law,

$$\lambda = 2d_{hkl} sin\theta_{hkl} \tag{2.36}$$

The sharp points of scattering intensity that arise when the Laue condition is met are known as Bragg peaks and the pattern of Bragg peaks observed in a diffraction pattern is characteristic of parallel *hkl* planes of atoms with different

d-spacings and orientations within a sample, see Figure 2.6.

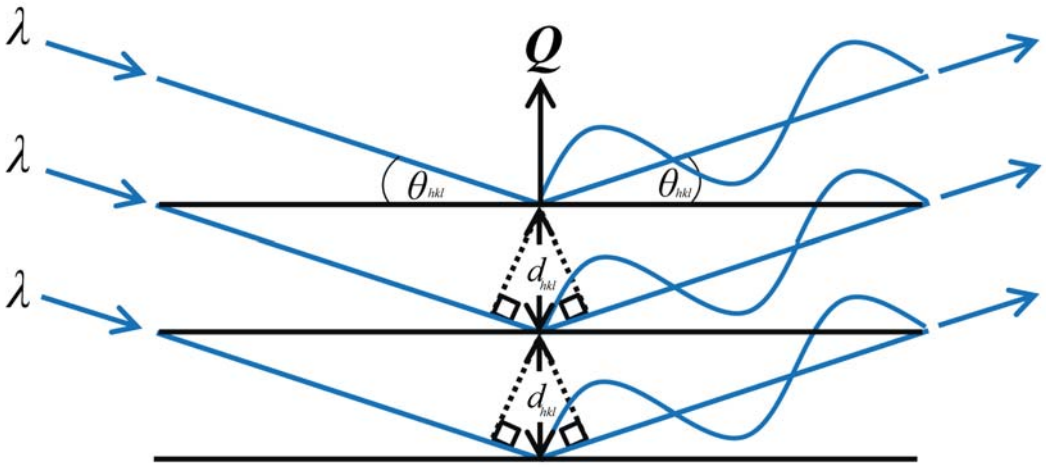

Figure 2.6 *Bragg's law can also be derived by considering the scattering from parallel Miller planes of d-spacing, d_{hkl}. If the path difference between neutron scattered from nuclei in neighbouring planes, $2d_{hkl}\sin\theta_{hkl}$, is an integer multiple of the incident neutron wavelength, λ, then constructive interference of the scattered neutron waves results and a Bragg peak corresponding to that particular d-spacing and scattering angle θ_{hkl} is observed in the diffraction pattern.*

The position vector $\mathbf{d}$ given in Equation 2.25 for a particular nucleus within the unit cell (see Figure 2.4) can be written in terms of its fractional coordinates, (x_d,y_d,z_d),

$$\mathbf{d} = x_d\mathbf{a} + y_d\mathbf{b} + z_d\mathbf{c} \tag{2.37}$$

Under the Laue condition, the differential cross section then becomes,

$$\frac{d\sigma}{d\Omega} = N^2|\sum_d b_d \exp(i(h\mathbf{a}^* + k\mathbf{b}^* + l\mathbf{c}^*)\cdot(x_d\mathbf{a} + y_d\mathbf{b} + z_d\mathbf{c}))|^2 = N^2|\mathbf{F}_{hkl}|^2 \tag{2.38}$$

where N is the number of unit cells within the crystal and $\mathbf{F}_{hkl}$ is known as the structure factor,

$$\mathbf{F}_{hkl} = \sum_d b_d \exp(2\pi i(hx_d + ky_d + lz_d)) \tag{2.39}$$

The structure factor, F_{hkl}, is related to the intensity of a particular Bragg reflection, I_{hkl}, by,

$$I_{hkl} \propto F_{hkl}^2 \tag{2.40}$$

such that the measurement of the intensity of a Bragg peak only yields the magnitude of its structure factor and not its sign. This is known as the crystallographic phase problem [80].

Powder Averaging and Rietveld Refinement

A powder or polycrystalline sample contains an infinite number of randomly orientated crystallites. Neutron scattering experiments on powder samples are important given that it is not always possible to prepare a single crystal of a material suitable for neutron diffraction. The lack of definite orientation of the crystallites in a powder means that the resulting differential cross section is spherically symmetric [80]. As a consequence, some of the directional information contained in the diffraction pattern is lost as it no longer depends upon the azimuthal angle ϕ, shown in Figure 2.2. This angular invariance gives rise to cones of diffraction, known as Debye-Scherrer cones shown in Figure 2.7, such that rings of equal scattering intensity are observed perpendicular to the incident beam. From this, one can obtain a two-dimensional powder diffraction pattern, which shows the intensity of the Bragg peaks typically as a function of 2θ or d-spacing.

The peaks in a powder diffraction pattern occur when the spacing between parallel planes of atoms and the diffraction angle satisfy Bragg's law. Since this condition may be satisfied by more than one set of Miller indices simultaneously, the area under one particular Bragg peak may be composed of intensities from more than one hkl reflection. This is known as the peak overlap problem. The Rietveld method is a procedure that addresses this problem of peak overlap in powder diffraction data [84]. It treats each data point in a diffraction pattern as an individually observed intensity and uses knowledge of instrument parameters, such as peak shape and width, and sample parameters, such as position and intensity of reflections, to model a diffraction profile which is refined against the experimental data by least squares methods in order to achieve a best fit. The Rietveld method, therefore, allows for structural information to be extracted

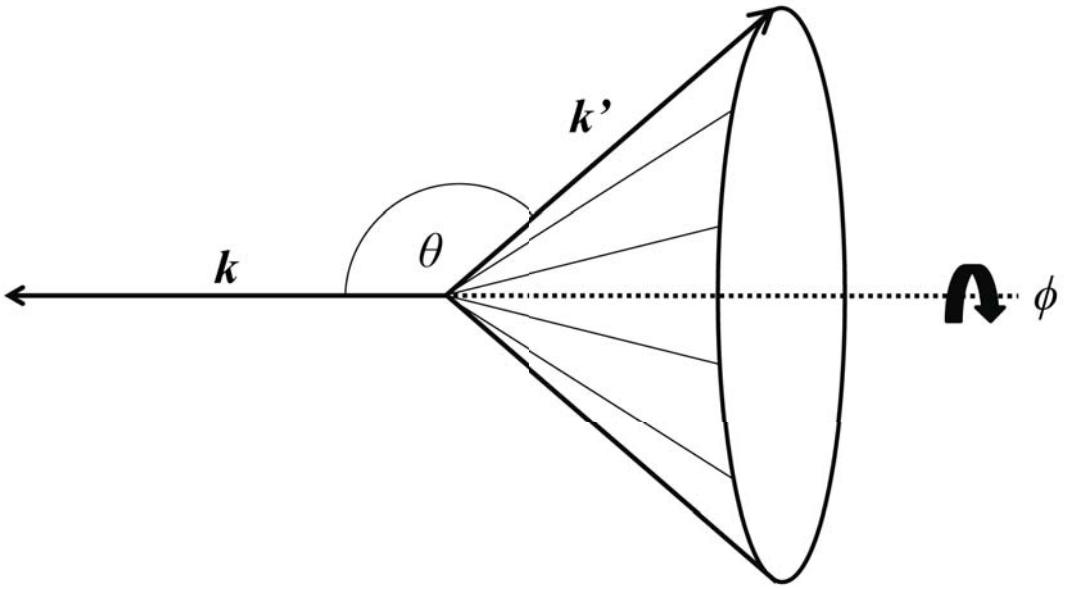

Figure 2.7 *A Debye-Scherrer cone that gives a ring of scattering intensity from a powder sample.*

from a powder diffraction pattern with peak overlap. In order to carry out a Rietveld analysis of powder diffraction data a reasonable starting structural model is required along with certain instrumental details specific to the diffractometer on which the data were collected. Parameters within the model are then refined in order to minimise the sum of the differences between the model data points, $y(calc)$, and the observed data points, $y(obs)$ in a least-squares process over all i steps within the diffraction pattern given by,

$$D = \sum w_i(y_i(obs) - y_i(calc))^2 \tag{2.41}$$

where w_i is the inverse of the total observed intensity at the ith step. One aims to obtain a stable refinement of the model to the data that converges to a global minimum. A criterion often used to determine the goodness of a fit is the weighted R-factor,

$$R_{wp} = \left(\frac{D}{\sum w_i(y_i(obs))^2} \right)^{\frac{1}{2}} \tag{2.42}$$

The χ^2-factor is also commonly quoted as an indication of how well the fitted

model accounts for the data, which is given by,

$$\chi^2 = \left(\frac{R_{wp}}{R_e}\right)^2 \tag{2.43}$$

where R_e is known as the expected R-factor, which is dependent upon the the counting statistics for the data in comparison to the model errors. For a statistically perfect fit, $\chi^2 = 1$.

The model parameters that are typically refined include structural parameters such as atomic coordinates, site occupancies and cell constants, thermal parameters, background coefficients and profile parameters including peak shape and sample displacement or zero point. Within this work, Rietveld refinements were performed using the GSAS program [85].

2.2.2 Magnetic Neutron Scattering

In addition to nuclear scattering, the neutron is also deflected through the interaction between its dipole moment and that of an unpaired electron in a magnetic sample. The scattering potential for magnetic scattering is far more complicated than for the nuclear case, which is a result of the long-range nature of the magnetic forces that are responsible for the scattering process. Magnetic scattering is ion specific and $\mathbf{Q}$ dependent, which is to say that it is subject to a form factor $F(\mathbf{Q})$ such that magnetic scattering intensity falls off with increasing $\mathbf{Q}$. Unlike nuclear scattering, magnetic neutron scattering is also highly anisotropic and a fundamental rule of magnetic scattering is that the neutron only experiences the component of the sample magnetisation that is perpendicular to the scattering vector [78], [86], denoted $\mathbf{M}_\perp$ and shown in Figure 2.8.

In order to obtain the scattering cross sections for the magnetic interaction between a neutron and a scattering system, it is necessary to consider the potential felt by the dipole moment of the neutron and the magnetic field generated by the unpaired electrons in a magnetic material [78], [87]. The magnetic dipole moment of the neutron is given by,

$$\boldsymbol{\mu}_n = -\gamma_n \mu_n \boldsymbol{\sigma} \tag{2.44}$$

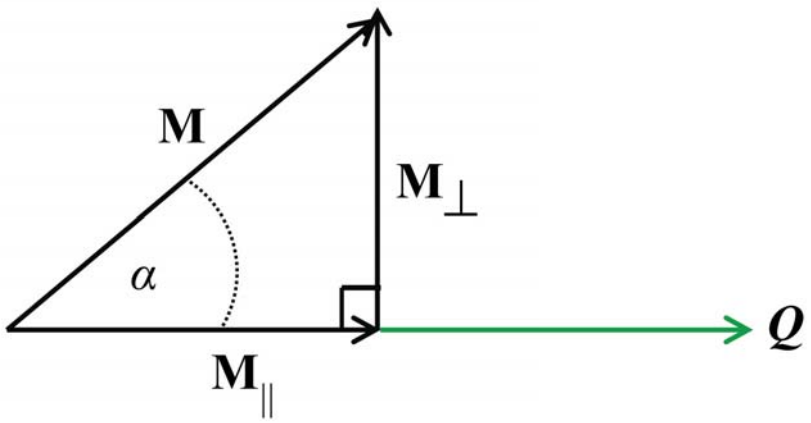

Figure 2.8 *The neutron only sees the component of the sample magnetisation,* $\mathbf{M}$*, that is perpendicular to the scattering vector,* $\mathbf{M}_\perp$*.*

where γ_n is the nuclear gyromagnetic ratio, μ_n is the nuclear magneton $e\hbar/2m_p$ and $\boldsymbol{\sigma}$ is the Pauli spin operator for the neutron [3]. The magnetic dipole moment corresponding to the unpaired electron in the scattering system is then,

$$\boldsymbol{\mu}_e = -2\mu_B \mathbf{s} \tag{2.45}$$

where μ_B is the Bohr magneton $e\hbar/2m_e$ and $\mathbf{s}$ is the spin of the unpaired electron. The total magnetic field generated by an unpaired electron of momentum $\mathbf{p}$ at a distance $\mathbf{R}$ from the electron consists of contributions from both spin (S)and orbital (L) moments,

$$\mathbf{B} = \mathbf{B}_S + \mathbf{B}_L = \frac{\mu_0}{4\pi}\left(\bigtriangledown\times\left(\frac{\mu_e\times\hat{\mathbf{R}}}{R^2}\right) - \frac{2\mu_B}{\hbar}\frac{\mathbf{p}\times\hat{\mathbf{R}}}{R^2}\right) \tag{2.46}$$

The potential felt by the neutron in this magnetic field is then given by,

$$V_m = -\boldsymbol{\mu}_n\cdot\mathbf{B} = -\frac{\mu_0}{4\pi}\gamma_n\mu_n 2\mu_B\sigma\cdot\left(\bigtriangledown\times\left(\frac{\mu_e\times\hat{\mathbf{R}}}{R^2}\right) + \frac{1}{\hbar}\frac{\mathbf{p}\times\hat{\mathbf{R}}}{R^2}\right) \tag{2.47}$$

which can be inserted into the partial differential cross section, where one must now also consider the spin state transition of the neutron during the scattering interaction, $|\mathbf{S}\rangle\rightarrow|\mathbf{S}'\rangle$ in addition to the wave vector state of the neutron and state

of the scattering system that were necessary in the case of nuclear scattering,

$$\frac{d^2\sigma}{d\Omega dE'} = \frac{k'}{k}\left(\frac{m}{2\pi\hbar^2}\right)^2 |\langle \mathbf{k}'\mathbf{S}'\lambda'|V_m|\mathbf{k}\mathbf{S}\lambda\rangle|^2 \delta(E_\lambda - E_{\lambda'} + \hbar\omega) \tag{2.48}$$

Evaluating the spatial part of the matrix element, $\langle \mathbf{k}'|V_m|\mathbf{k}\rangle$, for the ith electron with spin $\mathbf{s}_i$, position vector $\mathbf{r}_i$ and momentum $\mathbf{p}_i$ yields,

$$\langle \mathbf{k}'|V_m^i|\mathbf{k}\rangle = 4\pi \exp(i\mathbf{Q}\cdot\mathbf{r}_i)(\hat{\mathbf{Q}}\times(\mathbf{s}_i\times\hat{\mathbf{Q}}) + \frac{i}{\hbar Q}(\mathbf{p}_i\times\hat{\mathbf{Q}})) \tag{2.49}$$

Summing over all unpaired electrons one obtains,

$$\sum_i \langle \mathbf{k}'|V_m^i|\mathbf{k}\rangle = 4\pi\mathbf{M}_\perp(\mathbf{Q}) = \hat{\mathbf{Q}}\times(\mathbf{M}(\mathbf{Q})\times\hat{\mathbf{Q}}) \tag{2.50}$$

where $\mathbf{M}_\perp(\mathbf{Q})$ is the component of the Fourier transform of the sample magnetisation that is perpendicular to the scattering vector,

$$\mathbf{M}(\mathbf{Q}) = \int \mathbf{M}(\mathbf{r})\exp(i\mathbf{Q}\cdot\mathbf{r})d\mathbf{r} \tag{2.51}$$

Therefore, the incident neutron only experiences the component of the sample magnetisation that is perpendicular to the scattering vector. Assuming for now that the incident neutron beam is unpolarised, such that there are an equal number of spin-up $|\uparrow\rangle$ and spin-down $|\downarrow\rangle$ neutrons and summing and averaging over the scattering system states λ and λ' gives

$$\frac{d^2\sigma}{d\Omega dE'} = (\gamma_n r_0)^2 \frac{k'}{k}\sum_{\lambda\lambda'} p_\lambda \langle\lambda|\mathbf{M}_\perp^*|\lambda'\rangle\langle\lambda'|\mathbf{M}_\perp|\lambda\rangle\delta(E_\lambda - E_{\lambda'} + \hbar\omega) \tag{2.52}$$

where,

$$r_0 = \frac{\mu_0}{4\pi}\frac{e^2}{m_e} \tag{2.53}$$

is the classical radius of the electron (2.818×10^{-15} m).

The position vector $\mathbf{R}_{jd}$ denotes the position of a nucleus within a crystalline system where the subscript j gives the unit cell in which the nucleus sits and d its position within that unit cell. If $\mathbf{r}_e$ is the position of the eth unpaired electron of spin $\mathbf{s}_e$ relative to its nucleus then [86],

$$\mathbf{r}_i = \mathbf{R}_{jd} + \mathbf{r}_e \tag{2.54}$$

From the definition of $\mathbf{M}(\mathbf{Q})$ given in Equation 2.51, one obtains,

$$\mathbf{M}(\mathbf{Q}) = \sum_i \exp(i\mathbf{Q}\cdot\mathbf{r}_i)\mathbf{s}_i = \sum_{jd} \exp(\mathbf{Q}\cdot\mathbf{R}_{jd}) \sum_e \exp(i\mathbf{Q}\cdot\mathbf{r}_e)\mathbf{s}_e \tag{2.55}$$

such that the matrix element $\langle\lambda'|\mathbf{M}_\perp|\lambda\rangle$ becomes,

$$\langle\lambda'|\mathbf{M}_\perp|\lambda\rangle = \langle\lambda'|\sum_{jd} \exp(\mathbf{Q}\cdot\mathbf{R}_{jd}) \sum_e \exp(i\mathbf{Q}\cdot\mathbf{r}_e)\mathbf{s}_e|\lambda\rangle = F(\mathbf{Q})\langle\lambda'|\exp(i\mathbf{Q}\cdot\mathbf{R}_{jd})\mathbf{S}_{jd}|\lambda\rangle \tag{2.56}$$

Here, $F(\mathbf{Q})$, is known as the magnetic form factor and $\exp(i\mathbf{Q}\cdot\mathbf{R}_{jd})\mathbf{S}_{jd}$ the magnetic structure factor, which contains the spin orientation vectors $\mathbf{S}_{jd}$ in the unit cell. The magnetic form factor is given formally by,

$$F(\mathbf{Q}) = \int \rho(\mathbf{r})\exp(i\mathbf{Q}\cdot\mathbf{r}) \tag{2.57}$$

where $\rho(\mathbf{r})$ is the normalised density of unpaired electrons. It is the spatially diffuse nature of the unpaired electrons in the outer most electronic orbitals that gives rises to the Q-dependent scattering. It is important to note that X-ray scattering is also subject to a form factor since X-rays are scattered by their interaction with the electron density of an atom. There are several important differences, however, between the magnetic and X-ray form factors. For instance, the X-ray atomic form factor has a magnitude that increases proportionally with atomic number, where as the neutron magnetic form factor is specific to a particular ion and oxidation state and does not increase monotonically with atomic number. Furthermore, the drop-off in scattering intensity with increasing

Q, shown in Figure 2.9, is more significant in the case of magnetic neutron scattering since only the outermost valence orbitals that are most extended in space that contain an unpaired electron are involved in the scattering interaction, [80]. An analytical approximation for the magnetic form factor can be obtained from the following expression,

$$F(\mathbf{Q}) = C_0\langle j_0(Q/4\pi)\rangle + C_2\langle j_2(Q/4\pi)\rangle + C_4\langle j_4(Q/4\pi)\rangle + \cdots \tag{2.58}$$

where the constants C_0, C_2, C_4 and functions j_0, j_2, j_4 *etc.* are tabulated [88]. The $\langle j_0\rangle$ term gives the spin only contribution to the magnetic form factor, where as the higher order terms account for the orbital contribution.

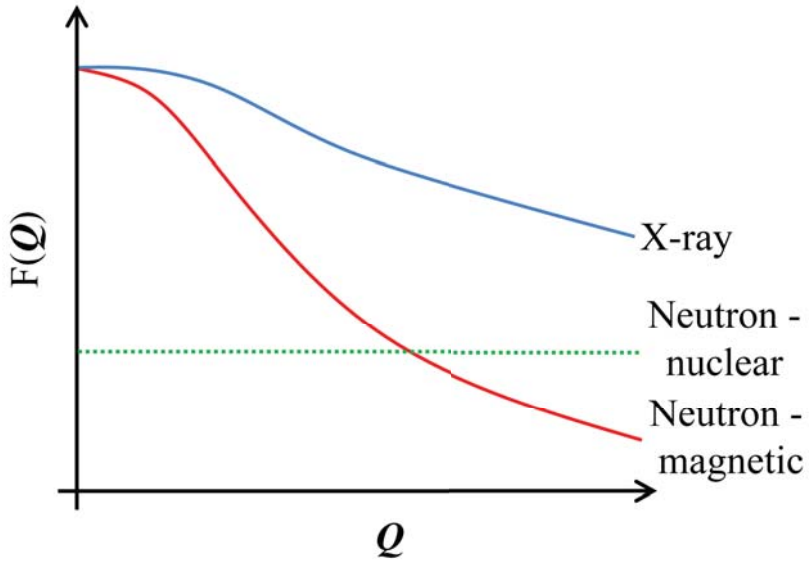

Figure 2.9 *The Q dependence of X-ray and magnetic and nuclear neutron scattering. X-ray and magnetic neutron scattering are subject to a form factor $F(\mathbf{Q})$ such that scattering intensity drops off at higher scattering angles.*

The magnetic differential cross section of a high temperature paramagnetic state of N magnetic ions of spin S is given by [86],

$$\frac{d\sigma}{d\Omega} = \frac{2}{3}(\gamma_n \mathbf{r}_0)^2 N(\frac{1}{2}gF(\mathbf{Q}))^2 \exp(-2W)S(S+1) \tag{2.59}$$

where g is the Landé g-factor and W is the Debye-Weller factor which takes into account thermal displacements of the nuclei in the scattering system. This paramagnetic scattering (in the absence of an applied magnetic field) is entirely

diffuse due to the disordered nature of the paramagnetic state discussed in Chapter 1. Magnetic diffuse scattering is discussed in more detail in this Chapter in § 2.2.4. As a magnetic crystalline solid is cooled it may undergo a magnetic phase transition to a long-range magnetically ordered state giving rise to magnetic Bragg scattering or diffraction. The differential cross section in this case is given by [86],

$$\frac{d\sigma}{d\Omega} = (\gamma_n \mathbf{r}_0)^2 N (\frac{1}{2} g F(\mathbf{Q}))^2 \exp(-2W) \sum_{\alpha\beta} (\delta_{\alpha\beta} - \hat{\mathbf{Q}}_\alpha \hat{\mathbf{Q}}_\beta) \times \sum_j \exp(i\mathbf{Q}\cdot\mathbf{R}_j) \langle \mathbf{S}_0^\alpha \rangle \langle \mathbf{Q}_j^\beta \rangle \tag{2.60}$$

where the sum over cartesian coordintates $\alpha\beta$ is the orientation factor for spin vectors perpendicular to the scattering vector and the sum over j is the structure factor $S(\mathbf{Q})$. In the case of a ferromagnetic state, in which all spins align parallel to one another, the magnetic unit cell coincides with the crystal unit cell such that one observes an increase in intensity of Bragg peaks upon cooling the system below its critical Curie temperature, T_C. In an antiferromagnetic state, in which neighbouring spins align anti-parallel with respect to each other, the magnetic unit cell is doubled with respect to the crystal unit cell and so additional peaks in between the structural Bragg peaks will appear below the Néel temperature, T_N. The archetypal example of this is manganese oxide MnO [89], shown in Figure 2.10, for which magnetic neutron scattering played a vital role in the experimental proof of antiferromagnetism that was first proposed by Néel in 1936 [50], [90].

Inelastic magnetic neutron scattering is somewhat beyond the scope of the work currently within this Thesis. However, it will form an extremely important part of the future work of the projects discussed with the results chapters and in general, inelastic magnetic neutron scattering plays a major role in the study and understanding of the nature of magnetic ground states in highly frustrated spin systems. Inelastic magnetic neutron scattering depends upon temporal and spatial correlations between spins and so can measure the energies of magnetic fluctuations in a system [91]. For completeness, the full inelastic magnetic partial differential cross section is given by,

$$\frac{d^2\sigma}{d\Omega dE'} = \frac{k'}{k} (\gamma_n r_0)^2 (F(\mathbf{Q}))^2 \frac{1}{2\pi\hbar} \sum_{\alpha\beta} (\delta_{\alpha\beta} - Q_\alpha Q_\beta) S^{\alpha\beta}(\mathbf{Q}, \omega) \tag{2.61}$$

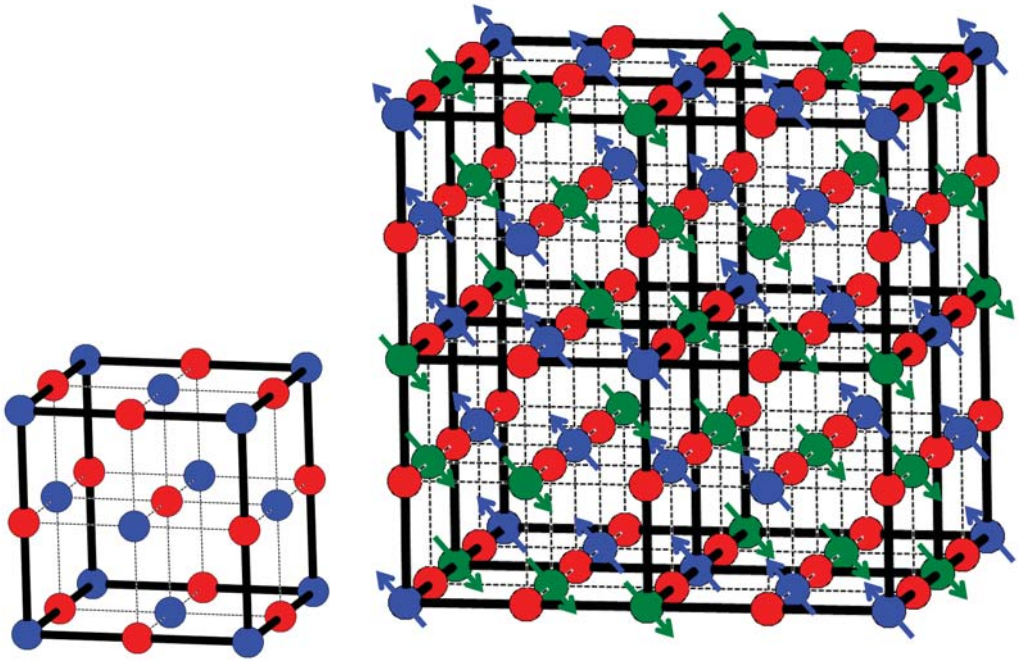

(a) *MnO crystal unit cell.*

(b) *MnO magnetic unit cell.*

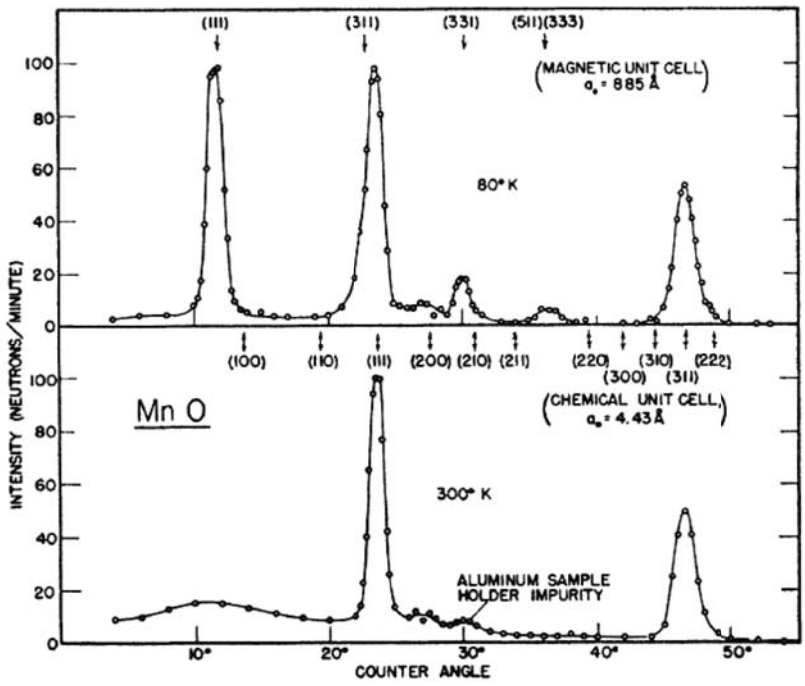

(c) *Powder neutron diffraction data of MnO, taken from reference [89].*

Figure 2.10 *The low temperature antiferromagnetic structure of MnO shown in (b) results in a doubling of the crystal unit cell in (a), which was confirmed by the seminal neutron diffraction work of Smart and Shull (c) that shows the appearance of additional magnetic Bragg peaks below the Néel temperature.*

where $S^{\alpha\beta}(\mathbf{Q},\omega)$ is the dynamical structure factor.

2.2.3 The Production of Neutrons for Neutron Scattering Experiments

There are two principal methods for the production of neutrons for scattering experiments, nuclear fission and spallation [66]. The Institut Laue-Langevin, is a high flux 60 MW nuclear reactor that produces a continuous source of neutrons by fission of enriched ^{235}U fuel. The neutrons that emerge from the nuclear reactor have a wide distribution of energies and so have to pass through a moderator in order to achieve the required energy and wavelength, see Table 2.1. D2B is a high resolution diffractometer at the Institut Laue Langevin that has been used for the study of materials in this Thesis by powder neutron diffraction. A schematic diagram of the instrument is shown in Figure 2.11 [92]. D2B uses a germanium crystal monochromator to select out a single neutron wavelength from the polychromatic beam of thermal neutrons from a D_2O moderator, which is incident upon the sample. The scattered neutrons are detected by a series of 128 detector banks that cover a 2θ range of 5 ° - 165 ° as they move around the sample such that counts of scattered neutrons are averaged over more than one bank. D2B uses ^{3}He tube detectors. Since the neutron is charge neutral, a charged particle has to be produced within the detector in order to count the scattered neutrons indirectly [80], and in the case of ^{3}He detectors this is the proton, $^1H_1$,

$$^3He_2 + {}^1n_0 \rightarrow {}^3H_1 + {}^1H_1 \tag{2.62}$$

Upon integration of intensities of the powder diffraction rings measured on the detectors, shown in Figure 2.12, one obtains a powder diffraction pattern for a sample as a function of 2θ. This is, therefore, an example of constant wavelength or angle dispersive diffraction.

The ISIS neutron facility of the Rutherford Appleton Laboratory is an example of a spallation or pulsed neutron source. Here, pulses of neutrons are produced when a high energy proton beam collides with a heavy-metal tungsten target which spallates neutrons and other high energy particles. After moderation, the *white* beam of neutrons is incident upon a sample, which after scattering are analysed

Table 2.1 *Neutron moderator characteristics at the Institut Laue-Langevin and ISIS neutron facilities.*

Moderator	T / K	Neutron E / meV	Neutron λ / Å	ILL	ISIS
Cold	$1 - 120$	$0.1 - 10$	$30 - 3$	D_2	D_2, CD_4
Thermal	$6 - 1000$	$5 - 100$	$4 - 1$	D_2O	D_2O
Hot	$1000 - 6000$	$100 - 500$	$1 - 0.4$	Graphite	-

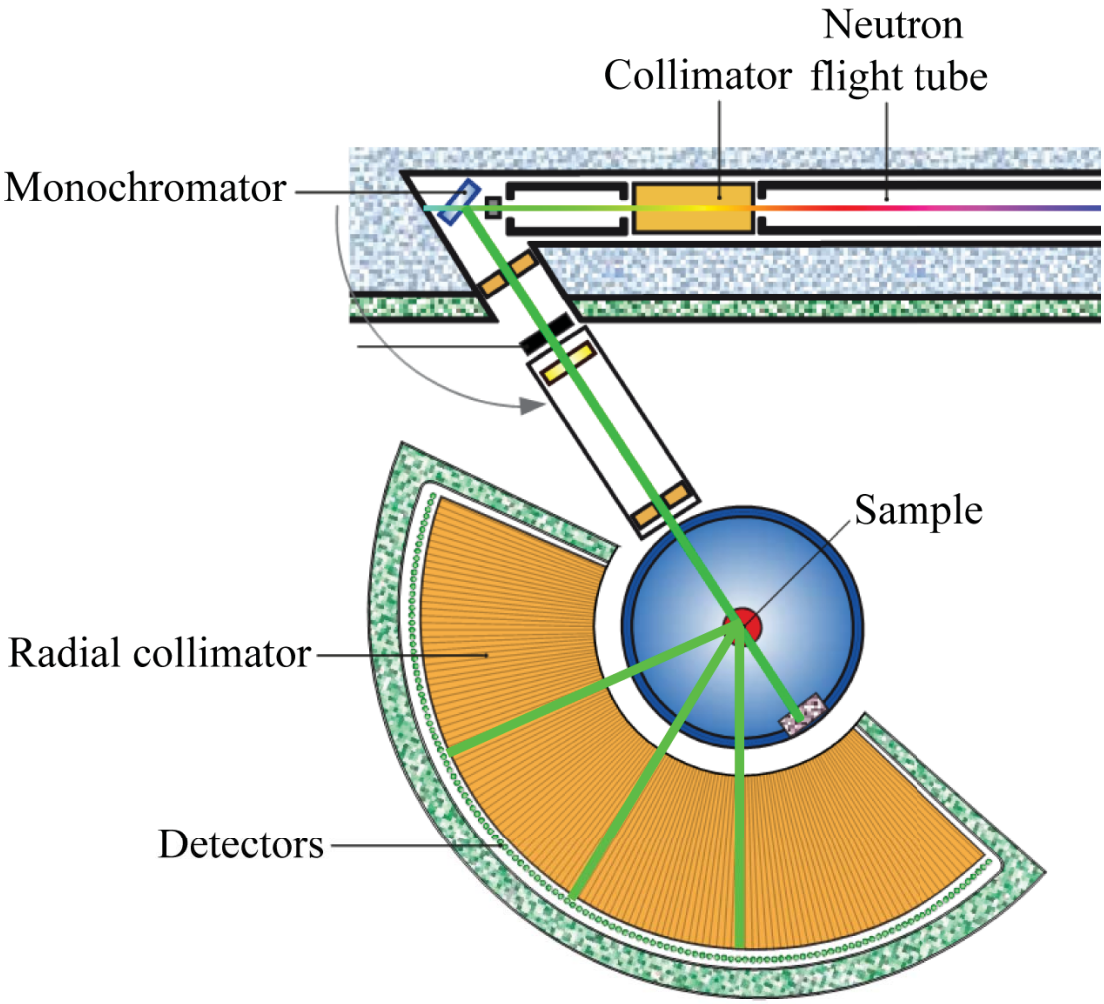

Figure 2.11 *Schematic diagram of the instrumental layout the high resolution diffractometer D2B at the Institut Laue Langevin.*

by fixed detector banks as a function of their time-of-flight, and hence wavelength. Faster neutrons, with a shorter wavelength will arrive at the detector banks first while the slower neutrons with a longer wavelength and time-of-flight arrive at a later time. The high resolution powder diffractometer (HRPD) is an example of an instrument at ISIS on which time-of-flight or energy dispersive neutron

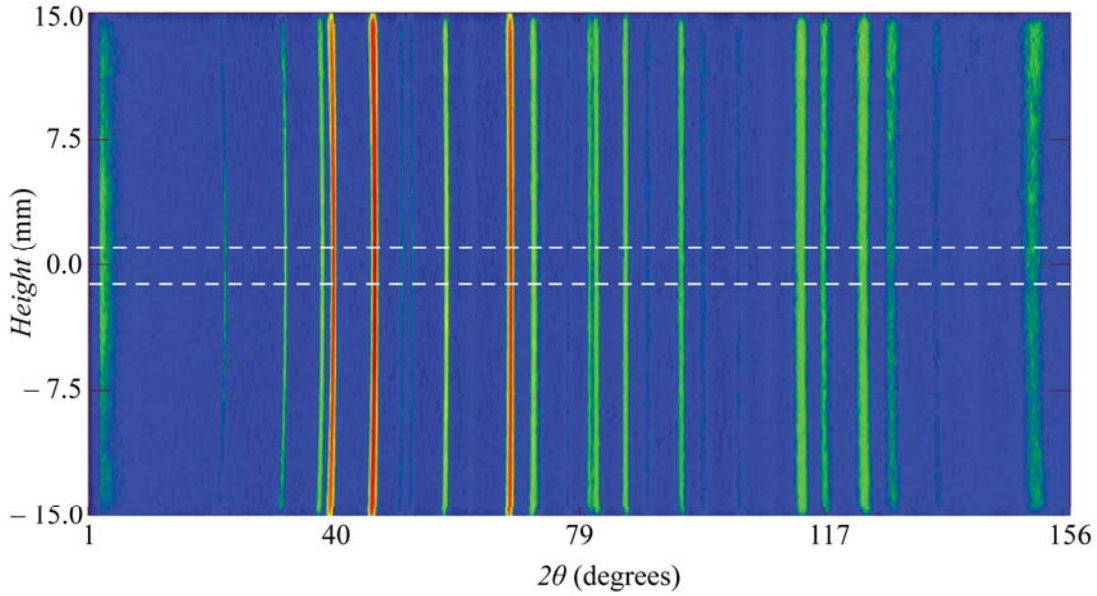

Figure 2.12 *Neutron powder diffraction rings measured on D2B. Integration of the intensities over the centre of the detector array (white-dotted lines) gives a high resolution powder diffraction pattern as a function of* 2θ.

diffraction has been performed in this Thesis. HRPD has three fixed detector banks, a high resolution backscattering bank ($2\theta = 168.3°$), 90 ° detector banks on either side of the sample ($2\theta = 89.6$ °) and a small angle bank ($2\theta = 30.0$ °) as shown in Figure 2.13, which cover regions of d-spacings of 0.6 - 2.6 Å, 0.9 - 3.8 Å and 2.0 - 10.0 Å, respectively. The particularly special feature of HRPD is its extremely long flight path; the instrument is situated 100 m away from the neutron target giving it one of the best $\Delta d/d$ resolutions in the world.

2.2.4 Neutron Polarisation Analysis and the Diffuse Scattering Spectrometer, D7

The underlying diffuse scattering found beneath the nuclear or magnetic Bragg peaks in a neutron diffraction pattern can often contain interesting and important information about structural and magnetic disorder and short range correlations in a system. This is especially the case in magnetically frustrated spin systems in which one does not expect to observe long range magnetic order upon cooling but rather diffuse, short range spin-spin interactions in a disordered magnetic ground state [93]. In order to unambiguously extract this kind of information and separate the different components of the total neutron scattering from a

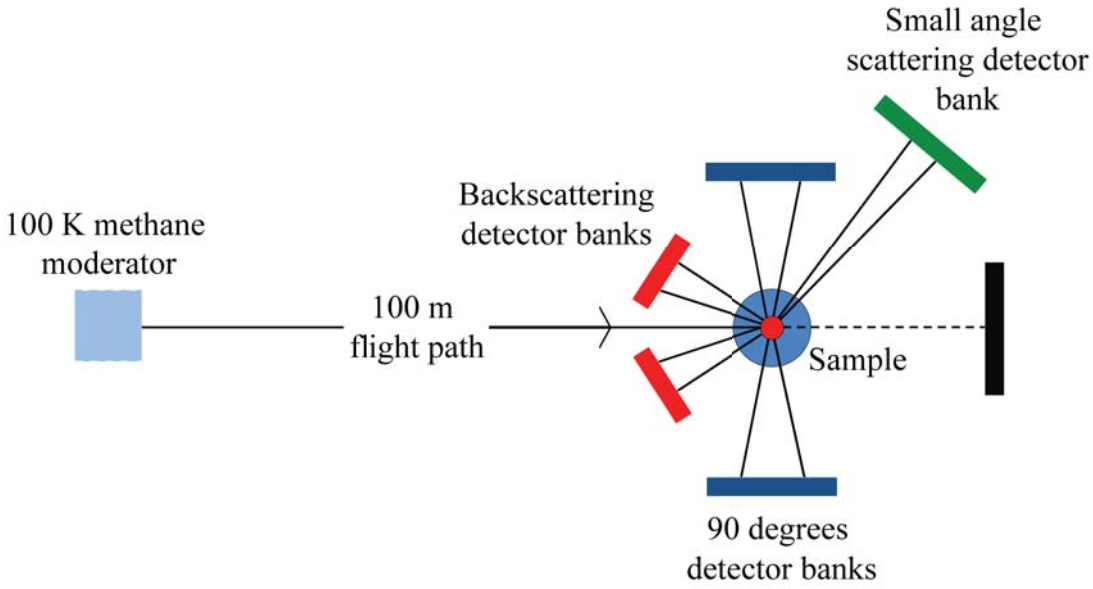

Figure 2.13 *The detector bank array at HRPD, with the backscattering,* 90 ° *and small angle banks fixed at* 2θ = 168.4 °, 89.6 ° *and* 30.0 °, *respectively. The incoming neutrons travel a flight path of* 100 *m from the moderator to the sample.*

sample one must apply neutron polarisation analysis techniques. The diffuse scattering spectrometer D7 at the Institut Laue-Langevin is the ideal instrument to perform such an experiment as it employs xyz polarisation analysis to separate out the nuclear, magnetic and nuclear spin incoherent scattering cross sections that contribute to total scattering over all scattering angles [94].

Neutron Polarisation

The neutron is a charge neutral particle with spin $s = \frac{1}{2}$ and an angular momentum of $\pm\frac{1}{2}\hbar$. If the spin vector of an individual neutron is denoted $\mathbf{s_n}$ then the polarisation of a beam of neutrons is given by [95],

$$\mathbf{P} = \langle \mathbf{s_n} \rangle / \frac{1}{2} = 2\langle \mathbf{s_n} \rangle \tag{2.63}$$

i.e. the ensemble average of all neutron spin vectors normalised by $|\mathbf{s_n}|$. In order to study the spin state transition of a neutron during the scattering process with a sample, one needs to produce a beam of polarised neutrons with a definite spin state. By applying a magnetic field on a scattering experiment, one creates a quantisation axis (usually defined along the z-axis), along which the neutron spin

can align parallel to give a spin-up state $|\uparrow\rangle = +\frac{1}{2}\hbar$ or anti-parallel to give a spin-down state $|\downarrow\rangle = -\frac{1}{2}\hbar$. A scattering experiment that has a single quantisation axis is known as a longitudinal polarisation analysis experiment. It is possible to express the neutron beam polarisation in such an experiment as a scalar,

$$P = \frac{N_+ - N_-}{N_+ + N_-} \tag{2.64}$$

where N_+ and N_- and spin-up and spin-down neutron spin states, respectively. A perfectly polarised neutron beam will, therefore, have $P = \pm 1$. A measurable quantity in a longitudinal neutron polarisation analysis experiment is the flipping ratio, $F = \frac{N_+}{N_-}$, such that the beam polarisation can also be defined in terms of F,

$$P = \frac{F-1}{F+1} \tag{2.65}$$

The equations for the spin-dependent scattering amplitudes are given by the Moon-Riste-Koehler equations [96]. The scattering amplitudes are a convenient way of describing how the incident neutron goes from an initial wavevector and spin state $|\mathbf{kS}\rangle$ to a final state $|\mathbf{k'S'}\rangle$ via an interaction potential, $V(\mathbf{Q})$ during the scattering process [79],

$$U = \langle \mathbf{k'S'}|V(\mathbf{Q})|\mathbf{kS}\rangle \tag{2.66}$$

For nuclear spin independent ($I = 0$), magnetic and nuclear spin dependent ($I \neq 0$) scattering processes, these scattering amplitudes can be derived from the nuclear and magnetic scattering potentials, to give the Moon-Riste-Koehler equations [96]:

$$U^{++} = |\uparrow\rangle\rightarrow|\uparrow\rangle = b_{coh} - \frac{\gamma_n r_0}{2\mu_B} M_{\perp z} + BI_z \tag{2.67}$$

$$U^{--} = |\downarrow\rangle\rightarrow|\downarrow\rangle = b_{coh} + \frac{\gamma_n r_0}{2\mu_B} M_{\perp z} - BI_z \tag{2.68}$$

$$U^{+-} = |\uparrow\rangle\rightarrow|\downarrow\rangle = -\frac{\gamma_n r_0}{2\mu_B}(M_{\perp x} - iM_{\perp_y}) + B(I_x - iI_y) \tag{2.69}$$

$$U^{-+} = |\downarrow\rangle\rightarrow|\uparrow\rangle = -\frac{\gamma_n r_0}{2\mu_B}(M_{\perp x} + iM_{\perp_y}) + B(I_x + iI_y) \tag{2.70}$$

where b_{coh} is the coherent scattering length and $B = (b_+ + b_-)/(2I+1)$ is the nuclear spin dependent scattering length from spin-singlet (b_-) and spin-triplet (b_+) neutron-nucleus compound states. The U^{++} and U^{--} scattering amplitudes do not result in a change in the spin state of the neutron and are, therefore, referred to as non-spin flip (NSF) amplitudes. U^{+-} and U^{-+} involve a change in the spin state of the neutron as a result of the scattering process and so are known as the spin flip (SF) amplitudes. It is important to note at this point that, with the neutron polarisation aligned along the z-axis in a longitudinal polarisation analysis experiment, the NSF scattering will be sensitive to components of the sample magnetisation that are parallel to the neutron polarisation and the SF scattering will be sensitive to those that are perpendicular to the polarisation given that neutrons only ever see components of the magnetisation perpendicular to the scattering vector.

The diffuse scattering of neutrons can arise from incoherent nuclear scattering, discussed in § 2.2.1, or incoherent magnetic scattering from a paramagnetic or disordered magnetic state. By including the contributions of nuclear isotope incoherent and spin incoherent scattering the spin-dependent scattering amplitudes in the Moon-Riste-Koehler equations become [96],

$$U^{++} = |\uparrow\rangle\rightarrow|\uparrow\rangle = b_{coh} - \frac{\gamma_n r_0}{2\mu_B}M_{\perp z} + b_{ii} + \frac{1}{3}b_{si} \tag{2.71}$$

$$U^{--} = |\downarrow\rangle\rightarrow|\downarrow\rangle = b_{coh} + \frac{\gamma_n r_0}{2\mu_B}M_{\perp z} + b_{ii} + \frac{1}{3}b_{si} \tag{2.72}$$

$$U^{+-} = |\uparrow\rangle\rightarrow|\downarrow\rangle = -\frac{\gamma_n r_0}{2\mu_B}(M_{\perp x} - iM_{\perp_y}) + \frac{2}{3}b_{si} \tag{2.73}$$

$$U^{-+} = |\downarrow\rangle\rightarrow|\uparrow\rangle = -\frac{\gamma_n r_0}{2\mu_B}(M_{\perp x} + iM_{\perp_y}) + \frac{2}{3}b_{si} \tag{2.74}$$

where $b_{ii} = \sqrt{\langle(\bar{b})^2\rangle - (\bar{b})^2}$ and $b_{si} = \sqrt{B^2 I(I+1)}$ are the isotope and spin incoherent scattering lengths, respectively. At this point, it is possible to see how in the absence of magnetic scattering one can separate the nuclear spin incoherent scattering from the nuclear coherent and isotope incoherent by subtracting half of

the SF scattering from the NSF. This could be useful, for example, in the study of hydrogenous organic substances where one may want to separate out the large incoherent scattering of ^{1}H.

xyz Polarisation Analysis

In order to fully separate nuclear coherent, nuclear spin incoherent and magnetic scattering, however, xyz polarisation analysis is required [94]. This makes use of a multi-detector in the xy-plane of the scattering experiment, which is able to observe $|\uparrow\rangle \rightarrow |\uparrow\rangle$ NSF and $|\downarrow\rangle \rightarrow |\uparrow\rangle$ SF transitions as it detects and analyses neutrons with a final spin-up spin state. The magnetic cross sections for these transitions, obtained by taking the square of the magnetic part of U^{++} and U^{-+}, respectively,

$$\left(\frac{d\sigma}{d\Omega}\right)_{NSF} = \left(\frac{\gamma_n r_0}{2\mu_B}\right)^2 \langle M^*_{\perp z} M_{\perp z}\rangle \tag{2.75}$$

and,

$$\left(\frac{d\sigma}{d\Omega}\right)_{SF} = \left(\frac{\gamma_n r_0}{2\mu_B}\right)^2 \langle M^*_{\perp x} M_{\perp x} + M^*_{\perp y} M_{\perp y}\rangle \tag{2.76}$$

For a fully disordered paramagnetic state, these expressions can be written in the form,

$$\left(\frac{d\sigma}{d\Omega}\right)^{x,y,z}_{NSF} = \frac{1}{3}\left(\frac{\gamma_n {r_0}^2}{2} g^2 F^2(\hat{\mathbf{Q}}) J(J+1)[1 - (\hat{\mathbf{Q}}\cdot\hat{\mathbf{P}})]^2\right) \tag{2.77}$$

$$\left(\frac{d\sigma}{d\Omega}\right)^{x,y,z}_{SF} = \frac{1}{3}\left(\frac{\gamma_n {r_0}^2}{2} g^2 F^2(\hat{\mathbf{Q}}) J(J+1)[1 + (\hat{\mathbf{Q}}\cdot\hat{\mathbf{P}})]^2\right) \tag{2.78}$$

and by setting the neutron polarisation direction (now x, y or z) along the unit scattering vector, such that $(\hat{\mathbf{Q}}\cdot\hat{\mathbf{P}}) = 1$, all of the magnetic scattering collapses into the SF cross section. With the multi-detector in the xy-plane, one measures a unit scattering vector $\hat{\mathbf{Q}}$ that can be defined by the angle α that is makes with

the x-axis, known as the Schärpf angle [97],

$$\hat{\mathbf{Q}} = \begin{pmatrix} \cos\alpha \\ \sin\alpha \\ 0 \end{pmatrix} \tag{2.79}$$

Substituting this scattering vector into the the cross sections, including nuclear coherent, isotope incoherent and spin incoherent terms, one obtains six cross sections, one SF and one NSF for the polarisation aligned along each of the xyz directions,

$$\left(\frac{d\sigma}{d\Omega}\right)^{x}_{NSF} = \frac{1}{2}\sin^2\alpha\left(\frac{d\sigma}{d\Omega}\right)_{mag} + \frac{1}{3}\left(\frac{d\sigma}{d\Omega}\right)_{si} + \left(\frac{d\sigma}{d\Omega}\right)_{nuc\ +\ ii} \tag{2.80}$$

$$\left(\frac{d\sigma}{d\Omega}\right)^{x}_{SF} = \frac{1}{2}(\cos^2\alpha + 1)\left(\frac{d\sigma}{d\Omega}\right)_{mag} + \frac{2}{3}\left(\frac{d\sigma}{d\Omega}\right)_{si} \tag{2.81}$$

$$\left(\frac{d\sigma}{d\Omega}\right)^{y}_{NSF} = \frac{1}{2}\cos^2\alpha\left(\frac{d\sigma}{d\Omega}\right)_{mag} + \frac{1}{3}\left(\frac{d\sigma}{d\Omega}\right)_{si} + \left(\frac{d\sigma}{d\Omega}\right)_{nuc\ +\ ii} \tag{2.82}$$

$$\left(\frac{d\sigma}{d\Omega}\right)^{y}_{SF} = \frac{1}{2}(\sin^2\alpha + 1)\left(\frac{d\sigma}{d\Omega}\right)_{mag} + \frac{2}{3}\left(\frac{d\sigma}{d\Omega}\right)_{si} \tag{2.83}$$

$$\left(\frac{d\sigma}{d\Omega}\right)^{z}_{NSF} = \frac{1}{2}\left(\frac{d\sigma}{d\Omega}\right)_{mag} + \frac{1}{3}\left(\frac{d\sigma}{d\Omega}\right)_{si} + \left(\frac{d\sigma}{d\Omega}\right)_{nuc\ +\ ii} \tag{2.84}$$

$$\left(\frac{d\sigma}{d\Omega}\right)^{z}_{SF} = \frac{1}{2}\left(\frac{d\sigma}{d\Omega}\right)_{mag} + \frac{2}{3}\left(\frac{d\sigma}{d\Omega}\right)_{si} \tag{2.85}$$

These equations are collectively known as the Schärpf equations [97] and they form the basis of the separation of total scattering components by xyz polarisation analysis. The required cross sections of interest can be extracted by combining the Schärpf equations in the necessary manner. For instance, the magnetic scattering

cross section can obtained independently for either the NSF or SF channels,

$$\left(\frac{d\sigma}{d\Omega}\right)_{mag} = 4\left(\frac{d\sigma}{d\Omega}\right)^{z}_{NSF} - 2\left(\frac{d\sigma}{d\Omega}\right)^{x}_{NSF} - 2\left(\frac{d\sigma}{d\Omega}\right)^{y}_{NSF} \tag{2.86}$$

or,

$$\left(\frac{d\sigma}{d\Omega}\right)_{mag} = 2\left(\frac{d\sigma}{d\Omega}\right)^{x}_{SF} + 2\left(\frac{d\sigma}{d\Omega}\right)^{y}_{SF} - 4\left(\frac{d\sigma}{d\Omega}\right)^{z}_{SF} \tag{2.87}$$

The Diffuse Scattering Spectrometer D7

D7 is a high flux, cold neutron multi-detector spectrometer that is specifically designed to perform xyz polarisation analysis for the study of diffuse scattering [94]. A schematic diagram of the instrument layout taken from reference [94] is shown in Figure 2.14. The diffuse scattering that is studied on D7 typically contains very broad features and so high Q resolution is not required. Instead a high neutron flux is favoured given that the polarisation analysis cuts down the total beam flux. The cold neutron source of D7 is also advantageous in the process of polarisation analysis as it helps to reduce the possibility of multiple scattering events that can lead to twice flipped spins being counted in the NSF channel. The monochromator at the neutron guide can be used to select incident neutron wavelengths of 3.1 or 4.8 Å. The neutron beam is polarised by a Co/Ti focusing super-mirror polariser [95]. For a single magnetic layer mirror polariser of N nuclei of scattering length b there are two critical glancing angles, $\theta_{c\pm}$, that give rise to total external reflection of the incident neutron beam,

$$\theta_{c\pm} = \lambda\left(\frac{N}{\pi}(b \pm p)\right)^{\frac{1}{2}} \tag{2.88}$$

and between these two critical angles a neutron beam of wavelength λ is fully polarised ($p = \pm 1$). However, the critical glancing angle is typically very small and, therefore, not suitable for a high flux neutron scattering instrument given the divergence of the incident neutron beam. In D7 a super-mirror arrangement of magnetic and non-magnetic Co/Ti layers is used, which increases the allowed divergence of the beam whilst still achieving polarisation. A gradient in the

thickness of the Co/Ti layers extends the reflectivity of the super-mirror system over a wide range of angles and the mirrors are bent to ensure reflection of the incident neutron beam. A magnetic guide field ensures that the beam polarisation is maintained as the neutrons travel through the D7 instrument. The polarisation can be flipped before the sample by activating the Mezei flipper such that $|\downarrow\rangle \rightarrow |\uparrow\rangle$ SF transitions can be monitored. The xyz field coils around the sample adiabatically rotate the neutron spin polarisation into the x, y or z directions *i.e.* the magnetic field direction is changed slowly such that there is a reversible rotation of the polarisation and the component of the polarisation parallel to the guide field is conserved [95]. The scattered beam is then analysed by an array of Co/Ti super-mirrors which cover three sets of detector banks over a horizontal scattering angle of 132 °. Within this Thesis, D7 has been used to study the magnetic diffuse scattering of neutrons from the disordered magnetic ground states of the geometrically frustrated pyrochlores $Lu_2Mo_2O_7$ and $Lu_2Mo_2O_{4.8}N_{1.7}$, which are presented in Chapters 3 and 4, respectively.

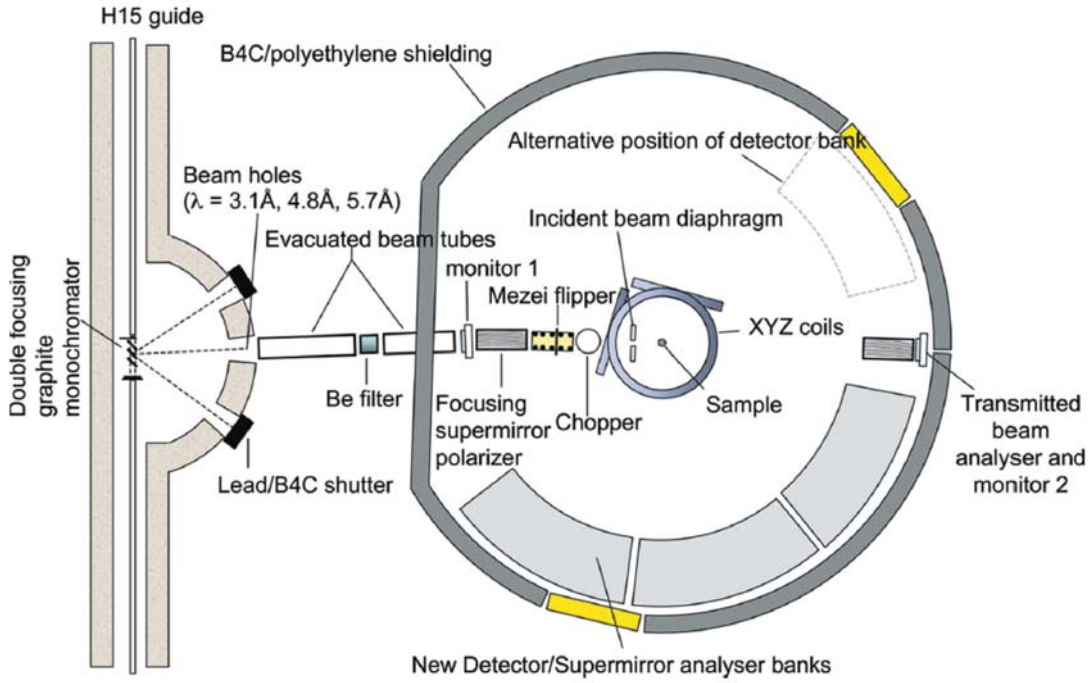

Figure 2.14 *Schematic diagram of the instrumental layout of the diffuse scattering spectrometer D7 at the Institut Laue Langevin.*

2.3 Muon Spin Relaxation

The positive muon is a spin-$\frac{1}{2}$ particle. Some of the important properties of the muon are summarised in Table 2.2. Muon spin relaxation (μSR) is an implantation technique where by spin polarised positively charged muons are implanted into a sample where they thermalise and come to rest at well defined, energetically favourable sites [98]. Within the sample, the large magnetic moment of the muon makes it an extremely sensitive local probe of any internal magnetic fields and is capable of distinguishing between static and slowly fluctuating magnetic moments. It is, therefore, an ideal tool for studying the dynamics of frustrated, low spin magnetic ground states. In spin relaxation studies, the time evolution of the muon spin polarisation is measured, which can be performed in the absence of an applied field (or zero field, ZF) or an applied longitudinal field (LF) in the direction of the initial muon spin polarisation [99].

Table 2.2 *Fundamental properties of the muon.*

Charge	Spin	Mass	Magnetic moment	$\gamma_\mu/2\pi$ / MHz T^{-1}	Lifetime / μs
$\pm e$	$\frac{1}{2}$	$207m_e \sim \frac{1}{9}m_p$	3.18 μ_p	135	2.2

100 % spin polarised positive muons, μ^+, are produced for condensed matter μSR studies by pion, π^+, decay. When high energy protons collide into a graphite target π^+ particles are produced, which undergo a two-body decay process to give μ^+ and a neutrino, ν_μ,

$$\pi^+ \rightarrow \mu^+ + \nu_\mu \quad (\tau_{\pi^+} = 26\ ns) \tag{2.89}$$

In order to conserve momentum, the resulting neutrino and muon must possess momentum of equal magnitude and opposite direction. The neutrino also has the property of negative helicity, which means that its spin is aligned in the opposite direction to its momentum. Given that the pion is a spin-0 particle, the muons produced by pion decay are thus also intrinsically 100 % spin polarised with its spin aligned in the opposite direction to its direction of travel [100]. The muon is an unstable particle and does not re-emerge from the sample in which it has been implanted. Instead it undergoes a three-body decay to give a positron, e^+,

a positron neutrino, ν_e and a muon anti-neutrino $\bar{\nu}_\mu$

$$\mu^+ \rightarrow e^+ + \nu_e + \bar{\nu}_\mu \quad (\tau_{\mu^+} = 2.2\ \mu s) \tag{2.90}$$

This decay process has the unusual property of the non-conservation or violation of parity [101], which means that the decay positron, which as a charged particle can be easily detected, is most likely to be emitted along the direction of the muon spin polarisation at the instant of decay, see Figure 2.15. The degree of anisotropy or asymmetry in the decay, therefore, gives a measure of the muon spin polarisation as a function of time. In a typical μSR experiment, the sample is placed between two sets of detector banks, a forwards set and a backwards set, as shown in Figure 2.16. The time evolution of the muon decay asymmetry is then given by,

$$A(t) = \frac{N_B(t) - N_F(t)}{N_B(t) + N_F(t)} \tag{2.91}$$

where N_B and N_F are the number of positron counts in the backwards and forwards detector banks, respectively. In the presence of a magnetic field, the muon spin polarisation will precess between the forwards and backwards detector banks, such that there is an oscillation in the asymmetry signal, see Figure 2.16 [100]. In the case of long range magnetic order, the muon spin will precess about the local internal field that it experiences at its particular stopping site, which will give rise to oscillations in the time dependent muon decay asymmetry that are characteristic of the internal field strength. This field dependent Larmour precession frequency for the muon is given by,

$$\omega_\mu = \gamma_\mu B \tag{2.92}$$

where γ_μ is the muon gyromagnetic ratio given in Table 2.2. It is common to report the time dependent muon spin polarisation, which is given by the time dependent muon decay asymmetry normalised by the initial asymmetry,

$$P(t) = \frac{A(t)}{A(t_0)} \tag{2.93}$$

In the presence of long range ordered magnetic field, the oscillations in the muon

spin polarisation are modelled by,

$$P(t) = \cos^2\theta + \sin^2\theta\cos(\omega_\mu t) \tag{2.94}$$

where θ is is angle between the local field direction and the muon spin. When the direction of the static magnetic field is entirely random, for example in a frozen spin glass state, the muons precess at several different rates which results in an averaging of the oscillations,

$$P(t) = \frac{1}{3} + \frac{2}{3}\cos(\omega_\mu t) \tag{2.95}$$

If the local field strength has a Gaussian distribution of width Δ/γ_μ this gives rise to the Kubo-Toyabe function,

$$P(t) = \frac{1}{3} + \frac{2}{3}\exp(-\Delta^2 t^2/2)(1 - \Delta^2 t^2) \tag{2.96}$$

which has a characteristic $\frac{1}{3}$-tail in the muon spin polarisation at long times, which indicates the presence of static or frozen disordered magnetic moments [102].

The muon is also sensitive to the the dynamics of any fluctuating fields within a magnetic system, which causes an exponential relaxation or depolarisation of the the muon spin,

$$P(t) = P(t_0)\exp(-\lambda t) \tag{2.97}$$

where λ is known as the relaxation or depolarisation rate. This relaxation rate is inversely proportional to the fluctuation frequency of the fluctuating fields, ν, such that the faster the internal field fluctuations the slower the relaxation rate, as shown in Figure 2.16.

Muon spin relaxation data have been collected for several of the magnetic systems presented within this Thesis. Zero field and longitudinal field data have been collected on the MuSR spectrometer at the ISIS Muon Facility, Rutherford Appleton Laboratory and on the General Purpose Spectrometer at the Swiss Muon Source, Paul Scherrer Institute and were analysed using the Windows

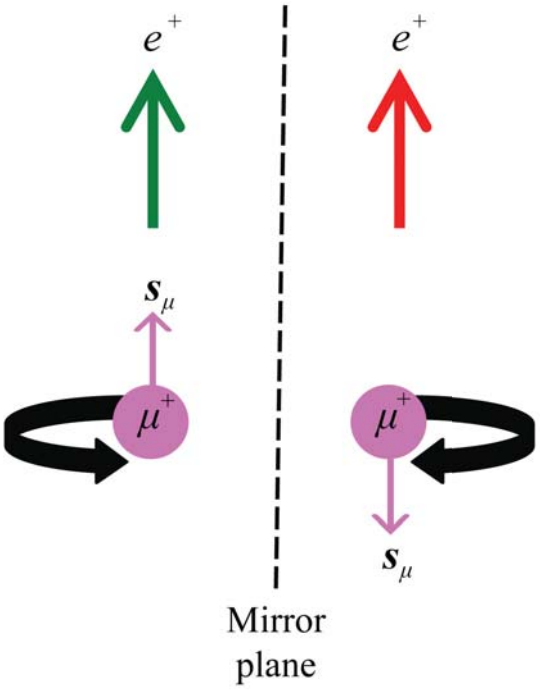

(a) *The muon spin is reversed upon reflection in a mirror plane, however, due to the violation of parity, only the decay process shown on the left hand side is ever observed with the decay positrons emitted preferentially in the direction of the muon spin.*

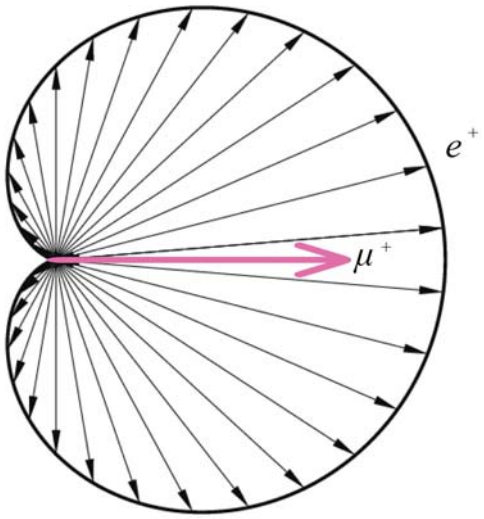

(b) *The asymmetry of the muon decay, shown here with respect to the initial muon spin polarisation for the highest energy muons.*

Figure 2.15 *Muon decay.*

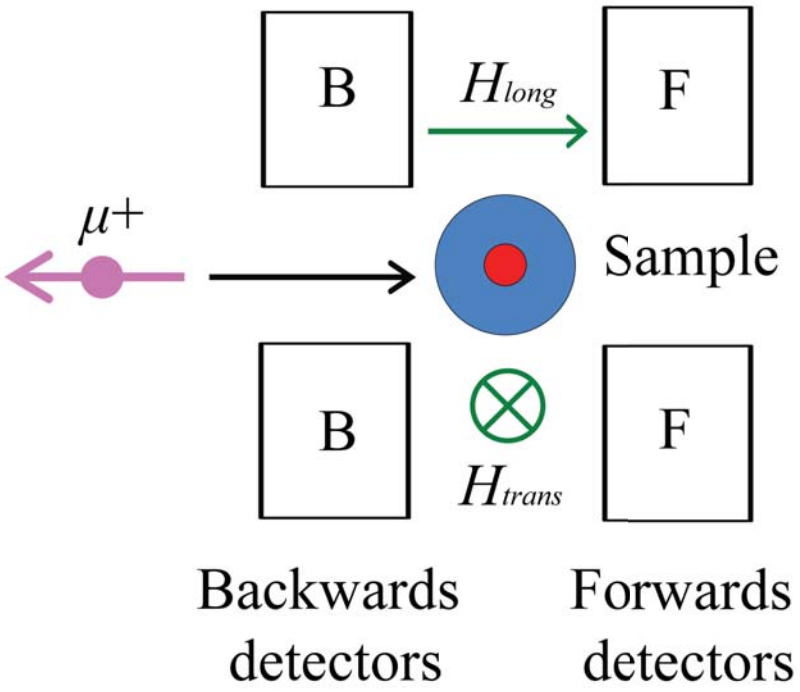

(a) *The typical experimental set-up of a μSR experiment with a sample placed in between forwards and backwards detector banks and the incoming muon with its spin polarisation aligned in the opposite direction to its momentum. μSR measurements can be performed in zero field or upon the application of a traverse field (H_{trans}), perpendicular to the initial muon spin polarisation or a longitudinal field (H_{long}), parallel to the initial muon spin polarisation.*

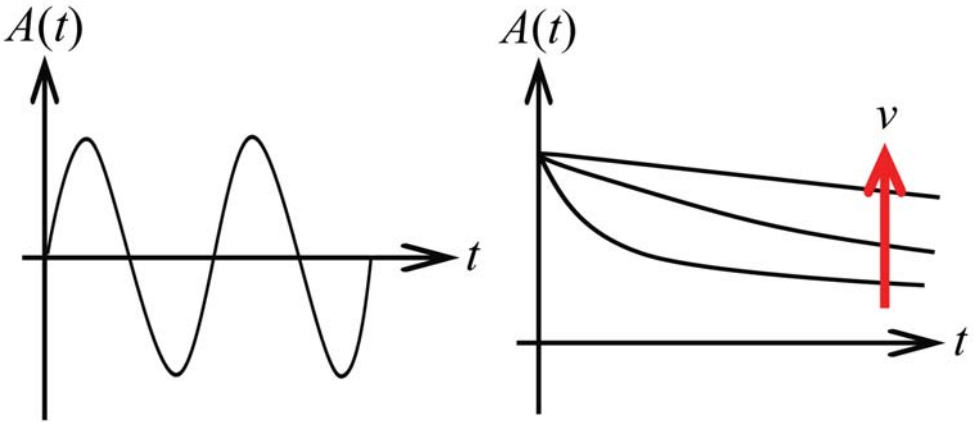

(b) *The muon will precess about the local field at its stopping site, which gives rise to oscillations in the decay asymmetry.*

(c) *If the muon experiences dynamical fluctuating fields at its stopping site, one will observe an exponential relaxation of the muon decay asymmetry. The greater the frequency of the field fluctuations, ν, the slower the rate of relaxation.*

Figure 2.16 *A typical μSR experiment.*

Muon Data Analysis (WiMDA) system [103]. The muon beam at the Swiss Muon Source is continuous, such that muons arrive at the sample one at a time. As a muon enters the sample it is detected, which begins a clock that is stopped once the corresponding decay positron is detected in one of the detector banks. If a second muon enters the experiment frame before the first muon has had time to decay the event is vetoed and discounted. This leads to considerable counting times in order to obtain good data statistics. At the ISIS muon facility, pulses of muons are produced at the target and so the detection of the decay positrons can be timed with respect to the start of the muon pulse. Each pulse from the target contains a large number of muons such that several million decay positrons are counted easily and the measurement of muons with a lifetime up to 30 μs becomes possible. The main disadvantage of the pulsed technique is that, due to the uncertainty in the beginning of each pulse of muons, phenomena that occur on very fast time scales (< 1 μs) are not observed. Pulsed and continuous muon experiments can, therefore, provide very complementary information [100].

2.4 Magnetic Susceptibility Measurements

Superconducting QUantum Interference Device (SQUID) magnetometry is an extremely sensitive experimental method that is widely used to measure the magnetisation of magnetic systems. The SQUID component consists of a superconducting ring with one or two small insulating layers, or weak links, which are extremely sensitive to changes in magnetic field [104]. In a direct current (DC) measurement, a fixed magnetic field is applied to a sample as it is moved through a set of superconducting detection coils. The magnetic moment of the sample induces a current in the detection coils, which are connected to the SQUID such that the induced current can couple to the SQUID sensor. The SQUID converts this current pattern into an output voltage as a function of the sample position within the detection coils that is proportional the magnetic moment, and hence, the magnetisation of a sample. In the measurement of the DC or linear magnetisation, it is assumed that the measured magnetisation, $\mathbf{M}$ is directly proportional to the applied field, $\mathbf{H}$, via the magnetic susceptibility χ,

$$\mathbf{M} = \chi \mathbf{H} \tag{2.98}$$

The measurement of the alternating current (AC) or differential susceptibility,

χ_{AC} does not require this assumption and is given by,

$$\chi_{AC} = \left(\frac{\partial \mathbf{M}}{\partial \mathbf{H}}\right)_T \tag{2.99}$$

In an AC measurement, an oscillating magnetic field is applied to the sample, which is held at a fixed position within the detector coils. The change in magnetisation that is measured as the sample responds to the change in magnetic field can, therefore, yield information about the dynamics of a magnetic system. AC susceptibility is described as having real and imaginary parts,

$$\chi_{AC} = \chi' + i\chi'' \tag{2.100}$$

where the imaginary susceptibility, χ'', arises from energy exchange processes within the systems related to resonance phenomena.

The magnetic susceptibility data that are presented within the following results chapters were measured on a Quantum Design Magnetic Properties Measurement System (MPMS) with a SQUID magnetometer. This experimental set-up is capable of measuring DC magnetisation in applied field strengths up to 7 T over a temperature range of 2 - 400 K. In AC mode, oscillating fields can be applied over a frequency range of 0.001 - 1000 Hz. It is good practice to correct experimentally determined magnetic susceptibilities for the diamagnetic contribution. All materials show some degree of diamagnetism, as discussed in the previous Chapter within § 1.2, which can be corrected for by subtracting tabulated values [3] of the temperature independent diamagnetic contribution from the data. Within this Thesis, estimates for the Weiss and Curie constants have been extracted from Curie-Weiss fits to inverse susceptibility data, from which a high temperature magnetic moment can be calculated, $\mu_{eff} = \sqrt{8C}$. However, it should be noted that in a true paramagnetic regime the most accurate way to extract the effective paramagnetic moment is to determine χT from a plot of χT against T, with $\mu_{eff} = \sqrt{8\chi T}$.

2.5 Heat Capacity Measurements

When a substance is heated, the temperature rise that results from the transfer of energy to the system depends on its heat capacity, C [105]. The heat capacity of a system at constant pressure is, therefore, given by [106],

$$C_p = \left(\frac{\partial U}{\partial T}\right)_p \tag{2.101}$$

where ∂T is the change in temperature brought about by the change in internal energy ∂U upon heating. The total heat capacity of a solid provides a wealth of information about its lattice, electronic, nuclear and magnetic properties,

$$C_{total} = C_{nuclear} + C_{electronic} + C_{magnetic} + C_{lattice} \tag{2.102}$$

At low temperatures, when the lattice contribution to the total heat capacity is negligible, the heat capacity directly probes the nuclear, electronic and magnetic energy levels of a system [106].

In order to measure heat capacity, heat must be added to and removed from a sample whilst the resulting change in temperature is monitored. During the measurement, a known amount of heat is applied at constant power for a fixed period of time, followed by a cooling period with the same time constant. A known mass of sample is attached to the sample platform with a thin layer of grease to provide thermal contact and the platform heater and thermometer are attached to the bottom side of the sample platform. After each measurement cycle *i.e.* a heating period followed by a cooling period, the temperature response or thermal relaxation of the sample platform is modelled in order to extract the heat capacity of the sample. Provided that the sample and the sample platform are in good thermal contact with each other, the temperature of the platform, T, as a function of time, t, can be modelled by [107],

$$C_{total}\frac{dT}{dt} = -K_w(T - T_b) + P(t) \tag{2.103}$$

where C_{total} is the total heat capacity of the sample and the sample platform, K_w is the thermal conductance of the wires within the sample platform, T_b is

the temperature of the sample puck frame that contains the sample platform and $P(t)$ is the power applied to the heater. The sample heat capacity can then be extracted from C_{total} by subtraction of the addenda. Within this Thesis, all heat capacity measurements were performed on a Quantum Design Physical Properties Measurement System (PPMS), which can measure heat capacity in zero field and applied fields strengths up to 9 T from 2 - 400 K. With the addition of a ^{3}He insert, temperatures as low as 300 mK can be accessed.

Chapter 3

Unconventional Spin Glass Ground State in the Geometrically Frustrated $S = 1$ Pyrochlore $Lu_2Mo_2O_7$

3.1 Introduction

The cubic pyrochlore lattice, $A_2B_2O_7$, is formed from a geometrically frustrated network of two interlinking networks of vertex-sharing A and B tetrahedra. The occupation of either or both of the cation sites by a magnetic ion can, therefore, result in interesting and unusual magnetic behaviours due to magnetic frustration. Rather than undergoing a transition to a long-range magnetically ordered state upon cooling, magnetic pyrochlore oxides display a variety of uncoventional grounds states including spin ice, spin glass and spin liquid states [108].

The rare earth, R, molybdate pyrochlores, $R_2Mo_2O_7$, are a series of materials whose ground state properties are known to depend strongly on lattice effects, such as the ionic radius of the rare earth cation occupying the A-site [109]. For instance, members of the series based on the larger rare earths with an ionic radius $r_{R^{3+}} > 1.04$ Å are metallic ferromagnets. On the other hand, for $R_2Mo_2O_7$ with smaller rare earth cations occupying the A-site insulating, antiferromagnetic behaviour is observed with a frustrated spin glass-like state

adopted at low temperatures. $Y_2Mo_2O_7$, which contains non-magnetic Y^{3+} and $S = 1$ $4d^2$ Mo^{4+}, is a very well studied member of the series that displays many of the characteristics typical of glassy systems [110], [111], [112]. It is well understood that the canonical spin-glass materials, such as magnetically dilute metal alloys, are a result of the combination of randomness, through site or bond disorder, and magnetic frustration [22]. In the case of $Y_2Mo_2O_7$, the frustration clearly arises from the geometric frustration of the pyrochlore lattice but the cause of disorder or lattice distortion in this material that results in spin freezing is an open and active area of research [113] that has prompted the use of several local structure probes [114], [115], [116], [117].

$Lu_2Mo_2O_7$ is based on non-magnetic Lu^{3+}, the smallest cation in the rare earth series and is, therefore, expected to show frustrated spin glass-like behaviour. The synthesis of $Lu_2Mo_2O_7$ has been discussed to a limited extent in earlier work but the magnetic properties of $Lu_2Mo_2O_7$ are not well reported [118], [119]. The synthesis and study of $Lu_2Mo_2O_7$ are important, given that it is expected to be another uncommon example of a spin glass-like material with no evident source of structural disorder, and may help to shed further light on the origin of spin freezing in other $R_2Mo_2O_7$ analogues.

Presented in the following Chapter is a detailed magnetic study of the spin glass-like state of $Lu_2Mo_2O_7$, which exists below an apparent spin freezing transition, $T_f \sim 16$ K. This study includes AC and DC magnetic susceptibility, heat capacity, muon spin relaxation and neutron scattering measurements. Furthermore, the sensitivity of the ground state magnetic properties to oxygen content of this material is discussed and the existence of a miscibility gap between stoichiometric and $Lu_2Mo_2O_{7-x}$ cubic pyrochlore phases is presented.

3.2 Synthesis and Characterisation

Polycrystalline samples of $Lu_2Mo_2O_7$ were prepared by ceramic solid state synthesis. Stoichiometric amounts of MoO_2 (Sigma Aldrich, 99.99 %) and Lu_2O_3 (Sigma Aldrich, 99.99 %) were ground and pelletised and heated to 1600 °C for 12 hours under flowing argon gas with intermediate re-grinding and re-pelletising [118]. A molybdenum powder oxygen-getter was required in order to prevent the oxidation of MoO_2 to the more volatile MoO_3 during heating. Powder X-ray diffraction data were collected on a Bruker D8 Advance diffractometer, with

monochromated Cu $K_{\alpha 1}$ radiation. Powder X-ray diffraction profiles of initial samples revealed that two pyrochlore phases are present, the reflections of which can be indexed by cubic lattice constants, a, of 10.14 Å and 10.17 Å. The relative amount of each phase appears to depend upon the distance between the samples and the oxygen-getter during synthesis, see Figure 3.1, and a single pyrochlore phase with the lattice constant $a = 10.14$ Å was prepared by increasing the separation between the sample and the getter to ~ 10 cm. A single phase sample of the $a = 10.17$ Å phase was obtained by reducing the $a = 10.14$ Å phase in a hydrogen atmosphere at 600 °C for 2 hours, see Figure 3.2. This indicates that the miscibility gap in the $Lu_2Mo_2O_{7-x}$ system at 1600 °C is related to the oxygen content of the pyrochlore phases.

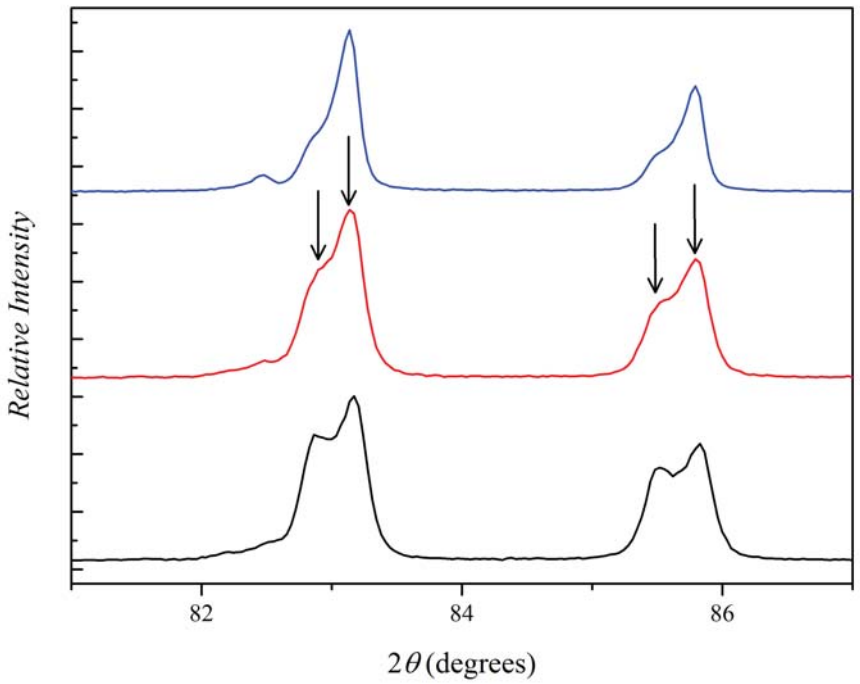

Figure 3.1 *A small region of the powder X-ray diffraction patterns for three samples of $Lu_2Mo_2O_{7-x}$ heated at 1600 °C for 12 hours under flowing Ar with a Mo-powder oxygen-getter. The arrows evidence the two pyrochlore phases and the changing phase proportions illustrate the effect of increasing the separation between the sample and the getter during synthesis from bottom sample to top sample.*

Heating the $a = 10.14$ Å phase in air at 750 °C for 2 hours resulted in complete oxidation of the sample to Lu_2O_3 and MoO_3 and a weight increase of 4.9(4) %, which corresponds to a chemical composition of $Lu_2Mo_2O_{7.00(1)}$. This confirms that the $a = 10.14$ Å phase is stoichiometric $Lu_2Mo_2O_7$. A weight loss of 1.03(1)

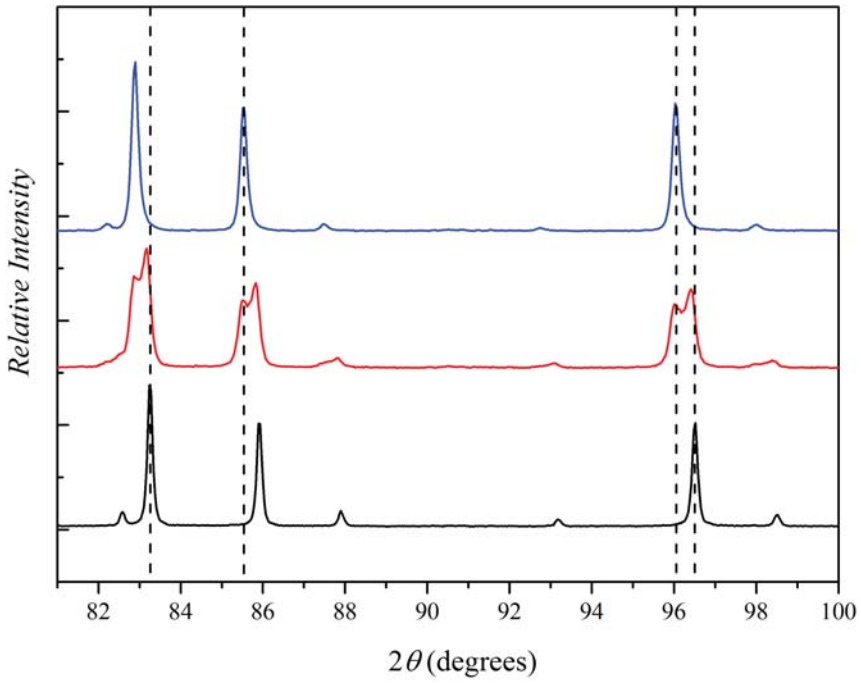

Figure 3.2 *Powder X-ray diffraction patterns for single phase samples at top and bottom with a two phase pattern shown in the centre.*

% was observed upon reduction of the sample to the $a = 10.17$ Å phase, which gives a chemical composition of $Lu_2Mo_2O_{6.58(1)}$ for the reduced phase.

3.3 Neutron Diffraction Study

High resolution neutron powder diffraction data were collected on the D2B powder diffractometer with a neutron wavelength $\lambda = 1.594$ Å at the high flux reactor of the Institut Laue-Langevin, France. Rietveld refinements of the cubic $Fd\bar{3}m$ (no. 227) pyrochlore model to the data were performed using the General Structure Analysis System (GSAS) program [85]. A joint analysis of the data collected at 300 K for samples of $Lu_2Mo_2O_7$ and $Lu_2Mo_2O_{7-x}$ was carried out, with a simultaneous refinement of both models to both data sets, in order to minimise correlation between atomic occupancies and thermal parameters. The oxygen site occupancies were fixed according to the gravimetric analysis of the $Lu_2Mo_2O_7$ phase but allowed to refine for $Lu_2Mo_2O_{7-x}$, while isotropic thermal parameters were constrained to refine together over the two phases. Linear interpolation functions were refined to the background of both data sets.

Figure 3.3 displays the Rietveld plots of the $Lu_2Mo_2O_7$ and $Lu_2Mo_2O_{7-x}$ phases, respectively and Table 3.1 summarises the results of the refinement. The refined oxygen content of the reduced phase of 6.69(6) agrees with the gravimetrically determined value of 6.58(1) and the reduced 10.17 Å phase is thus described as $Lu_2Mo_2O_{6.6}$.

Table 3.1 *Refined atomic coordinates and occupancies for* $Lu_2Mo_2O_7$ *(*a = 10.1478(1) *Å) and (lower values, where different)* $Lu_2Mo_2O_{6.69(6)}$ *(*a = 10.1789(1) *Å). Isotropic thermal parameters (*U_{iso}*) were* 0.0091(2) *Å*^{2} *for metal cations and* 0.0152(3) *Å*^{2} *for oxygen sites. Total* R_{wp} = 5.83 %, χ^2 = 6.89 *for* 62 *variables.*

Atom	Site	x	y	z	Occupancy
Lu	16d	$\frac{1}{2}$	$\frac{1}{2}$	$\frac{1}{2}$	1.0
Mo	16c	0	0	0	1.0
O	48f	0.3417(1) 0.3477(1)	$\frac{1}{8}$	$\frac{1}{8}$	1.0 0.97(1)
O'	8b	$\frac{3}{8}$	$\frac{3}{8}$	$\frac{3}{8}$	1.0 0.87(2)

Figure 3.4 shows the difference between neutron diffraction data collected at 1.5 K and 50 K for $Lu_2Mo_2O_7$ in the low 2θ region, which reveals an absence of magnetic Bragg scattering upon cooling.

3.4 Magnetic Susceptibility

DC magnetic susceptibilities of $Lu_2Mo_2O_7$ and $Lu_2Mo_2O_{6.6}$ were measured in an applied field of 1 T from 2 K to 300 K in a zero field cooled (ZFC) field cooled (FC) cycle, shown in Figure 3.5. At high temperatures, both samples follow Curie-Weiss behaviour with a fit,

$$\chi^{-1} = \left(\frac{C}{T-\theta}\right)^{-1} \tag{3.1}$$

to inverse susceptibilities between 150 K and 300 K yielding Weiss temperatures, θ, of $-158(1)$ K and $-329(1)$ K and Curie constants, C, of 0.892(3) K emu mol^{-1} and 1.323(3) K emu mol^{-1}, for $Lu_2Mo_2O_7$ and $Lu_2Mo_2O_{6.6}$, respectively. Both samples evidence the onset of an irreversible spin glass-like state with the

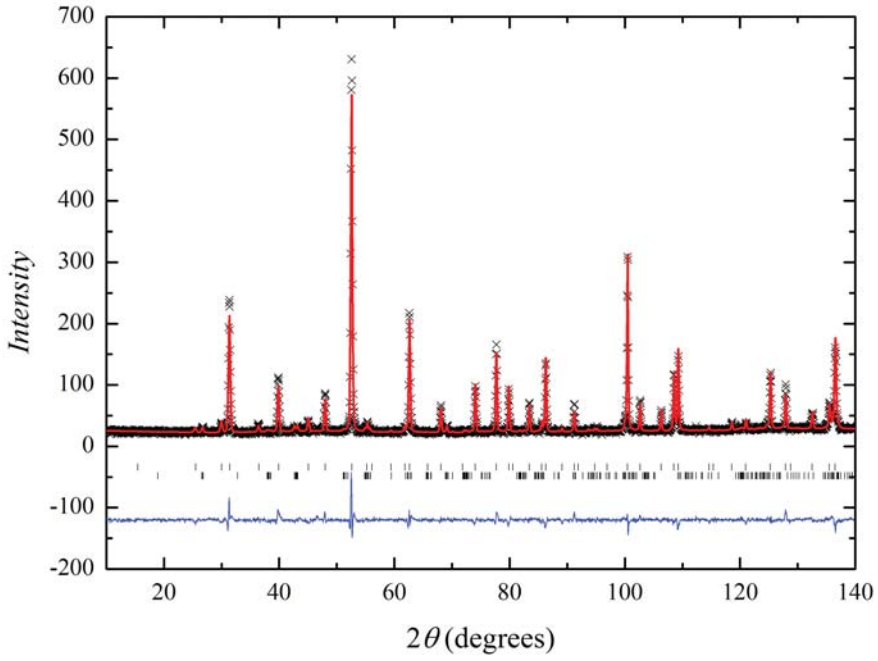

(a) $Lu_2Mo_2O_7$

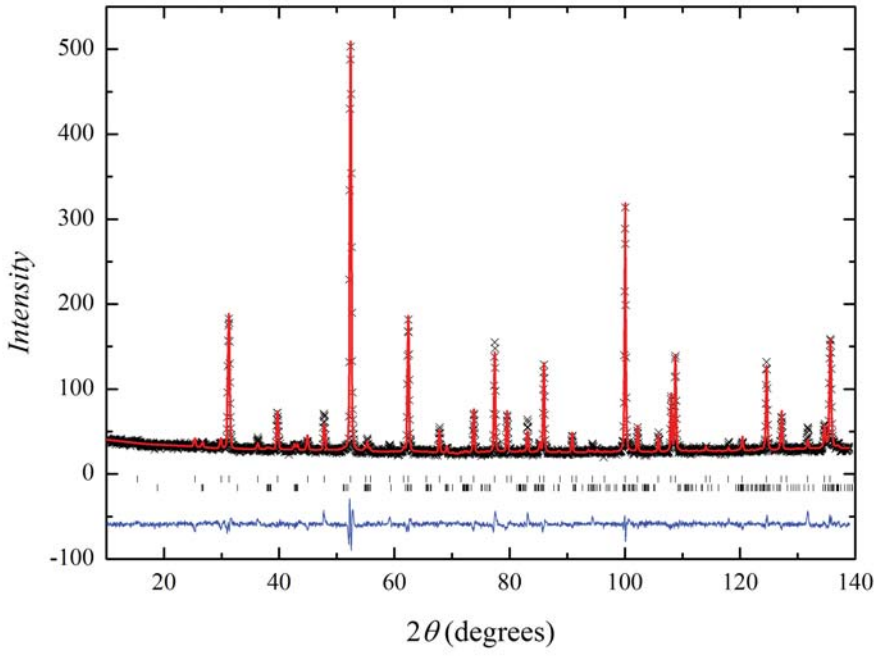

(b) $Lu_2Mo_2O_{6.6}$

Figure 3.3 *Rietveld refinement of the cubic $Fd\bar{3}m$ pyrochlore model to room temperature D2B data of $Lu_2Mo_2O_{7-x}$. Ticks mark reflections for the pyrochlore phase (top) and a MoO_2 impurity phase ($\sim$ 4 % phase fraction, bottom).*

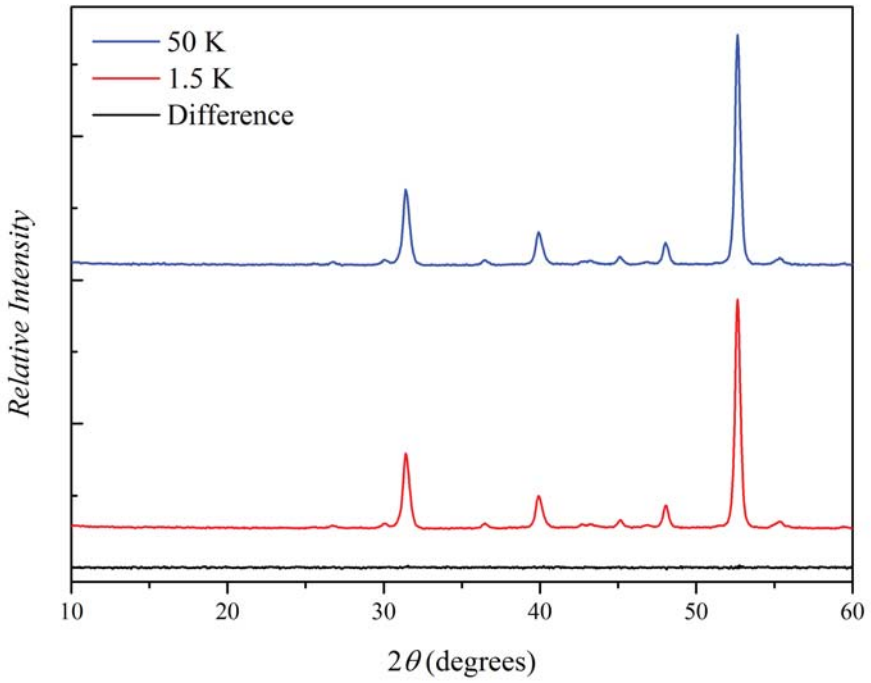

Figure 3.4 *The difference (bottom) between powder neutron diffraction data collected for $Lu_2Mo_2O_7$ at 1.5 K (middle) and 50 K (top) in the low 2θ region, showing no accumulation of magnetic scattering upon cooling.*

divergence of field cooled and zero field cooled susceptibilities at apparent spin freezing transitions, T_f. Figure 3.6 shows a shift in T_f from $\sim$ 16 K in $Lu_2Mo_2O_7$ to $\sim$ 20 K in $Lu_2Mo_2O_{6.6}$. A comparison of the energy scales of magnetic exchange correlations and spin freezing via the frustration index, $f = |\theta|/T_f$, $\sim$10 for $Lu_2Mo_2O_7$ and $\sim$16 for $Lu_2Mo_2O_{6.6}$, indicates strong geometric frustration [15]. The effective magnetic moments per Mo cation obtained from the Curie constants are $\mu_{eff} = 1.9\ \mu_B$ and $\mu_{eff} = 2.3\ \mu_B$ for $Lu_2Mo_2O_7$ and $Lu_2Mo_2O_{6.6}$, respectively.

AC susceptibility data were measured for $Lu_2Mo_2O_7$ in an oscillating applied field of 3.5×10^{-4} T at measuring frequencies, ω, from 5 Hz to 1053 Hz. Figure 3.7 shows the frequency dependence of the AC response of $Lu_2Mo_2O_7$ around the spin freezing transition, which was successfully modelled by the Vogel-Fulcher law [120], a modified Arrhenius-type equation commonly associated with glassy

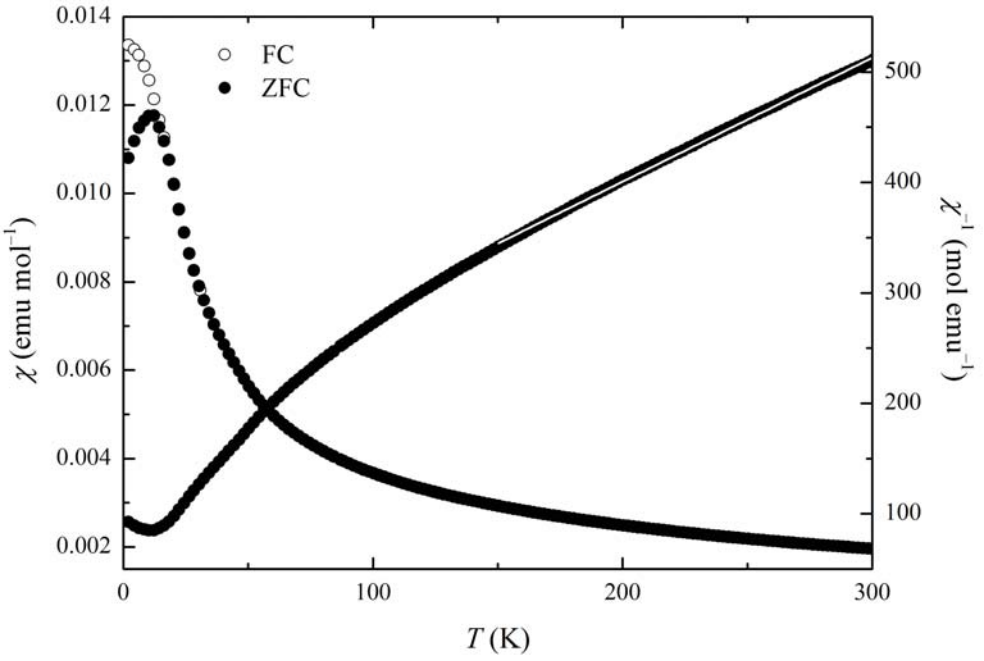

(a) $Lu_2Mo_2O_7$

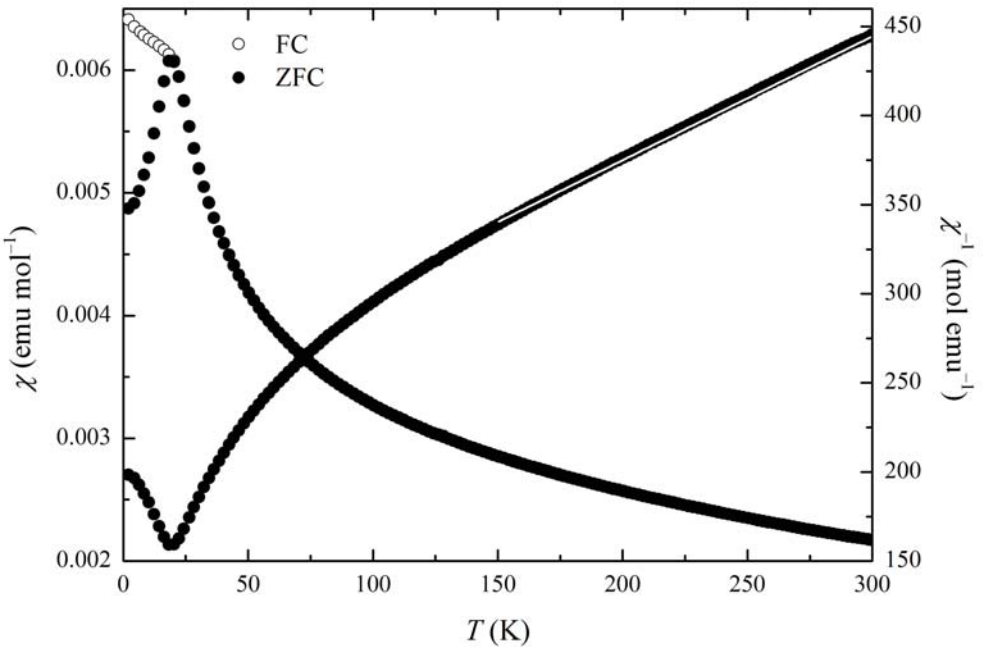

(b) $Lu_2Mo_2O_{6.6}$

Figure 3.5 *Magnetic and inverse susceptibilities measured for* $Lu_2Mo_2O_7$ *and* $Lu_2Mo_2O_{6.6}$ *in a 1 T field. Solid white line shows Curie-Weiss fit to inverse susceptibility between* 150 *K and* 300 *K.*

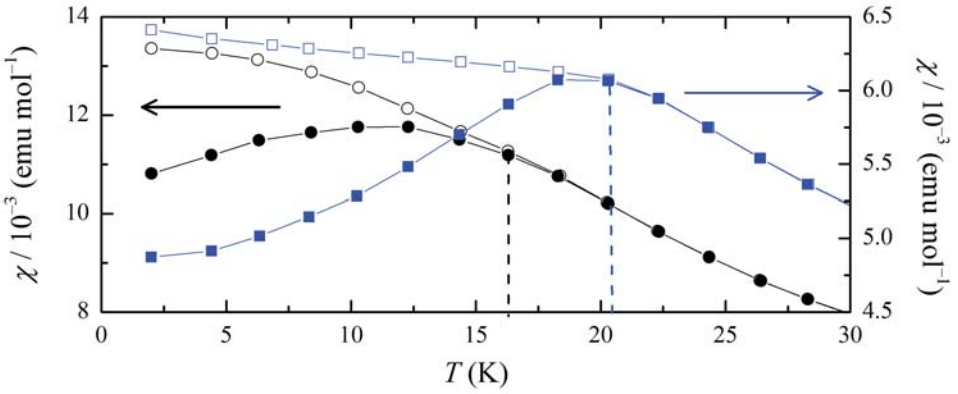

Figure 3.6 *Increase in the spin freezing temperature, T_f from $\sim$ 16 K in $Lu_2Mo_2O_7$ to $\sim$ 20 K in $Lu_2Mo_2O_{6.6}$.*

dynamics [13],

$$\omega = \omega_0 \exp\left(- \frac{E_a}{k_B(T_f - T_0)} \right) \tag{3.2}$$

where ω_0 is a characteristic frequency, E_a is the activation energy and T_0 is the ideal glass temperature, which allows for spin-spin interactions. The fit to the data shown in the inset of Figure 3.7 gives $\ln(\omega_0/s^{-1}) = 17.0(8)$, $E_a/k_B = 8.5(6)$ K and $T_0 = 15.300(5)$ K.

3.5 Heat Capacity

Zero field heat capacity was measured on a 9.0 mg pressed powder pellet of $Lu_2Mo_2O_7$ in a Quantum Design PPMS from 1.8 K to 300 K. In order to estimate the lattice contribution to the total heat capacity, shown in Figure 5.4, the high temperature data were modelled by the Debye equation [121],

$$C = 9N_A k_B \left(\frac{T}{\theta_D}\right) \int_0^{\frac{\theta_D}{T}} \frac{x^4 e^x dx}{(e^x - 1)^2} \tag{3.3}$$

where $x = \hbar ck/k_B T$ ($ck = \omega$ is the linear dispersion relation of the vibrational lattice modes), with a Debye temperature, which measures the stiffness or rigidity of a lattice, $\theta_D \sim 540$ K. Upon subtraction of the estimated lattice contribution

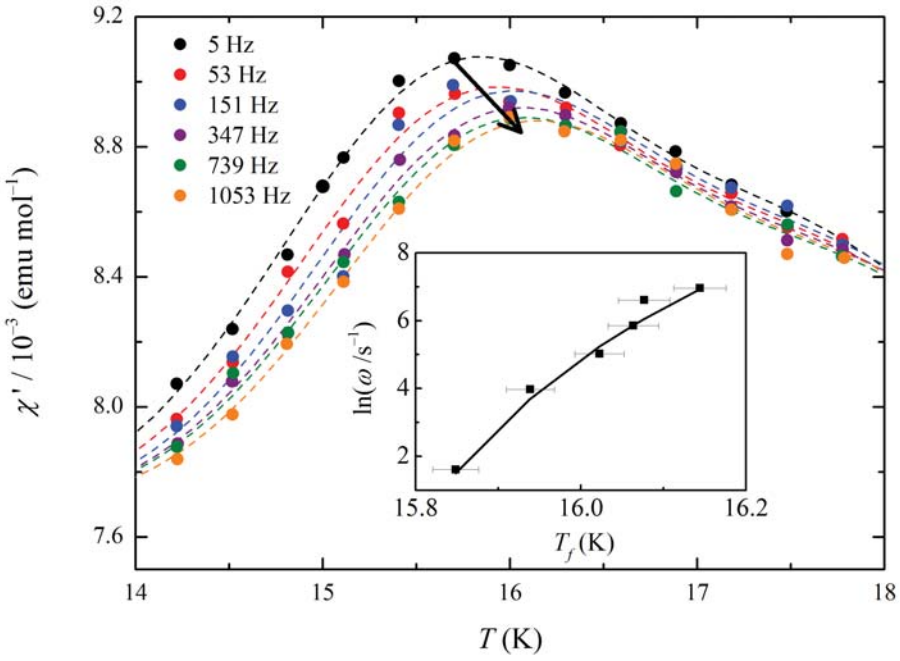

Figure 3.7 *Real AC susceptibility of $Lu_2Mo_2O_7$ showing the shift in T_f with measuring frequency. The inset shows the Vogel-Fulcher fit of the shift in spin freezing transition T_f as a function of the measuring frequency.*

one obtains the magnetic and electronic contributions, shown in Figure 3.8, which demonstrates a broad maximum $\sim$ 50 K.

The inset of Figure 3.8 shows the low temperature region of the magnetic heat capacity, which appears to follow T^2-behaviour and has been modelled by the expression $C = \beta T^2$, with $\beta = 8.6 \times 10^{-4}$ J mol^{-1} K^{-3} per formula unit.

3.6 Muon Spin Relaxation

Muon spin relaxation data were collected on a 3 g sample of $Lu_2Mo_2O_7$ on the MuSR spectrometer at the ISIS Muon Facility, Rutherford Appleton Laboratory, U.K. The sample was contained in an aluminium sample plate with a sheet of Mylar plastic in a Variox cryostat that allowed access down to temperatures of 1.5 K.

The time dependence of the muon decay asymmetry in $Lu_2Mo_2O_7$ in an applied

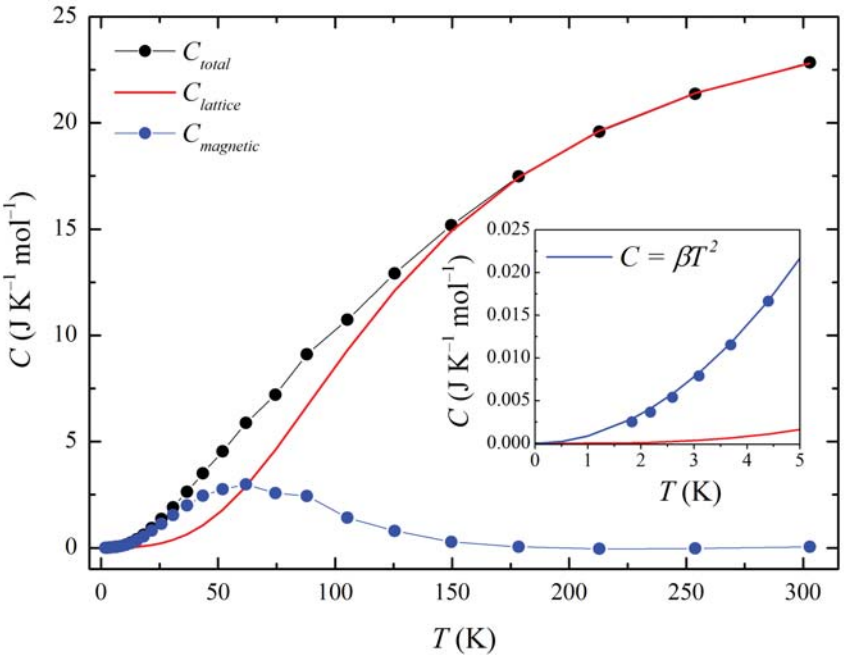

Figure 3.8 *Total heat capacity of $Lu_2Mo_2O_7$ with an estimation of the lattice contribution by means of a Debye fit to the data (red solid line). Upon subtraction of the lattice contribution, the magnetic component of the heat capacity shows a broad anomaly with a maximum ~ 50 K. Inset shows the low temperature region of the magnetic heat capacity, which can be modelled with $C \propto T^2$ behaviour (blue solid line).*

longitudinal field of 200 G is shown in Figure 3.9 measured at temperatures ranging from 1.5 K to 30 K. The data were modelled with a stretched exponential relaxation function given by,

$$A(t) = A_0 \exp(-\lambda t)^{\beta} + B \tag{3.4}$$

where A_0 is the initial asymmetry, B is the background asymmetry, λ is the muon spin relaxation rate and β is the stretching component. Initially, the data were fitted with $\beta = 1$, which yielded the relaxation rates shown in Figure 3.10. Fits to the data around the spin freezing transition (16 - 20 K) could be improved by letting the stretching component vary, with $\beta \rightarrow \frac{1}{3}$. Figure 3.11 shows the field dependence of the muon decay asymmetry from zero field to applied longitudinal field strengths of 2500 G at 30 K and 1.5 K, therefore, above and below the spin freezing transition observed in magnetic susceptibility measurements, $T_f \sim 16$ K.

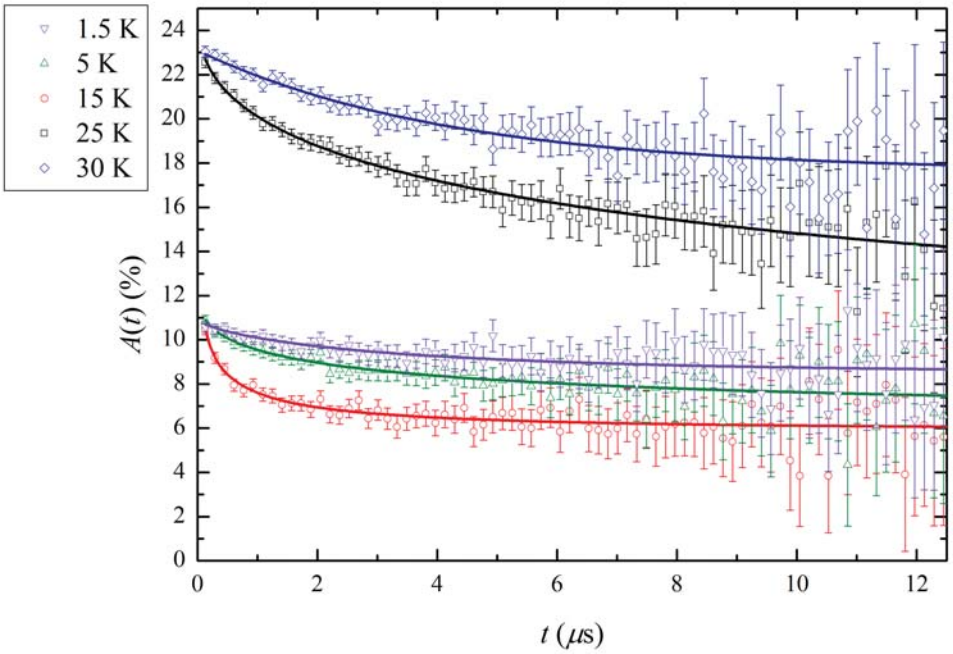

Figure 3.9 *Time dependence of muon decay asymmetry in $Lu_2Mo_2O_7$ measured in an applied longitudinal field of* 200 *G upon cooling. Solid lines are fits to the data.*

The the time dependence of the longitudinal 200 G muon asymmetry can also be successfully modelled by the Uemura spin glass function [122], which is given by,

$$A(t) = A_0\left(\frac{1}{3}\exp(-(4\alpha_d^2 t/\nu))^{\frac{1}{2}}) + \frac{2}{3}\left(1 - \frac{{a_s}^2 t^2}{(4\alpha_d^2 t/\nu + {a_s}^2 t^2)^{\frac{1}{2}}}\right)\exp(-(4\alpha_d^2 t/\nu + {a_s}^2 t^2))^{\frac{1}{2}}\right) + B \tag{3.5}$$

where A_0 is the initial asymmetry, B is the background asymmetry, α_s and α_d give the static and dynamic portions of the magnetic moment, respectively and ν is the fluctuation frequency. As $\alpha_d \rightarrow 0$ in the frozen spin glass state, the equation collapses to a Kubo-Toyabe function that is typically used to describe the dilute, randomly distributed magnetic moments in a canonical spin glass [123]. Figure 3.12 shows the fit of Equation 3.5 to the data.

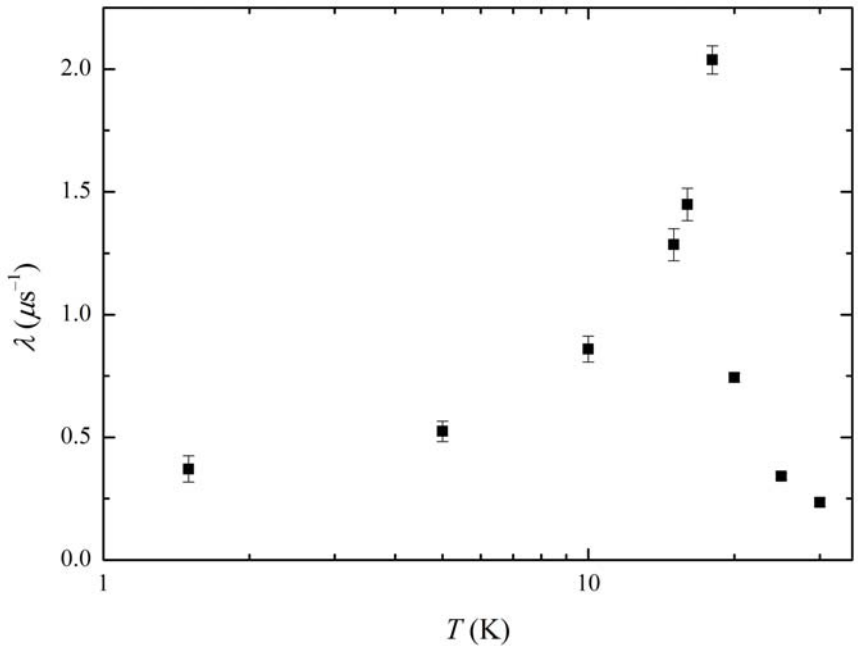

Figure 3.10 *Temperature dependence of the muon spin relaxation rate, λ, obtained from a fit of a single exponential relaxation function to the data measured in an applied longitudinal field of* 200 *G.*

3.7 Magnetic Diffuse Neutron Scattering Study

The magnetic diffuse neutron scattering data of $Lu_2Mo_2O_7$ were collected on an 18 g polycrystalline sample on the diffuse scattering spectrometer D7 at the Institut Laue-Langevin, France. The sample mass was distributed equally into two strips of aluminium foil packed on top of one another in an annular geometry inside a 2 cm diameter aluminium can. In this way, the sample covered the full 5 cm height of the neutron beam whilst minimising the beam attenuation by the sample. The data were initially collected with an incident neutron wavelength of 3.1 Å and without energy analysis the scattering was integrated up to energies of 8.5 meV. The transmission of the sample at this wavelength was determined by measuring the monitor counts of the direct beam through the sample with the monitor counts of the beam through the empty can, normalised by the counts measured for a cylinder of cadmium, which account for any neutrons that pass by the sample can. Each of these monitor count measurements were taken for a

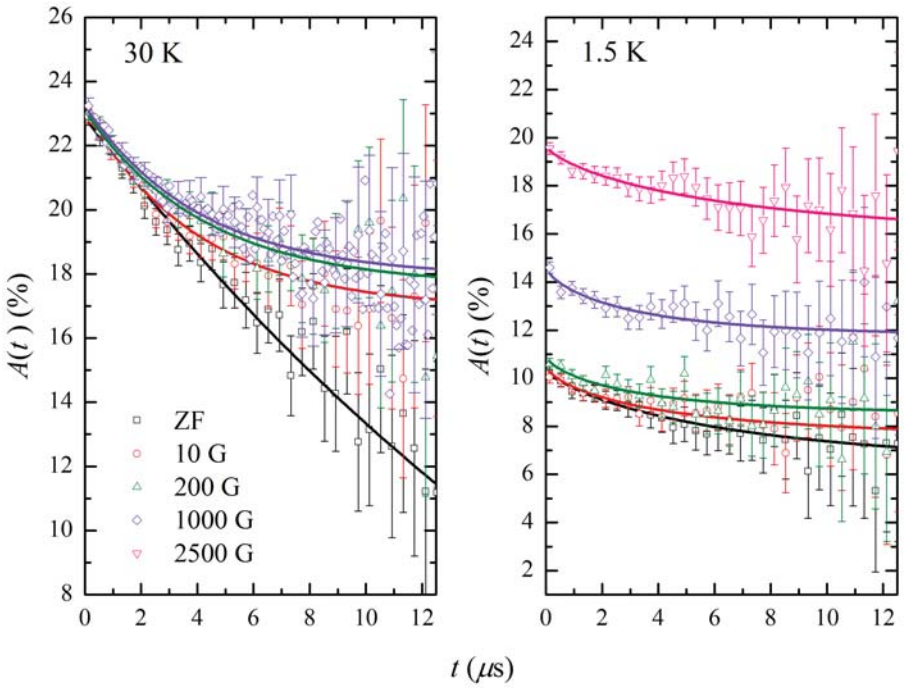

Figure 3.11 *The longitudinal field dependence of the muon decay asymmetry in $Lu_2Mo_2O_7$ above the spin freezing transition at 30 K, shown on the left, and below the transition at 1.5 K on the right.*

total of 120 s, such that the sample transmission is given by,

$$T = \frac{Counts_{Sample} - Counts_{Cd}}{Counts_{Empty\ can} - Counts_{Cd}} = \frac{7831 - 316}{10029 - 316} = 0.77 \tag{3.6}$$

i.e. 77 % of the incident neutron beam was transmitted through the sample with $\lambda = 3.1$ Å. Before the sample was measured, data correction measurements of quartz and cadmium were performed in addition to a vanadium standard, which allows the measured cross sections to be determined in absolute units of barns st.$^{-1}$ f. u.$^{-1}$ [124]. The sample was loaded into an Orange cryostat and data were collected at the base temperature of 1.5 K, below the spin freezing transition, and at 300 K with counting times of 24 hours per temperature. The xyz polarisation analysis of D7 allows for the complete separation of the nuclear, spin incoherent and magnetic cross sections from the total scattering [94]. Figure 3.13 shows this separation of the total scattering data of $Lu_2Mo_2O_7$ at 300 K. The magnetic scattering cross sections at 1.5 K and 300 K are shown in Figure 3.14. The Q dependence observed for both data sets appears to follow the form factor $|F(Q)|^2$ behaviour expected for a paramagnetic regime with no significant evidence of

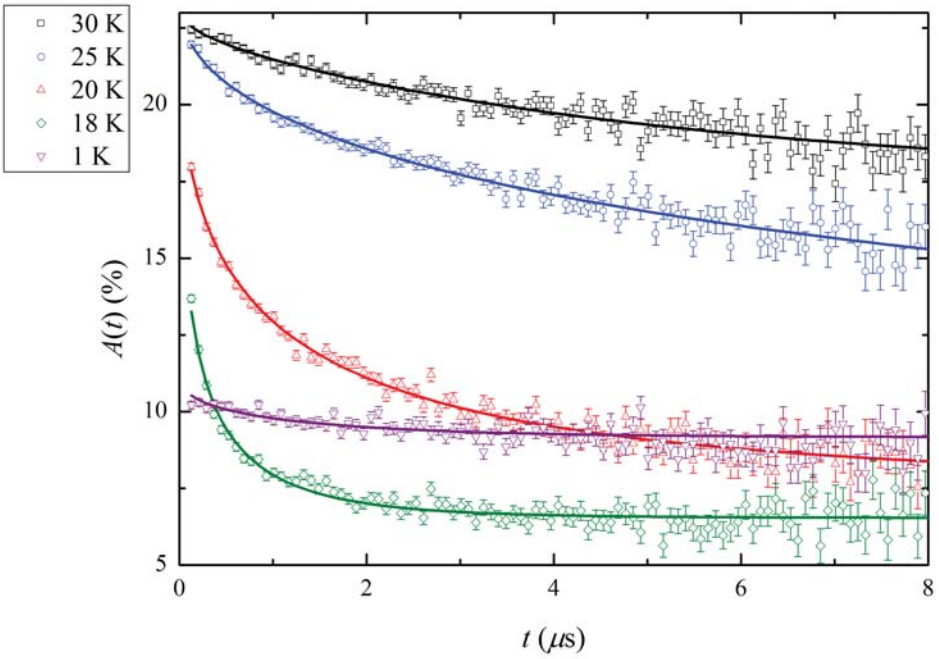

Figure 3.12 *Analysis of the muon decay asymmetry in $Lu_2Mo_2O_7$ in terms of the spin glass function described in the text. Solid lines show the fits to the data.*

spatial spin correlations. In this case, the elastic paramagnetic cross section is given by [124],

$$\frac{d\sigma}{d\Omega} = \frac{2}{3}(\gamma_n r_0)^2 \left(\frac{1}{2} g F(Q)\right)^2 S(S+1) \tag{3.7}$$

where γ_n is the neutron gyromagnetic ratio, r_0 is the classical radius of the electron and g is the g-factor. The magnetic scattering cross sections shown in Figure 3.14 were modelled by the expression given in Equation 3.7 with an analytical approximation of the spin-only magnetic form factor of a molybdenum cation [88],

$$F(Q) = 0.35\exp(-48.035s^2)+1.035\exp(-15.060s^2)-0.3929\exp(-7.479s^2)+0.0139 \tag{3.8}$$

where $s = Q/4\pi$. The total scattering observed at 300 K $g^2S(S+1) =$

1.20(4) $\mu_B^2 = \mu_{eff}^2$ gives a paramagnetic effective magnetic moment of $\mu_{eff} = 0.77(3)\ \mu_B$ per molybdenum cation. At 1.5 K the system is well within its spin glass state such that the spins can be considered to be static with only the lowest m_s states occupied and Equation 3.7 becomes [124],

$$\frac{d\sigma}{d\Omega} = \frac{2}{3}(\gamma_n r_0)^2 \left(\frac{1}{2} g F(Q)\right)^2 S^2 \tag{3.9}$$

The fit of Equation 3.9 to the data taken at 1.5 K yields $g^2 S^2 = 1.59(4)\ \mu_B^2 = \mu_{sat}^2$, which gives a low temperature saturated magnetic moment of $\mu_{sat} = 0.89(2)\ \mu_B$ per molybdenum cation.

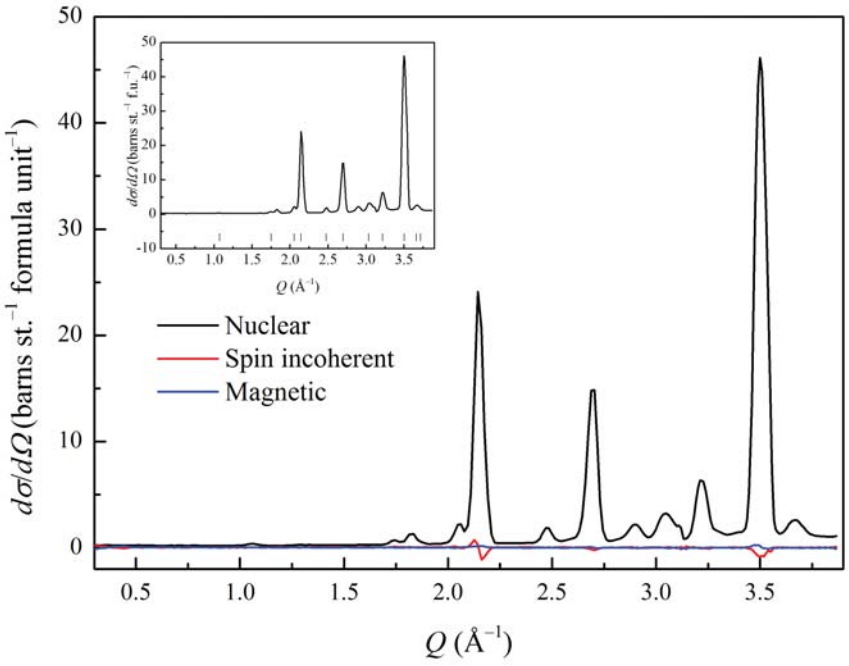

Figure 3.13 *The nuclear, spin incoherent and magnetic contributions to the total scattering cross section of $Lu_2Mo_2O_7$ measured at 300 K with an incident neutron wavelength of* 3.1 *Å. The inset shows the nuclear Bragg scattering with the reflections for the cubic pyrochlore phase marked.*

In a second experiment, the same sample was measured with an incident neutron wavelength of $\lambda = 4.8$ Å. At this wavelength, without analysis of the final energy of scattered neutrons, scattered neutron energies are integrated up to 4 meV. However, the longer wavelength allows for higher resolution and greater coverage

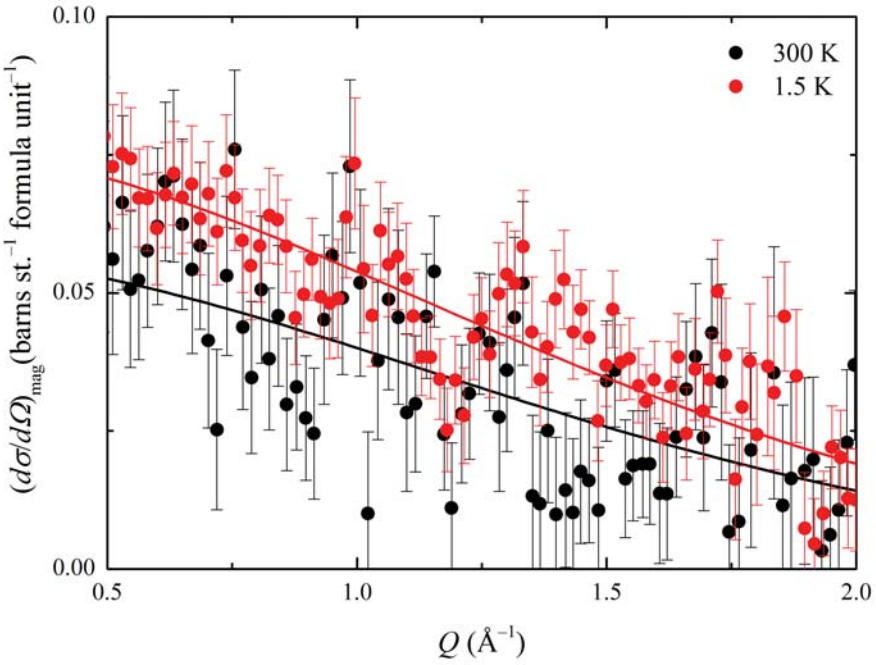

Figure 3.14 *The magnetic scattering cross section of* $Lu_2Mo_2O_7$ *at* 1.5 *K and* 300 *K with an incident neutron wavelength of* 3.1 *Å. The solids lines show the paramagnetic* $F(Q)^2$ *model to the data.*

at low Q such that there is a greater possibility to pick out any features within the magnetic cross section that result from spatial spin correlations. The data were collected according to the method given for the $\lambda = 3.1$ Å experiment, but counting times of approximately 48 hours per temperature were allowed to improve counting statistics. Another important difference to note is that with a longer incident neutron wavelength, the attenuation of the beam by the sample is significant. The transmission of the sample was once again measured and is given by,

$$T = \frac{Counts_{Sample} - Counts_{Cd}}{Counts_{Empty\ can} - Counts_{Cd}} = \frac{5015 - 70}{10224 - 70} = 0.49 \qquad (3.10)$$

such that only 49 % of the incident beam was transmitted through the sample. In order to account for the strong attenuation by the sample, it was necessary to apply an absorption correction to the data [125]. For a powder sample in an annular cylindrical geometry the attenuation of the incident neutron depends on two factors, μR and ρ, where μ is the linear attenuation coefficient, R is the outer radius of the annulus and ρ is the ratio between the radii of the inner and

outer cylinders in the annulus. For $Lu_2Mo_2O_7$, $\mu \sim 0.8$ cm^{-1} due to the large absorption cross section of lutetium, and with inner and outer annulus radii of approximately 0.5 cm and 1.0 cm, respectively, $\mu R \sim 0.8$ and $\rho \sim 0.5$. The transmission factors for an annular cylindrical sample with $\mu R = 1$ and $\rho = 1$ have been calculated at ~ 0.5, which is entirely consistent the experimentally determined sample transmission. These transmission factors are plotted in Figure 3.15 as a function of $\sin^2\theta$ and in order to account for the angular dependence in the absorption correction of the data, they have been fitted by a third order polynomial function [126],

$$T = 0.53922 + 0.06925\sin^2\theta - 0.18205 sin^4\theta + 0.14873\sin^6\theta \tag{3.11}$$

which was then used to correct the data as a function of Q. The magnetic scattering data measured at 1.5 K are shown in Figure 3.16 before and after absorption correction.

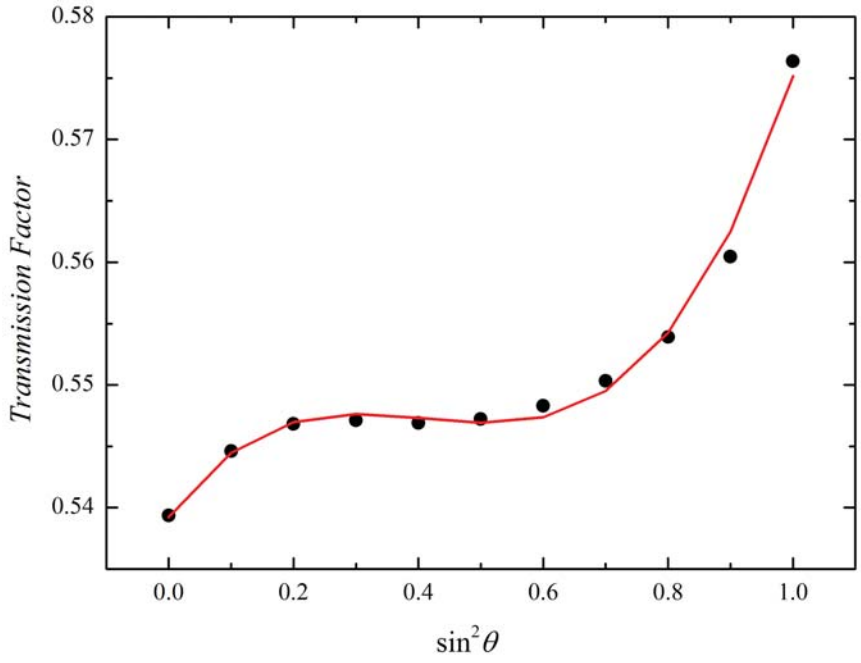

Figure 3.15 *The transmission factor for an annular cylindrical powder sample as a function of scattering angle, which was fitted by a third order polynomial function in $sin^2\theta$ shown by the red solid line.*

The most striking feature of the low temperature magnetic cross section measured at $\lambda = 4.8$ Å is the appearance of a broad, diffuse scattering feature centred about

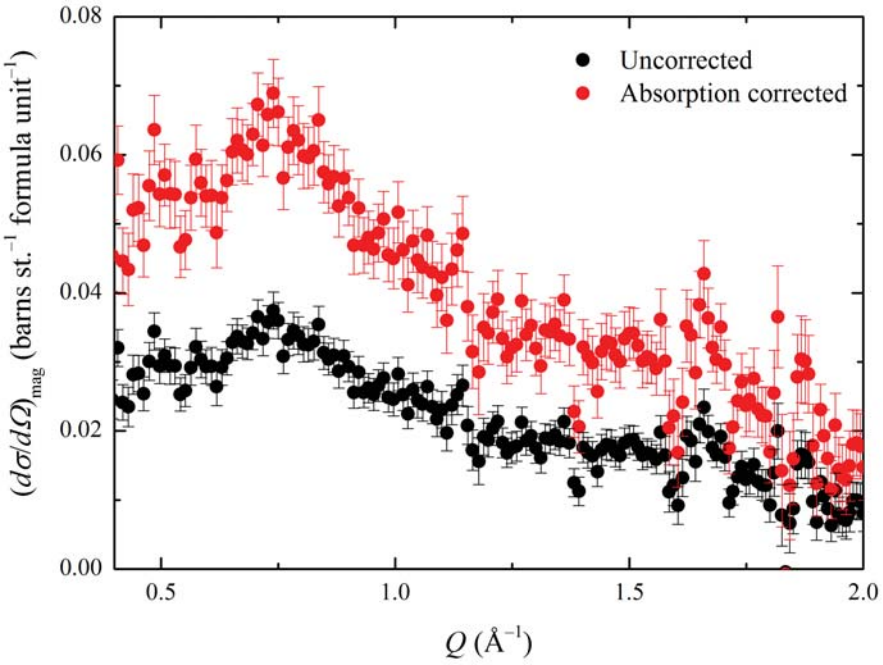

Figure 3.16 *The magnetic scattering cross section of $Lu_2Mo_2O_7$ measured at 1.5 K with an incident neutron wavelength $\lambda = 4.8$ Å before and after the angular dependent absorption correction for an annular cylindrical sample geometry.*

$Q \sim 0.6$ Å^{-1} which indicates the build-up of short range spin correlations. The Q dependence of these near neighbour spatial correlations were modelled by the expression [127], [93],

$$\frac{d\sigma}{d\Omega} = \frac{2}{3}(\gamma_n r_0)^2 \left(\frac{1}{2} gF(Q)\right)^2 \times \left(1 + \sum_i Z_i \langle \mathbf{S}_0 \cdot \mathbf{S}_i \rangle \frac{\sin Q r_i}{Q r_i}\right) \tag{3.12}$$

where $\langle \mathbf{S}_0 \cdot \mathbf{S}_i \rangle$ gives the correlation between a spin and its Z_i nearest neighbours at a distance r_i. Figure 3.17 shows the first three possible magnetic exchange distances within the $Lu_2Mo_2O_7$ structure. In order to obtain a reasonable fit of this model to the data shown in Figure 3.18, it was necessary to include spin correlations on the length scale of the next nearest neighbour (NNN) with $r_{NNN} = 6.203$ Å, $Z_{NNN} = 12$ and $\langle \mathbf{S}_0 \cdot \mathbf{S}_{NNN} \rangle = -0.056(7)$, which gave a $\chi^2 = 1.54$ for the goodness of fit. However, the fit was improved by allowing for nearest neighbour (NN) correlations with $r_{NN} = 3.581$ Å, $Z_{NN} = 6$ and $\langle \mathbf{S}_0 \cdot \mathbf{S}_{NN} \rangle = -0.029(6)$ to give $\chi^2 = 1.32$. The fit of this model to the low

temperature magnetic diffuse scattering data is shown in Figure 3.19. Including spin correlations on any longer length scale, such as third nearest neighbour (see Figure 3.17), did not significantly improve the quality of the fit. Figure 3.20 shows that upon warming above the spin freezing transition one recovers a paramagnetic-like Q-dependence of the magnetic scattering cross section, but with evidence of persisting NN correlations.

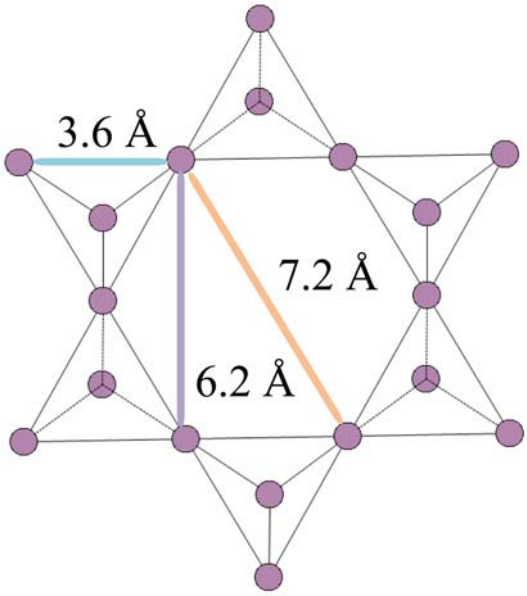

Figure 3.17 *The nearest neighbour, second and third nearest neighbour exchange distances in $Lu_2Mo_2O_7$.*

3.8 Discussion

Powder X-ray diffraction of the initial samples of $Lu_2Mo_2O_7$ clearly show the coexistence of two cubic pyrochlore phases, suggesting that a miscibility gap is present in the $Lu_2Mo_2O_{7-x}$ system at 1600 °C. The Rietveld fits to powder neutron diffraction data and chemical analyses show that the miscibility gap is between stoichiometric $Lu_2Mo_2O_7$ and oxygen deficient $Lu_2Mo_2O_{6.6}$. The refined room temperature cubic lattice constants of the stoichiometric and reduced phases, 10.1478(1) Å and 10.1789(1) Å, respectively, are consistent with the larger ionic radius of Mo^{3+} (0.69 Å) compared to that of Mo^{4+} (0.65 Å) [128]. The pyrochlore structure is known to tolerate considerable anion deficiencies. In certain systems, such as $Pb_2Ru_2O_{6.5}$, vacancy ordering on the O' site results in the lowering of symmetry from $Fd\bar{3}m$ to subgroup $F\bar{4}3m$ [129]. However, other

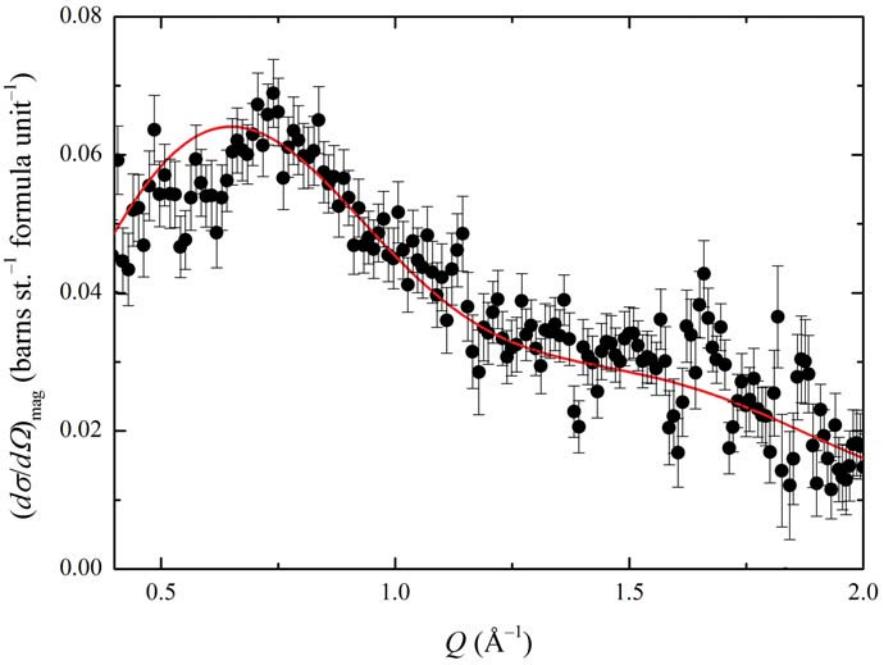

Figure 3.18 *Low temperature magnetic scattering cross section of $Lu_2Mo_2O_7$ with diffuse scattering evidencing short range Mo-Mo spin correlations on a next nearest neighbour correlation length scale of* 6.203 *Å.*

oxygen-deficient materials including $Bi_2Ru_2O_{6.9}$ and $Tl_2Ru_2O_{6.7}$ retain $Fd\bar{3}m$ symmetry with statistically disordered anion vacancies over the O' site [130] and the same structure is observed here for $Lu_2Mo_2O_{6.6}$ with no evidence for a vacancy-ordered superstructure in the neutron diffraction data. In general, oxygen-vacancy order is difficult to predict and depends on the specific details of a particular system [131], [132]. Miscibility gaps between pyrochlore phases have not been reported previously for $R_2Mo_2O_{7-x}$ systems, although a gap was found between $Eu_2Mo_2O_7$ and the derived $Eu_2Mo_2(O,N)_{7-x}$ oxynitride pyrochlore [133]. Phase coexistence driven by cation segregation has been observed in mixed A-cation pyrochlores such as $(Bi_{0.6}Y_{1.4})Sn_2O_7$ [134].

The difference between the 1.5 K and 300 K neutron diffraction data of $Lu_2Mo_2O_7$ is shown in Figure 3.4 in the low 2θ region where any build-up of magnetic scattering would be most evident. The absence of magnetic Bragg scattering demonstrates that there is no long range spin order down to at least 1.5 K. The DC magnetic susceptibility of $Lu_2Mo_2O_7$ (Figure 3.5) displays a clear divergence of field cooled (FC) and zero field cooled (ZFC) susceptibilities, characteristic of

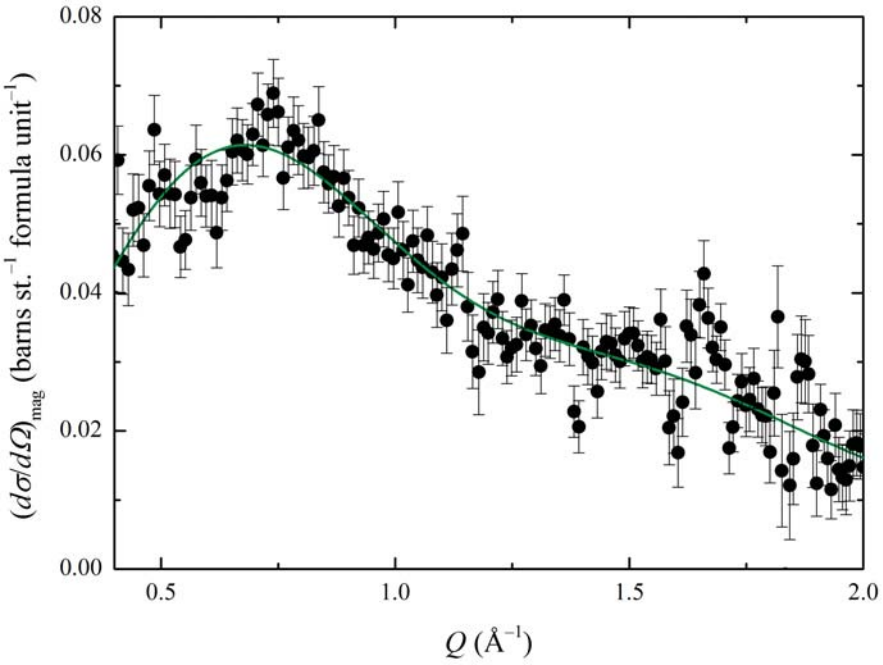

Figure 3.19 *The model of the low temperature magnetic diffuse scattering in $Lu_2Mo_2O_7$ is improved by including nearest neighbour and next nearest neighbour spin correlations.*

the onset of an irreversible glass-like state, at an apparent spin freezing transition, $T_f \sim 16$ K. A Curie-Weiss fit to the inverse of susceptibility between 150 K and 300 K gave a Weiss constant $\theta = -158(1)$ K, indicating a dominance of antiferromagnetic exchange interactions. A comparison of the energy scales of magnetic interactions and spin freezing via the frustration index, $f = |\theta|/T_f \sim 10$ implies that there is a significant frustration of spin order due to the geometrically frustrated pyrochlore network of antiferromagnetically interacting Mo^{4+} spins. An effective magnetic moment of $\mu_{eff} = 1.9\ \mu_B$ per Mo cation was obtained from the Curie-Weiss fit ($C = 0.892(3)$ K emu mol^{-1} formula unit^{-1}). The reduced effective moment compared with the expected spin only value for $S = 1$ Mo^{4+} is due to significant spin-orbit coupling in this $4d$ transition metal system. The AC magnetic response of $Lu_2Mo_2O_7$ can also be understood in terms of archetypal spin glass behaviour. The data show an increase in the spin freezing temperature with increasing frequency, which was measured over a range 5 - 1053 Hz. This behavior is typical of a glass-like state; as frequency is increased the spin directions are less able to follow the oscillating field and so appear frozen at progressively higher temperatures. The magnitude of this shift, given by

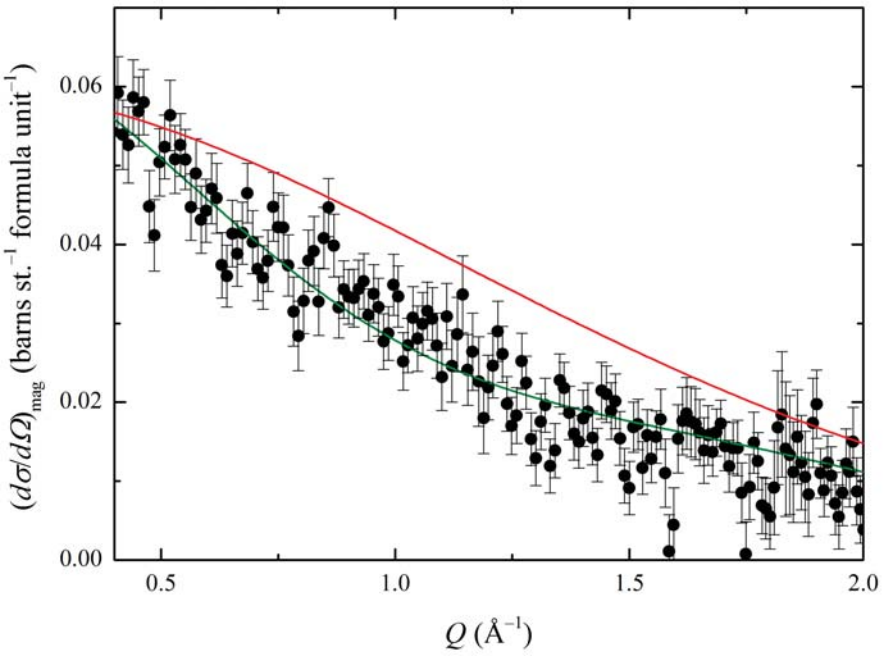

Figure 3.20 *The absorption corrected magnetic scattering cross section of $Lu_2Mo_2O_7$ measured at 300 K with an incident neutron wavelength $\lambda = 4.8$ Å. The red solid line shows a paramagnetic $F(\mathbf{Q})^2$ model (Equation 3.7) but the fit to the data is significantly improved by allowing for nearest neighbour correlations as a shown by the solid green line (Equation 3.12 with $Z = 6$, $r = 3.581$ and $\langle \mathbf{S}_0 \cdot \mathbf{S}_{NN} \rangle = 0.092(8)$.)*

$(\Delta T_f/T_f)\Delta(log\omega) = 0.008$, is of the order observed in many classical spin-glass systems [13]. A fit of the Vogel-Fulcher equation (Equation 3.2) to the data gave $\ln(\omega_0/s^1) = 17.0(8)$, $E_a/k_B = 8.5(6)$ K and $T_0 = 15.300(5)$ K. The observation that $T_0 \sim T_f$ is considered representative of canonical spin glasses [13].

The presence of a geometrically frustrated network of Mo^{4+} spins is further confirmed by the low temperature magnetic diffuse scattering data measured on the D7 spectrometer with an incident neutron wavelength of 4.8 Å. A broad peak centred around $Q \sim 0.6$ Å^{-1} (see Figure 3.19) indicated the build-up of short range magnetic correlations at low temperatures, which were successfully modelled by nearest neighbour and next nearest neighbour exchange. The negative sign and the the short range nature of these interactions, $\langle \mathbf{S}_0 \cdot \mathbf{S}_{NN} \rangle = -0.03$ and $\langle \mathbf{S}_0 \cdot \mathbf{S}_{NNN} \rangle = -0.06$, are indicative of the frustrated nature of the ground state [127]. Their similar magnitude also highlights the strong competition

between the nearest neighbour and next nearest neighbour exchange processes within the low temperature, spin frozen state. The data taken with an incident neutron wavelength of 3.1 Å were not able to resolve the short range correlations within the spin glass-like regime. At 300 K the observed magnetic moment is somewhat reduced, $\mu_{eff} = 1.1\ \mu_B$ per Mo^{4+}. This is due to the fact that in the fast fluctuating paramagnetic state, a significant portion of the magnetic scattering occurs outside of the window of energy integration and the quasi-static approximation on which D7 relies breaks down [93].

The magnetic susceptibility data for the reduced phase, $Lu_2Mo_2O_{6.6}$, are qualitatively similar to those for $Lu_2Mo_2O_7$, but with significant changes in the underlying parameters. The susceptibilities of both samples are shown in Figure 3.6 around the spin freezing transition, from which a shift in T_f from $\sim$ 16 K to $\sim$ 20 K is observed. A Curie-Weiss fit to the inverse susceptibility over the same temperature range as the fit to the $Lu_2Mo_2O_7$ data (150-300 K) gives an effective moment $\mu_{eff} = 2.3\ \mu_B$, reflecting the partial reduction of $S = 1$ Mo^{4+} to $S = \frac{3}{2}$ Mo^{3+}. The Weiss constant $\theta = -329(1)$ K shows that the strength of superexchange interactions is enhanced, but the frustration factor of $f \sim 16$ reveals that the disorder in $Lu_2Mo_2O_{7-x}$ markedly increases the degree of frustration in comparison to $Lu_2Mo_2O_7$. The results presented here for $Lu_2Mo_2O_{6.6}$ have demonstrated that the oxygen content of $Lu_2Mo_2O_{7-x}$ has a significant effect on magnetic properties, including the energy scale of antiferromagnetic exchange, the spin freezing temperature, and the frustration factor. This highlights the importance of the control of oxygen content in the $R_2Mo_2O_7$ series and the need for careful analysis of samples through diffraction and gravimetric techniques. A systematic study of the geometrically frustrated spin glass $LiCrMnO_{4-\delta}$ spinels [135] revealed that a deviation from oxygen stoichiometry as small as 0.63 % can have a profound effect on the magnetic properties of the spin glass state. Rietveld analyses of powder diffraction data have previously been reported to show no deviation from full oxygen occupancy in the average crystalline structure of the spin glass pyrochlores, which gives an upper limit of $\sim$1 % for oxygen non-stoichiometry [26]. In the case of $Lu_2Mo_2O_{6.6}$ the level of oxygen deficiency is more significant, at $\sim$6 %. The effect of oxygen deficiency in other $R_2Mo_2O_{7-x}$ is not well reported for the spin glass phases, but there has been some interest in $Gd_2Mo_2O_{7-x}$ given its close proximity to the metal-insulator transition in the series [108].

The muon spin relaxation data of $Lu_2Mo_2O_7$ also display many of the charac-

teristics expected for a spin glass-like state. At high temperatures, the data are well described by a single component lorentzian muon spin relaxation with a relaxation rate, λ, which is shown as a function of temperature in Figure 3.10. The sharp transition in the relaxation rate $\sim$ 18 K is in keeping with the spin freezing transition observed in the magnetic susceptibility data at 16 K. The single component nature of the high temperature muon spin relaxation data is a typical paramagnetic response. Upon cooling towards the transition temperature, the two component nature of the data becomes apparent and indicates the presence of randomly distributed, quasi-static internal fields at low temperatures [123]. This behaviour was also phenomenologically described by the spin glass function of Uemura (Equation 3.5), which was inititally developed during a muon spin relaxation study of the canonical spin glasses AuFe and CuMn [122].

From the point of view of the muon spin relaxation measurements and magnetic susceptility measurements, $Lu_2Mo_2O_7$ is a typical spin glass with a spin freezing transition $T_f \sim 16$ K. In this respect, it is very similar to $Y_2Mo_2O_7$, which shows a strong frequency dependence in its AC susceptibility around the spin freezing transition [112] $T_f \sim 22$ K and a sharp transition in the muon spin relaxation rate [136]. $Tb_2Mo_2O_7$ also displays spin glass characteristics with $T_f \sim 25$ K but the situation is somewhat complicated here with competition between ferromagnetic Tb-Tb interactions and antiferromagnetic Tb-Mo exchange [137]. Other insulating $R_2Mo_2O_7$ analogues are less well studied in comparison, but $Ho_2Mo_2O_7$ has a reported freezing temperature of 21 K and $Yb_2Mo_2O_7$, based on the second smallest rare earth cation, has $T_f \sim 18$ K [138], [139]. This reveals a trend of decreasing spin glass transition temperature with decreasing R^{3+} ionic radius. The trend is understandable from the variation of the Mo-O-Mo bond angle, α, that governs the magnitude and nature of the magnetic exchange between Mo^{4+} ions. The fit to the powder neutron diffraction data of $Lu_2Mo_2O_7$ gives $\alpha = 125.08(9)$ °, whereas, the angle reported for $Y_2Mo_2O_7$ is somewhat larger, $\alpha = 126.97$ °. A systematic study of $R_2Mo_2O_7$ (R = Dy, Gd, Sm and Nd) revealed an increase in α across the spin glass to ferromagnet transition, from $\alpha = 127.7$ ° in the spin glass $Dy_2Mo_2O_7$ to $\alpha = 131.5$ ° in ferromagnetic $Nd_2Mo_2O_7$ [140]. The magnetic phase diagram of the $R_2Mo_2O_7$ series is shown in Figure 3.21. The magnetic properties of the $R_2Mo_2O_7$ series are not, therefore, governed by the Kanamori-Goodenough rule which states that a larger M-O-M bonding angle favours an antiferromagnetic exchange interaction [141], [142]. It has been argued that the ferromagnetic ordering between the spins of Mo^{4+} cations in $R_2Mo_2O_7$ based on the larger rare earth cations is due to the double-

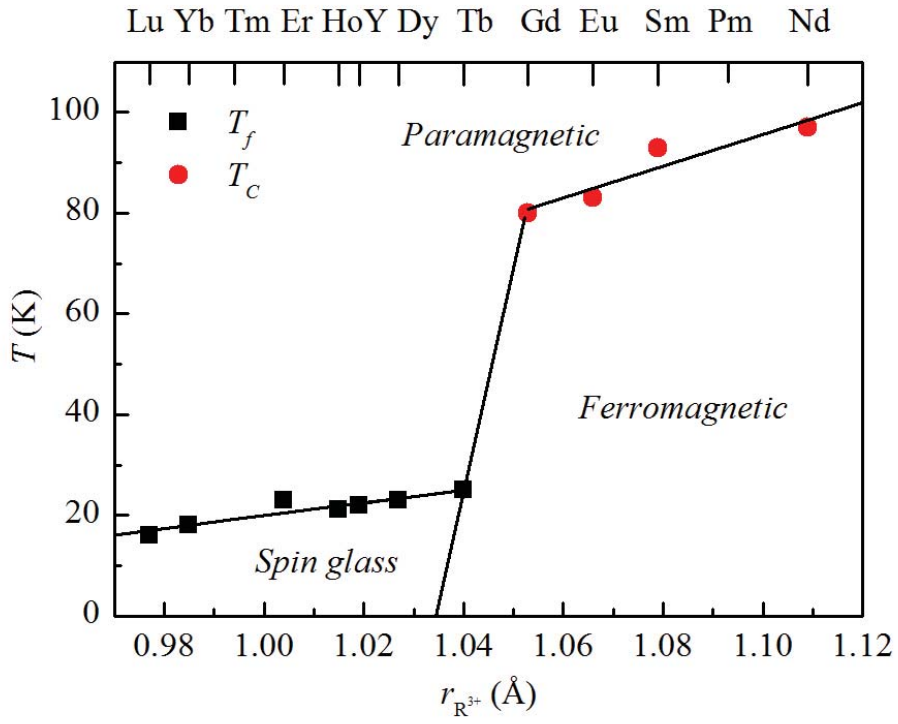

Figure 3.21 *The magnetic phase diagram of the $R_2Mo_2O_7$ series, including $Lu_2Mo_2O_7$.*

exchange mechanism. The t_{2g} orbital degernacy is lifted to give a higher lying level in which electrons are mobile to mediate the ferromagnetic interaction with the localised spins of the electrons in the lower lying level. As the ionic radius of the rare earth cation is increased, the inherent antiferromagnetic superexchange pathway is suppressed and the double-exchange mechanism dominates to give a metallic ferromagnetic ground state [140].

There are, however, certain aspects of $Lu_2Mo_2O_7$ that appear quite different from a canonical spin glass, and even $Y_2Mo_2O_7$. The magnetic heat capacity of a spin glass state is expected to show a broad feature $\sim$ 50 % above the spin freezing transition with linear T-dependence at low temperatures. The magnetic heat capacity of $Y_2Mo_2O_7$ has a broad hump between 10 K and 30 K and below this, clearly follows T-linear behaviour to low temperatures [111]. This linear variation of heat capacity indicates that there is a continuous density of magnetic states down to the lowest temperatures, which is characteristic of a spin glass state [15]. In the case of $Lu_2Mo_2O_7$, a broad hump is observed in the heat capacity upon subtraction of the estimated lattice contribution, which indicates that short-range correlations persist up to high temperatures. It is important

to note that this smeared-out feature extends out to $\sim$ 100 K, which is much higher in energy than for $Y_2Mo_2O_7$ and implies that the onset of the glassy state in $Lu_2Mo_2O_7$ occurs on a higher energy scale. This is consistent with the magnetic diffuse neutron scattering data, which suggest that short range Mo-Mo spin correlations persist up to 300 K. The most important difference between the heat capacities of $Lu_2Mo_2O_7$ and its yttrium based analogue is their low temperature behaviours. The heat capacity measured for $Lu_2Mo_2O_7$ clearly follows a T^2 dependence at low temperatures, with a fit of $C_v = \beta T^2$ yielding $\beta = 8.6\times10^{-}4$ J mol^{-1} K^{-3} per formula unit. A similar T^2-dependence has been observed in certain two-dimensional kagome based systems, such as the $S = \frac{5}{2}$ jarosite $(H_3O)Fe_3(SO_4)_2(OH)_6$ [25] and the kagome bilayer SCGO(x) [143]. Typically for a long range ordered antiferromagnet, the low temperature heat capacity follows a $C \propto T^{\frac{d}{\nu}}$ dependence, where d is the spatial dimensionality and ν is the exponent in the excitation dispersion, which is given by $\nu = 1$ in an antiferromagnetic. In the topological spin glass systems, the T^2 variation was, therefore, attributed to the presence of a gapless excitation spectrum that result from the propagation of a two-dimensional antiferromagnetic spin wave [15]. Interestingly, a T^2-dependence has recently been measured on the first single crystal sample of $Y_2Mo_2O_7$ [113]. The origin of this unusual low temperature behaviour displayed in the latest measurements of $Y_2Mo_2O_7$ are argued to result from the orbital degeneracy in the Mo^{4+} $S = 1$ cation. It has been proposed the the orbital degree of freedom in this $4d^2$ system could couple to the spin degrees of freedom to give rise to a T^2-dependence of the magnetic heat capacity at low temperatures [144], [145]. It is likely that this spin-orbit coupling between the spin and orbital degrees of freedom in the Mo^{4+} cation also plays an important role in $Lu_2Mo_2O_7$.

3.9 Conclusions

Polycrystalline $Lu_2Mo_2O_7$ has been prepared by solid state synthesis at 1600 °C. Powder X-ray and neutron diffraction and thermal gravimetric analysis have revealed the existence of a miscibility gap in the $Lu_2Mo_2O_{7-x}$ system at 1600 °C between stoichiometric $Lu_2Mo_2O_7$ and $Lu_2Mo_2O_{6.6}$. An extensive study of the ground state magnetic properties of $Lu_2Mo_2O_7$ has revealed an apparent spin freezing transition at $T_f \sim 16$ K, which given the significant energy scale of antiferromagnetic exchange ($\theta = -158$ K), implies that spin order in $Lu_2Mo_2O_7$

is highly frustrated with a frustration index, $f \sim 10$. Magnetic diffuse neutron scattering data reveal that this frustration arises from the strong competition between the nearest neighbour and next nearest neighbour exchanges correlations at low temperatures. The magnetic susceptibility data collected for the reduced phase $Lu_2Mo_2O_{6.6}$, show that the magnetic properties are qualitatively similar to those of $Lu_2Mo_2O_7$, but with significant changes in the underlying parameters. For instance, a shift in the spin freezing transition from 16 K to 20 K is observed and the Weiss constant $\theta = -329$ K shows that that the strength of superexchange interactions is enhanced. In addition, the frustration factor of $f \sim 16$ reveals that the disorder in $Lu_2Mo_2O_{7-x}$ markedly increases the degree of frustration in comparison to $Lu_2Mo_2O_7$.

$Lu_2Mo_2O_7$ displays certain properties expected for canonical spin glasses and many similarities to its widely studied yttrium based analogue $Y_2Mo_2O_7$. The apparent glassy behaviour in $Y_2Mo_2O_7$ sparked a quest to find the disorder that drives the formation a of spin glass ground state at low temperatures in a material, which on the average crystallographic scale, appears well ordered. It is important to note the unusual low temperature behaviour of the magnetic heat capacity, which unlike classical spin glasses and polycrystalline $Y_2Mo_2O_7$, shows a T^2-variation. Such behaviour had been observed in other glassy systems, where is has been predicted that the spin glass state can exist in the absence of disorder. $Lu_2Mo_2O_7$ could, therefore, provide another example of an ordered, topological spin glass state. In order to understand the magnetic ground state in $Lu_2Mo_2O_7$ further, an inelastic neutron scattering survey is necessary in order to observe the nature of the scattering out with the energy range that has been measured on D7 and to determine the form of magnetic excitations from the ground state.

Chapter 4

Spin Liquid-like Ground State in the Oxynitride Pyrochlore $Lu_2Mo_2O_{4.8}N_{1.7}$

4.1 Introduction

The antiferromagnetic pyrochlore lattice, formed of corner-sharing tetrahedra of antiferromagnetically interacting spins is one of the canonical examples of a geometrically frustrated lattice. The $S = \frac{1}{2}$ pyrochlore antiferromagnet is a prime candidate to host a quantum spin liquid ground state. The exact nature of this exotic ground state, however, is unknown and experimental candidates of a three-dimensional quantum spin liquid remain extremely rare. One way in which such a material could be realised is through the synthesis of oxynitride rare earth molybdate pyrochlores, which can be achieved through the thermal ammonolysis of $R_2Mo_2O_7$ phases. With an ideal composition of $R_2Mo_2O_5N_2$ the Mo^{4+} cations that reside on the tetrahedral oxide pyrochlore network are oxidised to the Mo^{5+} $4d^1$ oxidation state in order to compensate for the greater charge of the N^{3-} nitride anion in comparison with the O^{2-} oxide anion. Thermal ammonolysis is a topochemical reaction, which means that the geometrically frustrated pyrochlore structure is retained upon nitridation [133]. $R_2Mo_2O_5N_2$ oxynitride pyrochlores are thus excellent candidates to host quantum spin liquid phenomena.

Several members of the $R_2Mo_2O_7$ series have been nitrided by thermal ammonoly-

sis including $Sm_2Mo_2O_{3.83}N_{3.17}$ [146], $Y_2Mo_2O_{4.5}N_{2.5}$[147] and $Eu_2Mo_2(O,N)_{7-x}$ [133]. Most recently, the R = Eu analogue was investigated, which showed an absence of spin freezing or long range magnetic order down to 2 K from a magnetic susceptibility study of the $Eu_2Mo_2O_{3.75}N_{3.06}$ [133]. Oxynitrides of the $Lu_2Mo_2O_7$ pyrochlore have not been reported previously, and the non-magnetic nature of the Lu^{3+} cation means that the magnetism on the molybdenum sub-lattice can be investigated individually in the $Lu_2Mo_2O_5N_2$ system. In the following Chapter, the synthesis of a new oxynitride pyrochlore phase, $Lu_2Mo_2O_{4.8}N_{1.7}$, is reported along with a preliminary study of the material through magnetic susceptibility, heat capacity and neutron scattering measurements. In addition, a comparison of the low temperature magnetic behaviours of the spin glass $Lu_2Mo_2O_7$ presented in Chapter 3 and $Lu_2Mo_2O_{4.8}N_{1.7}$ is given.

4.2 Synthesis and Characterisation

Oxynitride pyrochlore samples were prepared by the thermal ammonlysis of $Lu_2Mo_2O_7$. The oxide precursor was synthesised by the solid state reaction of Lu_2O_3 and MoO_2 according to the method given in Chapter 3. 3 g of oxide precursor were ground into a fine powder in an agate mortar and pestle and spread thinly and evenly over a surface area of 10 cm × 1.5 cm in a large alumina crucible. The sample was then heated under flowing ammonia gas with a flow rate of 250 cm^3/min at 600 °C for 12 hours, before re-grinding and re-spreading and a second 600 °C 12 hours ammonia heat treatment. The sample was heated in a tube furnace with stainless steel fittings and ammonia-resistant teflon gas tubing. The system was purged with nitrogen gas before and after ammonia gas was allowed to flow through the system. The out-flowing ammonia was neutralised through a series of gas bubblers containing a solution of acetic acid and water.

The corresponding weight loss of the sample due to the ammonolysis was 1.87 %, which reflects the lower atomic mass of nitrogen in comparison with oxygen. The nitrogen content of the sample was determined to be 3.88 % by elemental analysis on a Carlo Erba CHNS analyser at the School of Chemistry, University of St Andrews. This gives an elemental composition of $Lu_2Mo_2O_{4.81}N_{1.71}$ and, thus, an average molybdenum oxidation state of $Mo^{4.4+}$. In order to scale up the sample size for neutron scattering studies, this method was repeated to prepare several 3 g samples that were well ground together to give a homogeneous sample of 18 g. The average weight loss of the large scale sample upon ammonolysis

was 1.83 % and the average nitrogen content was determined to be 3.92 % by elemental analysis, giving a chemical composition of $Lu_2Mo_2O_{4.75}N_{1.73}$, which is in good agreement with the composition of the initial 3 g sample.

4.3 Magnetic Susceptibility

The DC magnetic susceptibility of $Lu_2Mo_2O_{4.8}N_{1.7}$ was measured in an applied field of 1 T from 2 K to 300 K in a zero field cooled (ZFC) field cooled (FC) cycle, as shown in Figure 4.1. At high temperatures, the data can be described by Curie-Weiss behaviour and the solid white line in Figure 4.1 shows the fit of,

$$\chi^{-1} = \left(\frac{C}{T - \theta} \right)^{-1} \tag{4.1}$$

to the inverse susceptibility data. The Weiss constant $\theta = -121(1)$ K reflects the dominance of strong antiferromagnetic exchange, however, the data do not show any indication of long range magnetic order nor any significant glassy behaviour down to 1.8 K. The Curie constant, $C = 0.311(1)$ K emu mol^{-1}, gives an effective magnetic moment of 1.1 μ_B per molybdenum cation.

4.4 Neutron Diffraction Study

Powder neutron diffraction data were collected on a 3 g sample of $Lu_2Mo_2O_{4.8}N_{1.7}$ on the high resolution powder diffractometer (HRPD) at the ISIS spallation neutron source at the Rutherford Appleton Laboratory, U.K. The sample was contained within a 6 mm diameter vanadium can in a helium cryostat. Data were collected at 4 K for a total counting time of 20 hours. The Rietveld refinement of the cubic $Fd\bar{3}m$ pyrochlore model to the data collected on the backscattering and 90 ° detector banks is shown in Figure 4.2. Table 4.1 summarises the results of the Rietveld refinement, for which the total anion content was constrained to the analytically determined values whilst allowing the oxygen and nitrogen occupancies to refine over both anion sites to give a chemical composition of $Lu_2Mo_2O_{4.81(1)}N_{1.71}$. Isotropic thermal parameters were constrained together for cations and anions. The data are thus well described by a structural pyrochlore model and do not show any evidence of additional magnetic Bragg scattering at

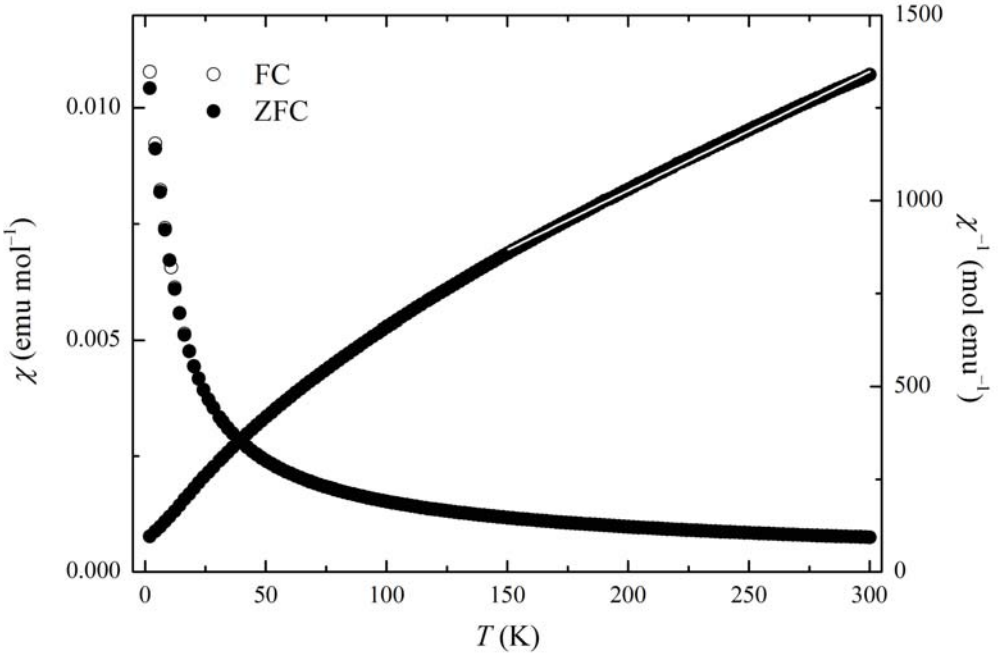

Figure 4.1 *The magnetic and inverse susceptibilities of* $Lu_2Mo_2O_{4.8}N_{1.7}$ *measured in an applied field of* 1 *T. The solid white line shows a Curie-Weiss fit to inverse susceptibility data.*

low temperatures, in agreement with the magnetic susceptibility data.

Table 4.1 *Refined atomic coordinates and occupancies for* $Lu_2Mo_2O_{4.8}N_{1.7}$ *(*a = 10.1428(2) *Å). Isotropic thermal parameters (*U_{iso}*) were* 0.0337(6) *Å*^{2} *for metal cations and* 0.0398(6) *Å*^{2} *for anion sites. Total* R_{wp} = 2.21 %, χ^2 = 14.58 *for* 64 *variables.*

Atom	Site	x	y	z	Occupancy
Lu	16*d*	$\frac{1}{2}$	$\frac{1}{2}$	$\frac{1}{2}$	1.0
Mo	16*c*	0	0	0	1.0
O / N	48*f*	0.3477(1)	$\frac{1}{8}$	$\frac{1}{8}$	0.663(2)/0.257
O' / N'	8*b*	$\frac{3}{8}$	$\frac{3}{8}$	$\frac{3}{8}$	0.831/0.169

4.5 Magnetic Diffuse Neutron Scattering Study

The magnetic diffuse neutron scattering data of $Lu_2Mo_2O_{4.8}N_{1.7}$ were collected on an 18 g polycrystalline sample on the diffuse scattering spectrometer D7 at

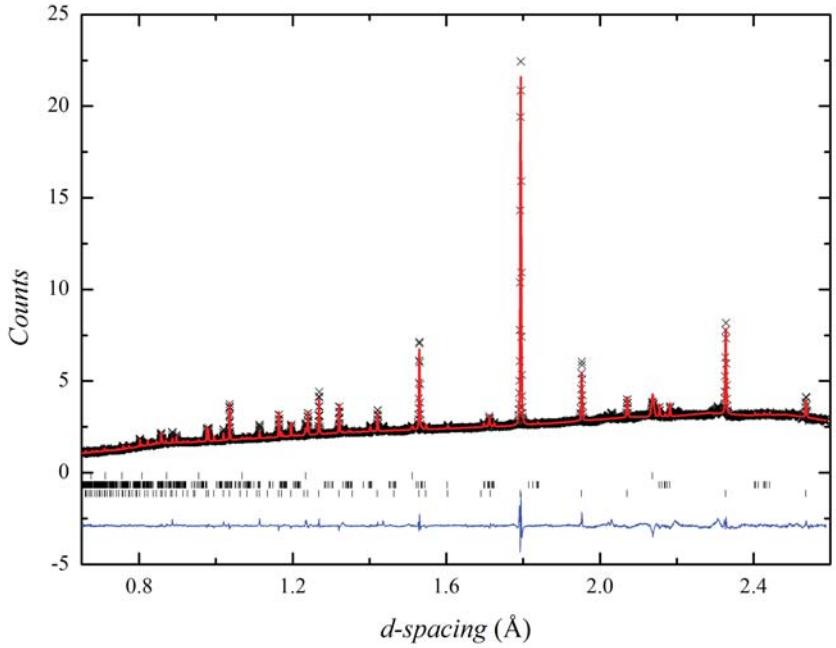

(a) *Backscattering detector bank.*

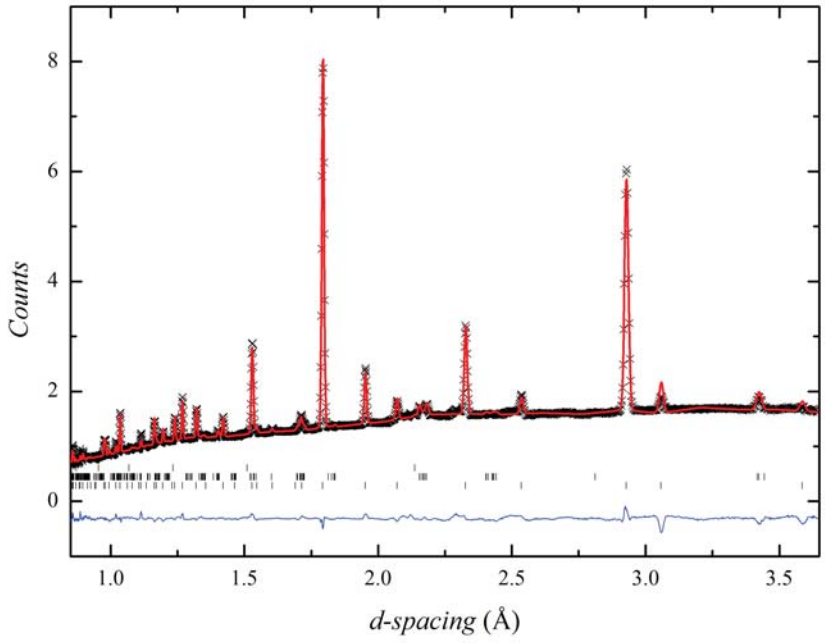

(b) 90 ° *detector bank.*

Figure 4.2 *Rietveld refinement of the cubic* $Fd\bar{3}m$ *model to 4 K HRPD data of* $Lu_2Mo_2O_{4.8}N_{1.7}$. *Bottom tick marks show the reflections for the* $Lu_2Mo_2O_{4.8}N_{1.7}$ *pyrochlore phase, middle tick marks a* MoO_2 *impurity phase (*$\sim$ 5 % *weight) and top ticks marks for scattering observed from the vanadium sample holder.*

the Institut Laue-Langevin, France. The sample was mass distributed equally into two strips of aluminium foil packed on top of one another in an annular geometry inside a 2 cm diameter aluminium can. In this way, the sample covered the full 5 cm height of the neutron beam whilst minimising the beam attenuation by the sample. The data were initially collected with an incident neutron wavelength of 3.1 Å without analysis of neutron energy, thus the scattered neutron energies were integrated up to 8.5 meV. A standard Orange cryostat allowed access to temperatures down to 1.5 K. Quartz, cadmium, and vanadium measurements were performed in order to correct flipping ratios, background and detector efficiencies, respectively. Data were collected for a total of 24 hours per temperature. Figure 4.3 shows the nuclear, spin incoherent and magnetic components of the total scattering cross section taken at 300 K, which were separated by the *xyz* polarisation analysis of the D7 spectrometer. The inset shows the magnetic scattering cross section measured at 1.5 K and 300 K, which coincide reasonably well. The solid blue line in the inset of Figure 4.3 shows an elastic paramagnetic cross section for molybdenum spin only cations,

$$\frac{d\sigma}{d\Omega} = \frac{2}{3}(\gamma_n r_0)^2 \left(\frac{1}{2} g F(Q)\right)^2 S(S+1) \tag{4.2}$$

where,

$$F(Q) = 0.35\exp(-48.035s^2)+1.035\exp(-15.060s^2)-0.3929\exp(-7.479s^2)+0.0139 \tag{4.3}$$

is an analytical approximation for the spin only magnetic form factor for molybdenum cations, with $s = Q/4\pi$ [88]. The magnetic scattering cross section is completely dwarfed by the strong nuclear Bragg scattering and the total magnetic scattering was found to be 0.11(1) μ_B per molybdenum cation, which corresponds to $\sim$ 30 % of the expected $gS(S+1)$ μ_B value.

The sample was also measured with an incident neutron wavelength $\lambda = 4.8$ Å at a temperature of 1.5 K. Data were acquired for a total of 48 hours and corrected for sample attenuation for an annulus [125], [126]. Figure 4.4 shows a comparison of the magnetic scattering cross section at 1.5 K of $Lu_2Mo_2O_7$, which shows a build up of magnetic diffuse scattering at $Q \sim 0.6$ Å^{-1}, and $Lu_2Mo_2O_{4.8}N_{1.7}$, which remains relatively flat and shows little Q-dependence. There may be evidence of

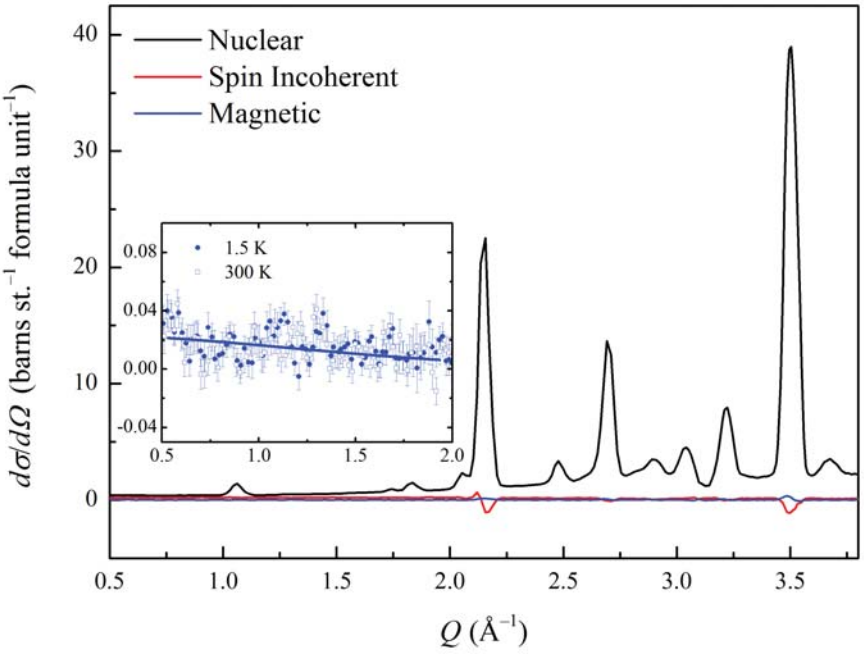

Figure 4.3 *The nuclear, spin incoherent and magnetic components of the total scattering cross section of $Lu_2Mo_2O_{4.8}N_{1.7}$ measured at 300 K with an incident neutron wavelength $\lambda = 3.1$ Å. The inset shows the magnetic scattering cross section in the low-Q region at 1.5 K and 300 K.*

features in the data centred about 0.6 Å and 1.0 Å, which are marked in Figure 4.4.

4.6 Heat Capacity

Zero field heat capacity data were collected for a 8.9 mg pressed powder pellet of $Lu_2Mo_2O_{4.8}N_{1.7}$. The data were taken over a temperature of 500 mK to 30 K with the use of a ^{3}He insert on a Quantum Design PPMS. The data are shown in Figure 4.5. The estimate of the lattice contribution to the total heat capacity of $Lu_2Mo_2O_7$ shown in Chapter 3 was also used here given the isostructural nature and similar formula weight of $Lu_2Mo_2O_{4.8}N_{1.7}$. The low temperature region of the heat capacity, which is mostly magnetic in origin, can be modelled by a linear $C = \gamma T$ dependence with $\gamma = 7.06(3)$ mJ K^{-2} mol^{-1}, shown by the black solid line in the inset of Figure 4.5. The fit to the data can be improved by letting the linear function take an intercept value of 0.8(1) J K^{-1} mol^{-1}, shown by the

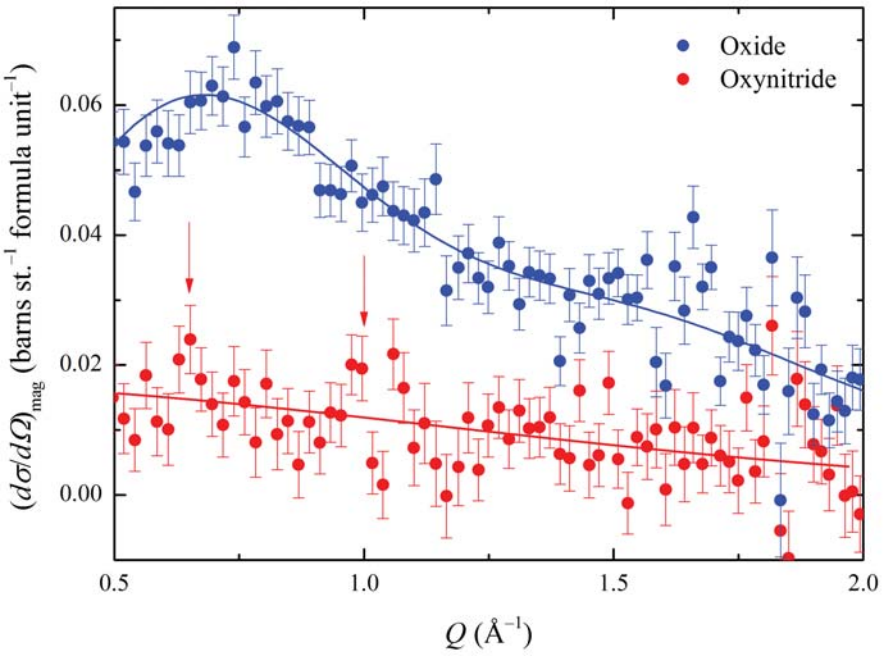

Figure 4.4 *The absorption corrected magnetic scattering cross sections of* $Lu_2Mo_2O_7$ *and* $Lu_2Mo_2O_{4.8}N_{1.7}$ *measured at* 1.5 *K with an incident neutron wavelength* $\lambda = 4.8$ *Å. Arrows mark* Q*-positions of potential features that may indicate Mo-Mo spin correlations.*

blue solid line in the inset of Figure 4.5. The corresponding non-zero entropy at $T = 0$ may result from the anion disorder in this oxynitride system. Figure 4.6 gives a comparison of the low temperature heat capacities of $Lu_2Mo_2O_{4.8}N_{1.7}$ and its parent oxide $Lu_2Mo_2O_7$.

4.7 Discussion

The thermal ammonolysis technique has been successful in synthesising oxynitride samples of the $Lu_2Mo_2O_7$ pyrochlore. The ideal composition for a $S = \frac{1}{2}$ system is $Lu_2Mo_2O_5N_2$, which induces an oxidation of the molybdenum cations to the Mo^{5+} $4d^1$ oxidation state. Thermal ammonolysis of $Lu_2Mo_2O_7$ at 600 °C for 24 hours produced an oxynitride pyrochlore with the chemical composition $Lu_2Mo_2O_{4.8}N_{1.7}$, which was determined through the combination of elemental and gravimetric analyses. Furthermore, the refinement of a cubic pyrochlore model with the analytically determined anion content to high resolution neutron powder

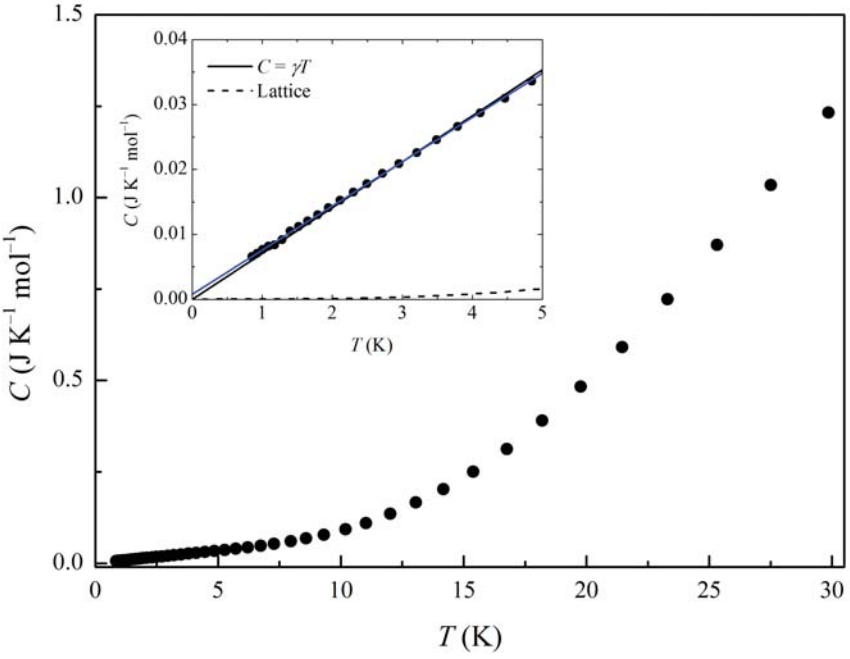

Figure 4.5 *The magnetic heat capacity of $Lu_2Mo_2O_{4.8}N_{1.7}$ over the entire measured temperature range with ^3He insert. The insert shows the low temperature region of the data, which can be modelled by T-linear behaviour (solid lines). An estimate of the lattice contribution is shown (dashed line), which is found to be negligible below 5 K.*

diffraction data gives very good agreement with $R_{wp} = 2.21$ %. The results of the Rietveld refinement shown in Table 4.1 suggest that the distribution of oxide and nitride anions is disordered over both of the anion sites in the pyrochlore structure. From this chemical composition, the molybdenum cations have a nominal oxidation state of $Mo^{4.4+}$, which results in a significant change in the magnetic properties of the system. The Weiss constant, $\theta = -121$ K obtained from the Curie-Weiss fit to the high temperature inverse of magnetic susceptibility shown in Figure 4.1 indicates that strong antiferromagnetic exchange interactions between molybdenum spins remain dominant upon nitridation. The reduction in the effective magnetic moment, $\mu_{eff} = 1.1\ \mu_B$, reflects the low spin nature of the oxynitride system in comparison with $Lu_2Mo_2O_7$. The most significant result obtained from the magnetic susceptibility study of $Lu_2Mo_2O_{4.8}N_{1.7}$ is the apparent loss of the spin freezing transition T_f ~16 K that was observed for the spin glass pyrochlore $Lu_2Mo_2O_7$ in Chapter 3. In fact, the magnetic susceptibility of $Lu_2Mo_2O_{4.8}N_{1.7}$ shows no evidence for any magnetic phase transitions or spin glass behaviour down to 2 K. This is supported by the low temperature neutron

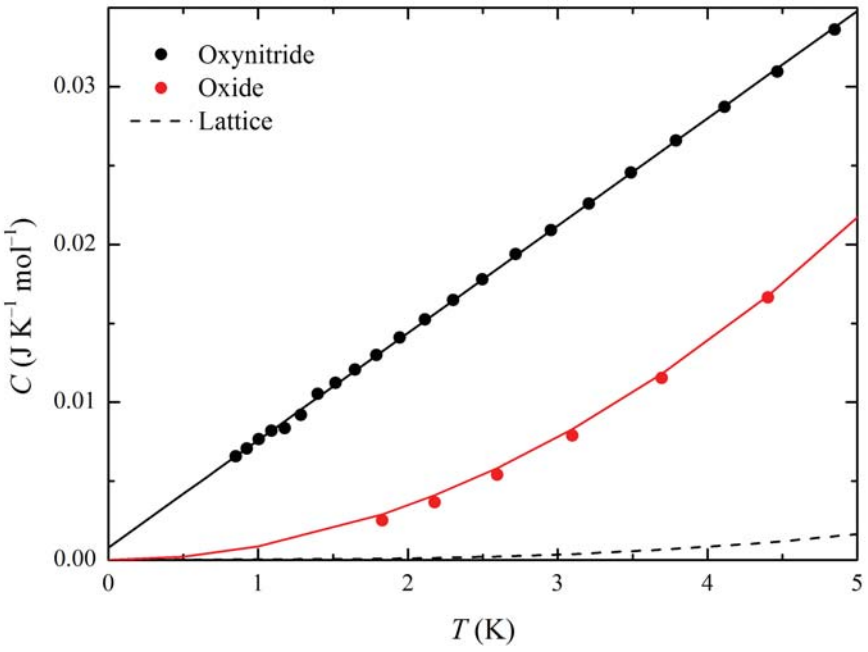

Figure 4.6 *A comparison of the low temperature magnetic heat capacity of $Lu_2Mo_2O_7$, which shows a $C \propto T^2$ behaviour and the T-linear dependence of $Lu_2Mo_2O_{4.8}N_{1.7}$.*

diffraction data, which do not show evidence of long range magnetic order due to the absence of magnetic Bragg scattering.

The magnetic scattering cross section measured on the diffuse scattering spectrometer D7 does not show any significant build-up of strong Q-dependent diffuse scattering upon cooling from room temperature to 1.5 K, as shown in the inset of Figure 4.3. The measured magnetic signal is extremely weak, which in part is a result of the reduced magnetic moment in the oxynitride system, but may also indicate that there is a significant proportion of inelastic neutron scattering from the system even at low temperatures, such that the quasi-static approximation breaks down and the majority of the magnetic neutron scattering occurs outside of the energy range of the D7 instrument [148]. There may be some evidence of peak like features in the magnetic scattering cross section centred around 0.6 Å and 1.0 Å shown in Figure 4.4, but these are difficult to distinguish within the experimental uncertainty of the data. The data are reasonably well described by a paramagnetic Q-dependence and certainly do not show such strong evidence of short range magnetic correlations as in the case of $Lu_2Mo_2O_7$ at low temperatures, which is illustrated in Figure 4.4.

The most striking difference in the behaviours of $Lu_2Mo_2O_{4.8}N_{1.7}$ and its parent oxide is revealed in the low temperature heat capacity. The heat capacity of $Lu_2Mo_2O_{4.8}N_{1.7}$ was measured over a temperature range of 500 mK to 30 K, shown in Figure 4.5 after subtraction of an estimate of the lattice contribution, which shows no temperature dependent anomalies or evidence of a magnetic ordering transition. The low temperature region of the data clearly follow T-linear behaviour, with a $C = \gamma T$ fit yielding $\gamma = 7.06(3)$ mJ K^{-2} mol^{-1}. This linear dependence is evidence for a large number or continuous density of low energy states in $Lu_2Mo_2O_{4.8}N_{1.7}$, which has been observed in a number of spin liquid candidates [49]. As discussed in Chapter 3, $Lu_2Mo_2O_7$ follows a T^2-law at low temperatures, which is rather unusual for a spin glass system. It should also be noted that the heat capacity of $Lu_2Mo_2O_{4.8}N_{1.7}$ appears to deviate from zero at $T = 0$, which may be a result of frozen-in zero-point entropy due to the disordered nature of the anions within the oxynitride system.

4.8 Conclusions

Polycrystalline samples of a novel pyrochlore oxynitride phase $Lu_2Mo_2O_{4.8}N_{1.7}$ have been prepared by the thermal ammonolysis of the $Lu_2Mo_2O_7$ oxide. The oxide precursor was heated under an ammonia gas flow rate of 250 cm^3/min for a total of 24 hours at a temperature of 600 °C. The anion content of the oxynitride phase was determined by chemical analysis and gravimetric analysis and confirmed by Rietveld fit to high resolution powder neutron diffraction data. Magnetic susceptibility confirms the persistence of strong antiferromagnetic exchange ($\theta = -121$ K) but an absence of a spin freezing transition down to at least 2 K. Futhermore, the low temperature magnetic heat capacity reveals an absence of magnetic phase transitions down to 500 mK and a large density of low energy states from its T-linear behaviour, with $\gamma \sim 7$ mJ K^{-2} mol^{-1}. The absence of magnetic diffuse scattering from the $Lu_2Mo_2O_{4.8}N_{1.7}$ systems implies that the majority of the magnetic neutron scattering at low temperatures is inelastic and that the magnetic ground state of $Lu_2Mo_2O_{4.8}N_{1.7}$ is dynamic. This is unlike a frozen spin glass state, in which all of the magnetic neutron scattering is expected to collapse into the elastic line [26]. In order to investigate the role of the low spin or quantum fluctuations in governing the ground state properties of $Lu_2Mo_2O_{4.8}N_{1.7}$, a proposal has been submitted to perform the first inelastic neutron scattering survey of the material on the Cold Neutron

Chopper Spectrometer (CNCS) at the Spallation Neutron Source of the Oak Ridge National Laboratory, U.S.A.

Chapter 5

Gapless Spin Liquid Ground State in the $S = \frac{1}{2}$ Vanadium Oxyfluoride DQVOF

5.1 Introduction

Experimental realisations of the $S = \frac{1}{2}$ kagome antiferromagnet (KAFM) are highly desirable as they are the prime candidate to host the exotic quantum spin liquid (QSL) ground state in two-dimensions. This results from the combination of the strong geometric frustration of antiferromagnetically coupled spins on the kagome lattice of vertex sharing equilateral triangles and the quantum effects that allow incoherent spin fluctuations to persist down to $T = 0$ [49]. A review of the literature reveals that, until very recently, all of the candidate compounds of $S = \frac{1}{2}$ kagome physics consisted of kagome networks of Cu^{2+} d^9 cations [149] [150] [151] [152]. The significance of this is that the d^9 electronic configuration is known to have strong Jahn-Teller effects, which in certain situations can affect low temperature structural and magnetic properties that can ultimately limit the potential of such systems as candidate QSLs [4]. A good example of this is the volborthite mineral, $Cu_3V_2O_7(OH)_2 2H_2O$, in which the $3d_{z^2}$ orbital is selected to release the e_g orbital degeneracy, resulting in a distortion of the kagome lattice and the loss of the crystallographic three-fold axis that acts to maintain spatially isotropic magnetic interactions [153]. The first example of a system containing a kagome network of d^1 ions was recently

reported by Aidoudi *et al.* [75] that, therefore, provides a novel opportunity in the study of frustrated quantum magnets. The system is an inorganic-organic hybrid vanadium oxyfluoride material, diammonium quinuclidinium vanadium (III,IV) oxyfluoride $[NH_4]_2[C_7H_{14}N][V_7O_6F_{18}]$, or DQVOF that was successfully prepared by ionothermal synthesis. The ionothermal preparative method uses an ionic liquid, defined as an ionic salt with a melting point of less than 100 °C, as the solvent for a reaction [70]. For the work presented in the following sections, samples were prepared by Dr Farida Aidoudi at the School of Chemistry, University of St Andrews, U.K. Exact details of the reaction conditions are given in [75] and the structure and purity of the samples were confirmed by powder X-ray diffraction and chemical analysis.

DQVOF crystallises in the trigonal $R\bar{3}m$ space group (*no.*166) and its structure is shown in Figure 5.1. Strictly speaking, DQVOF is a magnetic bilayer compound, with kagome layers of $S = \frac{1}{2}$ d^1 V^{4+} cations and $S = 1$ d^2 V^{3+} cations in between the kagome planes. These bilayer units propagate along the structure and are well separated by organic quinuclidinium cations, $C_7H_{14}N^+$, that act to reduce the magnetic dimensionality of the system. The initial magnetic study of DQVOF presented in [75] was extremely encouraging; the system revealed an absence of long range magnetic order and spin freezing in DC magnetic susceptibility measured down to 2 K despite significant antiferromagnetic exchange interactions. Furthermore, Aidoudi *et al.* [75] put forward an argument to suggest that there is negligible magnetic exchange between the kagome layers and the inter-plane V^{3+} due to a poor superexchange orbital overlap. At this point, further investigation was required in order to determine whether DQVOF displays true kagome or kagome bilayer behaviour and the nature of its magnetic ground state at the very lowest temperatures. Presented in this Chapter are the low temperature magnetisation and heat capacity data that show that the inter-plane $S = 1$ spins of the V^{3+} cations are well separated magnetically from the kagome layers. In addition, through the analysis of the low temperature heat capacity that is intrinsic to the kagome layers and muon spin relaxation data there is strong evidence to support the existence of a gapless spin liquid ground state in DQVOF.

5.2 Magnetisation and Magnetic Susceptibility

The magnetic susceptibility of DQVOF was measured in a superconducting quantum interference device (SQUID) magnetometer in an applied field of 5

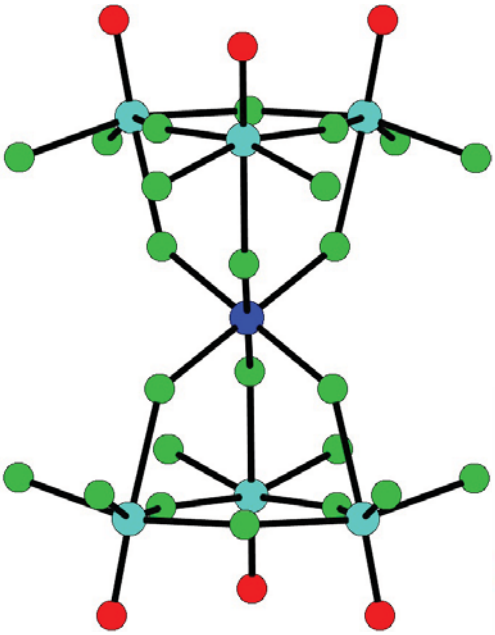

(a) *A magnetic bilayer unit with V^{4+} (cyan), V^{3+} (blue), F^{-} (green) and O^{2-} (red).*

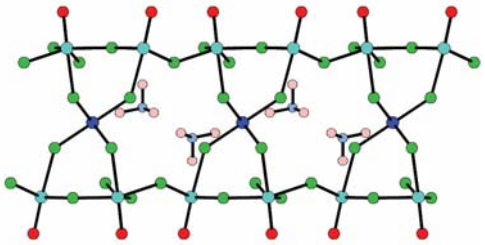

(b) *The bilayer units, viewed down the b-axis, with charge balancing ammonium, NH_4^+, cations.*

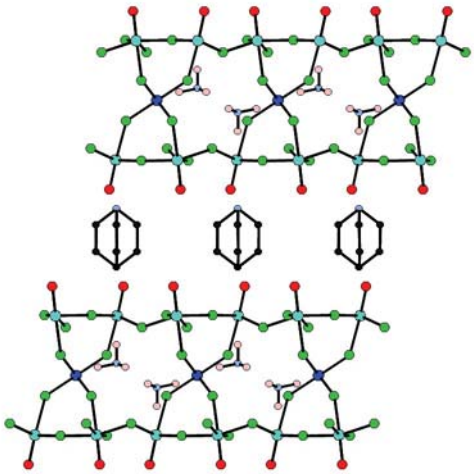

(c) *The bilayer units are magnetically isolated by quinuclidinium, $C_7H_{14}N^+$, cations.*

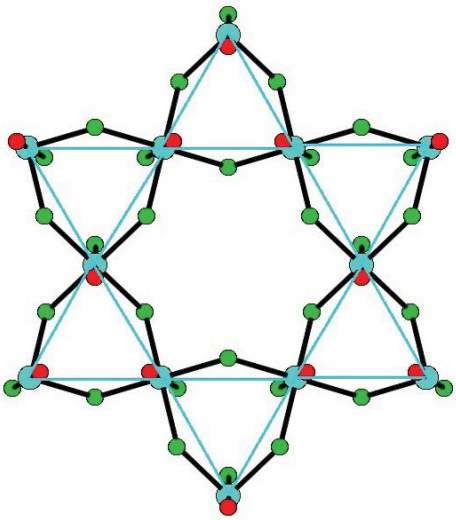

(d) *The V^{4+} kagome lattice, viewed down the c-axis.*

Figure 5.1 *The crystal structure of DQVOF.*

T. Figure 5.2 shows the magnetic and inverse susceptibilities as a function of temperature between 1.8 K and 300 K. The data show no evidence of a magnetic ordering transition within the measured temperature range. At high temperatures, the magnetic susceptibility is well described by Curie-Weiss behaviour, which is shown by the linear fit to the inverse of susceptibility in Figure 5.2. The Weiss constant obtained from the fit indicates the dominance of antiferromagnetic exchange, $\theta = -58(4)$ K, and the Curie constant, $C = 3.09(10)$ K emu mol^{-1} gives an effective magnetic moment $\mu_{eff} = 4.97(8)\mu_B$ per formula unit of six V^{4+} cations and one V^{3+} cation, which is in good agreement with the observations of [75].

Magnetisation against field data were collected by Dr Pierre Bonville at the Service de Physique de l'État Condensé of the CEA-CNRS Saclay, France in a vibrating sample magnetometer (VSM) in applied field strengths up to 14 T. The data measured at 1.7 K were normalised by the saturation magnetization, $M_{sat} = N_A g \mu_B S$, per formula unit of $S = (1 + \frac{6}{2})$ and taking $g = 2$. The net magnetisation is considered as a sum of two components; a linear component from the strongly interacting kagome layers of $S = \frac{1}{2}$ spins and a Brillouin-like contribution from the paramagnetic or weakly interacting inter-plane $S = 1$ spins. This approach has been successfully applied to several kagome systems in order to separate the magnetisation inherent to the kagome physics from that of anti-site spins [154][155]. A fit to the linear response is shown in Figure 5.3 above applied fields of 10 T. By subtracting this linear contribution, one can observe the saturated Brillouin-like magnetisation of the $S = 1$ spins of the inter-layer V^{3+} ions with $M/M_{sat} = 0.148(5)$. From this saturated magnetisation, one obtains a saturated magnetic moment of 1.18 μ_B for the interlayer V^{3+} spins. This moment reduction from the expected spin only value is due to the spin-orbit coupling that is prevalent in the V^{3+} cation [156], [157], for instance CdV_2O_4 [158] and $LaVO_3$ [159] have low temperature ordered moments of 1.19 μ_B and 1.15 μ_B, respectively. This demonstrates that to a good approximation, the kagome layers are magnetically decoupled from the inter-planes sites at 1.7 K.

5.3 Field Dependent Heat Capacity

The heat capacity of DQVOF was measured on a 1.3 mg pressed powder pellet in a physical properties measurement system (PPMS) with ^{3}He insert in zero field and applied fields of 3T, 5 T, 7 T and 9 T. Figure 5.4 and 5.5 show the

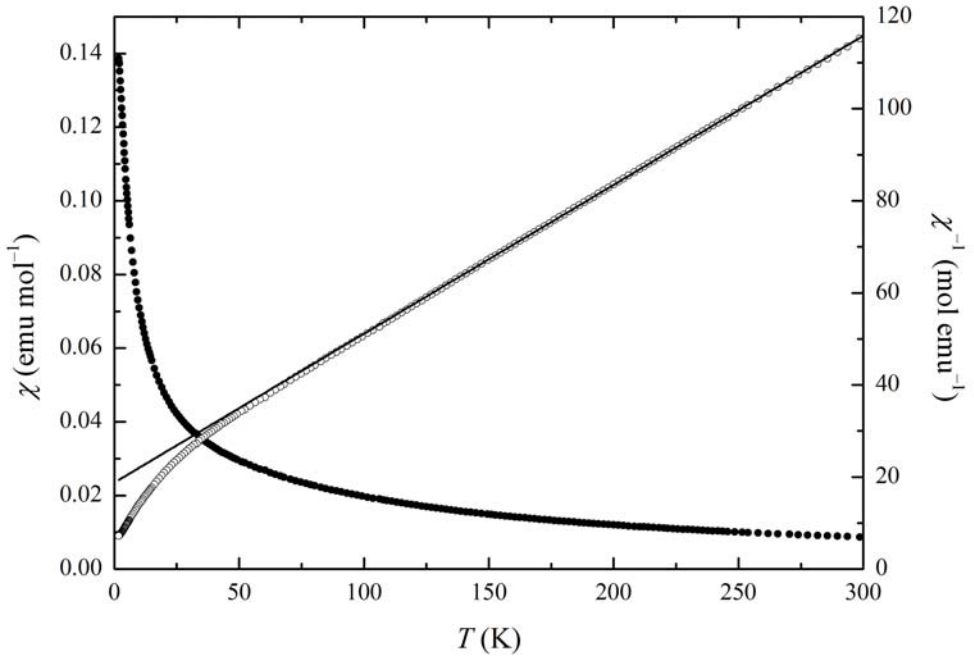

Figure 5.2 *Magnetic (closed circles) and inverse (open circles) susceptibilities measured in a 5 T field. The solid black line is a Curie-Weiss fit to the inverse of susceptibilty.*

heat capacity, C_v, against temperature, T, and to C_vT^{-1} against temperature, respectively. The data clearly show a broad, Schottky-like feature that shifts to higher energies in stronger applied fields. The field dependent Schottky behaviour arises from spins that are weakly interacting within the system *i.e.* paramagnetic, even at low temperatures. It is, therefore, possible to apply a similar analysis to the heat capacity of DQVOF as discussed in the previous section in the context of the low temperature magnetization against field data; first fit the Schottky anomaly associated with the weakly interacting $S = 1$ spins and subtract it from the data to reveal the underlying heat capacity of the strongly correlated kagome layers [160],[161].

The $2S + 1$ degenerate m_S levels of an $S = 1$ spin state in zero field are split upon application of an external field by the Zeeman interaction, $|\Delta E|$=g$\mu_B B$, as shown in Figure 5.6. The partition function, Z, of such a three level system, with energies of 0, E and $2E$ is given by,

$$Z = 1 + \exp\Big(-\frac{E}{T}\Big) + \exp\Big(-\frac{2E}{T}\Big) \tag{5.1}$$

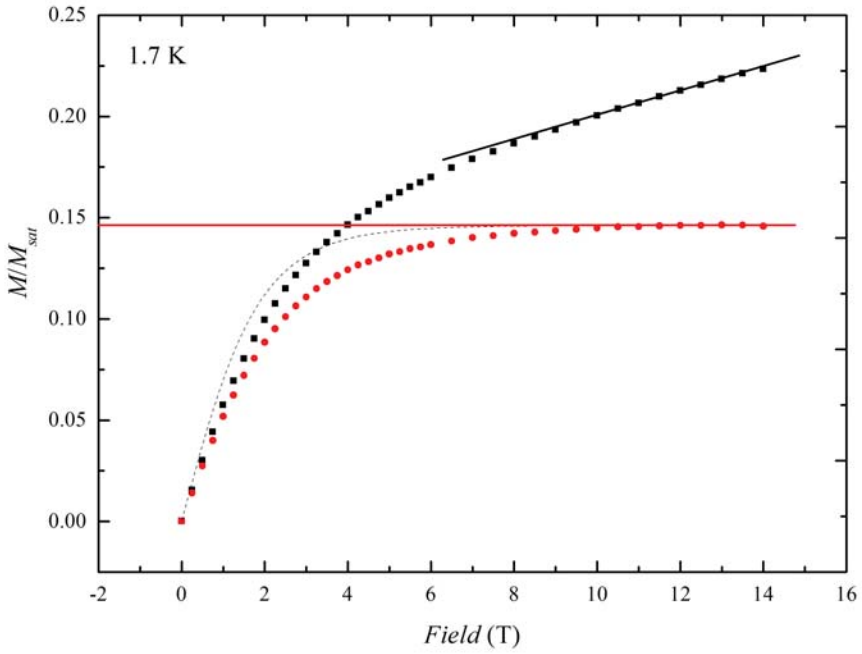

Figure 5.3 *Net normalised magnetisation against field (black squares) with a fit to the linear contribution above* 10 *T. Subtraction of the linear contribution gives the saturated magnetisation of the* $S = 1$ *spins (red circles) shown with the Brillouin curve for* $S = 1$ *spins (dashed black curve).*

The average energy, U, which is given by,

$$U = \frac{\sum E_S \exp(-\frac{E_S}{T})}{Z} \tag{5.2}$$

for E_S over all m_S states can, therefore, be taken as,

$$U = \frac{2E + E\exp(\frac{E}{T})}{1 + \exp(\frac{E}{T}) + \exp(\frac{2E}{T})} \tag{5.3}$$

Given that the heat capacity of constant volume is the partial derivative of the average energy with respect to temperature *i.e.* $C_v = (\frac{\partial U}{\partial T})_v$, one arrives at an expression for the heat capacity of an $S = 1$ spin triplet,

$$C_v = fN_A k_B \Big(\frac{E}{T}\Big)^2 \frac{\exp(\frac{E}{T}) + \exp(-\frac{E}{T}) + 4}{(1 + \exp(\frac{E}{T}) + \exp(-\frac{E}{T}))^2} \tag{5.4}$$

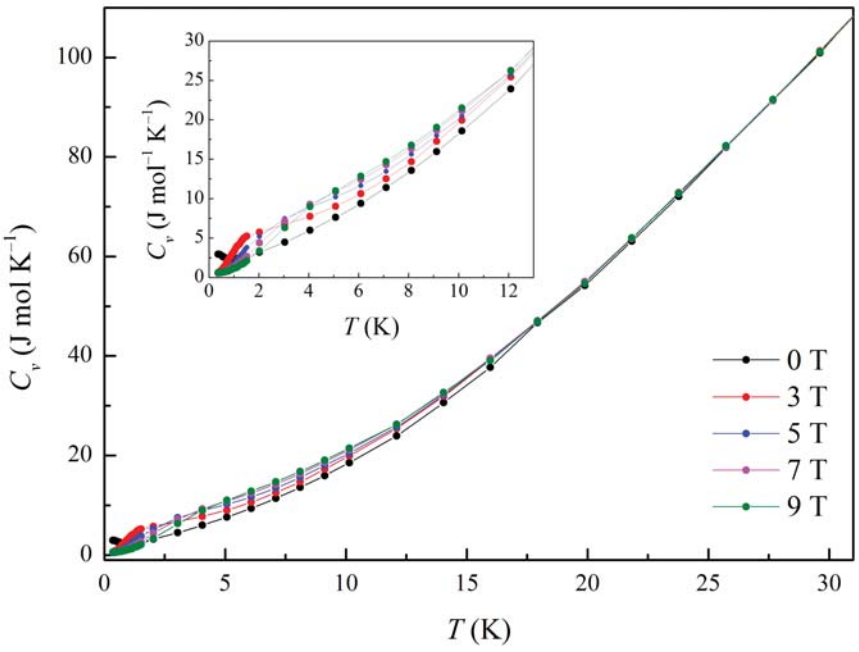

Figure 5.4 *Heat capacity, C_v, of DQVOF as a function of temperature from* 300 *mK to* 30 *K in zero field and applied fields up to* 9 *T. Inset shows low temperature region of the data.*

where f gives the number of moles of $S = 1$ spins per formula unit. Figure 5.7 shows the Schottky feature in each field. In applied fields up to 3 T, the Schottky behaviour can be well described by the expression given in Equation 5.4. However, as the applied field strength is increased a second feature appears within the energy scale of the experiment at the very lowest temperatures accessed with the ^{3}He insert. This can be attributed to the splitting of the nuclear spin, m_I, levels of the $I = \frac{1}{2}$ ^{1}H and ^{19}F nuclei that are abundant within the DQVOF system. Nuclear magnetic moments are typically much smaller than electronic magnetic moments, on the order of $10^{-3} - 10^{-4}\mu_B$, and the very weak interaction between neighbouring nuclear spins means that they tend to behave paramagnetically. Both ^{1}H and ^{19}F nuclei are 100 % abundant and have nuclear gyromagnetic ratios, γ_I, 26.75 and 25.16×10^7 rad T^{-1} s^{-1}, respectively. The magnitude of the splitting of the m_I levels of both nuclei in applied fields of 3 T, 5 T, 7 T and 9 T are approximately 6 mK, 10 mK, 14 mK and 20 mK, respectively, which were determined according to the expression,

$$|\Delta E| = \gamma_I \hbar B \tag{5.5}$$

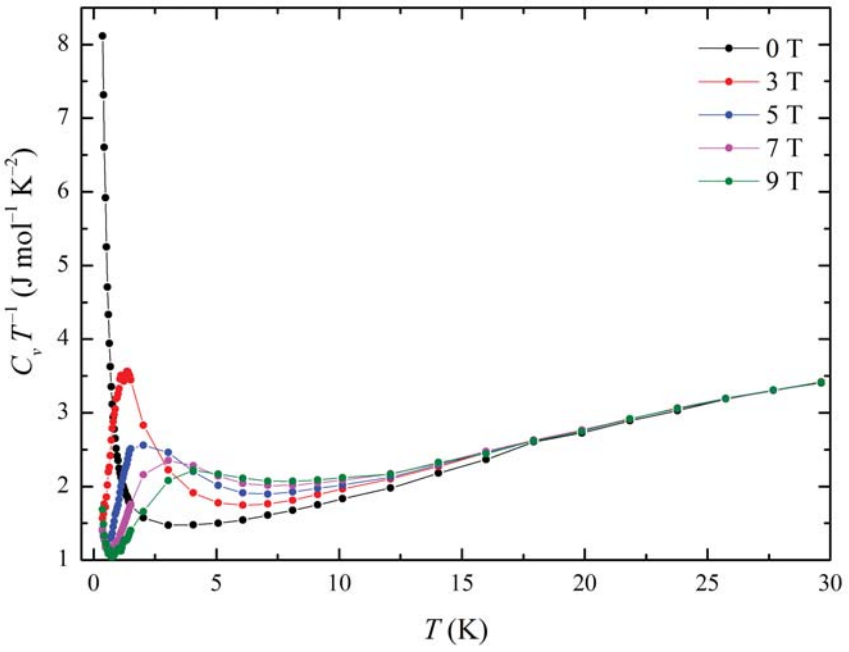

Figure 5.5 *C_vT^{-1} against T more clearly shows the field dependent Schottky behaviour of the weakly interacting spins in the DQVOF system.*

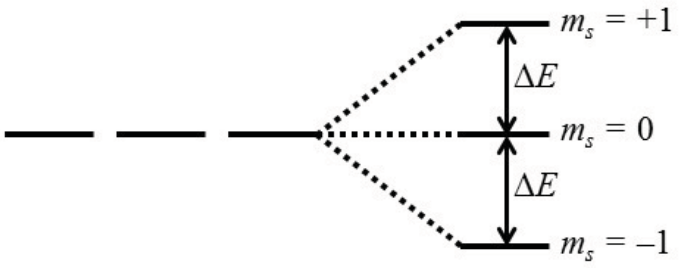

Figure 5.6 *The Zeeman splitting of the $2S + 1$ m_S states of an $S = 1$ spin system upon the application of an external magnetic field $\boldsymbol{B}$.*

where B is the magnitude of the applied magnetic field. The expression for the heat capacity of a two level $I = \frac{1}{2}$ system can be derived in a similar way to method described in Equations $5.1 - 5.4$ and can also be found in the literature [106]. The electronic and nuclear Schottky behaviour observed in C_vT^{-1} *vs.* T of DQVOF in applied fields can, therefore, be successfully modelled as a sum of

these two contributions,

$$C_v T^{-1} = \frac{f_S N_A k_B}{T}\left(\frac{E_S}{T}\right)^2 \frac{\exp(\frac{E_S}{T}) + \exp(-\frac{E_S}{T}) + 4}{(1 + \exp(\frac{E_S}{T}) + \exp(-\frac{E_S}{T}))^2} + \frac{f_I N_A k_B}{T}\left(\frac{E_I}{T}\right)^2 \frac{\exp(\frac{E_T}{T})}{(\exp(\frac{E_I}{T}) + 1)^2} \tag{5.6}$$

where f_S and f_I give the number of moles of $S = 1$ and $I = \frac{1}{2}$ spins per formula unit and E_S and E_I give the energies of the m_S and m_I states, respectively. The values of E_I were fixed at the values determined by Equation 5.5 and E_S, f_S and f_I were fit to the field dependent data. In order to isolate the field dependent heat capacity clearly and minimise the lattice contribution, the differences between heat capacity values measured in different fields were determined. Figure shows the fit of Equation 5.6 to $\Delta C_v T^{-1}$. An average value of $f_I = 39(3)$ is in excellent agreement the total number of 40 moles of ^{1}H and ^{19}F nuclei per formula unit of DQVOF. The splitting of the electronic m_s spin states as a function of applied field is shown in Figure 5.9. As expected, this follows linear Zeeman behaviour, $|\Delta E|$=g$\mu_B B$, with a g-factor, $g = 1.8(2)$, typical of V^{3+}. One should note the residual zero field splitting of the electronic spin states of $\sim$0.6 K. A value of $f_S = 0.5(2)$, for the fraction of $S = 1$ spins per formula unit shows a similar reduction as observed in the magnetisation data as a result of spin orbit coupling.

In analogy to the analysis of the magnetization against field data, the subtraction of the contribution of the weakly interacting electronic and nuclear spins from the heat capacity data should reveal the nature of the heat capacity that is intrinsic to the kagome layers of $S = \frac{1}{2}$ V^{4+} ions. Figure 5.10 shows the heat capacity of DQVOF upon subtraction of the Schottky contributions. The zero field data, shown in the inset of Figure 5.10, show no sharp peak structure indicating the absence of any magnetic phase transitions over the entire measured temperature range. Of particular interest here is the low temperature region of the data given that the lattice contribution will be minimal and the heat capacity will be mostly magnetic in origin. Figure 5.10 shows the heat capacity from 300 mK to 10 K in each measured field, which can be modelled by T-linear behaviour between 300 mK and 5 K, where the lattice contribution to the heat capacity is negligible,

$$C_v = \gamma T \tag{5.7}$$

with $\gamma\sim$200 mJ K^{-2} mol^{-1} per V^{4+} spin. Allowing a $C_v \propto T^{\alpha}$ model improves the

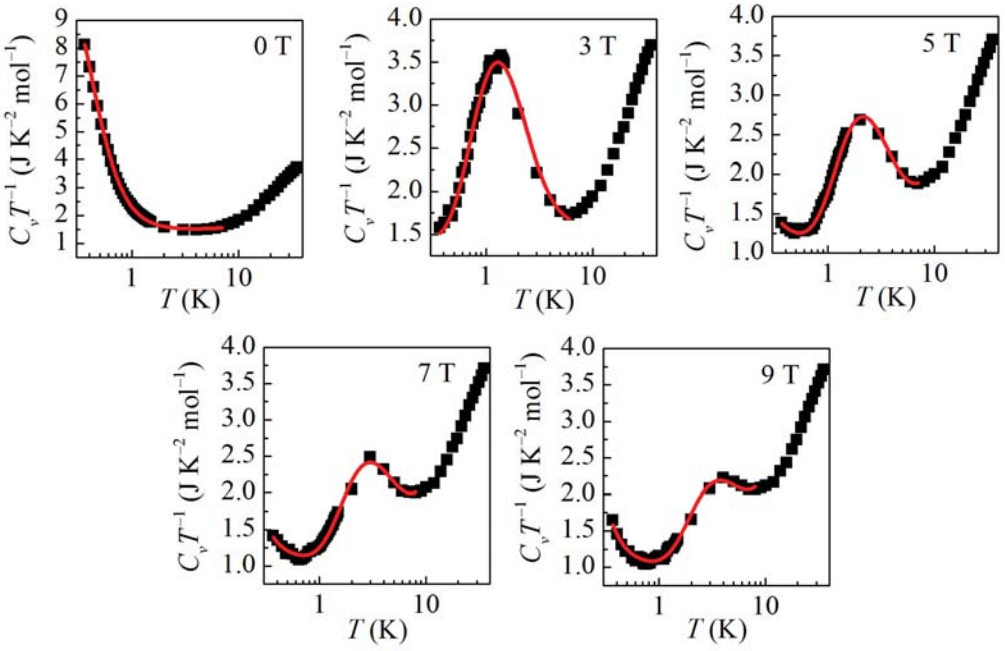

Figure 5.7 *The Schottky behaviour observed in the field dependent heat capacity of DQVOF, which was successfully modelled by the expression given in Equation* 5.6 *(solid red lines).*

fit to the data, with $\alpha = 1.2$ giving the best fit.

5.4 Muon Spin Relaxation

The muon spin relaxation (μSR) measurements were performed on a non-orientated 400 mg sample of DQVOF on the MuSR spectrometer at the ISIS Muon Facility, Rutherford Appleton Laboratory, U.K. The sample was loaded into a silver foil packet and attached to a silver foil backing plate in a Variox cryostat with dilution fridge insert. This sample environment allowed access to temperatures as low as 40 mK. Subsequent measurements were performed on the GPS beam line at the Swiss Muon Source, Paul Scherrer Institute, Switzerland. In particular, the background of the ISIS data, which arises from muons that fall outside of the sample and in the silver sample holder or elsewhere, was carefully measured by a veto measurement of the sample during which, the sample was contained in a thin aluminium foil packet held in place on a fork-shaped sample holder by a layer of aluminium tape. The veto measurement disregards any muons that do not hit the sample and is, therefore, a very low background measurement. Figure 5.11 shows a comparison of the zero field time

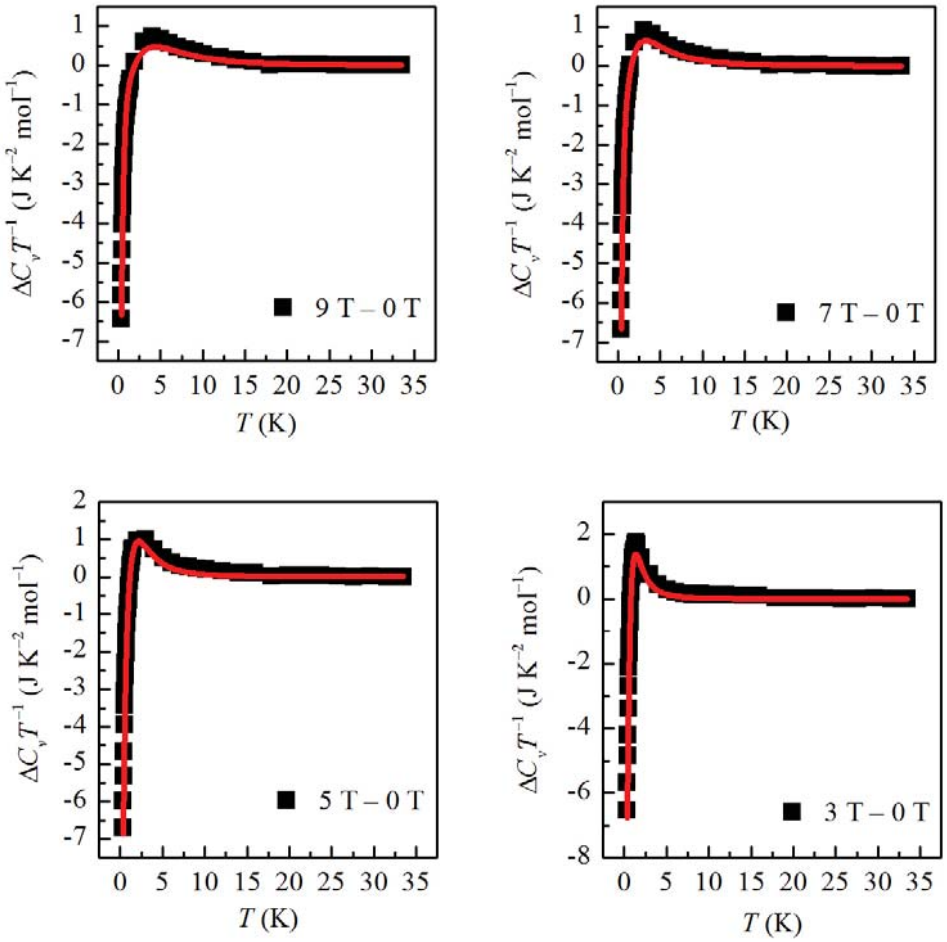

Figure 5.8 *In order to isolate the field dependent heat capacity more clearly, the difference between interpolated heat capacity measurements in different fields were also successfully modelled by Equation* 5.6.

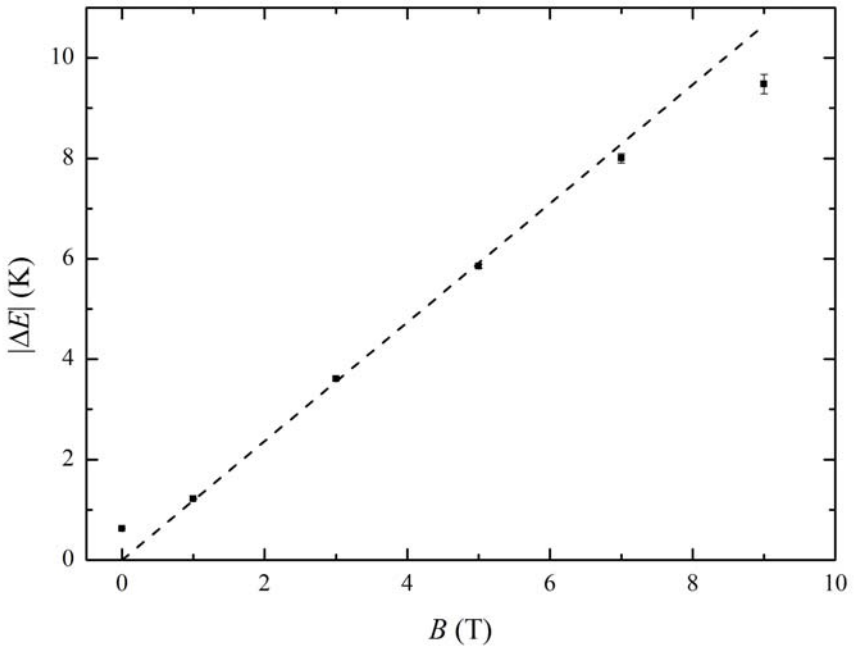

Figure 5.9 *The Zeeman splitting of the m_S levels of the V^{3+} $S = 1$ spins in DQVOF as a function of applied field.*

dependent muon asymmetries, $A(t)$ collected at 2.5 K on MuSR and GPS, from which a background asymmetry of 3.5 % can be determined for the ISIS data set. All subsequent ISIS data is presented as the background corrected muon spin polarisation, $P(t)$, given by,

$$P(t) = \frac{A(t) - Background}{A(t_0) - Background} \tag{5.8}$$

The zero field muon spin polarisation reflects the sum of the local responses of the muons implanted at different stopping sites within the sample. In the case of DQVOF, the most energetically favourable stopping sites for the positively charged implanted muon will be close to negatively charged fluoride and oxide anions within the structure. Figure 5.12 shows the time dependence of the zero field muon spin polarisation measured at 40 K and 40 mK, which have been

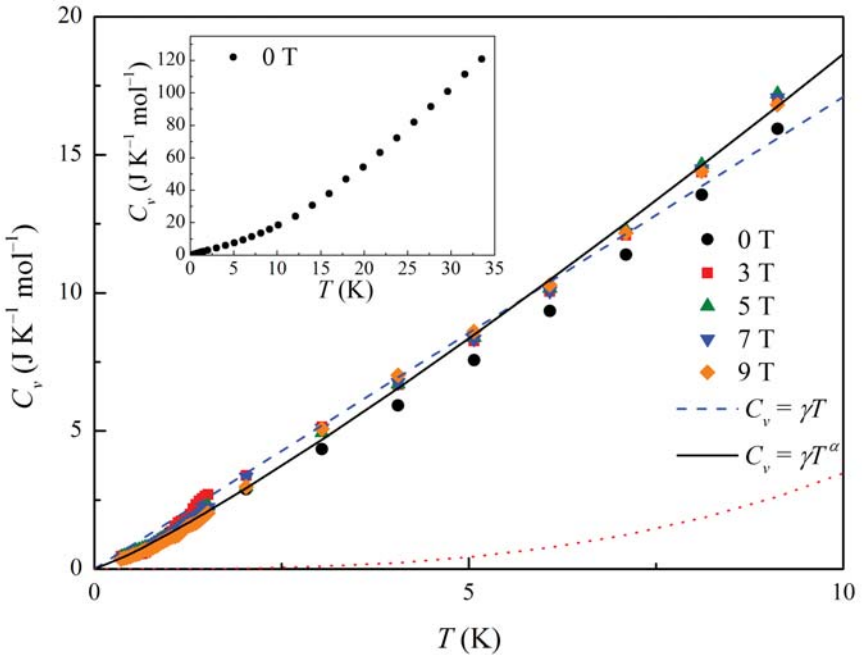

Figure 5.10 *Low temperature heat capacity of DQVOF upon subtraction of the Schottky anomaly with γT and γT^{α} fits. The red dotted line is an estimate of the lattice contribution. The inset shows the data of the entire measured temperature range.*

successfully modelled with the expression,

$$P_{ZF}(t) = f(F{-}\mu{-}F(t){\times}\exp(-\sigma^2t^2){\times}\exp(-\lambda_F t)){+}(1{-}f)(KT_O(t){\times}\exp(-\lambda_O t)^{\alpha}) \tag{5.9}$$

This expression describes the sum of the nuclear and electronic fields surrounding the implanted muon at the fluoride (F) and oxide (O) stopping sites in DQVOF and the effect that these internal fields have on the muon polarization as a function of time. $F - \mu - F(t)$ describes the strong dipole-dipole interaction between the muon spin and the fluorine nuclear spin at the fluorine stopping site, which gives rise to the characteristic kink in the polarisation data $\sim 2\mu$s, and is given by,

$$\begin{aligned} F - \mu - F(t) \quad = \quad & \tfrac{1}{6}(3 + \cos(\sqrt{3}\omega_d t) \\ & +(1 - \tfrac{1}{\sqrt{3}})\cos((\tfrac{3-\sqrt{3}}{2})\omega_d t) \\ & +(1 + \tfrac{1}{\sqrt{3}})\cos((\tfrac{3+\sqrt{3}}{2})\omega_d t)) \end{aligned} \tag{5.10}$$

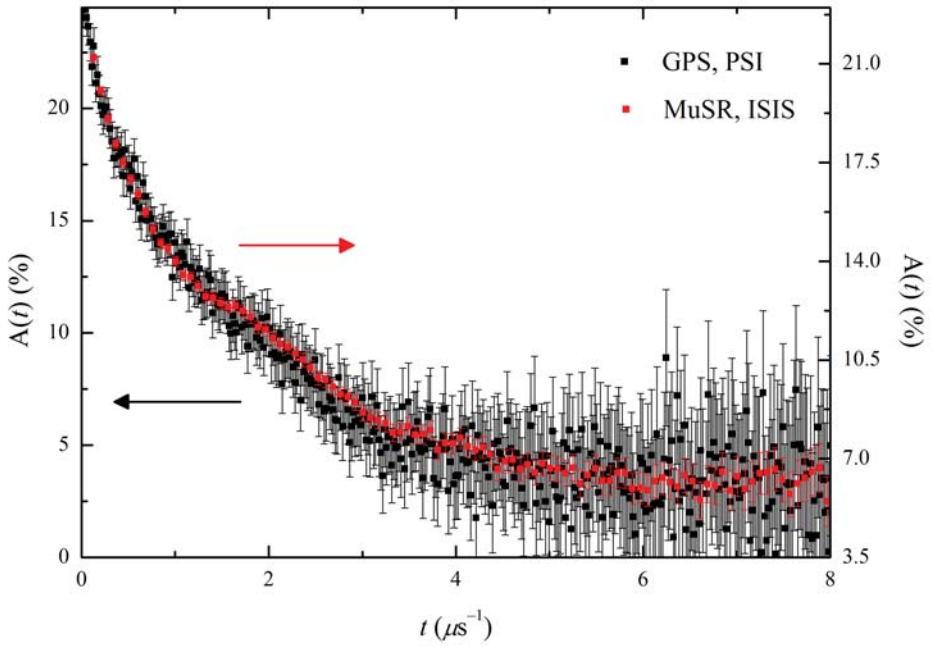

Figure 5.11 *Comparison of the zero field muon asymmetries measured on MuSR, ISIS and by veto measurement on GPS, PSI at 2 K.*

where,

$$\omega_d = \frac{\mu_0 \gamma_\mu \gamma_F}{4\pi r^3} \tag{5.11}$$

and μ_0, γ_μ and γ_F are the permeability of free space, muon and ^{19}F nuclear gyromagnetic ratios, respectively. r, is the F-μ separation distance in the strongly coupled F-μ-F state [162],[163]. The gaussian expression in Equation 5.9, $\exp(-\sigma^2 t^2)$, was included to account for the distribution of fluoride anions surrounding the muon at the stopping site. The expression, $KT_O(t)$, is the widely used Kubo-Toyabe function given by,

$$KT_O(t) = \frac{1}{3} + \frac{2}{3}(1 - \Delta^2 t^2)\exp(-\frac{\Delta^2 t^2}{2}) \tag{5.12}$$

that here describes the distribution, Δ, of nuclear fields surrounding the muon at the oxide stopping site. The nuclear fields are static on the time scale of the muon experiment and so are temperature independent. These parameters were, therefore, fitted to the high statistics data collected at 40 K and fixed at their

Table 5.1 *The parameters determined from the fit of Equation* 5.9 *to the high statistics zero field muon polarisation measured at* 40 *K.*

f	ω_d / MHz	σ / MHz	λ_F / MHz	Δ / MHz	λ_O / MHz	α_O
0.17(2)	1.17(5)	0.55(3)	0.06(5)	3.25(7)	0.08(1)	0.7(1)

high temperature values for all subsequent fits. These values are summarized in Table 5.1. The most important point to note for the zero field polarisation data shown in Figure 5.12 is that the 40 mK and 40 K data relax to the same value above the background. This non-relaxing component above the measured background can most likely be attributed to a small fraction of muons that fall far from the kagome planes, within the organic component of DQVOF.

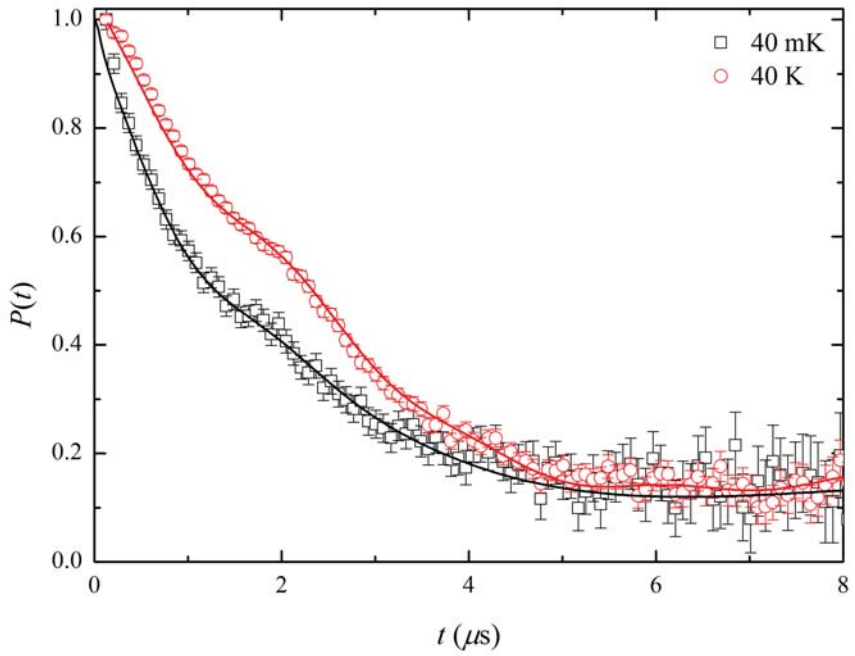

Figure 5.12 *Time dependence of the zero muon spin polarisation measured at* 40 *K and* 40 *mK. Solid lines represent fit of Equation* 5.9 *to the data.*

The temperature dependent, dynamical part of Equation 5.9 arises from the fluctuating fields of the electronic spins within the DQVOF system, which cause an exponential depolarisation of the muon spin. The rate of the muon spin depolarisation at the oxide and fluoride stopping sites are given by λ_O and λ_F in Equation 5.9, respectively. The fraction of spins, f, stopping at the fluoride site is 20 % of the total number of muons stopping in the sample. The feature

in the data ~ 2 μs that arises from the dipolar coupling between the muon spin and the fluorine nuclear spin remains apparent in the zero field data over the entire temperature range. This implies that the muon at the fluoride stopping site is only very weakly coupled to the electronic spins in the system as this kink is not washed out from the data as a result of the relaxation from the electronic field fluctuations. The application of a longitudinal field decouples the muon spin from the static nuclear fields of the sample such that the muon spin only probes the internal electronic field fluctuations. Figure 5.13 displays the muon spin polarisation in an applied longitudinal field of 200 G. The data have been modelled with a stretched exponential function over the entire measured temperature range,

$$P_{LF}(t) = P_{(non-relaxing)} + P_O \exp(-\lambda t)^{\beta} \tag{5.13}$$

Here, $P_{(non-relaxing)}$ was fixed at 0.5 polarisation, which reflects the sum of the non-relaxing contribution of the decoupled organic muon fraction (0.2), the fluoride fraction (0.1) and the measured background (0.2).

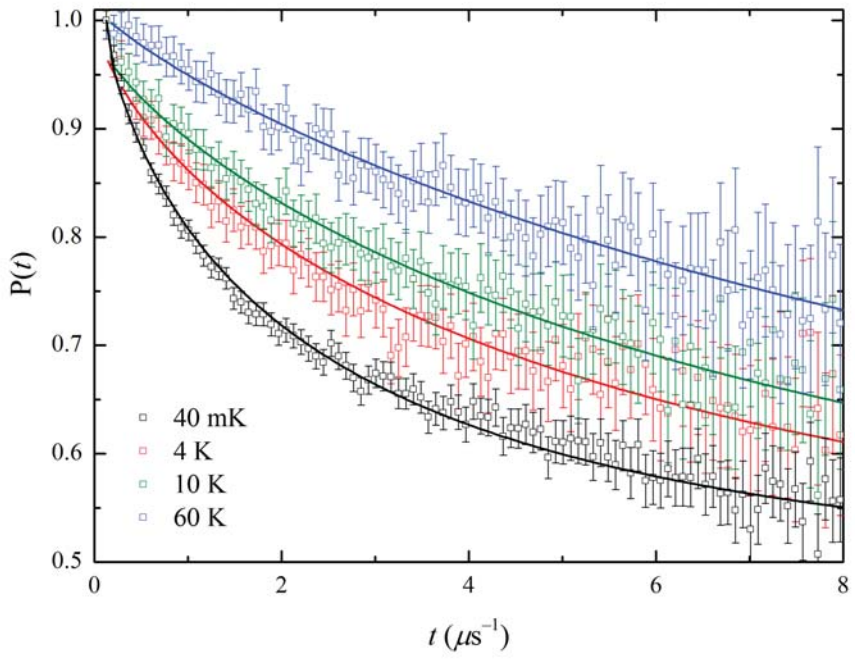

Figure 5.13 *Time dependence of the muon spin polarisation in an applied longitudinal field of* 200 *G measured at temperatures* 40 *mK,* 4 *K,* 10 *K and* 60 *K.*

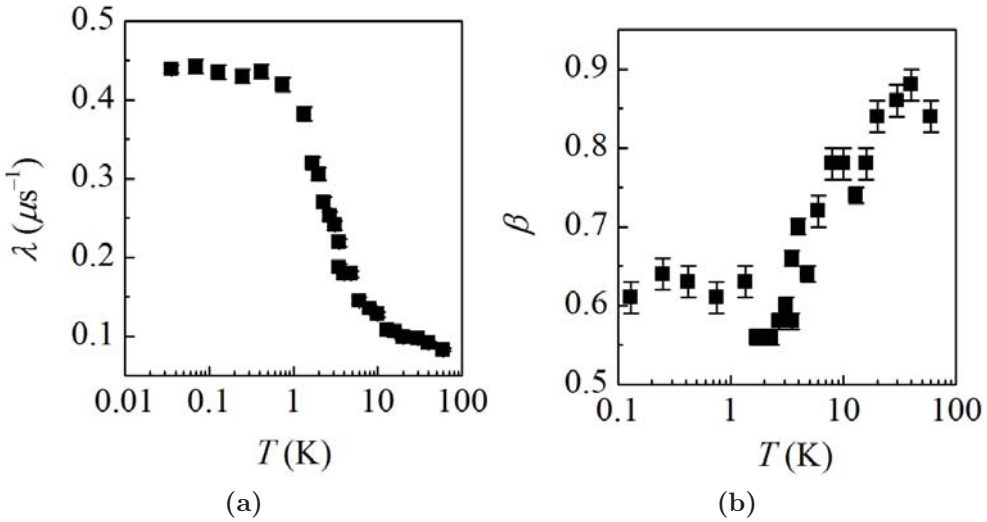

Figure 5.14 *The temperature dependence of (a) the muon spin depolarisation rate, λ, and (b) the stretching component, β, obtained from the fit of Equation* 5.13 *to the muon spin polarisation measured in a longitudinal field of* 200 *G.*

Figure 5.14 shows the temperature dependence of the muon spin depolarisation or relaxation rate, λ, and the stretching component, β. Upon cooling from 10 K, there is a slowing down of the internal electronic field fluctuations, which is reflected in the increase of the muon spin relaxation rate. However, from 1 K to 40 mK there is a clear plateau in the relaxation rate that strongly indicates the persistence of internal field fluctuations at the lowest temperatures accessed. At high temperatures, the system is in a fast fluctuating regime with $\beta \sim 1$, however, at low temperatures β approaches 0.5, which implies that the implanted muons are under the influence of more than one field fluctuation frequency.

Figure 5.15 shows the field dependence of the muon spin polarization in the low temperature limit up to the maximum longitudinal field of 2.5 kG for MuSR. At lower fields, one can clearly observe the decoupling of the nuclear fields. Stronger field strengths do not appear to have a great effect on the muon spin polarisation, with only a weak decoupling of the fluctuating electronic fields.

5.5 Discussion

The dominance of antiferromagnetic exchange, $\theta \sim -60$ K, and the absence of long range magnetic order down to 1.8 K as observed in the magnetic susceptibility

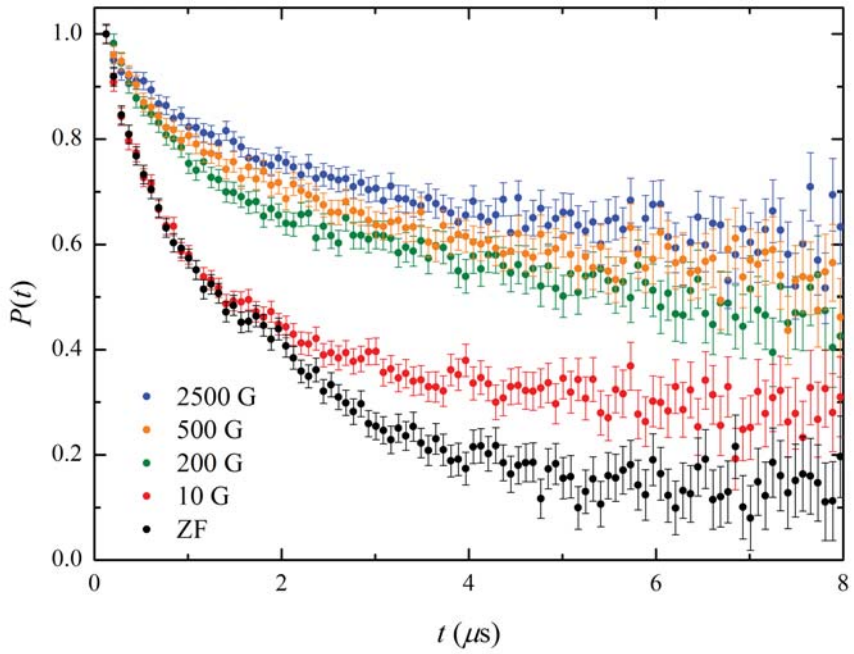

Figure 5.15 *The field dependence of the muon spin polarisation at 40 mK.*

presented for DQVOF is in excellent agreement with the original magnetic study of the system and demonstrates the consistency of the samples used here and in the report by Aidoudi *et al.* [75]. It also confirms the highly frustrated nature of the magnetic ground state in this vanadium oxyfluoride system [164].

One of the major questions regarding the low temperature magnetic properties of DQVOF was whether or not the system would be a good model for a two-dimensional magnetic kagome antiferromagnet. It is possible to explain the low temperature, field dependent magnetisation and heat capacity data presented here in terms of a paramagnetic behaviour of the inter-layer $S = 1$, which implies that they are very weakly interacting with the neighbouring $S = \frac{1}{2}$ spins that reside within the kagome layers. It is, therefore, concluded that to a good approximation the $S = \frac{1}{2}$ spins within the kagome layers in DQVOF are magnetically decoupled from the interlayer spins at low temperatures and that this vanadium oxyfluoride is considered as a novel $S = \frac{1}{2}$ kagome antiferromagnet model system.

There is strong evidence to suggest that DQVOF displays a gapless spin liquid ground state. The intrinsic heat capacity of the kagome layers shows an absence of any T-dependent anomalies that might indicate a magnetic phase transition

and instead displays a continuous density of states down to the lowest measured temperatures. Various models have been proposed for the low temperature heat capacity of gapless spin liquids on the kagome lattice. Theoretically, the gapless Dirac spin liquid [56], with a Dirac point-like Fermi surface, has been suggested as the ground state for the $S = \frac{1}{2}$ kagome antiferromagnet and is expected to demonstrate a C_vT^2 dependence at low temperature [57]. This does not appear to be applicable in the case of DQVOF. A better description may, therefore, be given by a more conventional spinon Fermi surface. Fermionic gapless spin liquids are predicted to demonstrate T-linear behaviour in the low temperature specific heat, with a distinct finite Sommerfield coefficient, γ. γ is related to the spinon density of states at the spinon Fermi surface, in analogy to the electron Fermi surface of metallic systems [121]. The low temperature heat capacity of DQVOF clearly displays T-linear behaviour and can be modelled with $C_v = \gamma T$. This finite value of γ may be taken as evidence for the existence of a dense spectrum of gapless excitations within the ground state of DQVOF. A value of $\gamma\sim$200 mJ K^{-2} mol^{-1} per V^{4+} spin is comparable with other experimental gapless spin liquids [165],[166]. The residual zero field splitting of $\sim$0.6 K is likely to result from a splitting of the t_{2g} crystal field of V^{3+} by, for example, a Jahn-Teller interaction or the distorted octahedral geometry of the surrounding fluoride anions. Similar field dependent behaviour, with zero field splitting, has also been observed in the herbertsmithite, $ZnCu_3(OH)_6Cl_2$, system [167],[161]. This was attributed to weakly coupled anti-site Cu^{2+} spins residing on the inter-plane Zn^{2+} sites. Upon removal of the Schottky anomaly of the anti-site spins, a $T^{1.3}$-dependence gave the best fit to the low temperature heat capacity. C_vT^2 behaviour could not be brought into agreement with the data. This is remarkably similar to the behaviour observed for DQVOF here, where a $C_vT^{1.2}$ dependence gave the best fit to the experimental data.

In a quantum spin liquid state, one would expect to observe incoherent spin fluctuations down to temperatures equal to the spin gap, or in the case of a gapless spin liquid, $T = 0$ [45]. Further evidence for the formation of such a ground state in DQVOF can be found in the muon spin relaxation data. Certainly, one can rule out any case for spin freezing within the system down to at least 40 mK; the zero field polarisation data in the high and low temperature limits relax to the same value at long times, with no signal of a $\frac{1}{3}$-tail component in the low temperature data that would be characteristic of frozen moments [168]. Furthermore, the weak field dependence of the muon spin polarisation at base temperature also implies that the electronic field fluctuations are dynamic on the

time scale of the muon experiment. The persistence of the internal electronic field fluctuations is also reflected in the plateau in the spin depolarisation rate, λ, below 1 K. This most likely demonstrates the gapless nature of DQVOF, as has been argued for a number of other systems [169],[170]. However, one must retain a certain degree of caution in the case of DQVOF given that there are two potential sources of electronic field fluctuations (V^{4+} and V^{3+} spins) and the origin of the muon spin depolarisation is not entirely certain. The situation at low temperatures is a complicated one, with the implanted muon under the influence of more than one field fluctuation frequency. However, from the inspection of the zero field polarisation data, the muon spins at the fluoride stopping site are weakly coupled to the electronic spins within DQVOF and the muon spin relaxation in an applied longitudinal field of 200 G can be attributed to the fluctuating electronic fields at the oxide stopping site. A muon will typically stop $\sim$ 0.1 nm from an O^{2-} anion, which in the crystal structure of DQVOF gives a μ^+-V^{3+} separation on the order of 5 Å, see Figure 5.16. The maximum dipolar field created by 1 μ_B is 1.85 T Å^{-3}, therefore, the internal fluctuating field, H_{fluc}, of the $S = 1$ V^{3+} cation at the oxide stopping site may be estimated by [155],

$$H_{fluc} = (1.85\ T\mu_B^{-1}\mathring{A}^{-3} \times 2.8\mu_B)/(5\ \mathring{A}^3) \sim 41\ mT \tag{5.14}$$

The relaxation rate, λ, resulting from this fluctuating field is given by,

$$\lambda = \frac{2{\gamma_\mu}^2{H_{fluc}}^2\nu}{\nu^2 + {\gamma_\mu}^2{H_{LF}}^2} \tag{5.15}$$

where γ_μ is the muon gyromagnetic ratio (135.5 $\times$ 2π MHz T^{-1}), H_{LF} is the applied longitudinal field (0.02 T) and ν is the fluctuation frequency given by,

$$\nu = \sqrt{4J^2zS(S+1)/3\pi\hbar} \tag{5.16}$$

Here, J is the effective coupling between neighbouring V^{3+} spins, which from the low temperature magnetisation data presented in Figure 5.3 is $\sim$ 1 K, and z is the number of nearest neighbours. Equations 5.14 - 5.16, therefore, allow for an estimation of the relaxation rate of the muon spin at the oxide stopping site through coupling to the fluctuating field of the inter-layer V^{3+} cations, which has an upper limit of $\sim$ 0.01 MHz. Given that the experimentally determined value

of λ at 1 K is ~ 0.4 MHz, it implies that the muon spin relaxation observed at low temperatures in DQVOF is intrinsic to the $S = \frac{1}{2}$ kagome layers.

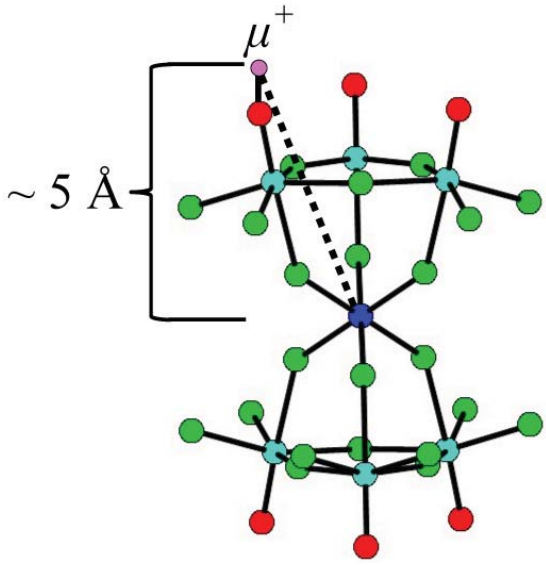

Figure 5.16 *Separation between an implanted muon (pink) and a V^{3+} cation (blue) at a potential oxide stopping site is on the order of 5 Å, which creates an internal fluctuating field ~ 40 mT.*

5.6 Conclusions

The vanadium oxyfluoride, DQVOF, is a geometrically frustrated magnetic kagome bilayer compound with an energy scale for antiferromagnetic exchange ~ 60 K. The $S = 1$ spins of the inter-plane V^{3+} are magnetically decoupled from the kagome planes, such that DQVOF can be viewed as an experimental model for the two-dimensional $S = \frac{1}{2}$ kagome antiferromagnet. Muon spin relaxation measurements clearly indicate the absence of spin freezing down to 40 mK. The T-linear dependence of low temperature heat capacity with a finite Sommerfield coefficient, γ, provides strong evidence for a gapless spin liquid ground state.

Future study will require a combination of techniques, including local probes such as muon spin rotation, which may help to clarify the origin of muon spin relaxation in DQVOF, and NMR, to reveal the local susceptibility of the V^{4+} kagome layers [171]. Thermal conductivity, κ, measurements may also prove important. Thermal transport is very powerful tool for the detection of elementary excitations in QSL systems, its main advantage being that it only probes itinerant excitations carrying entropy and so is free from localised effects, such as the Schottky anomaly

in heat capacity [172]. In the case of the $S = \frac{1}{2}$ organic triangular lattice system, κ-(BEDT-TTF)$_2$Cu$_2$(CN)$_3$, thermal conductivity measurements unambiguously demonstrated in presence of a spin gap in the ground state of the system, which was previously thought to be gapless on the basis of heat capacity data that was plagued by a Schottky anomaly at low temperature. Thermal conductivity could, therefore, directly reveal the low temperature excitation spectrum of DQVOF without the need for the subtraction of the Schottky behaviour as in the heat capacity. Finally an inelastic neutron scattering survey DQVOF will be vital to reveal the nature of magnetic excitations from the ground state. A continuum of spinon excitations was recently observed in single crystal inelastic neutron scattering spectra of herbertsmithite [61]. There are several materials chemistry issues that must first be dealt with before such an experiment can take place, such as sample deuteration and scale-up.

Chapter 6

Anion Ordering in Oxynitride Perovskites; a Neutron Diffraction Study

6.1 Introduction

The ideal perovskite has the general formula ABX_3, where A and B are cations, typically with ionic radii $r_A > r_B$ and X is an anion with $r_X \approx r_A$. The A-site cations are coordinated to 12 anions in a cubo-octahedral geometry and the B-site cations are surrounded by 6 anions in an octahedral coordination [173]. The ideal perovskite adopts a cubic structure in the $Pm\bar{3}m$ space group (no. 221). The B-cell setting of the ABX_3 perovskite structure is shown in Figure 6.1. If $r_A \equiv r_X$ such that the A-site cations are exactly accommodated within the 12-fold site, then the distance $X-A-X$ is given by $(2r_A+2r_X)$. It can also be observed that in this ideal case $(2r_A + 2r_X)$ is equal to $\sqrt{2}$ times the unit cell edge, which is given by $(2r_B + 2r_X)$, such that $(r_A + r_X) = \sqrt{2}(r_B + r_X)$. This gives the relationship known as the tolerance factor, t,

$$t = \frac{r_A + r_X}{\sqrt{2}(r_B + r_X)} \tag{6.1}$$

that in the ideal case is unity [174]. The tolerance factor gives a rough guide as to whether a perovskite structure will form at a given temperature and pressure

from a particular ensemble of ions, but is important to bear in mind that there are factors other than the ionic radii that play a vital role in the determination of structure and symmetry.

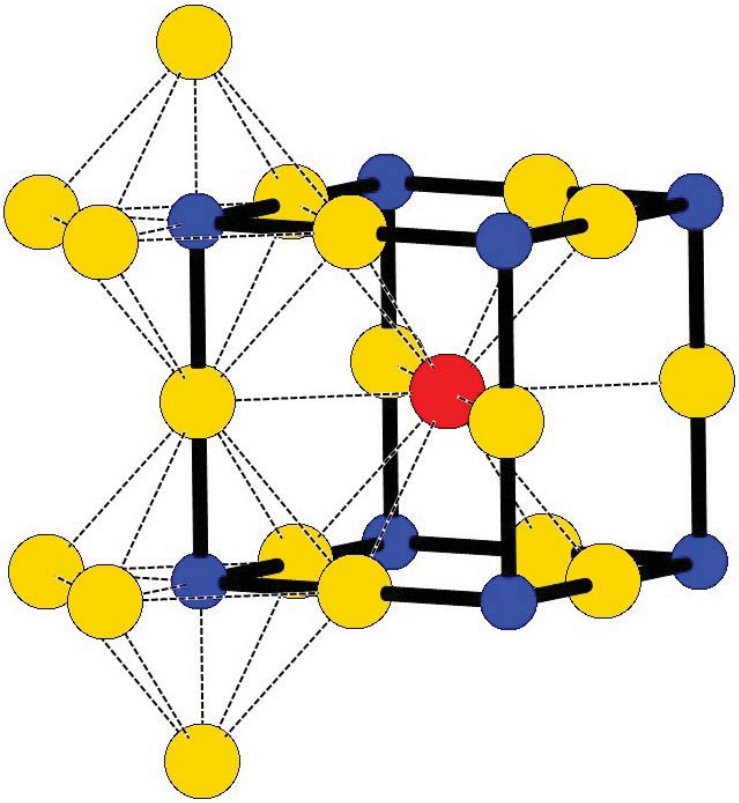

Figure 6.1 *The cubic perovskite structure, ABX_3 with A-site cation (red), B-site cations (blue) and X anions (yellow). The solid lines show the unit cell in the B-cell setting and the 12-fold coordination of the A-site and the BX_6 octahedra are depicted by the dashed lines.*

There is, in fact, a wealth of perovskites that can be derived from the ideal cubic $Pm\bar{3}m$ structure. These include distorted derivatives, which arise from tilting or rotation of the BX_6 octahedra, and substitutional derivatives such as double perovskites [175] and Ruddlesden-Popper phases [176], see Figures 6.2 and 6.3, respectively. The tilting or rotation of the BX_6 octahedra in distorted derivatives can result from a size mismatch of the A-site cation, displacement of the B-site cation within the octahedra or a distortion of the octahedra by, for example, Jahn-Teller effects. Octahedral tilting results in changes to $A-X$ bond lengths, A-site coordination and a reduction in the cubic $Pm\bar{3}m$ symmetry. Glazer notation [177], [178] is commonly used to describe the rotation of BX_6 octahedra about any 3 orthogonal Cartesian axes coincident with the axes of the cubic unit cell.

The tilting of the polyhedra may be in-phase (+), meaning that the tilts in successive layers within the structure are in the same direction, or anti-phase (−), such that rotation of neighbouring polyhedra occur in the opposite sense, see for example, Figure 6.4. There are 15 different tilt systems that necessarily lower the symmetry of the ideal $Pm\bar{3}m$ structure that are shown in Figure 6.5 with their group-subgroup relationships [179].

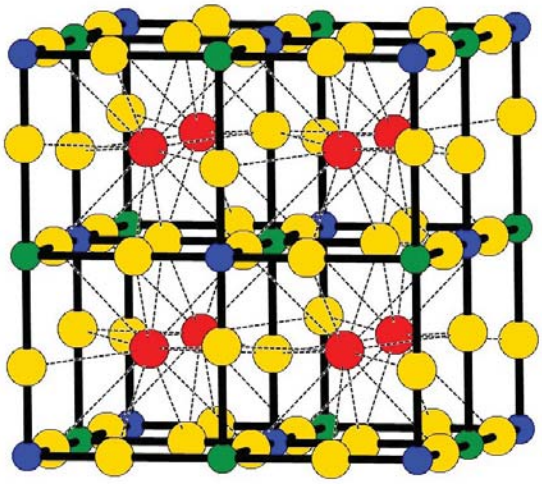

Figure 6.2 *A face centred cubic ($Fm\bar{3}m$) double perovskite, $A(B'B'')X_3$, with A-site cations (red) in 12-fold coordination, alternating B' (blue) and B'' (green) cations and X anions (yellow).*

A commonly observed perovskite structure is the orthorhombic $Pnma$ cell that results from the $a^+b^-b^-$ tilt system. Figure 6.6 shows the relationship between this orthorhombic unit cell and the $Pm\bar{3}m$ unit cell of edge length, a_{cubic}. There are six possible settings in space group 62, and within the results presented in this Chapter, the $Pbnm$ setting is used, which is obtained simply from the $Pnma$ setting by applying the matrix |001|100|010|. The tilt angles of orthorhombic perovskites are often expressed in terms of θ, ϕ and Φ, which describe the rotations about the [110], [001] and [111] pseudo-cubic axes, respectively, and are given by,

$$\cos\theta = \frac{a}{b} \tag{6.2}$$

$$\cos\phi = \frac{\sqrt{2}a}{c} \tag{6.3}$$

$$\cos\Phi = \frac{\sqrt{2}a^2}{bc} \tag{6.4}$$

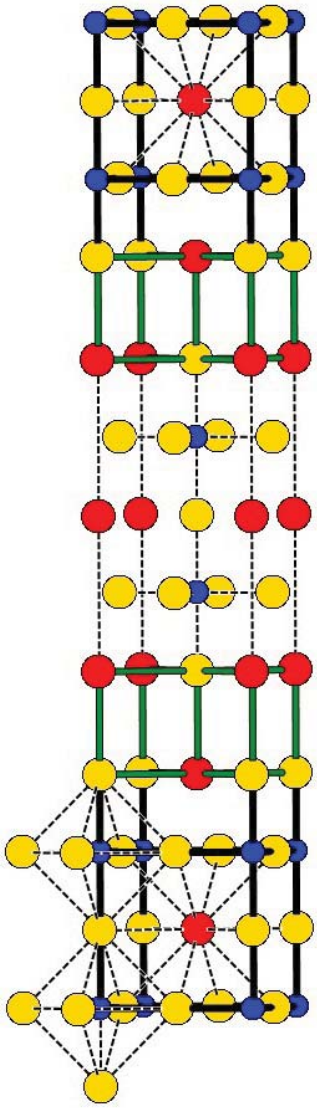

Figure 6.3 *An $n = 2$ Ruddlesden-Popper phase, $A_3B_2X_7$ or $(AX + 2ABX_3)$, with alternating perovskite (black bonds) and rock salt type (green bonds) layers. A cations (red), B cations (blue) and X anions (yellow).*

where a, b and c are the orthorhombic cell parameters.

Another distorted derivative of the ideal perovskite that will be used within this Chapter is the rhombohedral $R\bar{3}c$ cell that results from the $a^-a^-a^-$ tilt of the $Pm\bar{3}m$ system. Figure 6.7 shows the relationship between the two unit cells [180]. In the case of $R\bar{3}c$, the tilt angle, ω, is most accurately derived from the x

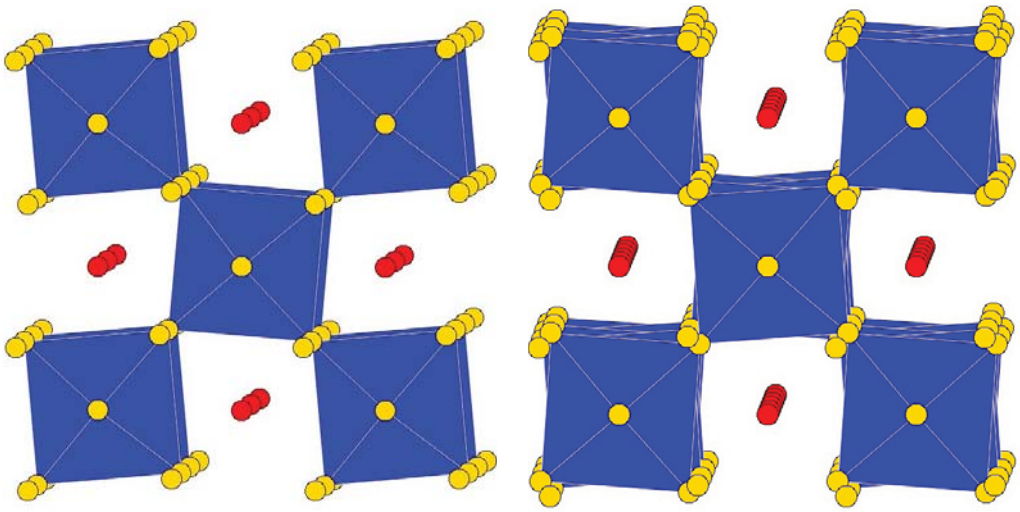

(a) $a^0a^0c^+$ *tilt,* $P4/mbm$. **(b)** $a^0a^0c^-$ *tilt,* $I4/mcm$.

Figure 6.4 *An (a) in-phase and (b) anti-phase tilt about the crystallographic c-axis generates tetragonal unit cells in space groups* $P4/mbm$ *and* $I4/mcm$*, respectively.*

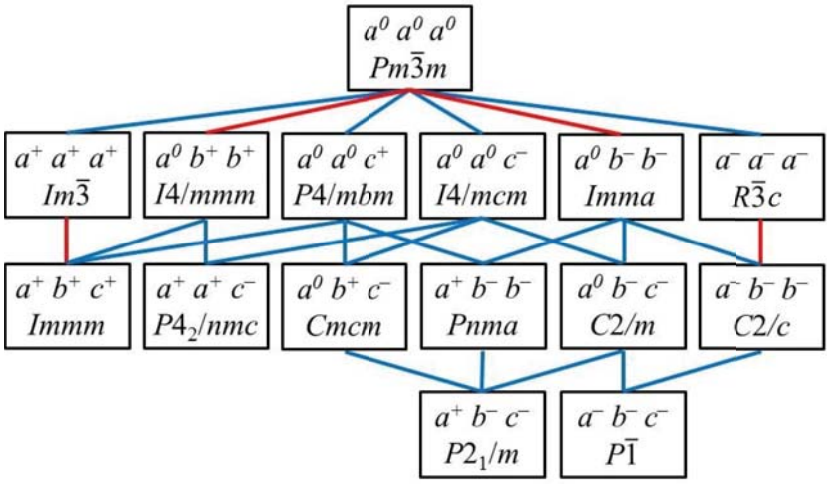

Figure 6.5 *Group-subgroup relationships between the* 15 *perovskite tilting systems in Glazer notation. Red lines indicate first order transitions and blue lines indicate second order transtions.*

coordinate of the displaced anion,

$$\tan\omega = \sqrt{3} + (x\sqrt{12}) \tag{6.5}$$

Transition metal oxynitride perovskites are an emerging class of functional materials [67] with a wide variety of interesting optical, photocatalytic [181], dielectric [182] and magnetoresistive properties [183] that may depend upon anion

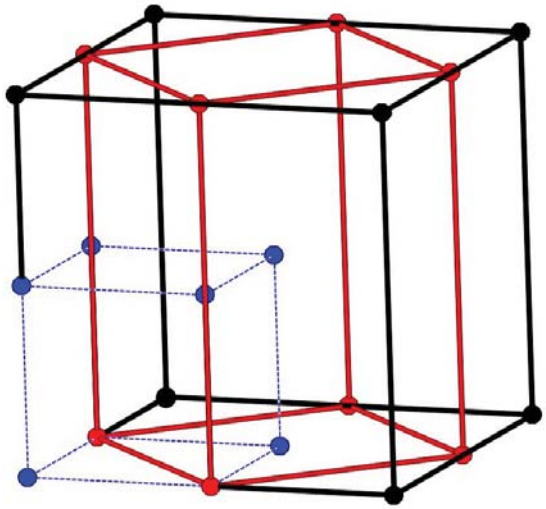

Figure 6.6 *The relationship between the cubic unit cell (cell edge length a_{cubic} in blue and the orthorhombic Pnma cell in red with $a_{ortho} \approx c_{ortho} \approx \sqrt{2}a_{cubic}$ and $c_{ortho} \approx 2a_{cubic}$.*

order. An understanding of the anion ordering principles that direct the structure of these materials is, therefore, necessary in order to understand the role it may play in governing the functionality, electronic and magnetic properties of these mixed anion systems. Despite its importance, the mechanism behind anion order in oxynitride perovskites was unclear until a recent electron and neutron diffraction study of the representative d^0 systems $SrMO_2N$ (M = Nb, Ta) revealed a robust anion ordering at high temperature that in turn directs the rotations of MO_4N_2 octahedra in rotationally ordered, low temperature superstructures [184].

In the initial study [184], refinements of high temperature neutron powder diffraction data for $SrMO_2N$ were performed in a tetragonal $P4/mmm$ model, which allows for long range anion order over the two inequivalent anion sites. The results of the refinements converged to an ordered model with full oxygen occupancy along one axis (1b site) and a 50 : 50 O : N distribution along the other two (2f site), see Figure 6.8. Below 200 °C, $SrMO_2N$ adopts a rotationally ordered superstructure, which is conventionally described by tetragonal $I4/mcm$ symmetry. Rotation of the octahedra around the unique c-axis creates two anion sites along the c-axis and in the ab-plane in a 1 : 2 ratio, respectively. The tetragonal $I4/mcm$ refinement gave near 50 : 50 O : N occupancies at the axial site, indicating that this corresponds to one of the 2f sites in the high-temperature structure. The O : N distribution across the equatorial sites of the tetragonal

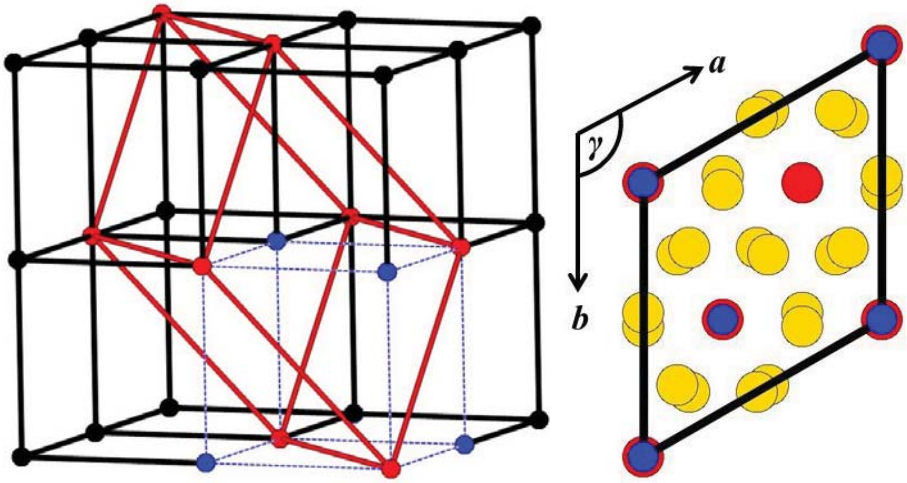

(a) *Rhomohedral cell in rhombohedral setting.*

(b) *Rhombohedral cell in hexagonal setting.*

Figure 6.7 *The (a) relationship between the cubic unit cell (cell edge length a_{cubic}) in blue and the rhombohedral cell in red in the rhomboheral setting with $a_{rhombo} \approx \sqrt{2}a_{cubic}$ and $\alpha = 60°$. The rhombohedral ABX_3 unit cell is often displayed in the (b) hexagonal setting with $a_{hex} \approx \sqrt{2}a_{cubic}$ and $c_{hex} \approx 3\sqrt{2}a_{cubic}$ with $\gamma = 120°$. Here, A-site cations are in red, B-site cations are in blue and X anions are in yellow.*

model refined to 75 : 25. This suggests that the two equatorial sites in the rotationally ordered room temperature structure are not equivalent; one should correspond to the 1*b* site (100 % O) and the other, the remaining 2*f* site (50 : 50 O : N) of the high temperature pseudo-cubic structure. This inequivalence lowers the symmetry from tetragonal $I4/mcm$ to monoclinic $I112/m$. The 75 : 25 O : N occupancy observed for the equatorial sites in the $I4/mcm$ model, therefore, reflects the average of the 100 : 0 and 50 : 50 O : N distributions of the true monoclinic symmetry, see Figure 6.9. The lower symmetry of room temperature $SrTaO_2N$ was also confirmed by electron diffraction, which showed the presence of weak $0kl$ and $h0l$ (k or h = odd) that would be systematically absent due to *c*-glide symmetry of tetragonal $I4/mcm$ if the overall symmetry was not lowered by anion order.

Within the following Chapter, the robustness of the anion ordering observed in the $SrTaO_2N$ oxynitride perovskite is investigated through a high temperature neutron diffraction study. These anion ordering principles are then extended to the d^1 perovskites $RVO_{2+x}N_{1-x}$, including a new oxynitride phase $NdVO_2N$ and its R = Pr and La analogues. These systems contain itinerant 3*d* electrons and it is, therefore, important to investigate whether or not the anion ordering

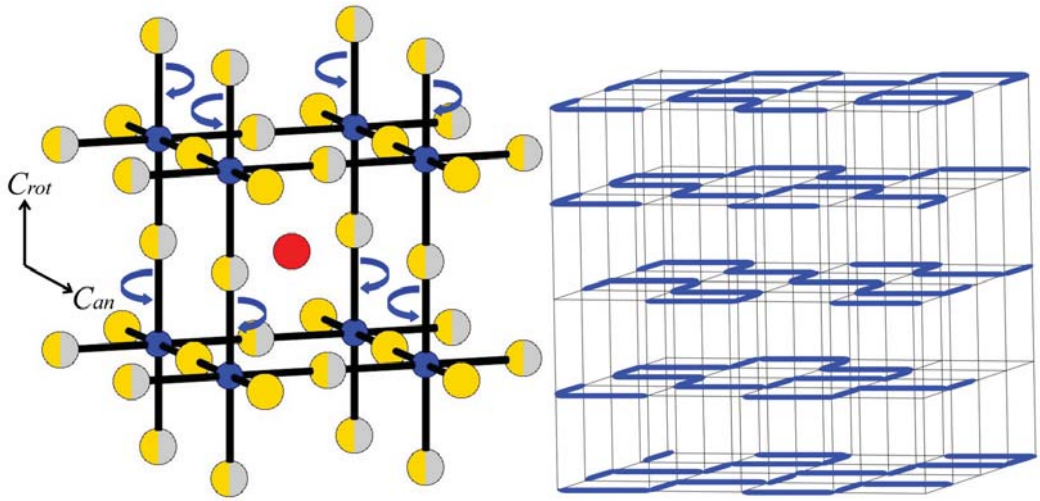

Figure 6.8 *The (a) anion order observed in the pseudo-cubic structure of $SrMO_2N$, with oxide anions (yellow) on one axis and a 50 : 50 O : N distribution along the other two (yellow/grey). The model shows the relationship between the unique axes of anion order (c_{an}) and rotation (c_{rot}) in the rotationally ordered, room temperature perovskite superstructure of $SrMO_2N$. The local anion ordering is governed by strong covalent effects that favour a cis-coordination of MO_4N_2 octahedra. This results in zig-zag M-N chains shown in (b) that propagate through the perovskite layers with a 90 ° turn at each metal centre. The heavy blue bonds depict layers of M-N chains.*

observed in their d^0 counterparts is robust and what effect it may have over their electronic and magnetic properties. All samples were prepared by Dr Judith Oró Solé and William Bonin through a collaboration with Prof Amparo Fuertes at the Institut de Ciència de Materials de Barcelona, Spain. $SrTaO_2N$ was synthesised by a reaction of stoichiometric amounts of $SrCO_3$ and Ta_2N_5 under flowing ammonia gas. $RVO_{2+x}N_{1-x}$ samples were prepared by thermal ammonolysis of RVO_4 precusors. Room temperature powder X-ray diffraction data collected for the $RVO_{2+x}N_{1-x}$ samples were indexed by an orthorhombic $Pbnm$ unit cell. The anion content of the samples was determined by combustion analysis to give compositions of $SrTaO_{1.99}N_{1.01}$, $NdVO_{2.01}N_{0.99}$, $PrVO_{2.24}N_{0.76}$ and $LaVO_{2.11}N_{0.89}$. Here, the neutron scattering studies of the samples that were performed at the ISIS and Institut Laue-Langevin neutron sources are discussed. Neutron diffraction allows for the determination of the anion order within these oxynitride systems due to the good contrast between the neutron scattering lengths of oxygen and nitrogen (5.8 and 9.4 fm, respectively [185]). Experimental details of the neutron diffraction experiments are given within each section and all Rietveld refinements were performed using the General Structure Analysis

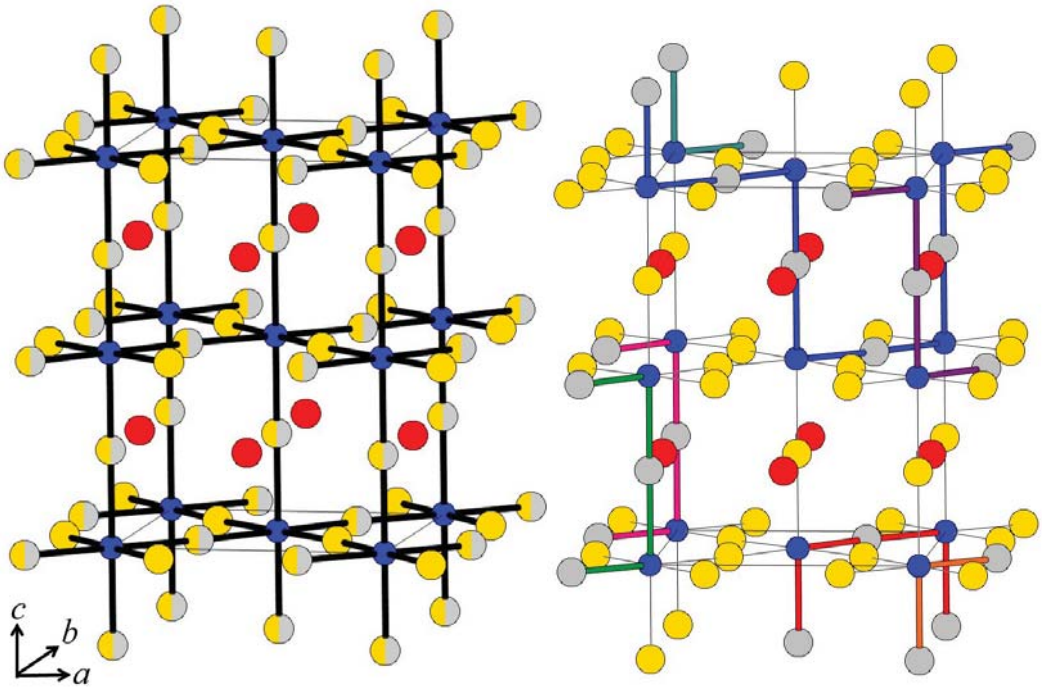

Figure 6.9 *The (a) average, rotationally ordered room temperature structure of $SrMO_2N$, conventionally described by tetragonal $I4/mcm$ symmetry. Here distinct O (yellow) and 50 : 50 O : N sites (yellow/grey) gives 50 : 50 and 75 : 25 O : N occupancies on the axial (along unique c-axis) and equatorial (in ab-plane) sites, respectively. The local ordering governed by covalent effects that favour the formation of cis-MO_4N_2 octahadra lowers the symmetry to monoclinic $I112/m$ as equatorial sites are no longer equivalent and leads to cis-MN chains that segregate into layers, depicted in (b) by the heavy coloured bonds between M octahedral centres (blue) and N (grey).*

System (GSAS) program [85].

6.2 $SrTaO_2N$

High temperature neutron powder diffraction data were collected on the High Resolution Powder Diffractometer (HRPD) at the ISIS spallation neutron source, Rutherford Appleton Laboratory, U.K. A 1 g sample was vacuum sealed in a quatz tube and placed in a vanadium jacket inside a vanadium element furnace which allowed access up to a maximum temperature of 1100 °C. Data were collected at room temperature, 500 °C, 700 °C, 900 °C and 1100 °C with a counting time of 3 hours per temperature.

Table 6.1 *Refined I4/mcm model to room temperature HRPD $SrTaO_2N$ data. $a = b = 5.7017(1)$ Å, $c/\sqrt{2} = 5.7718(2)$ Å. Total $R_{wp} = 2.83$ %.*

Atom	Site	x	y	z	Occupancy	U_{iso}*100 / Å^2
Sr	4*c*	0.0	$\frac{1}{2}$	$\frac{1}{4}$	1.0	0.30(3)
Ta	4*b*	$\frac{1}{2}$	$\frac{1}{2}$	0.0	1.0	0.09(3)
X1	4*b*	0.0	0.0	$\frac{1}{4}$	0.447(26)/0.553	0.86(2)
X2	8*d*	0.7687(2)	0.2687(2)	0.0	0.777/0.223	0.86

$SrTaO_2N$ undergoes a structural phase transition to a rotationally ordered perovskite superstructure at 300 °C, which is conventionally described by tetragonal $I4/mcm$ symmetry as discussed in the previous section. The tetragonal model was, therefore, refined to the room temperature $SrTaO_2N$ data. The model was simultaneously refined to the data collected on the backscattering and 90 ° detector banks, see Figure 6.10, with the fractional anion occupancies constrained by the total determined by chemical analysis and anion thermal parameters (U_{iso}) constrained to refine together. Linear interpolation background functions were refined to both histograms. Table 6.1 summarises the results of the room temperature refinements.

The pseudo-cubic $P4/mmm$ model, which allows for anion order, was refined to the high temperature powder neutron diffraction data of $SrTaO_2N$. Once again, the high temperature model was simultaneously refined to the data collected on the backscattering and 90 ° detector banks. Figure 6.11 shows the refinement of the $P4/mmm$ model to the highest temperature data set, measured at 1100 °C with the refinement results shown in Table 6.2. The data collected at each temperature were analysed consistently, with the same 58 parameters refined within the pseudo-cubic model. The fractional anion occupancies were constrained by the total determined by chemical analysis, anion thermal parameters were constrained to refine together and linear interpolation background functions were refined to both histograms as for the room temperature refinement. Figure 6.12 shows the temperature dependence of the lattice constants, anion occupancies and thermal parameters.

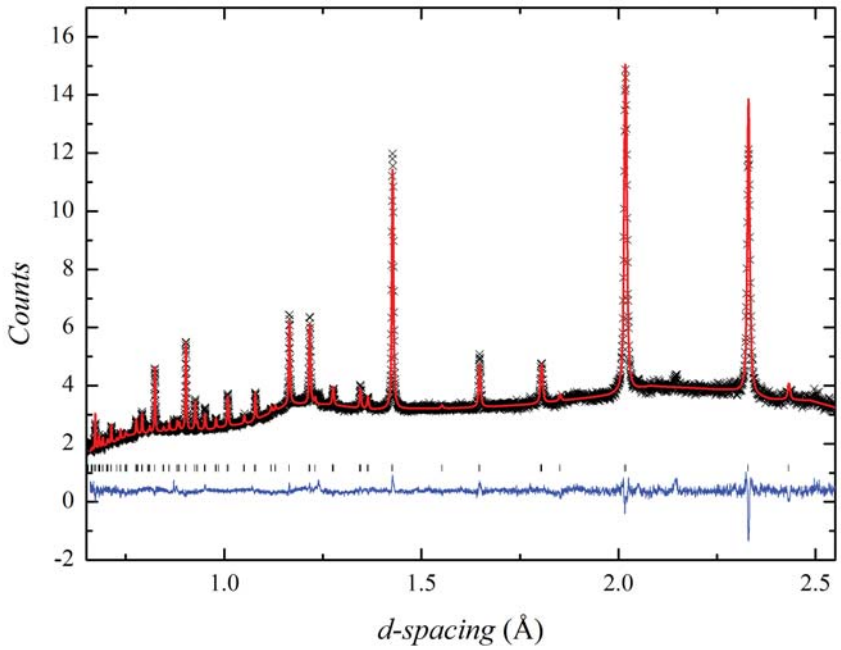

(a) *Backscattering detector bank.*

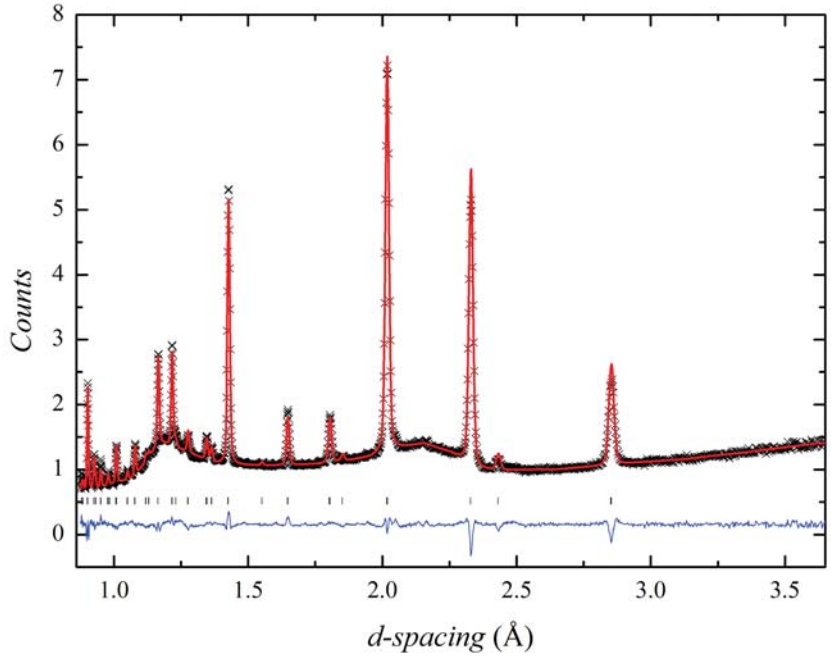

(b) 90 ° *detector bank.*

Figure 6.10 *Rietveld refinement of I4/mcm model to room temperature HRPD data of* $SrTaO_2N$.

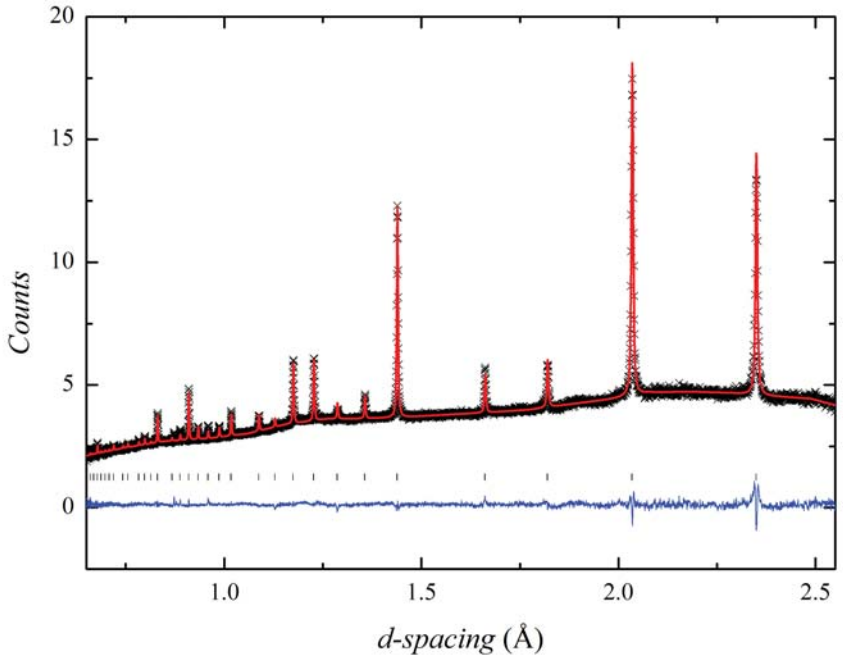

(a) *Backscattering detector bank.*

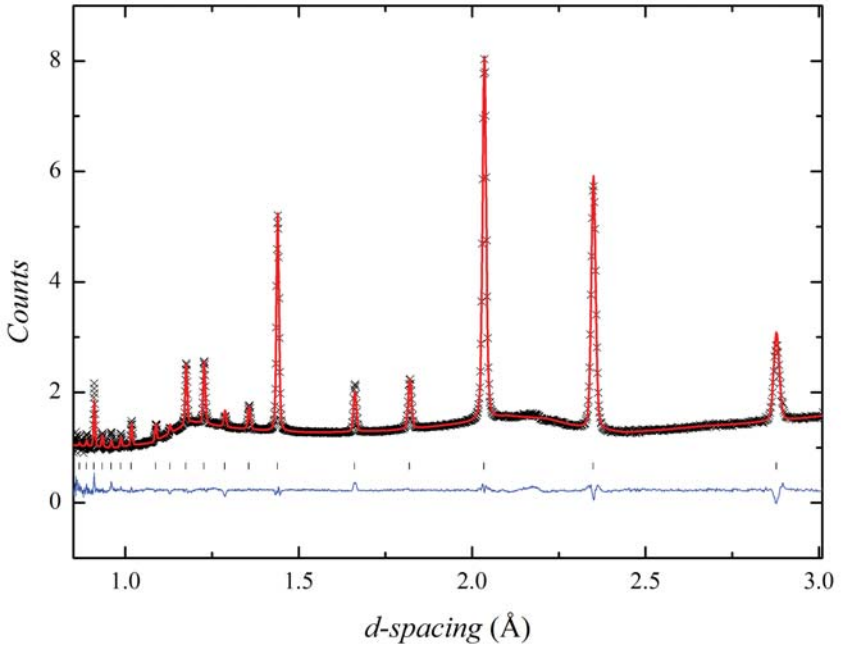

(b) 90 ° *detector bank.*

Figure 6.11 *Rietveld refinement of the pseudo-cubic P4/mmm model to high temperature (*1100 °*C) HRPD data of* $SrTaO_2N$.

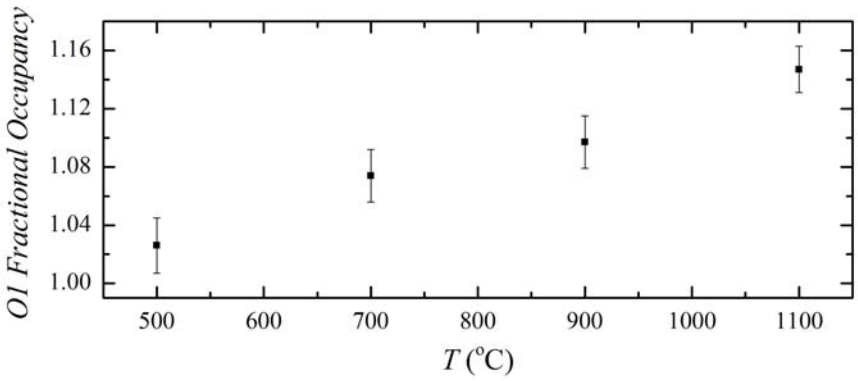

(a) *Fractional oxygen occupancy of X1 site*

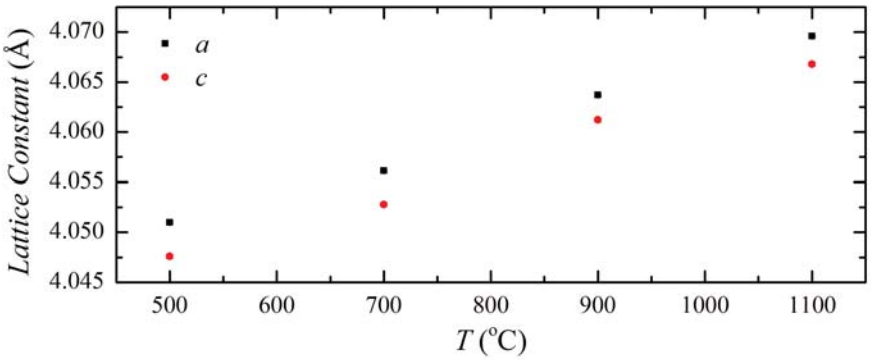

(b) *Lattice constants a (= b) and c.*

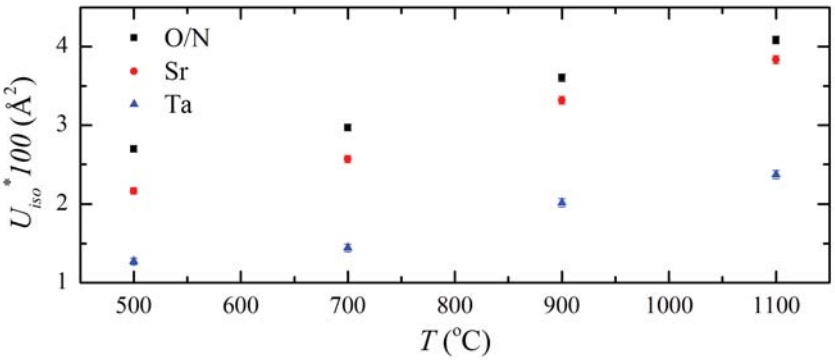

(c) *Isotropic thermal parameters.*

Figure 6.12 *Temperature dependence of various parameters obtained from the refinement of pseudo-cubic P4/mmm model to high temperature neutron diffraction data of $SrTaO_2N$.*

Table 6.2 *Refined P4/mmm model to high temperature (1100 °C) HRPD $SrTaO_2N$ data. $a = b = 4.0679(1)$ Å, $c = 4.0668(2)$ Å. Total $R_{wp} = 1.75$ %.*

Atom	Site	x	y	z	Occupancy	U_{iso}*100 / Å^2
Sr	$1d$	$\frac{1}{2}$	$\frac{1}{2}$	$\frac{1}{2}$	1.0	3.84(5)
Ta	$1a$	0.0	0.0	0.0	1.0	2.37(6)
X1	$1b$	0.0	0.0	$\frac{1}{2}$	$1.147(16)/-0.147$	4.09(5)
X2	$2f$	$\frac{1}{2}$	0.0)	0.0	0.427/0.573	4.09

6.3 $NdVO_2N$

The initial neutron diffraction study of $NdVO_2N$ was performed on the High Resolution Powder Diffractometer (HRPD) at the ISIS spallation neutron source, Rutherford Appleton Laboratory, U.K. The 650 mg powder sample was measured in a 6 mm vanadium can at room temperature for 3 hours. The data collected on the backscattering and 90° detector banks were analysed by means of a combined Rietveld refinement.

Figure 6.13 shows the refinement of the orthorhombic *Pbnm* model to the data. A vanadium oxynitride, V(O,N), impurity phase was observed within the data in addition to scattering from the vanadium sample holder and so a total of three phases were refined against the backscattering and 90° detector bank histograms. Table 6.3 summarises the results of the refinements. Fractional anion occupancies were constrained by the total determined by chemical analysis and thermal parameters were refined isotropically with anion and cation thermal parameters constrained together for all three phases in the refinement. Linear interpolation background functions were refined to both data sets.

In analogy to the $SrMO_2N$ systems, if the same local anion ordering principles are upheld then the true symmetry of $NdVO_2N$ should be lowered from orthorhombic *Pbnm* to monoclinic $P112_1/m$. In fact, the room temperature HRPD data were also successfully analysed by refining the monoclinic $P112_1/m$ model to the data to give a monoclinic angle $\gamma = 90.07(1)°$. Figure 6.14 displays the refinements performed in the monoclinic model and Table 6.4 summarises the results. Given the small magnitude of the monoclinic distortion, the atomic positions could not be refined freely within the $P112_1/m$ model and instead, were constrained by *Pbnm* pseudo-symmetry.

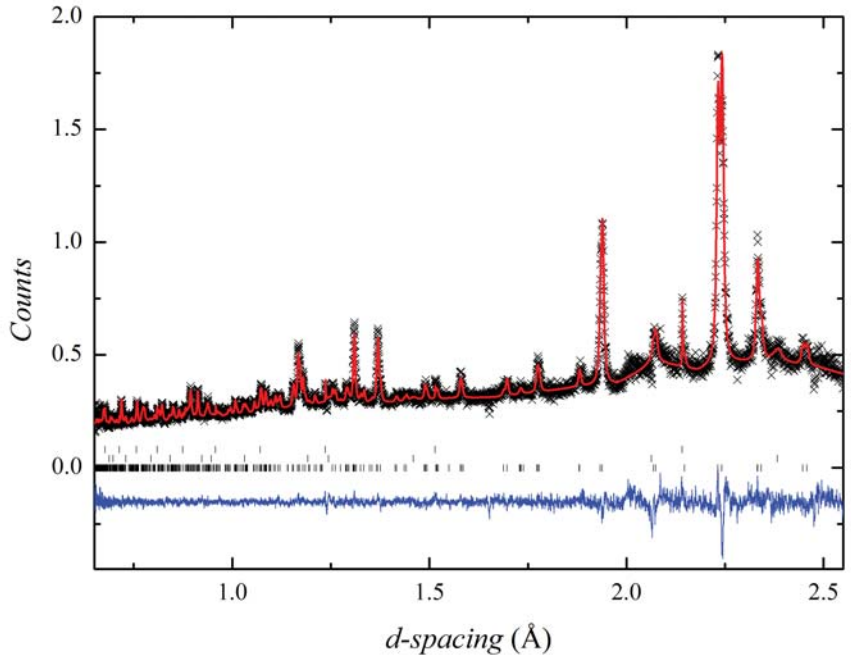

(a) *Backscattering detector bank.*

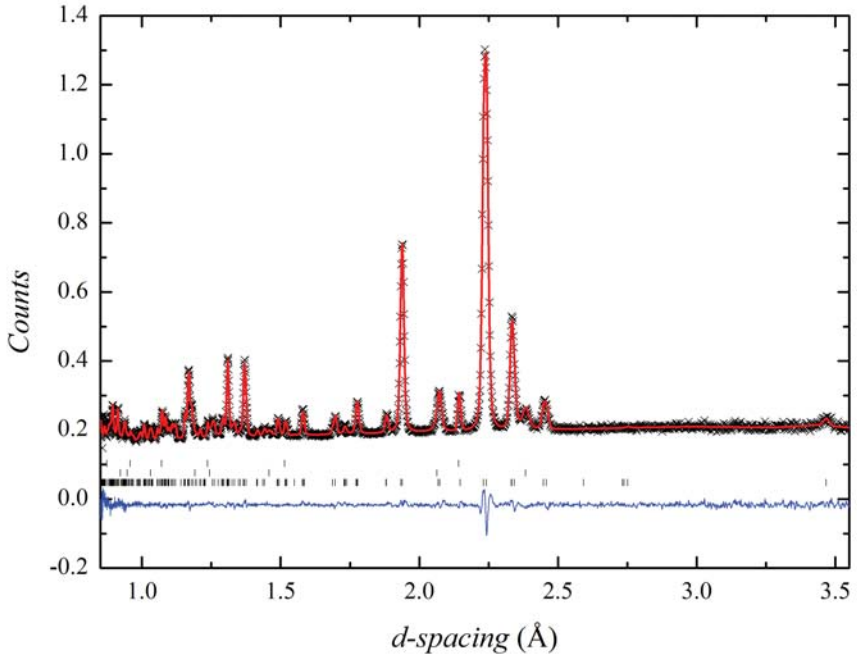

(b) 90 ° *detector bank.*

Figure 6.13 *Rietveld refinement of the orthorhombic Pbnm model to room temperature $NdVO_2N$ HRPD data. Ticks mark reflections for the perovskite phase (bottom), a vanadium oxynitride (V(O,N)) impurity phase (middle) and scattering from the vanadium sample holder (top).*

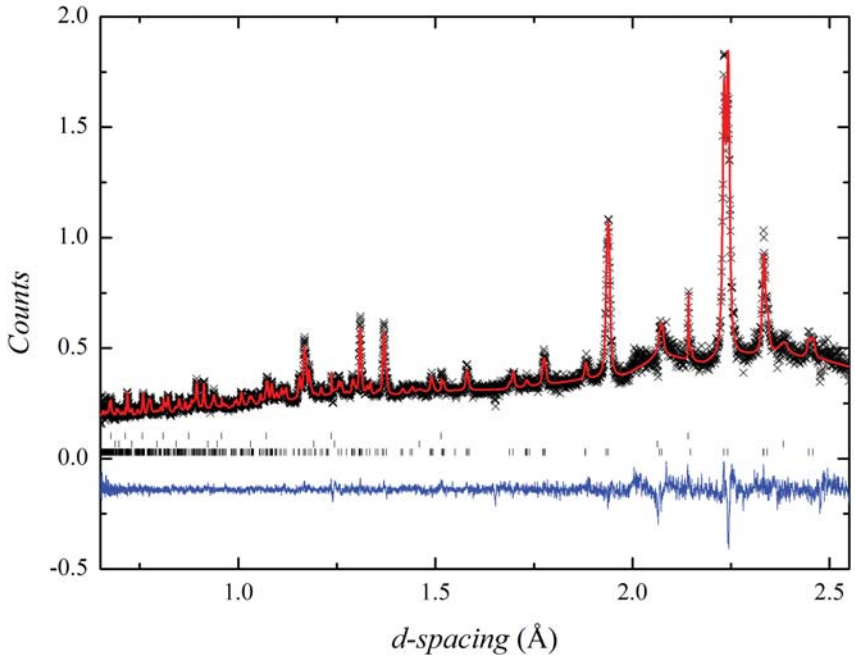

(a) *Backscattering detector bank.*

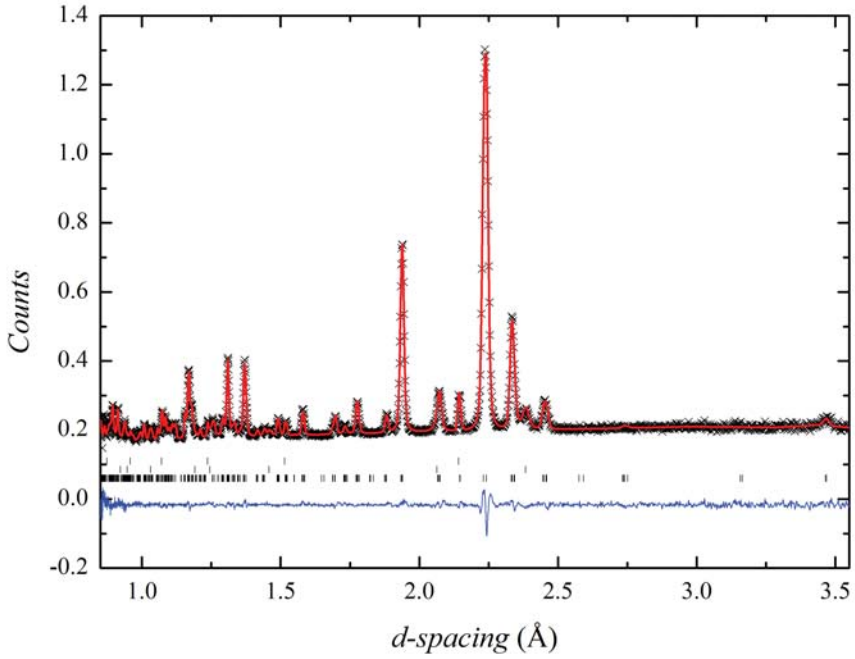

(b) 90 ° *detector bank.*

Figure 6.14 *Rietveld refinement of the monoclinic* $P112_1/m$ *model to room temperature* $NdVO_2N$ *HRPD data. Ticks mark reflections for the monoclinic perovskite phase (bottom), a vanadium oxynitride (V(O,N)) impurity phase (middle) and scattering from the vanadium sample holder (top).*

Table 6.3 *Atomic coordinates, occupancies and thermal parameters from refinement of Pbnm model to $NdVO_2N$ HRPD data, $a = 5.4637(3)$ Å, $b = 5.5022(3)$ Å, $c = 7.7329(5)$ Å. Total $R_{wp} = 3.03\%$ and $\chi^2 = 1.480$ for 68 variables.*

Atom	Site	x	y	z	Occupancy	U_{iso}*100 / Å^2
Nd	4c	0.9916(8)	0.0343(5)	$\frac{1}{4}$	1.0	0.21(5)
V	4b	$\frac{1}{2}$	0.0	0.0	1.0	0.21
X1	4b	0.0649(8)	0.4861(6)	$\frac{1}{4}$	0.55(2)/0.45	0.95(4)
X2	8d	0.7132(5)	0.2880(5)	0.0370(4)	0.73/0.27	0.95

Table 6.4 *Atomic coordinates, occupancies and thermal parameters from refinement of the $P112_1/m$ model to $NdVO_2N$ HRPD data, $a = 5.4645(3)$ Å, $b = 5.5030(3)$ Å, $c = 7.7352(5)$ Å, $\gamma = 90.07(1)^\circ$. Total $R_{wp} = 3.02\%$ and $\chi^2 = 1.474$ for 71 variables.*

Atom	Site	x	y	z	Occupancy	U_{iso}*100 / Å^2
Nd1	2e	0.0051(7)	0.0340(4)	$\frac{1}{4}$	1.0	0.09(3)
Nd2	2e	0.4949	0.5340	$\frac{1}{4}$	1.0	0.09
V1	2c	$\frac{1}{2}$	0.0	0.0	1.0	0.09
V2	2c	0.0	0.0	0.0	1.0	0.09
X11	2e	0.9348(6)	0.4864(4)	$\frac{1}{4}$	0.60(2)/0.40	0.67(3)
X12	2e	0.5652	0.9864	$\frac{1}{4}$	0.60/0.40	0.67
X21	4f	0.2838(4)	0.2890(4)	0.0382(3)	0.90(3)/0.10	0.67
X22	4f	0.2162	0.7890	0.4618	0.50(4)/0.50	0.67

Temperature dependent powder neutron diffraction data were collected on the D2B powder diffractometer at the high flux neutron reactor of the the Institut Laue-Langevin, France. A 150 mg sample of $NdVO_2N$ was measured in a 3 mm vanadium can at temperatures of 300 K, 150 K and 3.5 K in a Variox closed cycle refrigerator at full flux for 6 hours per temperature. High intensity data were obtained by integrating over the entire powder diffraction rings. All three data sets were analysed in a joint refinement of six structural phases, one perovskite phase in the *Pbnm* model and one V(O,N) impurity phase for each temperature. Temperature independent parameters, including fractional atomic coordinates and occupancies, were shared over all three histograms and once again the total anion content of the perovkite phase was constrained by the chemically determined value. Isotropic thermal parameters and unit cell constants were

allowed to refine to each temperature data set individually with anion and cation thermal parameters contrained to refine together between the perovskite phase and the impurity phase at each temperature. A linear interpolation background function was employed for each histogram. A total of 150 variables were refined to give $\chi^2 = 1.664$. Figures 6.15 - 6.17 show the refinement plots at each temperature. Table 6.5 gives the results of the shared parameters in the *Pbnm* model and Table 6.6 displays the temperature dependent model parameters. Selected bond lengths and angles obtained for $NdVO_2N$ in the *Pbnm* model are shown in Table 6.7.

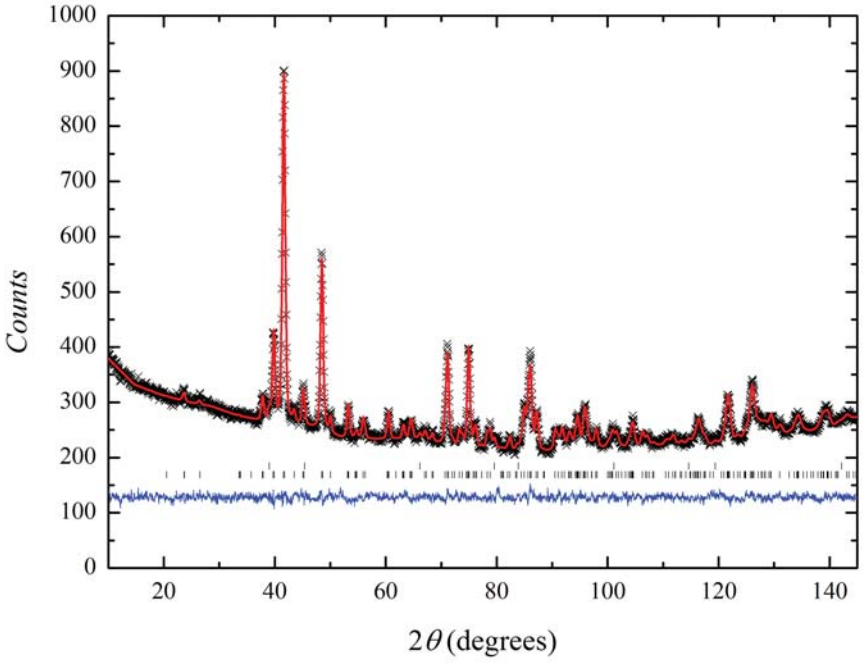

Figure 6.15 *Rietveld refinement of the Pbnm model to the* 300 *K* $NdVO_2N$ *D2B data. Ticks mark the reflections for the orthorhombic perovskite phase (bottom) and a vanadium oxynitride (V(O,N)) impurity phase (top).*

6.4 $PrVO_{2.24}N_{0.76}$

Neutron powder diffraction data were collected on a 1 g sample of $PrVO_{2.24}N_{0.76}$ on the D2B powder diffractometer of the Institut Laue-Langevin, France. The sample was loaded into a 6 mm vanadium can in a Variox closed cycle refrigerator and measured at full flux at temperatures of 300 K, 150 K and 3.5 K, with a

Table 6.5 *Summary of the refinement of the Pbnm model to $NdVO_2N$ D2B data.*

Atom	Site	x	y	z	Occupancy
Nd	4c	0.9938(7)	0.0352(4)	$\frac{1}{4}$	1.0
V	4b	$\frac{1}{2}$	0.0	0.0	1.0
X1	4b	0.0682(5)	0.4860(4)	$\frac{1}{4}$	0.560(16)/0.440
X2	8d	0.7140(4)	0.2887(3)	0.0374(2)	0.720/0.280

Table 6.6 *Temperature dependent variables refined in the Pbnm model to D2B data collected for $NdVO_2N$ at* 3.5, 150 *and* 300 *K. Total R_{wp} = 1.95 %, χ^2 = 1.644 for* 150 *variables.*

T / K	3.5	150	300
a / Å	5.4576(3)	5.4597(4)	5.4665(5)
b / Å	5.5036(3)	5.5038(3)	5.5053(4)
$c/\sqrt{2}$ / Å	5.4596(3)	5.4626(3)	5.4688(4)
V / Å^3	231.92(2)	232.14(2)	232.76(3)
Nd/V U_{iso}*100 / Å^2	0.13(5)	0.23(4)	0.41(6)
O/N U_{iso}*100 / Å^2	0.77(4)	0.85(4)	0.97(5)
R_{wp} / %	1.98	1.93	1.95

Table 6.7 *Selected bond lengths and angles for $NdVO_2N$ obtained from the simultaneous refinement of the Pbnm model to the D2B data collected at* 3.5, 150 *and* 300 *K.*

	Nd-X1	Nd-X2	V-X1	V-X2
Bond length / Å	2.410(5) 2.515(3) 3.051(3) 3.084(5)	2.416(3) (×2) 2.644(3) (×2) 2.707(3) (×2) 3.267(3) (×2)	1.9706(9) (×2)	1.970(1) (×2) 1.995(2) (×2)
	Nd-X1-Nd	Nd-X2-Nd	V-X1-V	V-X2-V
Bond Angle / °	105.8(1)	98.3(1) 163.1(1)	157.7(2)	156.2(1)

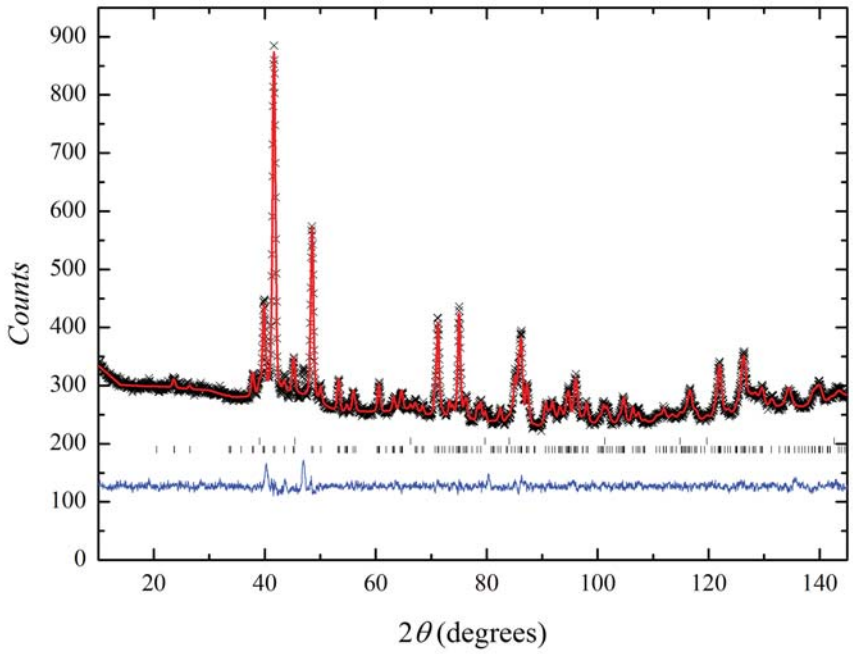

Figure 6.16 *Rietveld refinement of the Pbnm model to the* 150 *K* $NdVO_2N$ *D2B data. Ticks mark reflections for the orthorhombic perovskite phase (bottom) and a vanadium oxynitride (V(O,N)) impurity phase (top).*

counting time of approximately 6 hours per temperature. Six structural models were refined simultaneously to the data collected at each temperature, one *Pbnm* perovskite phase and one V(O,N) impurity phase for each temperature data set. Once again, fractional atomic coordinates and occupancies were shared over all three data sets and cation and anion isotropic thermal parameters and lattice constants were refined at each temperature. The total anion content in the perovskite phase was constrained by the chemically determined composition. A linear interpolation background function was refined against each histogram. A total of 100 variables were refined to give $\chi^2 = 4.011$. Figures 6.18 - 6.20 display the Rietveld refinement of the model to the data measured at each temperature. Table 6.8 shows the refined values for the parameters in the *Pbnm* model that were shared across all histograms. Table 6.9 displays the variation of the temperature dependent variables within the *Pbnm* model and Table 6.10 shows selected bond lengths and angles in the *Pbnm* structure.

Table 6.8 *Summary of refinement of the Pbnm model to $PrVO_{2.24}N_{0.76}$ D2B data.*

Atom	Site	x	y	z	Occupancy
Pr	4c	0.9894(7)	0.0320(4)	$\frac{1}{4}$	1.0
V	4b	$\frac{1}{2}$	0.0	0.0	1.0
X1	4b	0.0693(4)	0.4853(3)	$\frac{1}{4}$	0.561(11)/0.439
X2	8d	0.7135(3)	0.2891(3)	0.0367(2)	0.840/0.160

Table 6.9 *Temperature dependent variables refined in the Pbnm model to D2B data collected for $PrVO_{2.24}N_{0.76}$ at 3.5, 150 and 300 K. Total R_{wp} = 3.65 %, χ^2 = 4.011 for 100 variables.*

T / K	3.5	150	300
a / Å	5.4829(3)	5.4851(3)	5.4907(4)
b / Å	5.5138(3)	5.5127(3)	5.5092(3)
$c/\sqrt{2}$ / Å	5.4760(3)	5.4822(3)	5.4909(4)
V / Å^3	234.13(2)	234.43(2)	234.90(2)
Pr/V U_{iso}*100 / Å^2	0.10(1)	0.23(1)	0.42(1)
O/N U_{iso}*100 / Å^2	0.83(5)	0.92(5)	1.11(5)
R_{wp} / %	3.55	3.70	3.73

Table 6.10 *Selected bond lengths and angles for $PrVO_{2.24}N_{0.76}$ obtained from the simultaneous refinement of the Pbnm model to the D2B data collected at 3.5, 150 and 300 K.*

	Pr-X1	Pr-X2	V-X1	V-X2
Bond length / Å	2.436(4) 2.536(3) 3.043(3) 3.079(4)	2.404(3) (×2) 2.654(3) (×2) 2.728(3) (×2) 3.278(3) (×2)	1.9799(5) (×2)	1.976(2) (×2) 1.998(2) (×2)
	Pr-X1-Pr	Pr-X2-Pr	V-X1-V	V-X2-V
Bond Angle / °	106.0(1)	97.6(1) 163.7(1)	156.3(1)	156.2(1)

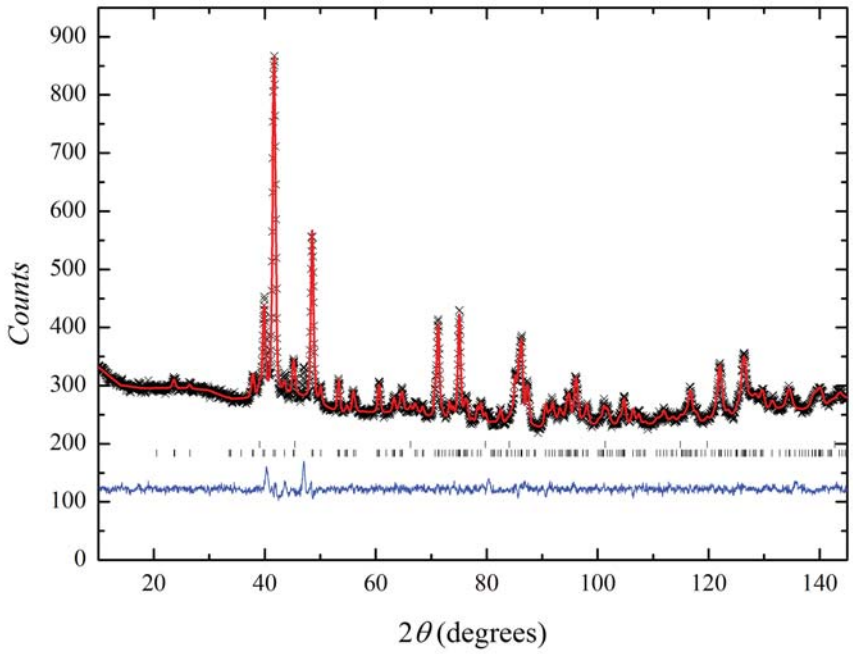

Figure 6.17 *Rietveld refinement of the Pbnm model to the* 3.5 *K* $NdVO_2N$ *D2B data. Ticks mark reflections for the orthorhombic perovskite phase (bottom) and a vanadium oxynitride (V(O,N)) impurity phase (top).*

6.5 $LaVO_{2.11}N_{0.89}$

Neutron powder diffraction data were collected on a 1 g sample of $LaVO_{2.11}N_{0.89}$ on the D2B powder diffractometer of the Institut Laue-Langevin, France. The sample was loaded into a 6 mm vanadium can in a Variox closed cycle refrigerator and measured at full flux at temperatures of 300 K, 150 K and 3.5 K, with a counting time of approximately 6 hours per temperature. Inspection of the data showed an unusual splitting of the peaks at high angle, see Figure 6.21. The splitting is most likely indicative of the coexistence of two perovskite phases. The data were successfully analysed by including a rhombohedral $R\bar{3}c$ (no. 167) phase along with the orthorhombic *Pbnm* model in a simultaneous refinement to all three data sets. Six structural phases were included in the refinement, one orthorhombic and one rhombohedral perovskite phase for each temperature dependent data set. Linear interpolation background functions were used to model the background of each histogram. Figures 6.22 - 6.24 display the Rietveld plots for each measured temperature. A total of 81 variables were

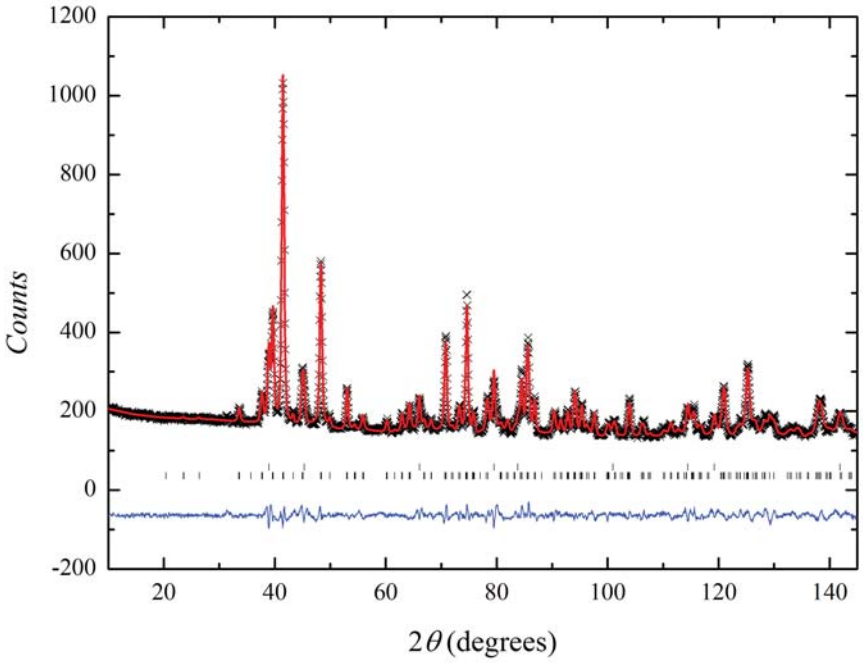

Figure 6.18 *Rietveld refinement of the Pbnm model to the* 300 *K* $PrVO_{2.24}N_{0.76}$ *D2B data. Ticks mark reflections for the orthorhombic perovskite phase (bottom) and a vanadium oxynitride (V(O,N)) impurity phase (top).*

refined to give $\chi^2 = 2.962$. Tables 6.11 and 6.12 summarise the temperature independent refinement results for the *Pbnm* and $R\bar{3}c$ models, respectively. The anion occupancies were constrained by the total anion content determined by the chemical analysis of the sample and refined within the *Pbnm* model. In the rhombohedral phase, they were fixed across the 18*e* anion site according to the chemical analysis. Table 6.13 summarises the temperature dependent parameters within the orthorhombic and rhombohedral models, including the weight percentages of the two phases at each temperature. Table 6.14 shows selected bond lengths and angles for the orthorhombic phase.

6.6 Discussion

The results of the room temperature refinement of the rotationally ordered tetragonal $I4/mcm$ model to the HRPD data collected for $SrTaO_2N$ gives O : N distributions that are in excellent agreement with the previous study and well

Table 6.11 *Summary of refinement of the Pbnm model to $LaVO_{2.11}N_{0.89}$ D2B data.*

Atom	Site	x	y	z	Occupancy
La	4c	0.9994(3)	0.0096(5)	$\frac{1}{4}$	1.0
V	4b	$\frac{1}{2}$	0.0	0.0	1.0
X1	4b	0.0570(2)	0.4978(3)	$\frac{1}{4}$	0.654(11)/0.346
X2	8d	0.7381(4)	0.2642(3)	0.0291(2)	0.728/0.272

Table 6.12 *Summary of refinement of the $R\bar{3}c$ model to $LaVO_{2.11}N_{0.89}$ data.*

Atom	Site	x	y	z	Occupancy
La	6a	0.0	0.0	$\frac{1}{4}$	1.0
V	6b	0.0	0.0	0.0	1.0
X	18e	0.4558(1)	0.0	$\frac{1}{4}$	0.703/0.297

Table 6.13 *Temperature dependent variables refined in the Pbnm and $R\bar{3}c$ models to D2B data collected for $LaVO_{2.11}N_{0.89}$ at 3.5, 150 and 300 K. Total R_{wp} = 3.34 %, χ^2 = 2.962 for 81 variables.*

T / K	3.5	150	300
		Pbnm phase	
a / Å	5.5393(1)	5.5415(2)	5.5453(8)
b / Å	5.5011(1)	5.4989(2)	5.5065(6)
$c/\sqrt{2}$ / Å	5.5011(1)	5.5024(2)	5.5002(7)
V / Å^3	236.89(1)	237.12(1)	237.51(4)
Phase fraction / Wt. %	82	67	19
		$R\bar{3}c$ phase	
a / Å	5.4829(3)	5.5256(2)	5.5341(1)
$c/\sqrt{6}$ / Å	5.4726(5)	5.4725(2)	5.4810(1)
V / Å^3	354.21(4)	354.45(2)	356.08(1)
Phase fraction / Wt. %	18	33	81
La/V U_{iso}*100 / Å^2	0.15(2)	0.16(2)	0.46(2)
O/N U_{iso}*100 / Å^2	0.65(2)	0.69(2)	0.96(2)
R_{wp} / %	3.34	3.28	3.39

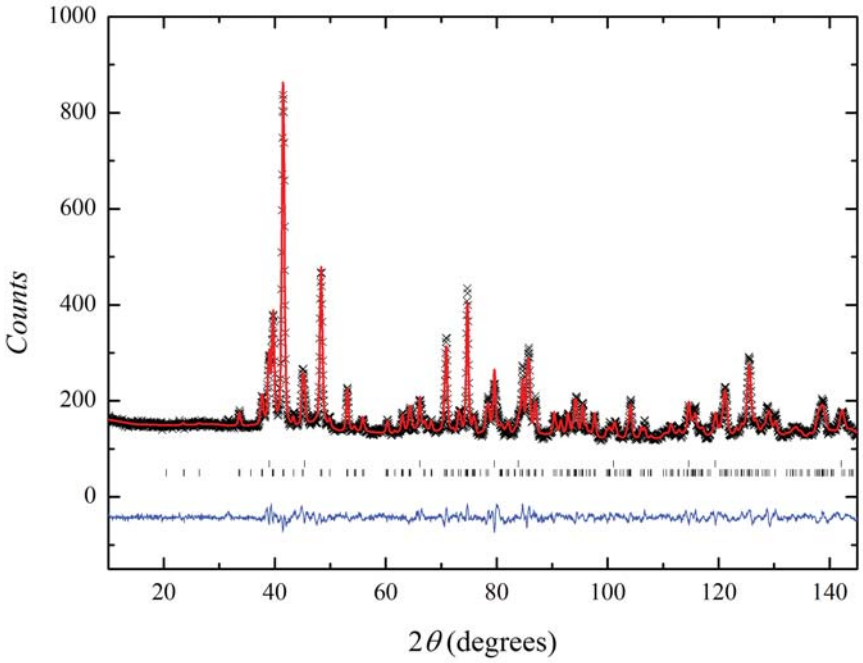

Figure 6.19 *Rietveld refinement of the Pbnm model to the* 150 *K* $PrVO_{2.24}N_{0.76}$ *D2B data. Ticks mark reflections for the orthorhombic perovskite phase (bottom) and a vanadium oxynitride (V(O,N)) impurity phase (top).*

reflect the average O : N occupancies of 50 : 50 and 75 : 25 across the two anion sites that result from the local anion ordering of *cis*-TaO_4N_2 octahedra. The high temperature neutron diffraction study presented here extends the previous work and shows that the anion order in the high temperature pseudo-cubic $P4/mmm$ phase is highly robust, with 100 % oxygen occupancy of the along one axis and 50 : 50 O : N along the other two persisting up to the highest measured temperature of 1100 °C. This indicates that zig-zag Ta-N chains that result from the local ordering remain well segregated in two-dimensional perovskite layers, with little mixing or hopping of chains between layers as shown in Figure 6.25. Unfortunately, the refined fractional oxygen occupancy of the 1*b* site remains above 100 % in all the high temperature refinements presented here. This most probably results from the strong correlation between fractional occupancies and thermal parameters within the model whilst refining the high temperature data sets.

The Rietveld refinement results for the novel oxynitride phase, $NdVO_2N$ presented in this chapter are significant because they imply that the local anion ordering

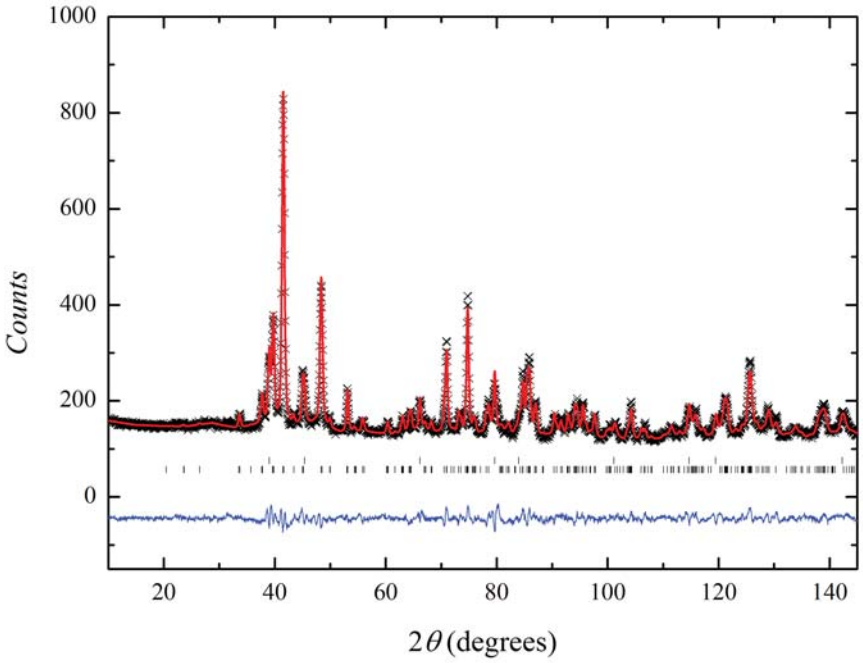

Figure 6.20 *Rietveld refinement of the Pbnm model to the* 3.5 *K* $PrVO_{2.24}N_{0.76}$ *D2B data. Ticks mark reflections for the orthorhombic perovskite phase (bottom) and a vanadium oxynitride (V(O,N)) impurity phase (top).*

principles discovered initially for the d^0 SrMO$_2$N perovskites is robust to electron doping. The $\sqrt{2}\times\sqrt{2}\times2$ *Pbnm* perovskite superstructure has axial and equatorial anion positions within the rotationally ordered octahedra in a 1 : 2 ratio. The refinement of the HRPD diffraction data in this orthorhombic model gives O : N occupancies close to 50 : 50 and 75 : 25 across the axial and equatorial sites and, therefore, appears to be very similar to the anion order observed in the $SrTaO_2N$ and $SrNbO_2N$ systems. In the SrMO$_2$N perovskites, this local anion ordering results in M-N chains that propagate throughout the structure with a 90° turn in the chain at each M cation centre, leading to a 50 : 50 O : N population of the anion sites within the layers and 100 : 0 at the inter-layer sites, see Figure 6.26. These M-N chains provide a physical realisation of the the statistical mechanics model of the self-avoiding walk [186]; although the chains are disordered on a long-range, crystallographic scale, they are highly constrained locally, giving rise to unusual properties, such as sub-extensive entropy [187]. In the *Pbnm* model of $NdVO_2N$ model the crystallographic c-axis lies within the layers of the disordered V-N chains, such that the refined occupancy of the axial X1 site is close to 50 : 50 O : N. The equatorial sites, therefore, represent the average of the 100 : 0 O :

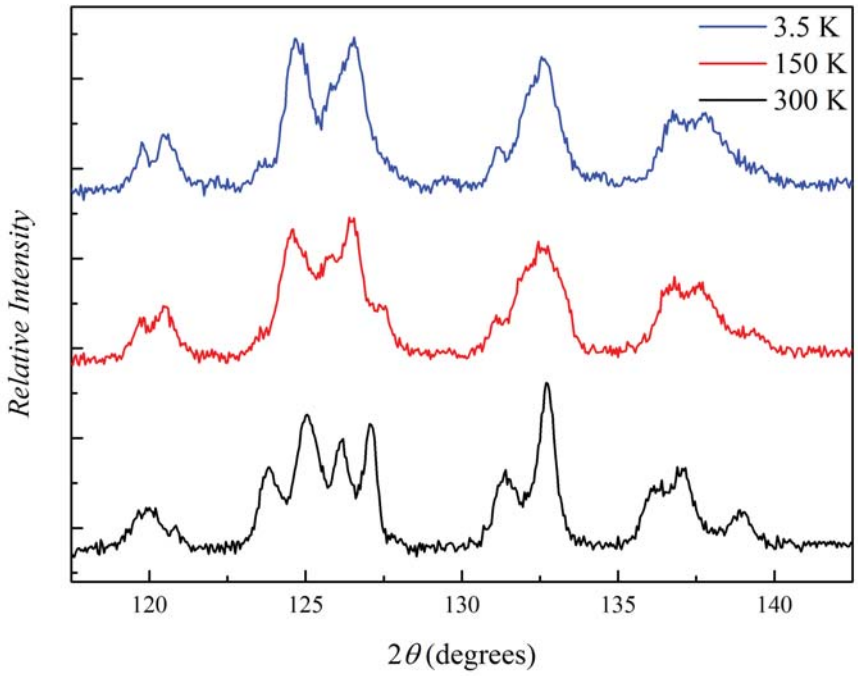

Figure 6.21 *Neutron powder diffraction data of* $LaVO_{2.11}N_{0.89}$ *shows an unusual splitting of peaks at high* 2θ *upon warming.*

N inter-layer position and the remaining 50 : 50 site within the zig-zag chains, giving a 75 : 25 O : N distribution in the *Pbnm* model. In analogy with the SrMO$_2$N systems, the in-equivalence of the equatorial anion sites due to the local anion ordering lowers the overall symmetry of the system, in this case, from orthorhombic *Pbnm* to monoclinic $P112_1/m$ (a non-standard setting of space group $P2_1/m$ no. 14). This symmetry lowering splits the equatorial X2 sites and a refinement of the HRPD diffraction data in the $P112_1/m$ model gives O : N distributions of 0.90(3) : 0.10 and 0.50(4) : 0.50 at X21 and X22, respectively (see Table 6.4). This is in excellent agreement with the 100 : 0, 50 : 50 distributions predicted for the local anion ordering, and a stable monoclinic refinement of the neutron diffraction data of NdVO$_2$N with $\gamma = 90.07°$ demonstrates that the anion ordering principles first discovered in SrMO$_2$N can be extended to this d^1 perovskite oxynitride. Further independent evidence for this subtle monoclinic lattice distortion is provided by an electron diffraction study that is presented in *ref.* [188]. The electron diffraction patterns collected for crystallites of NdVO$_2$N show additional k-odd $0kl$ reflections that result from the loss of the b-glide plane as the symmetry is lowered from *Pbnm* to $P112_1/m$.

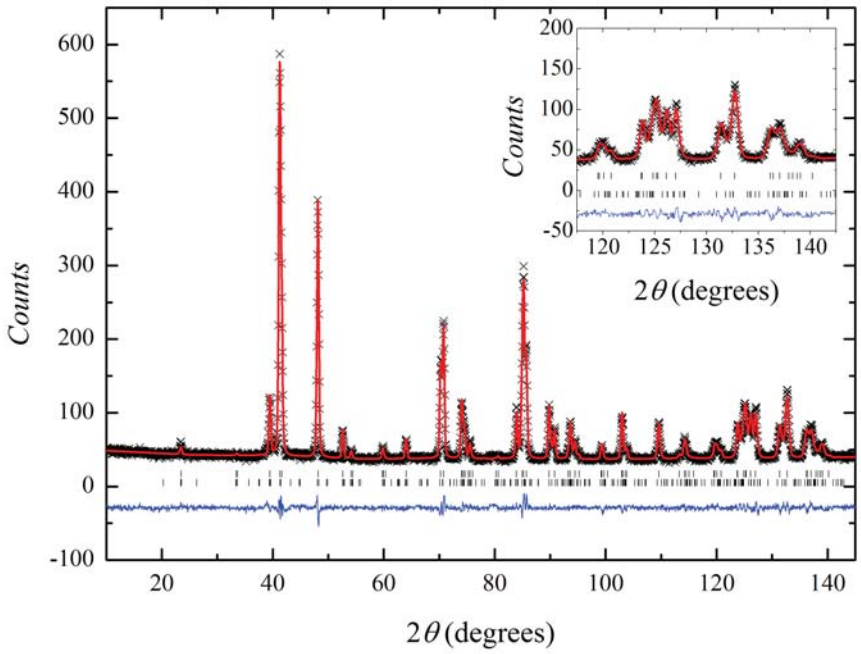

Figure 6.22 *Rietveld refinement of the Pbnm (bottom tick marks) and R$\bar{3}$c (top tick marks) models to the* 300 *K* $LaVO_{2.11}N_{0.89}$ *D2B data. Inset shows high* 2θ *region of the fit.*

The refinement of the temperature dependent diffraction data collected for $NdVO_2N$ on the D2B powder diffractometer at the Institute Laue-Langevin in the *Pbnm* model gives O : N distributions of 0.56(2) : 0.44 and 0.72 : 0.28 across the anion sites and is, therefore, entirely consistent with the analysis of time-of-flight neutron diffraction data of HRPD. Upon cooling from room temperature to 3.5 K there is a smooth decrease in the unit cell lattice constants, with an overall reduction in the orthorhombic cell volume of ~ 0.4 %. There is no evidence for any structural or magnetic phase transitions within the $NdVO_2N$ system upon cooling to 3.5 K. In fact, the magnetic susceptibility of $NdVO_2N$, shown in reference [188], displays paramagnetic behaviour down to 2 K with an absence of any spin ordering transition in agreement with the low temperature neutron diffraction data. The magnetic behaviour of $NdVO_2N$ can be understood in terms Curie-Weiss and Pauli paramagnetic contributions of the localised, weakly antiferromagnetic Nd^{3+} $4f^3$ spins and itinerant V^{4+} $3d^1$ spins, respectively.

The local anion ordering in the d^0 perovskite oxynitrides was rationalised in terms of the strong covalent effects that favour a *cis*-coordination of two strongly bonded ligands of high valence d^0 transitional metal octahedral complexes. This

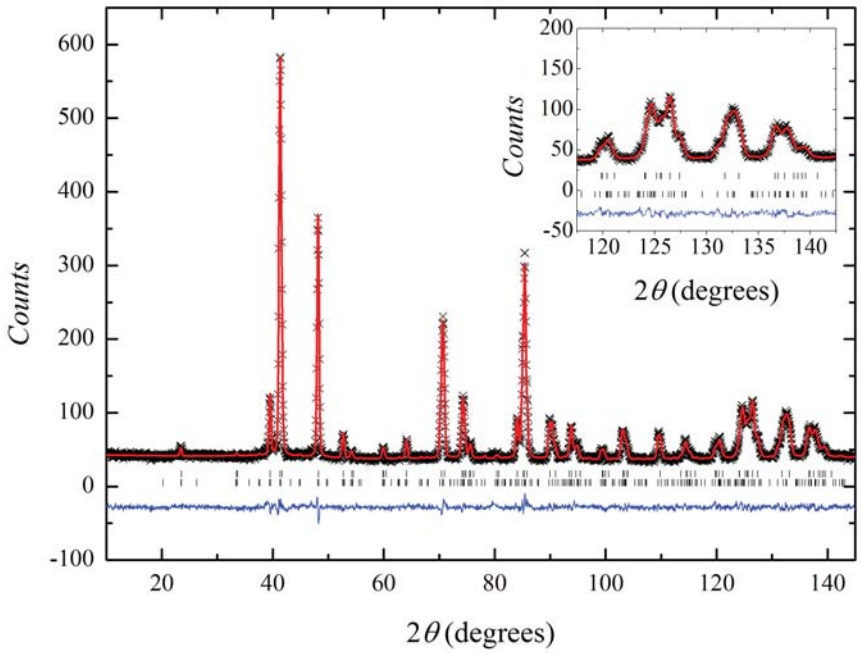

Figure 6.23 *Rietveld refinement of the Pbnm (bottom tick marks) and R$\bar{3}$c (top tick marks) models to the* 150 *K* $LaVO_{2.11}N_{0.89}$ *D2B data. Inset shows high* 2θ *region of the fit.*

90° arrangement allows for maximum π-bonding overlap of the d-orbital of the metal cation centre and the p-orbitals of the coordinated ligands [189]. This covalency, therefore, favours the formation of *cis*-MO_4N_2 octahedra in the perovskite oxynitrides given that N^{3-} is more strongly bonded to the M cation centre than O^{2-} and so a 90° arrangement of the nitride anions is observed. The observation of the *cis*-VN_2 units in $NdVO_2N$ implies that a strong, covalent second order Jahn-Teller interaction between V^{4+} and N^{3-} is also prevalent here. This is significantly different from the metallic RVO_3 oxide analogues, which undergo orbital ordering transitions as a results of first order Jahn-Teller effects due to the orbitally degenerate t_{2g} electrons [190]. The fact that $NdVO_2N$ displays itinerant electron behaviour in magnetic susceptibility measurements, however, implies that the oxynitrides do retain some of the metallic character of their parent RVO_3 oxides.

The study of the $PrVO_{2.24}O_{0.76}$ and $LaVO_{2.11}O_{0.89}$ oxynitride perovskites allows for an understanding of the anion ordering in these systems when there is a deviation from the RVO_2N stoichiometry. The R = Pr analogue is another new oxynitride phase and R = La has previously been reported with a molar

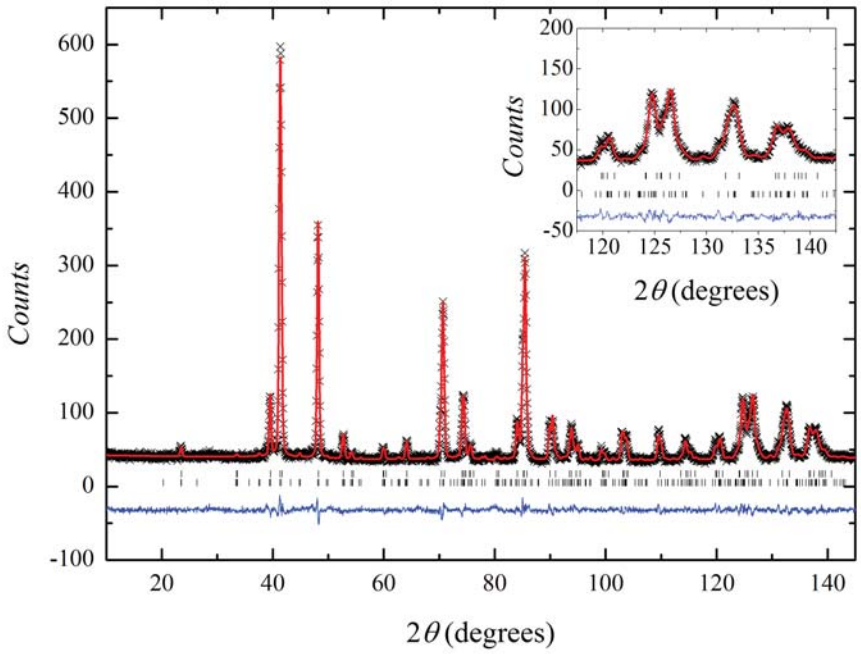

Figure 6.24 *Rietveld refinement of the Pbnm (bottom tick marks) and$R\bar{3}c$ (top tick marks) models to the 3.5 K $LaVO_{2.11}N_{0.89}$ D2B data. Inset shows high 2θ region of the fit.*

nitrogen content of 0.99 [191]. The $PrVO_{2.24}N_{0.76}$ data, like those of $NdVO_2N$, were successfully refined by the orthorhombic *Pbmn* model at all measured temperatures. There are no apparent structural or magnetic phase transitions upon cooling the system to 3.5 K. There does, however, appear to be some anisotropy in the thermal evolution of the lattice parameters, with a reduction in a and c lattice constants upon cooling but an increase in b from 5.5093(3) Å at 300 K to 5.5138(3) Å at 3.5 K. Refinement of the O and N distributions over the anion sites shows that the near 50 : 50 O : N ratio on the axial X1 site observed in stoichiometric $NdVO_2N$ is retained and that the non-stoichiometry appears across the X2 site with a 0.84 : 0.16 O : N distribution.

The *Pbnm* model could not be refined to the data collected for $LaVO_{2.11}N_{0.89}$ alone. The splitting of the peaks at high angle indicated that there may be two coexisting pervoskite phases within the R = La system. The structural evolution from orthorhombic *Pbnm* to a rhombohedral $R\bar{3}c$ phase has been reported in other lanthanum based perovskites, such as $LaFeO_3$ [192]. According to group theory there is no second-order phase transition between the *Pbnm* and $R\bar{3}c$ symmetries [193], however the first-order transition appears to be hysteretic

Table 6.14 *Selected bond lengths and angles for $LaVO_{2.11}N_{0.89}$ obtained from the simultaneous refinement of the Pbnm model to the D2B data collected at 3.5, 150 and 300 K.*

	La-X1	La-X2	V-X1	V-X2
Bond length / Å	2.461(2) 2.708(5) 2.836(5) 3.086(2)	2.552(2) (×2) 2.649(2) (×2) 2.832(2) (×2) 3.017(2) (×2)	1.9702(3) (×2)	1.961(2) (×2) 1.978(2) (×2)
	La-X1-La	La-X2-La	V-X1-V	V-X2-V
Bond Angle / °	98.3(1) 166.7(1)	97.23(4) 170.37(6)	161.51(8)	165.52(6)

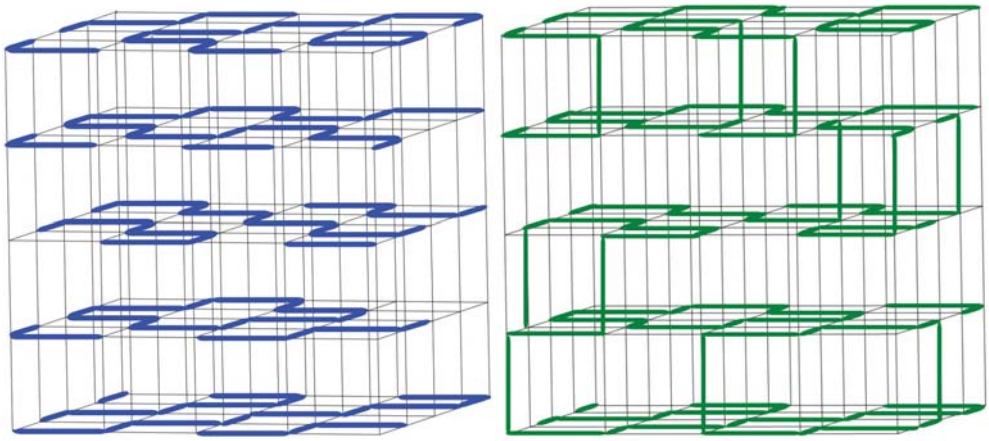

(a) **(b)**

Figure 6.25 *The local anion ordering that favour a cis-coordination of MO_4N_2 octahedra resulting in zig-zag M-N chains that segregate into (a) two dimensional layers is robust to very high temperatures. The 100 % oxygen occupancy along one axes in the high temperature pseudo-cubic model of $SrTaO_2N$ and 50 : 50 O : N along the other two indicates that the chains remain separated into layers up to at least 1100 ° with very little jumping of chains between layers as depicted in (b). The heavy bonds show M-N chains.*

in nature given the clear coexistence of both phases over the entire measured temperature range. As such, it is difficult pin-point the transition temperature with the current data set, but one can estimate a transition temperature, $T_c \sim 200$ K.

Figure 6.27 shows the variation in the refined fractional occupancies of the oxygen sites as a function of x, where x gives the deviation from 2 : 1 O : N stoichiometry in the $R\mathrm{VO}_{2+x}\mathrm{N}_{1-x}$ systems. The materials studied here have $x = 0, 0.11$ and

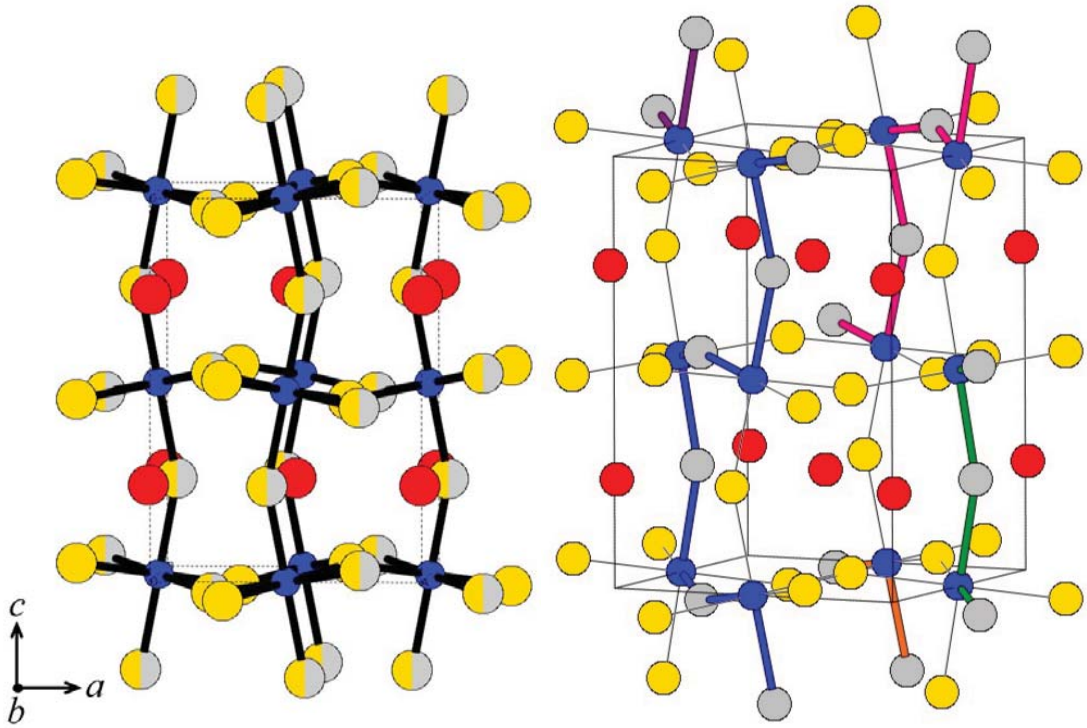

Figure 6.26 *The (a) rotationally ordered perovskite superstructure of $NdVO_2N$ in $P112_1/m$ has distinct oxygen (yellow) and 50 : 50 O : N (yellow/grey) sites. The local ordering that results from covalent effects gives rise to (b) disordered zig-zag chains of V-N units that propagate through the structure with a 90° turn at each V (blue) centre. Here the V-N chains are shown as coloured bonds with O (yellow), N (grey), V (blue) and Nd (red).*

0.24 for the R = Nd, La and Pr analogues, respectively. The refined fractional occupancies are compared to the ideal values expected for oxygen on the X1 and X2 sites from the local anion ordering principles in the *Pbnm* model in addition to the statistically averaged distribution, which in the $x = 0$ case is given by $(2\times0.75) + 0.5/3 = 0.67$ for oxygen. Figure 6.27 shows that in the case of the R = Nd and Pr materials the refined occupancies are well described by the 50 : 50 75 : 25 O : N distributions predicted for the local anion ordering. In the case of $NdVO_2N$, this is further supported by the stable monoclinic refinement and electron diffraction results. Any local anion ordering in the $LaVO_{2.11}N_{0.89}$ sample is less clear given that the refined anion occupancies lie close to the statistically averaged distribution. This may, however, be an artefact of strong correlations between parameters in the refinement and the significant presence of the rhombohedral perovskite phase in each of the data sets currently available for $LaVO_{2.11}N_{0.89}$.

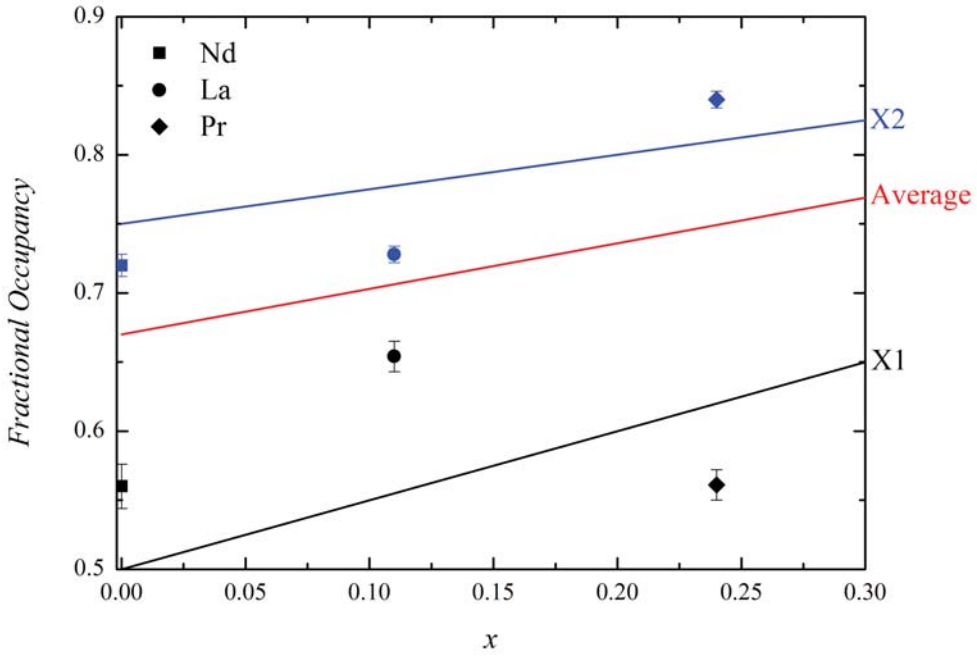

Figure 6.27 *Refined fractional occupancies for oxygen in the Pbnm model as a function of x in the $RVO_{2+x}N_{1-x}$ phases compared with the values expected for anion ordered and statistically averaged models.*

6.7 Conclusions

The local anion ordering principles established for the d^0 SrMO$_2$N perovskites [184] have been shown to be highly robust, resulting in M-N chains that remain separated into two-dimensional layers up to temperatures above 1000 °C. These anion ordering principles have also been extended here to the d^1 RVO$_2$N systems by means of a powder neutron diffraction study. Covalent, second-order Jahn-Teller interactions favour a *cis*-coordination of the more strongly bonded N^{3-} anions to the centre of the VO_4N_2 octahedra, which results in disordered V-N chains that propagate throughout the structure. This local ordering results in a 50 : 50 O : N distribution within the zig-zag layers and 100 : 0 O : N at the inter-layer sites, which lowers the symmetry of the rotationally ordered *Pbnm* perovskite superstructure to monoclinic $P112_1/m$. The refinement of the high resolution time-of-flight neutron diffraction data collected for the novel oxynitride NdVO$_2$N phase in the $P112_1/m$ model with $\gamma = 90.07(1)°$ confirms the subtle monoclinic lattice distortion resulting from anion order. The same mechanism is also apparent within the PrVO$_{2.24}$N$_{0.76}$ system, which was refined successfully in

the *Pbnm* model with O : N distributions close to the ideal 50 : 50 and 75 : 25 values expected for the anion ordered model. In the case of $LaVO_{2.11}N_{0.89}$, the local anion ordering is not immediately obvious with the current data, which contain a significant contribution from a coexisting rhombohedral oxynitride perovskite phase.

In order to further validate the anion ordering principles in these oxynitride perovskites it will be important to make use of local structural probes. For instance pair distribution function analysis of total neutron scattering data should unambiguously confirm the local anion order, making use of the contrast between V-O and V-N bond lengths [194]. It will also be interesting to perform a high temperature neutron diffraction study in order to determine the nature of the high temperature structural phases of the R = Nd and Pr materials and in the case of the R = La system, at what temperature the orthorhombic perovskite phase appears from the high temperature rhombohedral phase. It will be important to establish the anion ordering mechanism of the high temperature RVO_2N phases and how this relates to the low temperature rotationally ordered superstructures.

Chapter 7

Conclusions

This Thesis has reported the synthesis and study of several geometrically frustrated magnetic materials, including novel oxyfluoride and oxynitride materials. In addition, a discussion of the anion ordering principles in such mixed anion systems was given. This final Chapter aims to provide a summary of the main experimental results and conclusions that can be drawn from the work presented here, in addition to a brief outlook of future research prospects.

In Chapter 3, the spin glass ground state of the geometrically frustrated $S = 1$ pyrochlore, $Lu_2Mo_2O_7$, was investigated. It was discovered that $Lu_2Mo_2O_7$ undergoes a spin freezing transition at $T_f \sim 16$ K, which was initially observed from a bifurcation of ZFC and FC magnetic susceptibilities. The AC response of the system about this transition follows conventional spin glass dynamics. The spin freezing transition is further confirmed by a sharp transition in the muon spin relaxation rate. Powder neutron diffraction data confirm the absence of long range magnetic order in the spin glass regime and neutron polarisation analysis reveals the presence of competing nearest- and next-nearest neighbour Mo-Mo spin correlations that persist up to at least 300 K. Importantly, the low temperature magnetic heat capacity of $Lu_2Mo_2O_7$ follows a T^2-dependence. This has not been observed in polycrystalline samples of the related pyrochlore $Y_2Mo_2O_7$ but was recently measured on the first single crystal of this widely studied material [113]. Further investigation of $Lu_2Mo_2O_7$ will be important, in particular, the origin of the spin glass behaviour such as lattice distortions, which may be more evident in this system than in other members of the rare earth molybdate pyrochlore series given the small ionic radius of Lu^{3+}. The spin

glass state is sensitive to oxygen vacancy disorder, with an oxygen deficiency of ∼6 % leading to an increase in frustration and spin freezing temperature [195].

The synthesis and initial study of a new oxynitride pyrochlore phase $Lu_2Mo_2O_{4.8}N_{1.7}$ is outlined in Chapter 4. By incorporating the N^{3-} nitride anion into the $Lu_2Mo_2O_7$ structure, such that the molybdenum cations are oxidised towards the Mo^{5+} $4d^1$ oxidation state, it is expected that quantum fluctuations will become increasingly important in determining the ground state properties of the material. The magnetic susceptibility data collected for $Lu_2Mo_2O_{4.8}N_{1.7}$ revealed an absence of spin freezing down to 2 K despite strong antiferromagnetic exchange, $\theta = -121$ K. Furthermore, the elastic magnetic scattering cross section measured by neutron polarisation analysis is extremely small, which implies that the majority of the magnetic neutron scattering at low temperatures is inelastic. It is hoped that a temperature dependent inelastic survey of the material of the Cold Neutron Chopper Spectrometer at the Spallation Neutron Source of the Oak Ridge National Laboratory will help to clarify the low temperature nature of $Lu_2Mo_2O_{4.8}N_{1.7}$. It can be concluded for the T-linear behaviour in the low temperature magnetic heat capacity of $Lu_2Mo_2O_{4.8}N_{1.7}$ that there is a large density of low energy levels within the excitation spectrum and an absence of magnetic ordering down to 500 mK. This puts forward an argument for the exciting prospect that $Lu_2Mo_2O_{4.8}N_{1.7}$ may be a good candidate for a three-dimensional spin liquid material.

Chapter 5 presents the low temperature magnetic study of the $S = \frac{1}{2}$ vanadium oxyfluoride kagome antiferromagnet, DQVOF. Magnetization against field and field dependent heat capacity data revealed the free-ion paramagnetic behaviour of the $S = 1$ V^{3+} cations that reside between the $S = \frac{1}{2}$ V^{4+} kagome planes. As such, DQVOF is confirmed as an experimental realisation of a two-dimensional $S = \frac{1}{2}$ antiferromagnet. μSR confirms the absence of spin freezing in the DQVOF system down to 40 mK. The T-linear behaviour of the low temperature heat capacity and its lack of field dependence implies that DQVOF forms a gapless quantum critical phase at low temperatures [196]. The data do not show any evidence for a spin gap at $0.13J \sim 8$ K that was recently predicted for gapped Z_2 spin liquids on the kagome lattice. It will be extremely useful to measure the thermal conductivity of DQVOF, which will reveal the nature of the low energy excitation spectrum without the complication of the Schottky anomaly that plagues the low temperature heat capacity. Furthermore, an inelastic neutron scattering study should be carried out in attempt to observe the nature of the

excitations from the spin liquid ground state in DQVOF. Before this can be performed, there are several materials chemistry issues that must be overcome, such as sample scale up and deuteration.

In the final results chapter, a discussion of the anion ordering in several oxynitride perovskites was given. The ordering of mixed anion systems is important to understand given that it can have consequences on a material's electronic and magnetic properties. Here, the anion ordering principles initially discovered for the d^0 $SrMO_2N$ (M = Nb, Ta) perovskites were shown to persist up to temperatures of 1100 $^\circ$ through a high temperature high resolution neutron diffraction study. Furthermore, they were shown to be robust to electron doping in the d^1 system $NdVO_2N$ [188] and the related $RVO_{2+x}N_{1-x}$ (R = La, Pr) analogues. The R = La based material also provides the first example of a rhombohedral oxynitride perovskite phase. The local anion ordering observed in these materials leads to disordered, two-dimensional V-N chains that propagate through the perovskite structure, providing a physical realisation of the statistical self-avoiding walk model. Future study of these materials will include an investigation of the anion ordering with local structural probes, such as neutron pair distribution function analysis.

Appendix A

Reprint of Publications

Anion-ordered Chains in a d^1 perovskite oxynitride: $NdVO_2N$

J. Oró-Solé, L. Clark, W. Bonin, J. P. Attfield and A. Fuertes.

Chemical Communications, vol. 49, pp. 2430 - 2432, 2013.

Oxygen miscibility gap and spin glass formation in the pyrochlore $Lu_2Mo_2O_7$

L. Clark, C. Ritter, A. Harrison and J. P. Attfield.

Journal of Solid State Chemistry, vol. 203, pp. 199 - 203, 2013.

Gapless spin liquid ground state in the $S = \frac{1}{2}$ kagome antiferromagnet $[NH_4]_2[C_7H_{14}N][V_7O_6F_{18}]$

L. Clark, J. C. Orain, F. Bert, M. A. de Vries, F. H. Aidoudi, R. E. Morris, P. Lightfoot, J. S. Lord, M. T. F. Telling, P. Bonville, J. P. Attfield, P. Mendels and A. Harrison.

Physical Review Letters, vol. 110, p. 207208, 2013.

ChemComm

RSC Publishing

COMMUNICATION

View Article Online
View Journal | View Issue

Anion-ordered chains in a d^1 perovskite oxynitride: $NdVO_2N$†

Cite this: *Chem. Commun.*, 2013, **49**, 2430

Received 5th December 2012,
Accepted 5th February 2013

DOI: 10.1039/c3cc38736d

www.rsc.org/chemcomm

Judith Oró-Solé,[a] Lucy Clark,[b] William Bonin,[a] J. Paul Attfield*[b] and Amparo Fuertes*[a]

The correlated anion order in the oxynitride perovskite $NdVO_2N$, where disordered zig-zag VN chains segregate into planes within a pseudo-cubic lattice, is similar to that in materials such as $SrTaO_2N$ containing d^0 transition metal cations. However, $NdVO_2N$ has $3d^1$ V^{4+} cations and the 3d-electrons are itinerant, showing that the anion chain order in oxynitride perovskites is robust to electron-doping.

The d^n electron configurations of transition metal cations have a profound influence on the properties of their solid compounds. d^0 phases are typically wide-bandgap insulators, and off-centre (locally acentric) cation displacements resulting from second order Jahn–Teller (SOJT) effects can give rise to ferroelectricity. In contrast, materials with $n > 0$ electrons often show magnetic and conducting phenomena, and centric first order Jahn–Teller (FOJT) distortions for degenerate d^n configurations. An unusual correlated anion order driven by d^0 effects was recently discovered in oxynitride perovskites of high valent transition metals.[1] These AMO_2N or $AMON_2$ materials are insulators with notable optical, photocatalytic, and dielectric properties.[2,3] Although a full long-range anion order is not observed in these materials, the recent neutron and electron diffraction analysis of $SrMO_2N$ (M = Nb, Ta)[1] showed that well-defined *cis*-MO_4N_2 octahedra are present, resulting in disordered zig-zag MN chains that segregate into two-dimensional perovskite layers. Covalent SOJT type d^0 effects favour the local *cis*-MN_2O_4 configurations, as nitride is more strongly bonded to the M cations than oxide. Unusual sub-extensive configurational entropies that vary with particle size and tend to zero per atom in macroscopic samples are predicted for these correlated anion orders.[4]

Non-stoichiometry can introduce electron carriers into oxynitride perovskites, giving rise to notable electronic transport properties such as thermoelectricity in $SrMoO_{2-x}N_{1+x}$[5] and colossal magnetoresistances (CMR) in $EuNbO_{2+x}N_{1-x}$[6] and $EuWO_{1+x}N_{2-x}$.[7,8] To discover whether the above anion order is stable to electron doping, we have explored stoichiometric d^1 materials, and we describe here the synthesis, magnetic properties and structure of a new oxynitride $NdVO_2N$ containing $3d^1$ V^{4+}. Oxynitride perovskites were previously reported in the related $LaVO_{3-x}N_x$ system, but the reported samples had a maximum N content of $x = 0.9$.[9]

$NdVO_2N$ was prepared by treating $NdVO_4$ precursors under NH_3 at a flow rate of 600 cm^3 min^{-1} at 700 °C for 80 hours with one intermediate regrinding. The colour of the new compound is black. Combustion analysis for the sample used for neutron diffraction gave a nitrogen content of 1.02 moles per formula unit. The X-ray diffraction pattern was indexed in an orthorhombic perovskite supercell of dimensions a = 5.4596(7), b = 5.5002(6) and c = 7.7264(1) Å with space group *Pbnm* (see ESI†).

The magnetic susceptibility of $NdVO_2N$ measured in a 1 T field shows paramagnetic behavior down to 2 K (Fig. 1), with no evidence of a spin ordering transition. The inverse susceptibility has a significant curvature, indicating that both Curie–Weiss and temperature-independent paramagnetic contributions are present, and was fitted as $\chi^{-1} = [C/(T - \theta) + \chi_0]^{-1}$.

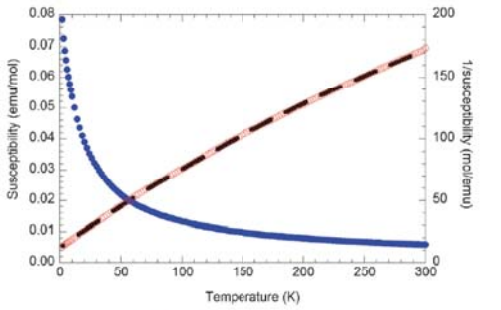

Fig. 1 Magnetic susceptibility (closed points) and inverse susceptibility (open points) for $NdVO_2N$. The fit of the function described in the text to the inverse susceptibility is shown as a broken line.

[a] *Institut de Ciència de Materials de Barcelona (ICMAB-CSIC), Campus UAB, 08193 Bellaterra, Spain. E-mail: amparo.fuertes@icmab.es; Fax: +34 935805729; Tel: +34 935801853*

[b] *CSEC and School of Chemistry, University of Edinburgh, King's Buildings, Mayfield Road, Edinburgh EH9 3JZ, UK. E-mail: j.p.attfield@ed.ac.uk; Fax: +44 (0)1316517049; Tel: +44 (0)1316517229*

† Electronic supplementary information (ESI) available: Details of the synthesis, analysis, structural characterisations, and property measurements. See DOI: 10.1039/c3cc38736d

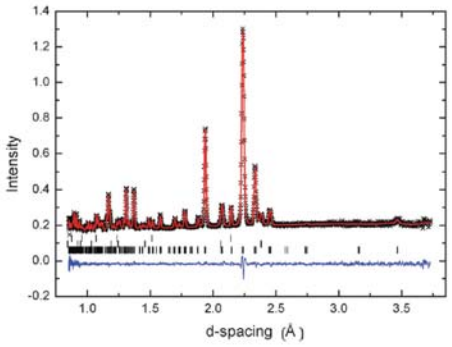

Fig. 2 Fit of the monoclinic $P112_1/m$ model for $NdVO_2N$ to powder neutron diffraction data from the 90° detector bank of instrument HRPD. Reflection markers from bottom to top are for $NdVO_2N$, a small amount of V(O,N) impurity phase, and scattering from the V sample holder.

The Curie–Weiss parameters (C = 1.37 emu K mol^{-1}, corresponding to a paramagnetic moment of 3.32 μ_B, and θ = −17 K) describe localised 4f^3 Nd^{3+} moments (ideal value 3.62 μ_B) with weak antiferromagnetic interactions. The large χ_0 = 0.0015 emu mol^{-1} term reveals Pauli paramagnetism from correlated itinerant V^{4+} 3d^1 electron spins.

Powder neutron diffraction data for a 350 mg $NdVO_2N$ sample (Fig. 2) were recorded at room temperature on a high-resolution diffractometer HRPD at the ISIS spallation source, Rutherford Appleton Laboratory, UK. Neutron profile refinements of the structural models and texture analysis were performed with the General Structure Analysis System (GSAS) software.[10]

The observed neutron diffraction peaks of $NdVO_2N$ were consistent with an orthorhombic $\sqrt{2} \times \sqrt{2} \times 2$ superstructure of a cubic perovskite cell having space group *Pbnm*. This $GdFeO_3$-type superstructure is common in perovskites and results from two ordered tilts of the transition metal coordination octahedra. Distinct axial (Y1) anion sites, close to the *c*-axis, and equatorial (Y2) sites, near the *ab*-plane, are present in a 1:2 ratio. Refinement of their O/N occupancies subject to the overall composition gave values of 0.55(2)/0.45 and 0.73(1)/0.27, respectively. These occupancies are very close to those observed in $SrMO_2N$ (M = Nb, Ta)[1] and evidence the same formation of *cis*-nitride chains as follows.

Disordered –M–N– chains with a 90° turn at M exist within perovskite layers in $SrMO_2N$ and lead to statistical 0.5 O/0.5 N populations at the two anion sites in the layers and full 1.0 O occupancy at the third site between layers. The *c*-axis of the tilted *Pbnm* superstructure lies in the anion-chain layers so that the axial Y1 O/N population is 0.5/0.5, and the equatorial Y2 population is averaged over in-chain-layer 0.5/0.5 and out-of-chain-layer 1.0/0 sites, giving 0.75/0.25 occupancy. The proximity of the refined anion site populations in $NdVO_2N$ to these ideal values demonstrates that *cis*-VN chains are formed in the latter d^1 material.

A corollary of the anion-chain model is that the true space group symmetry of $NdVO_2N$ is lower than *Pbnm* because the equatorial Y2 sites are averaged over two anion positions with inequivalent (0.5/0.5 and 1.0/0) O/N occupancies. Breaking the equivalence of these sites lowers symmetry to monoclinic $P112_1/m$ (a non-standard setting of $P2_1/m$) with cell angle $\gamma \neq 90°$.

Table 1 Atomic coordinates, anion site occupancies, and V–O/N bond distances for $NdVO_2N$ refined in $P112_1/m$ with *Pbnm* constraints

Site	*x*	*y*	*z*	O/N
Nda	0.0051(7)	0.0340(4)	0.25	
Ndb	0.4949	0.5340	0.25	
Va	0.5	0.0	0.0	
Vb	0.0	0.5	0.0	
Y1a	0.9348(6)	0.4864(4)	0.25	0.60(2)/0.40
Y1b	0.5652	0.9864	0.25	0.60(2)/0.40
Y2a	0.2838(4)	0.2890(4)	0.0382(3)	0.90(3)/0.10
Y2b	0.2162	0.7890	0.4618	0.50/0.50

Bond	Distance (Å)	Bond	Distance (Å)
Va–Y1b (×2)	1.968(1)	Vb–Y1a (×2)	1.968(1)
Va–Y2a (×2)	2.004(2)	Vb–Y2a (×2)	1.961(2)
Va–Y2b (×2)	1.959(2)	Vb–Y2b (×2)	2.002(2)

Estimated standard deviations in parentheses are shown once for each independent variable. Pairs of sites ending 'a' and 'b' are equivalent in the parent *Pbnm* structure and their coordinates were constrained accordingly. O/N occupation factors at the anion sites Y were refined subject to the ideal stoichiometry, and with equal occupancies at the Y1a and Y1b sites. Refined isotropic U-factors were 0.0009(3) Å^2 for metal atoms and 0.0067(3) Å^2 for anions. Refined cell parameters were a = 5.4645(3) Å, b = 5.5030(3) Å, c = 7.7352(4) Å, γ = 90.072(9)°.

We attempted to refine the $P112_1/m$ model but the monoclinic lattice distortion was found to be very small (γ = 90.07°), so it was not possible to refine the full structure. However, by constraining the atomic coordinates to have *Pbnm* pseudosymmetry, a refinement of split Y2-site occupancies converged, giving the results shown in Table 1. The refined Y2a and Y2b O/N occupancies of 0.90/0.10 and 0.50/0.50 are in excellent agreement with the prediction. Hence, the neutron analysis evidences a very small monoclinic distortion of the pseudo-*Pbnm* perovskite superstructure of $NdVO_2N$ driven by the anion-chain order.

Independent evidence for the lowering of symmetry was obtained from electron diffraction patterns of individual $NdVO_2N$ crystallites of the powder. Many grains were twinned, but patterns from $\langle 110 \rangle_p$ zone axes of the cubic perovskite subcell were successfully obtained by tilting around the c^*-axis of single-domain crystallites (Fig. 3). These show additional weak reflections that result from loss of the glide planes, as symmetry is lowered from *Pbnm* to $P112_1/m$,[11] consistent with the neutron results. Double diffraction reflections along [001]* were also observed in these patterns.

The crystal structure of $NdVO_2N$ is shown in Fig. 4. The octahedra are highly tilted with V–Y–V bond angles in the range 156–159°. The V–Y bond distances are slightly unequal, but similar differences are found in the *Pbnm* superstructures of $NdMO_3$ perovskites with non-degenerate ground state cations such as M = Cr^{3+} and Fe^{3+}, so they are most probably a consequence of the tilting distortions and do not necessarily evidence a FOJT effect from V^{4+}. A similar distribution of bond distances has been observed for metallic $CaVO_3$, which has *Pbnm* symmetry. The local order of O/N atoms into *cis*-VN chains within the crystallographically averaged $V(O_{0.5}N_{0.5})_2$ planes following the previously reported rules is shown on the right side in Fig. 4. Randomized left/right turns of the chains at the V sites lead to the statistical averaging of the anion site populations within these layers.

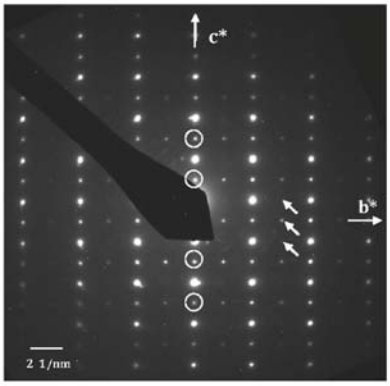

Fig. 3 Electron diffraction pattern from a $\langle 110 \rangle_p$ cubic subcell zone axis, equivalent to the [100] axis for the $\sqrt{2} \times \sqrt{2} \times 2$ superstructure of a single-domain $NdVO_2N$ crystallite. The presence of weak $0kl$; $k = 2n + 1$ reflections (diagonal arrows) shows that b-glide plane symmetry is broken, consistent with the descent from *Pbnm* to $P112_1/m$ due to the anion order. Double diffraction reflections $00l$; $l = 2n + 1$ are indicated by circles.

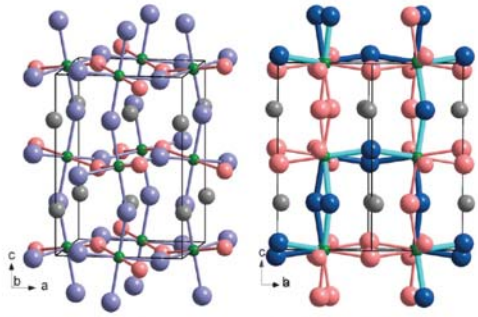

Fig. 4 The tilted perovskite superstructure of $NdVO_2N$ with Nd/V/O/$O_{0.5}N_{0.5}$/N sites shown as grey/green/pink/lilac/blue spheres. The left view shows the average $P112_1/m$ model with distinct O and $O_{0.5}N_{0.5}$ sites, and local ordering of O/N atoms at the latter sites to give *cis*-VN chains is shown at the right with chains in one layer highlighted.

The discovery of anion order characteristic of planes of *cis*-nitride chains in $NdVO_2N$ containing $3d^1$ V^{4+} is significant as this order has previously only been established in insulating materials based on d^0 ions. The chains in $NdVO_2N$ result from corner-sharing of *cis*-VO_4N_2 octahedra, which are stabilised by strong SOJT type covalent interactions in *cis*-VN_2 units. *cis*-MX_2 groups formed by covalent bonding of d^0 cations to two oxo or imido ligands X are very common in the coordination chemistry of high valent transition metals such as V^{5+} or Mo^{6+}. d^1 analogues are rarer and are not known for V^{4+}, but reported examples of *cis*-dioxomolybdenum(V) complexes[12] complement our observation that the *cis*-VN_2 geometry is preferred in $NdVO_2N$.

However, an important difference between *cis*-MX_2 units in molecular and extended solids is the possibility of itinerant electron behaviour in the latter case. AVO_3 perovskites and other V^{4+} oxides can show metallic and insulating properties. Perovskites of A = Ca, Sr, Cd and Mn are metallic without off-center V displacements, although a possible FOJT distortion was reported in $MnVO_3$.[13] However, a pronounced SOJT off-center distortion to form a short V–O vanadyl bond was observed in insulating $PbVO_3$[14] driven by cooperative displacements of lone pair Pb^{2+} cations. $NdVO_2N$ appears to have features from both types of V^{4+} perovskite – the observed anion order implies that SOJT type covalent V–N interactions are significant, but the observed Pauli paramagnetism shows that the system is metallic, like most AVO_3 and electron-doped oxynitride perovskites. The *cis*-VO_4N_2 geometry is evidently robust to dopings into π^*-bands formed from V:t_{2g} and O:$2p_\pi$ orbitals of at least 1/6 electrons per V–O/N bond. It will be interesting to explore whether the anion order persists at higher electron concentrations, and in insulating d^1 analogues, if these can be synthesised. Spin and orbital states of localised d-electrons could be coupled to the O/N and octahedral tilt orders in the latter case, enabling novel electronic and magnetic properties to emerge.

In conclusion, this study has demonstrated that the structure of $NdVO_2N$ contains layers of spontaneously segregated *cis*-nitride chains, like those in $SrTaO_2N$ and other d^0 oxynitride perovskites. The underlying formation of *cis*-VO_4N_2 octahedra is thus stable in the presence of the d^1 cation V^{4+}. The 3d-electrons are itinerant in this material, so a future challenge is to design and explore the properties of perovskite oxynitrides in which spin and orbital states of localised d-electrons may be coupled to the O/N and octahedral tilt orders.

We thank Dr Kevin Knight for assistance with neutron data collection at ISIS. This work was supported by the Spanish Ministerio de Economía y Competitividad, Spain (Projects MAT2011-24757 and SAB2011-0047) and EPSRC, the Leverhulme Trust and the Royal Society, UK.

Notes and references

1 M. Yang, J. Oró-Solé, J. A. Rodgers, A. B. Jorge, A. Fuertes and J. P. Attfield, *Nat. Chem.*, 2011, **3**, 47.
2 A. Fuertes, *J. Mater. Chem.*, 2012, **22**, 3293.
3 S. G. Ebbinghaus, H.-P. Abicht, R. Dronskowski, T. Müller, A. Reller and A. Weidenkaff, *Prog. Solid State Chem.*, 2009, **37**, 173.
4 P. J. Camp, A. Fuertes and J. P. Attfield, *J. Am. Chem. Soc.*, 2012, **13**, 6762.
5 D. Logvinovich, R. Aguiar, R. Robert, M. Trottmann, S. G. Ebbinghaus, A. Reller and A. Weidenkaff, *J. Solid State Chem.*, 2007, **180**, 2649.
6 A. B. Jorge, J. Oró-Solé, A. M. Bea, N. Mufti, T. T. M. Palstra, J. A. Rodgers, J. P. Attfield and A. Fuertes, *J. Am. Chem. Soc.*, 2008, **130**, 12572.
7 A. Kusmartseva, M. Yang, J. Oró-Solé, A. M. Bea, A. Fuertes and J. P. Attfield, *Appl. Phys. Lett.*, 2009, **95**, 02110.
8 M. Yang, J. Oró-Solé, A. Kusmartseva, A. Fuertes and J. P. Attfield, *J. Am. Chem. Soc.*, 2010, **132**, 4822.
9 P. Antoine, R. Assaba, P. L'Haridon, R. Marchand, Y. Laurent, C. Michel and C. B. Raveau, *Mater. Sci. Eng.*, 1989, **B5**, 43–46.
10 A. C. Larson and R. B. Von Dreele, *Los Alamos National Laboratory Report No LAUR*, 1994, pp. 86–748.
11 D. I. Woodward, P. L. Wise, W. E. Lee and I. M. Reaney, *J. Phys.: Condens. Matter*, 2006, **18**, 2401.
12 X.-M. Lu, J.-F. Lu and X. A. Mao, *Chin. J. Chem.*, 2002, **20**, 617.
13 M. Markkula, A. M. Arevalo-Lopez, A. Kusmartseva, J. A. Rodgers, C. Ritter, H. Wu and J. P. Attfield, *Phys. Rev. B: Condens. Matter Mater. Phys.*, 2011, **84**, 094450.
14 (*a*) R. V. Shpanchenko, V. V. Chernaya, A. A. Tsirlin, P. S. Chizhov, D. E. Sklovsky, E. V. Antipov, E. P. Khlybov, V. Pomjakushin, A. M. Balagurov, J. E. Medvedeva, E. E. Kaul and C. Geibel, *Chem. Mater.*, 2004, **16**, 3267; (*b*) A. A. Belik, M. Azuma, T. Saito, Y. Shimakawa and M. Takano, *Chem. Mater.*, 2005, **17**, 269.

Journal of Solid State Chemistry 203 (2013) 199–203

Contents lists available at SciVerse ScienceDirect

Journal of Solid State Chemistry

journal homepage: www.elsevier.com/locate/jssc

Oxygen miscibility gap and spin glass formation in the pyrochlore $Lu_2Mo_2O_7$

L. Clark [a], C. Ritter [b], A. Harrison [a,b], J.P. Attfield [a,*]

[a] Centre for Science at Extreme Conditions and School of Chemistry, University of Edinburgh, King's Buildings, Mayfield Road, Edinburgh EH9 3JZ, United Kingdom
[b] Institut Laue Langevin, 6 rue Jules Horowitz, 38042 Grenoble Cedex 9, France

ARTICLE INFO

Article history:
Received 15 March 2013
Received in revised form
11 April 2013
Accepted 13 April 2013
Available online 25 April 2013

Keywords:
Pyrochlore oxides
Frustrated magnets
Phase separation

ABSTRACT

Rare earth (R) molybdate pyrochlores, $R_2Mo_2O_7$, are of interest as frustrated magnets. Polycrystalline samples of $Lu_2Mo_2O_{7-x}$ prepared at 1600 °C display a coexistence of cubic pyrochlore phases. Rietveld fits to powder neutron diffraction data and chemical analyses show that the miscibility gap is between a stoichiometric $x=0$ and an oxygen-deficient $x\approx0.4$ phase. $Lu_2Mo_2O_7$ behaves as a spin glass material, with a divergence of field cooled and zero field cooled DC magnetic susceptibilities at a spin freezing temperature $T_f=16$ K, that varies with frequency in AC measurements following a Vogel–Fulcher law. $Lu_2Mo_2O_{6.6}$ is more highly frustrated spin glass and has $T_f=20$ K.

1. Introduction

The phenomenon of geometrically frustrated magnetism arises in materials with magnetic lattices built up from antiferromagnetically interacting spins on triangular or tetrahedral units. Such geometry renders the simultaneous satisfaction of each pairwise magnetic exchange interaction impossible to achieve, such that geometrically frustrated magnets (GFMs) are able to evade classical long-range antiferromagnetic order upon cooling. Instead, GFMs often display unusual liquid or glass like magnetic behavior at low temperatures [1]. Geometric frustration on the cubic pyrochlore lattice, $A_2B_2X_7$, which consists of two interlinking networks of corner-sharing cation tetrahedra, has been of great interest in recent years as the host for many intriguing phenomena, such as the spin and charge ice ground states and the possible emergence of magnetic monopoles [2–4].

The rare earth (R) molybdate pyrochlores, $R_2Mo_2O_7$, are an interesting family of materials whose electronic and magnetic properties are known to depend strongly upon lattice effects, such as the size of the ionic radius of the R^{3+} cation on the A-site sub-lattice [5]. It is well reported that for the smaller rare earths ($R^{3+}<1.06$ Å), insulating antiferromagnetic interactions are dominant, resulting in a frustrated spin-glass like ground state. Less understood, however, is the effect that oxygen non-stoichiometry has over the properties of the $R_2Mo_2O_7$ series and in particular the spin glass-like ground state. Rietveld analyses of powder diffraction data have previously been reported to show no deviation from full oxygen occupancy in the average crystalline structure of the spin glass pyrochlores, which gives an upper limit of ~1% for oxygen non-stoichiometry [6]. However, a systematic study of the geometrically frustrated spin glass $LiCrMnO_{4-\delta}$ spinels revealed that a deviation from oxygen stoichiometry as small as 0.63% can have a profound effect on the magnetic properties of the spin glass state [7].

A well-studied member of the $R_2Mo_2O_7$ series is $Y_2Mo_2O_7$, which contains non-magnetic Y^{3+} and $4d^2$ $S=1$ Mo^{4+} cations, and displays many of the characteristics typical of glassy systems [8–10]. It has long been established that the canonical spin-glass materials, such as magnetically dilute metal alloys, are a result of the combination of randomness, through site or bond disorder, and magnetic frustration [11]. In the case of $Y_2Mo_2O_7$, the frustration clearly arises from the geometric frustration of the pyrochlore lattice but the cause of disorder or lattice distortion in this material that results in spin freezing is an open and active area of research that has prompted the use of several local structure probes [12–15]. A material that may shed further light on this issue is $Lu_2Mo_2O_7$, based on non-magnetic Lu^{3+}, the smallest cation in the rare earth series, and is therefore expected to be another uncommon example of a spin-glass in a material with no evident source of structural disorder. Early work discusses the synthesis of $Lu_2Mo_2O_7$ to a limited extent [16,17], but to the best of our knowledge, the magnetic properties of $Lu_2Mo_2O_7$ have not been reported previously. We have discovered coexistence of two pyrochlore phases, apparently related to an oxygen deficiency in the $Lu_2Mo_2O_7$ system and we discuss the effects on the magnetic properties of the spin glass ground state.

2. Experimental section

Polycrystalline $Lu_2Mo_2O_7$ was prepared by solid state reaction of stoichiometric ratios of pelletized Lu_2O_3 and MoO_2 heated to

* Corresponding author. Fax: +44 131 651 7049.
E-mail address: j.p.attfield@ed.ac.uk (J.P. Attfield).

0022-4596/$ - see front matter © 2013 Elsevier Inc. All rights reserved.
http://dx.doi.org/10.1016/j.jssc.2013.04.012

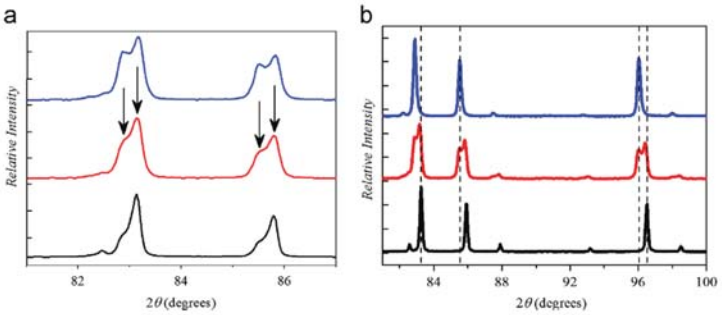

Fig. 1. Selected regions of powder X-ray diffraction profiles for $Lu_2Mo_2O_7$ samples. (a) Patterns for three samples heated at 1600 °C for 12 h under flowing Ar with a Mo-power oxygen getter. The arrowed components of the peaks evidence the two pyrochlore phases; changing phase proportions illustrate the effect of increasing separation of sample and getter during synthesis (from top to bottom sample).(b) Profiles for single phase samples at top and bottom, with a two phase pattern shown in the center.

1600 °C for 12 h under flowing argon gas with intermediate regrinding and repelletizing. A molybdenum powder oxygen getter was employed to prevent the oxidation of the MoO_2 precursor to more volatile MoO_3. The metal powder getter was contained in a separate alumina crucible adjacent to the sample pellet. Powder X-ray diffraction of initial samples revealed that two pyrochlore phases are present (Fig. 1), suggesting that a miscibility gap is present in the $Lu_2Mo_2O_{7-x}$ system at 1600 °C. The cubic lattice parameters, a, of the two phases consistently refine to 10.14 Å and 10.17 Å by Rietveld analysis of the X-ray data, however, the relative amount of each phase appears to depend upon the separation of the sample and the oxygen getter during synthesis. A single pyrochlore phase with lattice constant $a=10.14$ Å was prepared by increasing the distance between sample and getter crucibles to ~10 cm. A single phase sample of the $a=10.17$ Å phase was prepared by reducing the $a=10.14$ Å phase in flowing H_2 at 600 °C for 2 h. This suggests that the cause of the phase separation is related to the oxygen content of the pyrochlore phases. The more reduced sample has the larger lattice constant, consistent with the larger ionic radius of Mo^{3+} (0.69 Å) compared to that of Mo^{4+} (0.65 Å).

Oxygen contents of the two pyrochlore phases were obtained from gravimetric analysis. Heating the $a=10.14$ Å phase in air at 750 °C for 2 h resulted in complete oxidation of the sample to give Lu_2O_3 and MoO_3. The weight increase of 4.9(4) % corresponds to a chemical composition of $Lu_2Mo_2O_{7.00(1)}$, confirming that this phase is oxygen-stoichiometric $Lu_2Mo_2O_7$. A weight loss of 1.03(1)% was observed upon reduction of this sample to the $a=10.17$ Å phase giving a chemical composition of $Lu_2Mo_2O_{6.58(1)}$ for the reduced phase.

Powder neutron diffraction data were collected on the high resolution powder diffractometer D2B with a neutron wavelength $\lambda=1.594$ Å at the high flux reactor of the Institut Laue Langevin, France. Rietveld refinements were performed using the GSAS program using the cubic *Fd-3m* pyrochlore model. Magnetic susceptibilities were measured in a Quantum Design SQUID magnetometer. DC susceptibilities were measured in an applied field of 1 T. AC susceptibilities were measured in an oscillating field of 3.5×10^{-4} T at measuring frequencies ω from 5 to 1053 Hz.

3. Results and discussion

Fig. 2 displays the Rietveld plots obtained from a joint refinement of the neutron diffraction data collected at 300 K for samples of $Lu_2Mo_2O_7$ and $Lu_2Mo_2O_{7-x}$. A simultaneous refinement of both models against both data sets was performed in order to minimize correlation between atomic occupancies and thermal parameters. The oxygen site occupancies of the $Lu_2Mo_2O_7$ phase were fixed according to the gravimetric analysis, but allowed to refine for $Lu_2Mo_2O_{7-x}$, while isotropic thermal parameters were constrained to be the same for both phases. The results, summarized in Table 1, reveal that the O′ sites have a high concentration of defects whereas the O sites are almost fully occupied. The refined oxygen content of 6.69(6) agrees with the gravimetrically determined value of 6.58(1); the reduced $a=10.17$ Å phase is thus described as $Lu_2Mo_2O_{6.6}$.

Pyrochlores are known to tolerate considerable anion deficiencies. In some cases, such as $Pb_2Ru_2O_{6.5}$, vacancy ordering on the O′ site results in the lowering of symmetry from *Fd-3m* to subgroup *F-43m* [18]. However, other oxygen-deficient materials including $Bi_2Ru_2O_{6.9}$ and $Tl_2Ru_2O_{6.7}$ retain *Fd-3m* symmetry with statistically disordered anion vacancies over the O′ site [19], and the same structure is observed here for $Lu_2Mo_2O_{6.6}$ with no evidence for a vacancy-ordered superstructure in the neutron data. Oxygen-vacancy order is difficult to predict in general and depends on details of specific systems, for example, vacancies are ordered in perovskite layers of T′-type $Nd_4Cu_2O_7$ [20], but are disordered in T-type $La_4Li_2O_7$ [21].

Oxygen-content miscibility gaps are observed in some transition metal oxide systems, for example, between insulating and superconducting $La_2CuO_{4+\delta}$ phases [22]. However miscibility gaps are less common in pyrochlores and have not been reported previously for $R_2Mo_2O_{7-x}$ systems, although a gap was found between $Eu_2Mo_2O_7$ and the derived $Eu_2Mo_2(O,N)_{7-x}$ oxynitride pyrochlore [23]. Phase coexistence driven by cation segregation has been observed in mixed A-cation pyrochlores such as $(Bi_{0.6}Y_{1.4})Sn_2O_7$ [24].

Fig. 2(c) shows the difference between neutron diffraction data at 1.5 K and 50 K in the low 2θ region for $Lu_2Mo_2O_7$. The absence of magnetic Bragg scattering demonstrates that there is no long range spin order down to at least 1.5 K. The DC magnetic susceptibility of $Lu_2Mo_2O_7$ is shown in Fig. 3(a). The data display a clear divergence of field cooled (FC) and zero field cooled (ZFC) susceptibilities at a spin freezing temperature $T_f=16.2$ K, characteristic of the onset of an irreversible glass-like state. A Curie–Weiss fit to high temperature inverse susceptibility over the temperature range 150–300 K gives a Weiss constant $\theta=-158(1)$ K, indicating a dominance of antiferromagnetic exchange interactions. A comparison of the energy scales of magnetic interactions and spin freezing via the frustration index, $f=|\theta|/T_f\approx10$ implies that there is a significant frustration of spin order due to the geometrically frustrated pyrochlore network of antiferromagnetically interacting Mo^{4+} spins in $Lu_2Mo_2O_7$ [25]. An effective magnetic

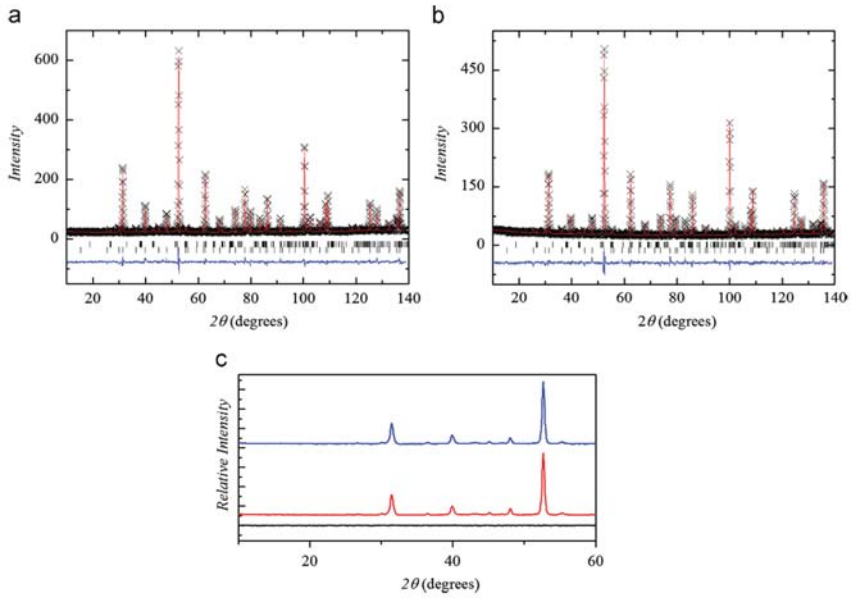

Fig. 2. (a) Rietveld fits to 300 K powder neutron diffraction data for $Lu_2Mo_2O_7$. Reflection marks are for the cubic *Fd*-3*m* pyrochlore phase (bottom) and MoO_2 impurity (top, 4% phase fraction). (b) Rietveld refinement of the reduced $Lu_2Mo_2O_{6.6}$ pyrochlore phase. (c) The difference (bottom) between powder neutron data collected at 1.5 K (top) and 50 K (middle) for $Lu_2Mo_2O_7$ in the low 2θ region, showing no accumulation of magnetic scattering upon cooling.

Table 1
Refined atomic coordinates and occupancies for $Lu_2Mo_2O_7$ (a=10.1478(1) Å) and (lower values where different) for $Lu_2Mo_2O_{6.69(6)}$ (a=10.1789(1) Å). Isotropic U-factors were 0.0091(2) Å^2 for metal cations and 0.0152(3) Å^2 for oxygen sites. Residuals for the combined refinement were R_{wp}=5.83%, and χ^2=6.9.

Atom	Site	x	y	z	Occupancy
Lu	16*d*	0.5	0.5	0.5	1.0
Mo	16*c*	0.0	0.0	0.0	1.0
O	48*f*	0.3417(1) 0.3477(1)	0.125	0.125	1.0 0.97(1)
O′	8*b*	0.375	0.375	0.375	1.0 0.87(2)

moment of μ_{eff}= 1.9 μ_B per Mo cation was obtained from the Curie–Weiss fit (C=0.892(3) K emu mol^{-1} formula unit^{-1}). The reduced effective moment compared with the expected spin only value for S=1 Mo^{4+} is due to significant spin–orbit coupling in this 4*d* transition metal system.

To confirm the spin-glass nature of $Lu_2Mo_2O_7$, AC magnetic susceptibilities were measured at frequencies, ω, of 5–1053 Hz. The data, displayed in Fig. 3(b), show an increase in the spin freezing temperature with increasing frequency. This behavior is typical for spin glasses; as frequency is increased the spin directions are less able to follow the oscillating field and so appear frozen at progressively higher temperatures. The magnitude of this shift, given by $(\Delta T_f/T_f)\Delta(\log\omega)$=0.008, is of the order observed in many classical spin-glass systems [26]. The variation of T_f with ω follows a Vogel–Fulcher law, a modified Arrhenius-type equation commonly associated with glassy dynamics [27], given by $\omega=\omega_0\ exp\ [-E_a/k_B(T_f - T_o)]$ where ω_0 is a characteristic frequency, E_a is an activation energy and the ideal glass temperature T_0 allows for spin–spin interactions. The fit shown in the inset to Fig. 3(b) gives $\ln(\omega_0/s^{-1})$=17.0(8), E_a/k_B=8.5(6) K and T_0= 15.300(5) K. The observation that $T_0 \approx T_f$ is considered representative of canonical spin-glasses.

The spin-glass behavior of $Lu_2Mo_2O_7$ is similar to that of $Y_2Mo_2O_7$, which shows frequency dependent AC magnetic susceptibility around its spin freezing transition, T_f~22 K.[10] $Tb_2Mo_2O_7$ also displays spin glass characteristics with T_f~25 K but the situation is complicated by the competition between ferromagnetic Tb–Tb interactions and antiferromagnetic Tb–Mo exchange [28] The other insulating $R_2Mo_2O_7$ analogs are less well studied in comparison, but $Ho_2Mo_2O_7$ has a reported freezing temperature of 21 K and $Yb_2Mo_2O_7$, based on the second smallest rare earth cation in the series has T_f≈18 K [29,30]. This suggests that there may be a trend for a decreasing spin glass transition temperature with decreasing ionic radius of R^{3+}. This is understandable from the variation of the Mo–O–Mo bond angle, α, that governs the magnitude and nature of the magnetic exchange between neighboring Mo^{4+} ions. The fit to the powder neutron diffraction data of $Lu_2Mo_2O_7$ gives α=125.08(9)°, whereas, the angle reported for $Y_2Mo_2O_7$ is somewhat larger, α=126.97° [8]. A systematic study of $R_2Mo_2O_7$ (R=Dy, Gd, Sm and Nd) revealed an increase in α across the spin glass to ferromagnet transition with α=127.7° in the spin glass $Dy_2Mo_2O_7$ to α=131.5° in ferromagnetic $Nd_2Mo_2O_7$ [31]. Fig. 4 shows a complete magnetic phase diagram for the $R_2Mo_2O_7$ pyrochlores (R=Nd–Lu) as a function of rare earth ionic radius [32]. The transition temperatures of other $R_2Mo_2O_7$ materials are taken from various reports [8,28–30,33]. The spin freezing and ferromagnetic transitions show comparable rates of change with R^{3+} radius, as both are controlled by the variation of Mo–O–Mo angle.

Susceptibility data for the reduced $Lu_2Mo_2O_{6.6}$ phase are qualitatively similar to those for $Lu_2Mo_2O_7$, but with significant changes in the underlying parameters. Fig. 3(c) shows the susceptibilities of both samples around the spin freezing transition, from

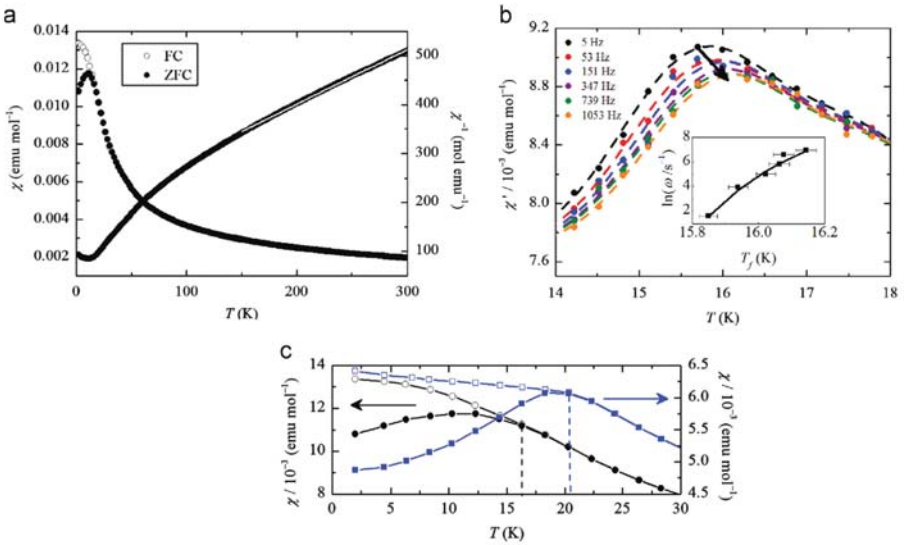

Fig. 3. (a) Magnetic and inverse susceptibilities of $Lu_2Mo_2O_7$ measured in a 1 T field with Curie–Weiss fit to high temperature inverse susceptibility data. (b) Real part of the AC susceptibility for $Lu_2Mo_2O_7$ showing the shift in T_f with measuring frequency. Inset shows Vogel–Fulcher fit of $\ln(\omega/s^{-1})$ against temperature. (c) Increase in spin freezing temperature, T_f, defined by the divergence of FC and ZFC susceptibilities from ~16 K in $Lu_2Mo_2O_7$ (left scale) to ~20 K in $Lu_2Mo_2O_{6.6}$ (right scale).

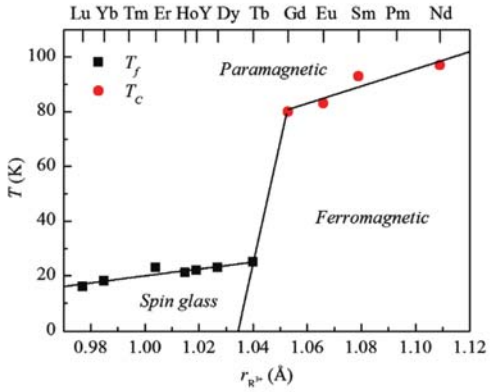

Fig. 4. The magnetic phase diagram for the $R_2Mo_2O_7$ pyrochlores showing the spin freezing, T_f, and ferromagnetic ordering, T_C, temperatures as a function of the rare earth ionic radii (r_R^{3+}, 8-fold coordination).

which a shift in T_f from 16.2 K to 20.3 K is observed. Hence the disorder created by introduction of oxygen vacancies enhances spin freezing. A Curie–Weiss fit to the inverse susceptibility over the same temperature range (150–300 K) gives an effective moment $\mu_{eff}=2.3\ \mu_B$, reflecting the partial reduction of $S=1$ Mo^{4+} to $S=3/2$ Mo^{3+}. The Weiss constant $\theta=-329(1)$ K shows that that the strength of superexchange interactions is enhanced, but the frustration factor of $f\approx16$ reveals that the disorder in $Lu_2Mo_2O_{7-x}$ markedly increases the degree of frustration in comparison to $Lu_2Mo_2O_7$.

The above results demonstrate that the oxygen content of $Lu_2Mo_2O_{7-x}$ has a significant effect on magnetic properties, as the energy scale of antiferromagnetic exchange, the spin freezing temperature, and the frustration factor are all increased in the reduced phase. This highlights the importance of the control of oxygen content in the $R_2Mo_2O_7$ series and the need for careful analysis of samples through diffraction and gravimetric techniques. In the case of $Lu_2Mo_2O_7$, the spin glass like state at low temperatures is stable in the absence of any significant site or bond disorder on a crystallographic length scale. $Lu_2Mo_2O_7$ may, therefore, provide an example of a disorder free or topological spin glass state [34,35]. Although structural disorder may not be a necessary condition for spin freezing in $Lu_2Mo_2O_7$, the oxygen-vacancy disorder in $Lu_2Mo_2O_{7-x}$ favors the onset of a glassy state at higher temperatures and enhances the degree of frustration. An oxygen miscibility gap might also drive electronic phase separation, as reported in the $Y_2Ti_2O_{7-x}$ system [36]. Future study of the spin glass ground states in the $Lu_2Mo_2O_{7-x}$ system will be of great importance in order to further understand how they compare to the canonical spin glasses and to determine the origin of their spin freezing.

Acknowledgments

The authors acknowledge EPSRC, STFC, Leverhulme Trust, the Royal Society, and University of Edinburgh for funding and facilities access.

References

[1] J.E. Greedan, J. Mater. Chem. 11 (2001) 37.
[2] S.T. Bramwell, M.J.P. Gingras, Science 29 (2001) 1495.
[3] R. Seshadri, Solid State Sci. 8 (2006) 259.
[4] T. Fennell, P.P. Deen, A.R. Wildes, K. Schmalzl, D. Prabhakaran, A.T. Boothroyd, R.J. Aldus, D.F. McMorrow, S.T. Bramwell, Science 326 (2009) 415.
[5] N. Hanasaki, K. Watanabe, T. Ohtsuka, I. Kézsmárki, S. Iguchi, S. Miyasaka, Y. Tokura, Phys. Rev. Lett. 99 (2007) 086401.
[6] J.S. Gardner, B.D. Gaulin, S.-H. Lee, C. Broholm, N.P. Raju, J.E. Greedan, Phys. Rev. Lett. 83 (1999) 211.

[7] M. Tachibana, T. Tojo, H. Kawaji, T. Atake, H. Ikuta, Y. Uchimoto, M. Wakihara, Phys. Rev. B 66 (2002) 092406.
[8] J.E. Greedan, M. Sato, X. Yan, F.S. Razavi, Solid State Commun. 59 (1986) 895.
[9] N.P. Raju, E. Gmelin, R.K. Kremer, Phys. Rev. B 46 (1992) 5405.
[10] K. Miyoshi, Y. Nishimura, K. Honda, K. Fujiwara, J. Takeuchi, J. Phys. Soc. Jpn. 69 (2000) 3517.
[11] J.A. Mydosh, J. Magn. Magn. Mater. 157–158 (1996) 606.
[12] C.H. Booth, J.S. Gardner, G.H. Kwei, R.H. Heffner, F. Bridges, M.A. Subramanian, Phys. Rev. B 62 (2000) R755.
[13] A. Keren, J.S. Gardner, Phys. Rev. Lett. 87 (2001) 177201.
[14] E. Sagi, O. Ofer, A. Keren, Phys. Rev. Lett. 94 (2005) 237202.
[15] J.E. Greedan, D. Gout, A.D. Lozano-Gorrin, S. Derahkshan, T. Proffen, H.J. Kim, E. Bozin, S.J.L. Billinge, Phys. Rev. B 79 (2009) 014427.
[16] P.H. Hubert, Bull. Soc. Chim. Fr. 11 (1974) 2385.
[17] E.A. Tkachenko, P.P. Fedorov, Inorg. Mater. 39 (2003) S25.
[18] D.P. Shoemaker, A. Llobet, M. Tachibana, R. Seshadri, J. Phys.: Condens. Matter 23 (2011) 315404.
[19] B.J. Kennedy, T. Vogt, J. Solid State Chem. 126 (1996) 261.
[20] D.R. Pederzolli, J.P. Attfield, J. Solid State Chem. 136 (1998) 137.
[21] J.P. Attfield, G. Ferey, J. Solid State Chem. 80 (1989) 112.
[22] P.G. Radaelli, J.D. Jorgensen, R. Kleb, B.A. Hunter, F.C. Chou, D.C. Johnston, Phys. Rev. B 49 (1994) 6239.
[23] M. Yang, J. Oró-Solé, A. Fuertes, J.P. Attfield, Chem. Mater. 22 (2010) 4132.
[24] I. Kennedy, B.J. Kennedy, B.A. Hunter, T. Vogt, J. Solid State Chem. 131 (1997) 317.
[25] A.P. Ramirez, Annu. Rev. Mater. Sci. 24 (1994) 453.
[26] J.A. Mydosh, Spin Glasses: An Experimental Introduction, Taylor & Francis, London, 1993.
[27] S. Shtrikman, E.P. Wolhfarth, Phys. Lett. A 85 (1981) 467.
[28] G. Ehlers, J.E. Greedan, J.R. Stewart, K.C. Rule, P. Fouquet, A.L. Cornelius, C. Adriano, P.G. Pagliuso, Y. Qiu, J.S. Gardner, Phys. Rev. B 81 (2010) 224405.
[29] K. Miyoshi, Y. Nishimura, K. Honda, K. Fujiwara, J. Takeuchi, Physica B 284–288 (2000) 1463.
[30] J.A. Hodges, P. Bonville, A. Forget, J.P. Sanchez, P. Vulliet, M. Rams, K. Królas, Eur. Phys. J. B 33 (2003) 173.
[31] Y. Moritomo, Sh. Xu, A. Machida, T. Katsufuji, E. Nishibori, M. Takata, M. Sakata, S.-W. Cheong, Phys. Rev. B 63 (2001) 144425.
[32] R.D. Shannon, Acta. Cryst. A 32 (1976) 751.
[33] N. Ali, M.P. Hill, S. Labroo, J.E. Greedan, J. Solid State Chem. 83 (1989) 178.
[34] H.D. Zhou, C.R. Wiebe, J.A. Janik, B. Vogt, A. Harter, N.S. Dahal, J.S. Gardner, J. Solid State Chem. 183 (2010) 890.
[35] A.S. Wills, G.S. Oakley, D. Visser, J. Frunzke, A. Harrison, K. Andersen, Phys. Rev. B 64 (2001) 094436.
[36] M.A. Hayward, Chem. Mater. 17 (2005) 670.

Gapless Spin Liquid Ground State in the $S = 1/2$ Vanadium Oxyfluoride Kagome Antiferromagnet $[NH_4]_2[C_7H_{14}N][V_7O_6F_{18}]$

L. Clark,[1] J. C. Orain,[2] F. Bert,[2] M. A. De Vries,[1] F. H. Aidoudi,[3] R. E. Morris,[3] P. Lightfoot,[3] J. S. Lord,[4] M. T. F. Telling,[4,5] P. Bonville,[6] J. P. Attfield,[1,*] P. Mendels,[2,7] and A. Harrison[1,8]

[1]*CSEC and School of Chemistry, The University of Edinburgh, Edinburgh EH9 3JZ, United Kingdom*
[2]*Laboratoire de Physique des Solides, UMR CNRS, Université Paris-Sud, 91504 Orsay, France*
[3]*School of Chemistry and EaSTChem, University of St. Andrews, St. Andrews KY16 9ST, United Kingdom*
[4]*ISIS Facility, Rutherford Appleton Laboratory, Chilton, Didcot, Oxon OX110QX, United Kingdom*
[5]*Department of Materials, University of Oxford, Parks Road, Oxford OX1 3PH, United Kingdom*
[6]*Service de Physique de l'État Condensé, CEA-CNRS, CE-Saclay, F-91191 Gif-Sur-Yvette, France*
[7]*Institut Universitaire de France, 103 bd Saint Michel, F-75005 Paris, France*
[8]*Institut Laue Langevin, 6 Rue Jules Horowitz, 38042 Grenoble Cedex 9, France*

(Received 12 February 2013; published 16 May 2013)

The vanadium oxyfluoride $[NH_4]_2[C_7H_{14}N][V_7O_6F_{18}]$ (DQVOF) is a geometrically frustrated magnetic bilayer material. The structure consists of $S = 1/2$ kagome planes of V^{4+} d^1 ions with $S = 1$ V^{3+} d^2 ions located between the kagome layers. Muon spin relaxation measurements demonstrate the absence of spin freezing down to 40 mK despite an energy scale of 60 K for antiferromagnetic exchange interactions. From magnetization and heat capacity measurements we conclude that the $S = 1$ spins of the interplane V^{3+} ions are weakly coupled to the kagome layers, such that DQVOF can be viewed as an experimental model for $S = 1/2$ kagome physics, and that it displays a gapless spin liquid ground state.

DOI: 10.1103/PhysRevLett.110.207208 PACS numbers: 75.50.Lk, 75.40.Cx, 76.75.+i

The search for quantum spin liquids (QSLs) has been a major theme in condensed matter research since the proposal by Anderson of the "resonating valence bond" (RVB) state [1] that can rival the conventional Néel ground state of long range antiferromagnetic order. The RVB state is formed from a superposition of strongly entangled spin singlet pairings whose interactions may be short- (nearest neighbor) or long-range, resonating over the entire spin lattice [2]. The $S = 1/2$ kagome antiferromagnet (KAFM), which is composed of corner-sharing equilateral triangles of antiferromagnetically interacting $S = 1/2$ ions, is the prime candidate to host this exotic state of matter in two dimensions. This stems from the combination of geometric frustration and strong quantum effects that allow spin fluctuations to persist down to $T = 0$. The exact ground state of the $S = 1/2$ KAFM remains controversial as theory predicts several possibilities for the low energy excitation spectra of QSLs. They may be gapped, such as Z_2 or short-range RVB liquids, or gapless, with the existence of zero energy spin excitations, which are known as algebraic or long-range RVB liquids [3]. Predictions from density matrix renormalization group algorithms are that the ground state is a fully gapped, topologically ordered Z_2 spin liquid, with an estimated spin gap of 0.13(1) J (where J is the antiferromagnetic exchange energy) to deconfined, fractional spinon (spin-1/2, charge-0) excitations [4,5]. However, other theories expect a gapless spin liquid ground state [6–8], and the best experimental candidate to date, the $S = 1/2$ KAFM herbertsmithite, $[ZnCu_3(OH)_6Cl_2]$, appears to be a gapless QSL [9,10].

Experimental realizations of the $S = 1/2$ KAFM remain rare and are all based on kagome networks of Cu^{2+} d^9 $S = 1/2$ cations [11–14]. However, Aidoudi *et al.* recently reported the synthesis of $[NH_4]_2[C_7H_{14}N][V_7O_6F_{18}]$ [diammonium quinuclidinium vanadium(III,IV) oxyfluoride; DQVOF] [15] that contains a $S = 1/2$ KAFM network of V^{4+} d^1 cations and thus provides a new opportunity for the study and understanding of kagome physics, as the role played by interactions such as Jahn-Teller distortions that can govern the low temperature magnetic properties of Cu^{2+} kagome systems [16], may be suppressed here. The trigonal $R\bar{3}m$ structure of DQVOF contains two distinct vanadium sites, with V^{4+} $S = 1/2$ ions in the kagome layers and V^{3+} $S = 1$ ions between layers. The system was reported to show an absence of long-range magnetic order down to 2 K from the initial magnetic susceptibility measurements despite evidence for significant antiferromagnetic exchange interactions. In addition, Aidoudi *et al.* put forward an orbital coupling argument to suggest that the poor $V^{4+} - V^{3+}$ superexchange pathway within the structure should result in magnetically isolated $S = 1/2$ kagome planes at low temperatures. In this Letter we present further magnetization and susceptibility measurements plus low temperature heat capacity and muon spin relaxation (μSR) data which demonstrate that DQVOF is a good candidate QSL material with a gapless ground state.

All measurements were performed on a polycrystalline single-phase sample of DQVOF, prepared by the method given in Ref. [15]. Magnetic susceptibility was measured in a Quantum Design SQUID magnetometer from 1.8 to

300 K. Magnetization data were collected at a temperature of 1.7 K in applied fields up to 14 T in a Cryogenic vibrating sample magnetometer. The magnetization-field variation is shown in Fig. 1. The net magnetization may be considered as a sum of two components, a Brillouin-like component, which we tentatively attribute to the V^{3+} spins between the kagome layers and a linear contribution, expected from the strongly interacting V^{4+} kagome layers [17,18]. Subtraction of the linear contribution leaves the saturated magnetization of the interlayer V^{3+} spins, which was normalized by $M_{sat} = N_A g \mu_B + 6 N_A g \mu_B/2 = 8 N_A \mu_B$ for $g = 2$, to account for the ideal total of 6 V^{4+} and 1 V^{3+} spins per formula unit of DQVOF. The experimentally determined value of $M/M_{sat} = 0.148(5)$ corresponds to a saturated moment of $1.18\mu_B$ for the interlayer $S = 1$ V^{3+} ions. Such moment reductions due to spin-orbit coupling are typical for V^{3+} [19,20], for example CdV_2O_4 [21] and $LaVO_3$ [22] have low temperature ordered moments of $1.19\mu_B$ and $1.15\mu_B$, respectively. In agreement with Ref. [15], the susceptibility of DQVOF shows Curie-Weiss behavior with a Weiss temperature $\theta = -58(4)$ K indicating the dominance of antiferromagnetic exchange interactions (Fig. 1, inset). The small reduction in effective moment, $\mu_{eff} = 4.97(8)\mu_B$ per formula unit, with respect to the expected value of $5.1\mu_B$ is again in keeping with V^{3+} spin-orbit coupling.

Low-temperature heat capacity was measured on a 1.6 mg pressed powder pellet in a Quantum Design Physical Properties Measurement System with a ^{3}He insert, in zero field (ZF) and applied fields up to 9 T. The data, presented in Fig. 2(a), show a broad Schottky feature that shifts to higher energies in stronger applied fields. This is most likely due to the weakly interacting $S = 1$ spins of the V^{3+} ions located in between the kagome planes. In stronger applied fields ($H \geq 5$ T) a second feature appears within the low temperature region of the data. We attribute this to the splitting of the $I = 1/2$ nuclear spins of the ^{1}H and ^{19}F nuclei that are abundant within the system. The lattice heat capacity and the contribution from the $S = 1/2$ spins of the V^{4+} ions within the kagome layers are most likely field independent at these field strengths, given the relatively strong antiferromagnetic interaction [23,24]. In order to isolate the field dependent contributions, the zero field heat capacity was subtracted from the applied field data, for example, the difference between 9 T and zero field heat capacities is shown as $\Delta C_v T^{-1}$ in the left-hand inset of Fig. 2(a). These difference curves were all successfully fitted by a model consisting of two Schottky anomalies. The nuclear Schottky term corresponding to the 40 hydrogen and fluorine nuclei per formula unit has no free parameters. The electronic Schottky contribution was fitted well by the expression for an $S = 1$ system,

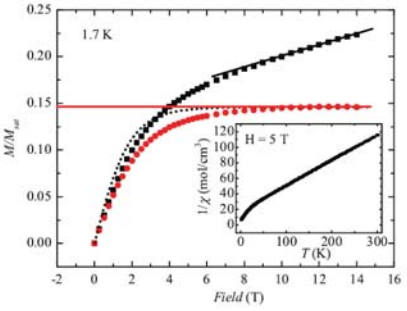

FIG. 1 (color online). Squares: normalized magnetization of DQVOF at 1.7 K with a linear fit to the data above $H = 10$ T. This response is most likely representative of the nonsaturated intrinsic susceptibility of the V^{4+} kagome layers. Circles: the contribution of the V^{3+} spins obtained by subtracting the linear contribution from the total magnetization curve. The dashed curve is the Brillouin function for noninteracting $S = 1$ spins. Inset: inverse susceptibility measured in a 5 T field.

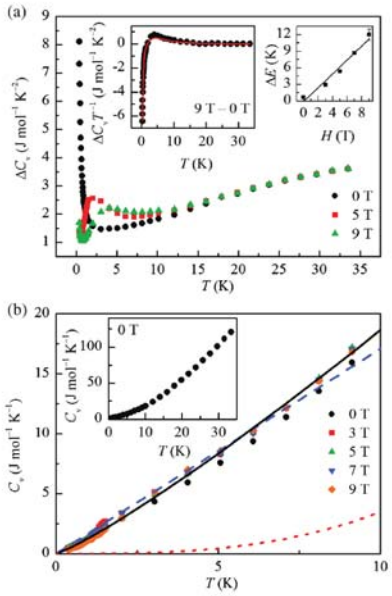

FIG. 2 (color online). (a) $C_v T^{-1}$ of DQVOF against temperature measured in ZF and applied fields of 5 T and 9 T. Left-hand inset the fit to the Schottky anomaly (solid line) to the difference of interpolated heat capacity in 9 and 0 T. The right-hand inset shows the Zeeman splitting of the $S = 1$ levels. (b) The low temperature heat capacity after subtraction of the Schottky anomaly with $C_v = \gamma T$ (dashed line) and $C_v = \gamma T^{1.2}$ (solid line) models. The dotted red curve gives an estimate of the lattice contribution to the heat capacity. Inset shows the ZF data over the entire measured temperature range.

$$C_v T^{-1} = \frac{f_{S=1} k_B N_A}{T}\left(\frac{E_{S=1}}{T}\right)^2 \times \frac{\exp(E_{S=1}/T) + \exp(-E_{S=1}/T) + 4}{[1 + \exp(E_{S=1}/T) + \exp(-E_{S=1}/T)]^2}. \quad (1)$$

The fitted value of $f_{S=1} = 0.5(2)$ for the fraction of $S = 1$ spins per formula unit shows a similar reduction to the magnetization, as a result of spin-orbit coupling. The obtained Zeeman splitting energy ($E_{S=1} = g\mu_B H$) shown in the right-hand inset of Fig. 2(a), gives $g = 1.8(2)$, which is typical for V^{3+} ions. We note the existence of a small (~ 0.7 K) zero field splitting of the $S = 1$ levels, which is also likely to result from spin-orbit coupling in the t_{2g}^2 V^{3+} ground state. The magnetization and heat capacity results show that the interlayer V^{3+} ions behave as spin-orbit coupled but noninteracting paramagnetic spins, and that to a good approximation DQVOF contains magnetically isolated kagome layers of strongly correlated $S = 1/2$ spins of V^{4+} ions.

The field dependent Schottky features were subtracted from the heat capacity data to give, in Fig. 2(b), the contribution of the strongly correlated spins within the kagome layers together with the lattice contribution, which is expected to be vanishingly small at low temperatures. The observation that all subtracted curves approximately coincide reflects the quality of the fit of the field dependant heat capacity to our model. It also implies that the low temperature ground state of DQVOF is robust to the application of fields up to 9 T, and so forms a quantum critical phase rather than sitting at a quantum critical point. The data show no sharp peak structure within the measured temperature range indicating the absence of any magnetic phase transitions. This is in agreement with the magnetization data and the μSR measurements discussed below. In the absence of a nonmagnetic analogue, the phonon contribution cannot be subtracted accurately but an upper bound of the lattice contribution is estimated by a T^3 phonon contribution that matches the total heat capacity at 30 K. This lattice contribution is found to be negligible below 5 K. A recent estimate for the spin gap in a topologically ordered spin liquid [4,5] is $0.13J \approx 7.5$ K for DQVOF, taking the nearest neighbor exchange energy as $J = -\theta$ from the mean-field description of the $S = 1/2$ KAFM. However, the continuous density of states observed down to 300 mK implies that there is no complete spin excitation gap in the spectrum of DQVOF within the measured energy range. Various models have been proposed for the low temperature heat capacity of gapless spin liquids. Algebraic or Dirac spin liquids are expected to show a $C_v \propto T^2$ dependence at low temperature [6,7]. This does not appear to be applicable to DQVOF. A better description seems to be given by a more conventional spinon Fermi surface with a T-linear behavior in the low temperature specific heat. Modeling the data with $C_v = \gamma T$ between 300 mK and 5 K gives a reasonable fit to the data with $\gamma \sim 200$ mJ K^{-2} mol^{-1} per V^{4+} spin. γ is related to the spinon density of states at the spinon Fermi surface, and the value found here is comparable to those from other experimental gapless spin liquids [25–27]. However, the fit in Fig. 2(b) is improved by using a $C_v = \gamma T^\alpha$ term with exponent $\alpha = 1.2$. This is remarkably similar to the behavior of herbertsmithite where the low temperature heat capacity data was modeled with a $T^{1.3}$ dependence [24].

A key feature of a vanishing spin gap in a QSL is the absence of spin freezing and persistence of internal field fluctuations down to $T = 0$. Experimentally, this can be observed by μSR due to the extreme sensitivity of the muon to small magnetic moments. Measurements were performed on the MuSR spectrometer at the ISIS pulsed muon facility, Rutherford Appleton Laboratory, UK. The background fraction of muons landing in the sample backing plate or elsewhere was determined by comparison of the data with those taken on the GPS instrument at the Laboratory for Muon Spin Spectroscopy, Paul Scherrer Institute, Switzerland at the same temperature and magnetic field. The PSI equipment used an active veto detector to give very low background [28]. Figure 3 shows the time dependence of the background corrected muon spin polarization in zero field (ZF) and an applied longitudinal fields (LF) of 200 G at 40 mK and 40 K.

The ZF depolarization reflects the sum of the local responses of muons implanted at different stopping sites within the sample. Implanted muons are likely to be at sites near oxide or fluoride anions, due to their favorable electrostatic interactions with the positive muons. A fit to the high temperature ZF depolarization data (see the Supplemental Material [29]) reveals that the kink at 2 μs can be ascribed to a strong dipolar coupling between the muon spin and the fluorine $I = 1/2$ nuclear spin [30,31]. This fluorine response accounts for 10% of the muons stopping within the sample. The presence of this characteristic feature in the ZF data at all temperatures indicates that the muons implanted at the fluorine site are only very weakly coupled to the electronic spins of the system (see the Supplemental

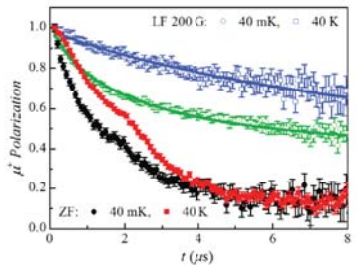

FIG. 3 (color online). Time dependent muon spin polarization of DQVOF at 40 mK and 40 K in zero field (ZF) and an applied longitudinal field (LF) of 200 G. Solid lines are fits to the data [Eq. (2)].

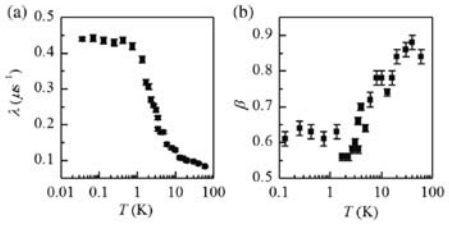

FIG. 4. The temperature dependence of (a) the muon spin depolarization rate, λ, and (b) the stretching component, β, of DQVOF.

Material [29]). In addition, a small fraction of muons most likely stop far from the kagome planes and give rise to a small nonrelaxing polarization, ~0.1, clearly visible at long time. The remainder of the implanted muons fall at sites situated near oxide anions.

Both the 40 K and 40 mK data in Fig. 3 relax to the same value of polarization pointing to the absence of a "1/3-tail" component characteristic of a magnetically frozen state at long times in the 40 mK data. This precludes any argument for static magnetism in the sample upon cooling [32]. Hence the moderate increase of the relaxation upon cooling from high temperature reflects only a slowing down of the electronic spin dynamics. The local nuclear fields at each stopping site are static on the time scale of the muon experiment and can be decoupled from the muon upon application of a LF of 200 G. As a result, the muon spin only probes the dynamical, temperature dependent field fluctuations arising from the electronic spins within the system, which are of principal interest here. The time evolution of the spin depolarization in an applied LF of 200 G was modeled with a stretched exponential relaxation function over the entire measured temperature range,

$$P(t) = P_{\text{nonrelaxing}} + P_O \exp(-\lambda t)^{\beta}. \quad (2)$$

Figures 4(a) and 4(b) show the temperature dependence of the spin depolarization rate, λ, and the stretching component, β, respectively.

Above 10 K, the system is in a fast fluctuating regime from which there is a slowing of spin dynamics down to 1 K. Below 1 K the data show a plateau in the depolarization rate, a clear indicator of persistent dynamics at low temperatures. The limiting value of $\beta \sim 0.5$ implies a distribution of dynamical correlations at low temperatures and the muons implanted at the oxygen site are most likely under the influence of more than one fluctuation frequency. The origin of the muon spin relaxation in DQVOF requires some consideration given that there are two potential sources of electronic field fluctuations, namely, the V^{3+} $S = 1$ and the V^{4+} $S = 1/2$ spins. We estimate that the relaxation rate, λ, due to the $S = 1$ spins of V^{3+} is ~0.01 MHz, from the effective interaction between $S = 1$ spins of ~1 K as observed from the magnetization against field data shown in Fig. 1 (see the Supplemental Material [29]). Given that the experimentally determined value is larger than this, it implies that the slowing down of electronic spin dynamics and the relaxation shown in Fig. 4(a) is intrinsic to the kagome layers. The persistence of electronic field fluctuations within the kagome layers at the lowest measured temperatures, therefore, supports the existence of a gapless spin liquid state in DQVOF as deduced from the low temperature heat capacity data.

In summary, this study of low temperature magnetism in DQVOF demonstrates that the interplane V^{3+} $S = 1$ spins show paramagnetic single-ion ion behavior with significant spin-orbit coupling effects, while the V^{4+} layers are a good experimental realization of an $S = 1/2$ kagome antiferromagnet. μSR shows that there is no spin freezing within DQVOF down to 40 mK. Such persistent spin dynamics at low temperatures are a key requirement for a QSL state. The low temperature heat capacity of the V^{4+} kagome planes displays a continuous density of magnetic states down to 300 mK demonstrating that there is no complete spin gap in the low energy excitation spectrum, and shows little variation in fields up to 9 T, consistent with a gapless quantum critical phase spin liquid ground state. This heat capacity varies as $T^{1.2}$ which is remarkably similar to the $T^{1.3}$ dependence of herbertsmithite [24]. DQVOF joins just two Cu^{2+} materials, herbertsmithite and vesignieite, as experimental realizations of the $S = 1/2$ kagome lattice. None of these materials show the theoretically favored gapped spin liquid behavior of the pure Heisenberg KAFM model [4,5]. Vesignieite orders at a fairly high temperature [33], while both herbertsmithite and DQVOF are found to be gapless spin liquids. It is also notable that a significant, although not critical, slowing of the spin dynamics is detected in DQVOF at low temperatures, but not in herbertsmithite [18]. This suggests that the quantum critical phase in DQVOF lies closer to some uncovered phase transition than in the case of herbertsmithite. Such a phase transition will be driven by perturbations that will differ in magnitude between d^1 and d^9 systems, for example the spin-orbit driven Dzyaloshinskii-Moriya interaction. It will be thus be particularly interesting to discover possible instabilities of the liquid ground state of DQVOF by applying stronger magnetic fields [34] or pressure [35] and, hence, explore the perturbations that can pin the ground state of these kagome models.

This work was supported in part by the Grant No. ANR-09-JCJC-0093-01, and by EPSRC, STFC, and the Royal Society. We thank A. Amato for assistance at PSI.

*Corresponding author.
j.p.attfield@ed.ac.uk

[1] P. W. Anderson, Mater. Res. Bull. **8**, 153 (1973).
[2] L. Balents, Nature (London) **464**, 199 (2010).

[3] G. Misguich, in *Introduction to Frustrated Magnetism*, edited by C. Lacroix, P. Mendels, and F. Mila (Springer-Verlag, Berlin, 2011).
[4] S. Yan, D.A. Huse, and S.R. White, Science **332**, 1173 (2011).
[5] S. Depenbrock, I. P. McCulloch, and U. Schollwöck, Phys. Rev. Lett. **109**, 067201 (2012).
[6] Y. Ran, M. Hermele, P. A. Lee, and X. G. Wen, Phys. Rev. Lett. **98**, 117205 (2007).
[7] M. Hermele, Y. Ran, P. A. Lee, and X. G. Wen, Phys. Rev. B **77**, 224413 (2008).
[8] Y. Iqbal, F. Becca, and D. Poilblanc, Phys. Rev. B **84**, 020407(R) (2011); Y. Iqbal, F. Becca, S. Sorella, and D. Poilblanc, arXiv:1209.1858.
[9] A. Olariu, P. Mendels, F. Bert, F. Duc, J. Trombe, M. de Vries, and A. Harrison, Phys. Rev. Lett. **100**, 087202 (2008).
[10] M. A. de Vries, J. Stewart, P. Deen, J. Piatek, G. Nilsen, H. Rønnow, and A. Harrison, Phys. Rev. Lett. **103**, 237201 (2009).
[11] Z. Hiroi, M. Hanawa, N. Kobayashi, M. Nohara, H. Takagi, Y. Kato, and M. Takigawa, J. Phys. Soc. Jpn. **70**, 3377 (2001).
[12] M. P. Shores, E. A. Nytko, B. M. Bartlett, and D. G. Nocera, J. Am. Chem. Soc. **127**, 13462 (2005).
[13] B. Fåk *et al.*, Phys. Rev. Lett. **109**, 037208 (2012).
[14] Y. Okamoto, H. Yoshida, and Z. Hiroi, J. Phys. Soc. Jpn. **78**, 033701 (2009).
[15] F. H. Aidoudi, D. W. Aldous, R. J. Goff, A. M. Z. Slawin, J. P. Attfield, R E. Morris, and P. Lightfoot, Nat. Chem. **3**, 801 (2011).
[16] H. Yoshida, J. Yamaura, M. Isobe, Y. Okamoto, G. J. Nilsen, and Z. Hiroi, Nat. Commun. **3**, 860 (2012).
[17] F. Bert, S. Nakamae, F. Ladieu, D. L'Hôte, P. Bonville, F. Duc, J.-C. Trombe, and P. Mendels, Phys. Rev. B **76**, 132411 (2007).
[18] E. Kermarrec, P. Mendels, F. Bert, R. H. Colman, A. S. Wills, P. Strobel, P. Bonville, A. Hillier, and A. Amato, Phys. Rev. B **84**, 100401(R) (2011).
[19] B. N. Figgis and M. A. Hitchman, *Ligand Field Theory and Its Applications* (Wiley-VCH, New York, 2000).
[20] Z. Ropka and R. J. Radwanski, Physica (Amsterdam) **378–380B**, 301 (2006).
[21] E. M. Wheeler, B. Lake, A. T. M. Nazmul Islam, M. Reehuis, P. Steffens, T. Guidi, and A. H. Hill, Phys. Rev. B **82**, 140406(R) (2010).
[22] J. S. Zhou, Y. Ren, J. Q. Yan, J. F. Mitchell, and J. B. Goodenough, Phys. Rev. Lett. **100**, 046401 (2008).
[23] A. P. Ramirez, S. W. Cheong, and M. L. Kaplan, Phys. Rev. Lett. **72**, 3108 (1994).
[24] M. A. de Vries, K. V. Kamenev, W. A. Kockelmann, J. Sanchez-Benitez, and A. Harrison, Phys. Rev. Lett. **100**, 157205 (2008).
[25] J. S. Helton, H. Martinho, M. S. Sercheli, P. G. Pagliuso, D. D. Jackson, M. Torelli, J. W. Lynn, C. Rettori, Z. Fisk, and S. B. Oseroff, Phys. Rev. Lett. **98**, 107204 (2007).
[26] S. Yamashita, Y. Nakazawa, M. Oguni, Y. Oshima, H. Nojiri, Y. Shimizu, K. Miyagawa, and K. Kanoda, Nat. Phys. **4**, 459 (2008).
[27] S. Yamashita, T. Yamamoto, Y. Nakazawa, M. Tamura, and R. Kato, Nat. Commun. **2**, 275 (2011).
[28] ISIS MuSR measurements were performed on a 400 mg sample in an Ag foil packet on an Ag backing plate in a Variox cryostat with dilution fridge insert. A background asymmetry of 3.5% was determined by veto measurement of the sample on the GPS spectrometer at the Laboratory for Muon Spin Spectroscopy, PSI, Switzerland.
[29] See Supplemental Material at http://link.aps.org/supplemental/10.1103/PhysRevLett.110.207208 for details on ZF fits.
[30] I. A. Campbell, A. Amato, F. N. Gygax, D. Herlach, A. Schenck, R. Cywinski, and S. H. Kilcoyne, Phys. Rev. Lett. **72**, 1291 (1994).
[31] J. H. Brewer, S. Kreitzman, D. Noakes, E. Ansaldo, D. Harshman, and R. Keitel, Phys. Rev. B **33**, 7813 (1986).
[32] T. Lancaster, S Blundell, P. Baker, M. Brooks, W. Hayes, F. Pratt, J. Manson, M. Conner, and J. Schlueter, Phys. Rev. Lett. **99**, 267601 (2007).
[33] M. Yoshida, Y. Okamoto, M. Takigawa, and Z. Hiroi, J. Phys. Soc. Jpn. **82**, 013702 (2012).
[34] M. Jeong, F. Bert, P. Mendels, F. Duc, J. C. Trombe, M. A. de Vries, and A. Harrison, Phys. Rev. Lett. **107**, 237201 (2011)
[35] D. P. Kozlenko, A. F. Kusmartseva, E. V. Lukin, D. A. Keen, W. G. Marshall, M. A. de Vries, and K. V. Kamenev, Phys. Rev. Lett. **108**, 187207 (2012).

Bibliography

[1] J. H. Van Vleck, "Quantum mechanics-The key to understanding magnetism," *Reviews of Modern Physics*, vol. 50, pp. 181–189, 1978.

[2] I. S. Osborne, "The Attraction of Magnetism," *Science*, vol. 294, p. 1483, 2001.

[3] S. Blundell, *Magnetism in Condensed Matter*. U.K.: Oxford University Press, 2001.

[4] P. A. Cox, *Transition Metal Oxides*. U.K.: Clarendon Press, 1992.

[5] R. L. Carlin, *Magnetochemistry*. Germany: Springer-Verlag, 1986.

[6] J. E. Greedan, "Geometrically frustrated magnetic materials," *Journal of Materials Chemistry*, vol. 11, pp. 37–53, 2001.

[7] C. Zener, "Interaction between the *d*-Shells in the Transition Metals. II. Ferromagnetic Compounds of Manganese with Perovskite Structure," *Physical Review*, vol. 82, pp. 403–405, 1951.

[8] M. F. Collins, *Magnetic Critical Scattering*. U.K.: Oxford University Press, 1989.

[9] B. D. Gaulin, "Geometrically-frustrated magnetism on triangular and tetrahedral lattices," *Hyperfine Interactions*, vol. 85, pp. 159–171, 1994.

[10] A. P. Ramirez, *More is Different*, ch. Geometric Frustration and Marginal Constraint. U.S.A.: Princeton University Press, 2001.

[11] M. A. Ruderman and C. Kittel, "Indirect Exchange Coupling of Nuclear Magnetic Moments by Conduction Electrons," *Physical Review*, vol. 96, pp. 99–102, 1954.

[12] K. Yosida, "Magnetic Properties of Cu-Mn Alloys," *Physical Review*, vol. 106, pp. 893–898, 1957.

[13] J. A. Mydosh, *Spin glasses: an experimental introduction*. London: Taylor and Francis, 1993.

[14] A. J. Berlinsky and C. Kallin, "Frustration, satisfaction and degeneracy in triangle-based lattices," *Hyperfine Interactions*, vol. 85, pp. 173–179, 1994.

[15] A. P. Ramirez, "Strongly Geometrically Frustrated Magnets," *Annual Review of Materials Science*, vol. 24, pp. 453–480, 1994.

[16] J. T. Chalker, *Introduction to Frustrated Magnetism*, ch. Geometrically Frustrated Antiferromagnets: Statistical Mechanics and Dynamics. Germany: Springer-Verlag, 2011.

[17] P. Lecheminant, *Frustrated Spin Systems*, ch. One-Dimensional Spin Liquids. Singapore: World Scientific, 2004.

[18] A. Harrison, "First catch your hare: the design and synthesis of frustrated magnets," *Journal of Physics: Condensed Matter*, vol. 16, pp. S553–S572, 2004.

[19] G. H. Wannier, "Antiferromagnetism. The Triangular Ising Net," *Physical Review*, vol. 79, pp. 357–364, 1950.

[20] R. M. F. Houtappel, "Order-disorder in hexagonal lattices," *Physica*, vol. 16, pp. 425 – 455, 1950.

[21] H. T. Diep and H. Giacomini, *Frustrated Spin Systems*, ch. Frustration - Exactly solved frustrated models. Singapore: World Scientific, 2004.

[22] J. Mydosh, "Disordered magnetism and spin glasses," *Journal of Magnetism and Magnetic Materials*, vol. 157158, pp. 606 – 610, 1996.

[23] J. Villain, "Insulating spin glasses," *Zeitschrift für Physik B Condensed Matter*, vol. 33, pp. 31–42, 1979.

[24] M. J. P. Gingras, C. V. Stager, B. D. Gaulin, N. P. Raju, and J. E. Greedan, "Nonlinear susceptibility measurements at the spin-glass transition of the pyrochlore antiferromagnet $Y_2Mo_2O_7$," *Journal of Applied Physics*, vol. 79, pp. 6170–6172, 1996.

[25] A. Wills, "Conventional and unconventional orderings in the jarosites.," *Canadian Journal of Physics*, vol. 79, p. 1501, 2001.

[26] J. S. Gardner, B. D. Gaulin, S.-H. Lee, C. Broholm, N. P. Raju, and J. E. Greedan, "Glassy Statics and Dynamics in the Chemically Ordered Pyrochlore Antiferromagnet $Y_2Mo_2O_7$," *Physical Review Letters*, vol. 83, pp. 211–214, 1999.

[27] S. T. Bramwell and M. J. P. Gingras, "Spin Ice State in Frustrated Magnetic Pyrochlore Materials," *Science*, vol. 294, pp. 1495–1501, 2001.

[28] M. J. Harris, S. T. Bramwell, D. F. McMorrow, T. Zeiske, and K. W. Godfrey, "Geometrical Frustration in the Ferromagnetic Pyrochlore $Ho_2Ti_2O_7$," *Physical Review Letters*, vol. 79, pp. 2554–2557, 1997.

[29] S. Rosenkranz, A. P. Ramirez, A. Hayashi, R. J. Cava, R. Siddharthan, and B. S. Shastry, "Crystal-field interaction in the pyrochlore magnet $Ho_2Ti_2O_7$," *Journal of Applied Physics*, vol. 87, pp. 5914–5916, 2000.

[30] S. T. Bramwell and M. J. Harris, "Frustration in Ising-type spin models on the pyrochlore lattice," *Journal of Physics: Condensed Matter*, vol. 10, p. L215, 1998.

[31] J. D. Bernal and R. H. Fowler, "A Theory of Water and Ionic Solution, with Particular Reference to Hydrogen and Hydroxyl Ions," *The Journal of Chemical Physics*, pp. 515–548, 1933.

[32] E. O. Wollan, W. L. Davidson, and C. G. Shull, "Neutron Diffraction Study of the Structure of Ice," *Physical Review*, vol. 75, pp. 1348–1352, 1949.

[33] L. Pauling, *The Nature of the Chemical Bond*. Ithaca, New York: Cornell University Press, 1945.

[34] W. F. Giauque and J. W. Stout, "The Entropy of Water and the Third Law of Thermodynamics. The Heat Capacity of Ice from 15 to 273° K.," *Journal of the American Chemical Society*, vol. 58, pp. 1144–1150, 1936.

[35] A. P. Ramirez, A. Hayashi, R. J. Cava, R. Siddharthan, and B. S. Shastry, "Zero-point entropy in 'spin ice'," *Nature*, vol. 399, pp. 333–335, 1999.

[36] C. Castelnovo, R. Moessner, and S. L. Sondhi, "Magnetic monopoles in spin ice," *Nature*, vol. 451, pp. 42–45, 2008.

[37] D. J. P. Morris, D. A. Tennant, S. A. Grigera, B. Klemke, C. Castelnovo, R. Moessner, C. Czternasty, M. Meissner, K. C. Rule, J.-U. Hoffmann, K. Kiefer, S. Gerischer, D. Slobinsky, and R. S. Perry, "Dirac Strings and Magnetic Monopoles in the Spin Ice $Dy_2Ti_2O_7$," *Science*, vol. 326, pp. 411–414, 2009.

[38] T. Fennell, P. P. Deen, A. R. Wildes, K. Schmalzl, D. Prabhakaran, A. T. Boothroyd, R. J. Aldus, D. F. McMorrow, and S. T. Bramwell, "Magnetic Coulomb Phase in the Spin Ice $Ho_2Ti_2O_7$," *Science*, vol. 326, pp. 415–417, 2009.

[39] S. T. Bramwell, S. R. Giblin, S. Calder, R. Aldus, D. Prabhakaran, and T. Fennell, "Measurement of the charge and current of magnetic monopoles in spin ice," *Nature*, vol. 461, pp. 956–959, 2009.

[40] S. R. Giblin, S. T. Bramwell, P. C. W. Holdsworth, D. Prabhakaran, and I. Terry, "Creation and measurement of long-lived magnetic monopole currents in spin ice," *Nature Physics*, vol. 7, pp. 252–258, 2011.

[41] S. R. Dunsiger, A. A. Aczel, C. Arguello, H. Dabkowska, A. Dabkowski, M.-H. Du, T. Goko, B. Javanparast, T. Lin, F. L. Ning, H. M. L. Noad, D. J. Singh, T. J. Williams, Y. J. Uemura, M. J. P. Gingras, and G. M.

Luke, "Spin Ice: Magnetic Excitations without Monopole Signatures Using Muon Spin Rotation," *Physical Review Letters*, vol. 107, p. 207207, 2011.

[42] L. Bovo, J. A. Bloxsom, D. Prabhakaran, G. Aeppli, and S. T. Bramwell, "Brownian motion and quantum dynamics of magnetic monopoles in spin ice," *Nature Communications*, vol. 4:1535, 2013.

[43] A. M. Hallas, J. A. M. Paddison, H. J. Silverstein, A. L. Goodwin, J. R. Stewart, A. R. Wildes, J. G. Cheng, J. S. Zhou, J. B. Goodenough, E. S. Choi, G. Ehlers, J. S. Gardner, C. R. Wiebe, and H. D. Zhou, "Statics and dynamics of the highly correlated spin ice $Ho_2Ge_2O_7$," *Physical Review B*, vol. 86, p. 134431, 2012.

[44] C. Lhuillier and G. Misguich, *Introduction to Frustrated Magnetism*, ch. Introduction to Quantum Spin Liquids. Germany: Springer-Verlag, 2011.

[45] G. Misguich, *Introduction to Frustrated Magnetism*, ch. Quantum Spin Liquids and Fractionalization. Germany: Springer-Verlag, 2011.

[46] F. Mila, "Quantum spin liquids," *European Journal of Physics*, vol. 21, p. 499, 2000.

[47] P. Anderson, "Resonating valence bonds: A new kind of insulator?," *Materials Research Bulletin*, vol. 8, pp. 153 – 160, 1973.

[48] P. W. Anderson, "The Resonating Valence Bond State in La_2CuO_4 and Superconductivity," *Science*, vol. 235, pp. 1196–1198, 1987.

[49] L. Balents, "Spin liquids in frustrated magnets," *Nature*, vol. 464, pp. 199 – 208, 2010.

[50] P. A. Lee, "An End to the Drought of Quantum Spin Liquids," *Science*, vol. 321, pp. 1306–1307, 2008.

[51] D. A. Tennant, R. A. Cowley, S. E. Nagler, and A. M. Tsvelik, "Measurement of the spin-excitation continuum in one-dimensional $KCuF_3$ using neutron scattering," *Physical Review B*, vol. 52, pp. 13368–13380, 1995.

[52] H.-C. Jiang, Z. Wang, and L. Balents, "Identifying topological order by entanglement entropy," *Nature Physics*, vol. 8, pp. 902–905, 2012.

[53] S. R. White, "Quantum spin liquids: Tell-tale topology," *Nature Physics*, vol. 8, pp. 863–864, 2012.

[54] S. Depenbrock, I. P. McCulloch, and U. Schollwöck, "Nature of the Spin-Liquid Ground State of the $S = 1/2$ Heisenberg Model on the Kagome Lattice," *Physical Review Letters*, vol. 109, p. 067201, 2012.

[55] S. Yan, D. A. Huse, and S. R. White, "Spin-Liquid Ground State of the S = 1/2 Kagome Heisenberg Antiferromagnet," *Science*, vol. 332, pp. 1173–1176, 2011.

[56] M. B. Hastings, "Dirac structure, RVB, and Goldstone modes in the *kagomé* antiferromagnet," *Physical Review B*, vol. 63, p. 014413, 2000.

[57] Y. Ran, M. Hermele, P. A. Lee, and X.-G. Wen, "Projected-Wave-Function Study of the Spin-1/2 Heisenberg Model on the Kagome Lattice," *Physical Review Letters*, vol. 98, p. 117205, 2007.

[58] Y. Ran, W.-H. Ko, P. A. Lee, and X.-G. Wen, "Spontaneous Spin Ordering of a Dirac Spin Liquid in a Magnetic Field," *Physical Review Letters*, vol. 102, p. 047205, 2009.

[59] M. Barkeshli, H. Yao, and S. A. Kivelson, "Gapless spin liquids: Stability and possible experimental relevance," *Physical Review B*, vol. 87, p. 140402, 2013.

[60] M. A. de Vries, J. R. Stewart, P. P. Deen, J. O. Piatek, G. J. Nilsen, H. M. Rønnow, and A. Harrison, "Scale-Free Antiferromagnetic Fluctuations in the $s = 1/2$ Kagome Antiferromagnet Herbertsmithite," *Physical Review Letters*, vol. 103, p. 237201, 2009.

[61] T.-H. Han, J. S. Helton, S. Chu, D. G. Nocera, J. A. Rodriguez-Rivera, C. Broholm, and Y. S. Lee, "Fractionalized excitations in the spin-liquid state of a kagome-lattice antiferromagnet," *Nature*, vol. 492, pp. 406–410, 2012.

[62] E. Berg, E. Altman, and A. Auerbach, "Singlet Excitations in Pyrochlore: A Study of Quantum Frustration," *Physical Review Letters*, vol. 90, p. 147204, 2003.

[63] B. Canals and C. Lacroix, "Pyrochlore Antiferromagnet: A Three-Dimensional Quantum Spin Liquid," *Physical Review Letters*, vol. 80, pp. 2933–2936, 1998.

[64] M. Hermele, M. P. A. Fisher, and L. Balents, "Pyrochlore photons: The $U(1)$ spin liquid in a $S = \frac{1}{2}$ three-dimensional frustrated magnet," *Physical Review B*, vol. 69, p. 064404, 2004.

[65] R. Coldea, D. A. Tennant, and Z. Tylczynski, "Extended scattering continua characteristic of spin fractionalization in the two-dimensional frustrated quantum magnet Cs_2CuCl_4 observed by neutron scattering," *Physical Review B*, vol. 68, p. 134424, 2003.

[66] A. K. Cheetham and P. Day, eds., *Solid State Chemisty Techniques*. Oxford University Press, 1987.

[67] A. Fuertes, "Synthesis and properties of functional oxynitrides - from photocatalysts to CMR materials," *Dalton Transactions*, vol. 39, pp. 5942–5948, 2010.

[68] S. H. Elder, F. J. DiSalvo, L. Topor, and A. Navrotsky, "Thermodynamics of ternary nitride formation by ammonolysis: application to lithium molybdenum nitride ($LiMoN_2$), sodium tungsten nitride (Na_3WN_3), and sodium tungsten oxide nitride (Na_3WO_3N)," *Chemistry of Materials*, vol. 5, pp. 1545–1553, 1993.

[69] P. A. Wright, *Microporous Framework Solids*. U.K.: RSC Publishing, 2008.

[70] R. E. Morris, "Ionothermal synthesis-ionic liquids as functional solvents in the preparation of crystalline materials," *Chemical Communications*, vol. 21, pp. 2990–2998, 2009.

[71] E. R. Cooper, C. D. Andrews, P. S. Wheatley, P. B. Webb, P. Wormald, and R. E. Morris, "Ionic liquids and eutectic mixtures as solvent and template in synthesis of zeolite analogues," *Nature*, vol. 430, pp. 1012–1016, 2004.

[72] J. M. Griffin, L. Clark, V. R. Seymour, D. W. Aldous, D. M. Dawson, D. Iuga, R. E. Morris, and S. E. Ashbrook, "Ionothermal O-17 enrichment of oxides using microlitre quantities of labelled water," *Chemical Science*, vol. 3, pp. 2293–2300, 2012.

[73] E. R. Parnham, E. A. Drylie, P. S. Wheatley, A. M. Z. Slawin, and R. E. Morris, "Ionothermal materials synthesis using unstable deep-eutectic solvents as template-delivery agents," *Angewante Chemie-International Edition*, vol. 45, pp. 4962–4966, 2006.

[74] E. R. Parnham and R. E. Morris, "Ionothermal synthesis of zeolites, metal-organic frameworks, and inorganic-organic hybrids," *Accounts of Chemical Research*, vol. 40, pp. 1005–1013, 2007.

[75] F. H. Aidoudi, D. W. Aldous, R. J. Goff, A. M. Z. Slawin, J. P. Attfield, R. E. Morris, and P. Lightfoot, "An ionthermally prepared $S = \frac{1}{2}$ vanadium oxyfluoride kagome lattice," *Nature Chemistry*, vol. 3, pp. 801–806, 2011.

[76] C. N. R. Rao and J. Gopalakrishnan, *New Directions in Solid State Chemistry*. Cambridge University Press, 1986.

[77] S. G. Ebbinghaus, H.-P. Abicht, R. Dronskowski, T. Müller, A. Reller, and A. Weidenkaff, "Perovskite-related oxynitrides Recent developments in synthesis, characterisation and investigations of physical properties," *Progress in Solid State Chemistry*, vol. 37, pp. 173 – 205, 2009.

[78] G. L. Squires, *Introduction to the Theory of Thermal Neutron Scattering*. U.K.: Cambridge University Press, 3rd ed., 2012.

[79] S. W. Lovesey, *Theory of Neutron Scattering from Condensed Matter*, vol. I. U.K.: Oxford University Press, 1986.

[80] D. S. Sivia, *Elementary Scattering Thoery For X-ray and Neutron Users*. U.K.: Oxford University Press, 2011.

[81] P. A. M. Dirac, *The Priciples of Quantum Mechamics*. U.K.: Oxford University Press, 4 ed., 1958.

[82] A. Boothroyd, *Introductory Theory*. Oxford, U.K.: 12th Oxford School on Neutron Scattering, 2011.

[83] C. Hammond, *The Basics of Crystallography and Diffraction*. U.K.: Oxford Univerisy Press, 2001.

[84] R. A. Young, ed., *The Rietveld Method*. U.K.: Oxford University Press, 1993.

[85] A. C. Larson and R. B. Von Dreele, "General Structure Analysis System," *Los Alamos National Laboratory Report No. LAUR 86-748*, 1994.

[86] J. R. Stewart, *Magnetic Neutron Scattering*. Rutherford Appleton Laboratory, U.K.: ISIS Neutron Training Course, 2011.

[87] S. W. Lovesey, *Theory of Neutron Scattering from Condensed Matter*, vol. II. U.K.: Oxford University Press, 1986.

[88] P. J. Brown, *International Tables for Crystallography*, vol. C, ch. Production and Properties of Radiation. London: Kluwer Academic Publishers, 2004.

[89] C. G. Shull and J. S. Smart, "Detection of antiferromagnetism by neutron diffraction," *Physical Review*, vol. 76, pp. 1256–1257, 1949.

[90] L. Néel, "Propriétés magnétiques de l'état magnétique et énergie d'interaction entre atomes magnétiques.," *Annales de Physique*, vol. 5, pp. 232–279, 1936.

[91] S. T. Bramwell, *Introduction to Frustrated Magnetism*, ch. Neutron Scattering and Highly Frustrated Magnetism. Berlin: Springer-Verlag, 2011.

[92] *http://www.ill.eu/instruments-support/instruments-groups/instruments/d2b/how-it-works/simulated-experiment*.

[93] R. Cywinski, S. Kilcoyne, and J. R. Stewart, "Diffuse magnetic scattering of polarised neutrons," *Physica B: Condensed Matter*, vol. 267268, pp. 106 – 114, 1999.

[94] J. R. Stewart, P. P. Deen, K. H. Andersen, H. Schober, J.-F. Barthélémy, J. M. Hillier, A. P. Murani, T. Hayes, and B. Lindenau, "Disordered materials studied using neutron polarization analysis on the multi-detector spectrometer, D7," *Journal of Applied Crystallography*, vol. 42, pp. 69–84, 2009.

[95] J. R. Stewart, *Polarised Neutrons*. Oxford, U.K.: 12th Oxford School on Neutron Scattering, 2011.

[96] R. M. Moon, T. Riste, and W. C. Koehler, "Polarization Analysis of Thermal-Neutron Scatterinf," *Physical Review*, vol. 181, pp. 920–931, 1969.

[97] O. Schärpf and Capellmann, "The *xyz* Difference Method with Polarized Neutrons and the Separation of Coherent, Spin Incoherent, and Magnetic Scattering Cross Sections in Multidetector," *Physica Status Solidi A*, vol. 135, pp. 359–379, 1993.

[98] S. L. Lee, R. Cywinski, and S. L. Kilcoyne, eds., *Muon Science: Muons in Physics, Chemistry and Materials*. New York: Taylor and Francis Group, 1999.

[99] S. F. J. Cox, "Implanted muon studies in condensed matter science," *Journal of Physics C: Solid State Physics*, vol. 20, pp. 3187–3319, 1987.

[100] S. J. Blundell, "Spin-polarized muons in condensed matter physics," *Contempory Physics*, vol. 40, p. 175, 1999.

[101] R. L. Garwin, L. M. Ledermann, and M. Weinrich, "Observations of the Failure of the Conservation of Parity and Charge Conjugation in Meson Decays: the Magnetic Moment of the Free Muon," *Physical Review*, vol. 105, pp. 1415–1417, 1957.

[102] T. Lancaster, *μSR and Magnetism*. Rutherford Appleton Laboratory, U.K.: ISIS Muon Training School, 2012.

[103] F. L. Pratt, "WiMDA: a muon data analysis program for the Windows PC," *Physica B*, vol. 289-290, pp. 710–714, 2000.

[104] S. Elliot, *The Physics and Chemistry of Solids*. U.K.: Wiley, 1998.

[105] P. Atkins and J. de Paula, *Elements of Physical Chemistry*. U.K.: Oxford Univerity Press, 4th ed., 2005.

[106] C. Kittel and H. Kroemer, *Thermal Physics*. New York: W. H. Freeman and Co., 1980.

[107] Quantum Design, *PPMS Heat Capacity Option User's Manual*.

[108] J. S. Gardner, M. J. P. Gingras, and J. E. Greedan, "Magnetic pyrochlore oxides," *Review of Modern Physics*, vol. 82, pp. 53–107, 2010.

[109] N. Hanasaki, K. Watanabe, T. Ohtsuka, I. Kézsmárki, S. Iguchi, S. Miyasaka, and Y. Tokura, "Nature of the Transition between a Ferromagnetic Metal and a Spin-Glass Insulator in Pyrochlore Molybdates," *Physical Review Letters*, vol. 99, p. 086401, Aug 2007.

[110] J. Greedan, M. Sato, X. Yan, and F. Razavi, "Spin-glass-like behavior in $Y_2Mo_2O_7$, a concentrated, crystalline system with negligible apparent disorder," *Solid State Communications*, vol. 59, pp. 895 – 897, 1986.

[111] N. P. Raju, E. Gmelin, and R. K. Kremer, "Magnetic-susceptibility and specific-heat studies of spin-glass-like ordering in the pyrochlore compounds $R_2Mo_2O_7$ (R = Y, Sm, or Gd)," *Physical Review B*, vol. 46, pp. 5405–5411, 1992.

[112] K. Miyoshi, Y. Nishimura, K. Honda, K. Fujiwara, and J. Takeuchi, "Successive Spin Freezing Behavior in a Pyrochlore Antiferromagnet $Y_2Mo_2O_7$ under Magnetic Fields," *Journal of the Physical Society of Japan*, vol. 69, pp. 3517–3520, 2000.

[113] H. J. Silverstein, K. Fritsch, F. Flicker, A. M. Hallas, J. S. Gardner, Y. Qiu, G. Ehlers, A. T. Savici, Z. Yamani, K. A. Ross, B. D. Gaulin, M. J. P. Gingras, J. A. M. Paddison, K. Foyevtsova, R. Valenti, F. Hawthorne, C. R. Wiebe, and H. R. Zhou, "Novel liquid-like correlations in single crystalline $Y_2Mo_2O_7$: an unconventional spin glass," *arXiv:1305.1274*, 2013.

[114] C. H. Booth, J. S. Gardner, G. H. Kwei, R. H. Heffner, F. Bridges, and M. A. Subramanian, "Local lattice disorder in the geometrically frustrated spin-glass pyrochlore $Y_2Mo_2O_7$," *Physical Review B*, vol. 62, pp. R755–R758, 2000.

[115] A. Keren and J. S. Gardner, "Frustration Driven Lattice Distortion: An NMR Investigation of $Y_2Mo_2O_7$," *Physical Review Letters*, vol. 87, p. 177201, 2001.

[116] E. Sagi, O. Ofer, A. Keren, and J. S. Gardner, "Quest for Frustration Driven Distortion in $Y_2Mo_2O_7$," *Physical Review Letters*, vol. 94, p. 237202, 2005.

[117] J. E. Greedan, D. Gout, A. D. Lozano-Gorrin, S. Derahkshan, T. Proffen, H.-J. Kim, E. Božin, and S. J. L. Billinge, "Local and average structures of the spin-glass pyrochlore $Y_2Mo_2O_7$ from neutron diffraction and neutron pair distribution function analysis," *Physical Review B*, vol. 79, p. 014427, 2009.

[118] P. H. Hubert, "Contribution à l'étude des molybdites des terres rares: 1. Bimolybdites $Ln_2Mo_2O_7$," *Bulletin de la Société Chimique de France*, vol. 11, pp. 2385–2386, 1974.

[119] E. Tkachenko and P. Fedorov, "Lower Rare-Earth Molybdates," *Inorganic Materials*, vol. 39, pp. S25–S45, 2003.

[120] S. Shtrikman and E. Wohlfarth, "The theory of the Vogel-Fulcher law of spin glasses," *Physics Letters A*, vol. 8, pp. 467 – 470, 1981.

[121] N. W. Ashcroft and N. D. Mermin, *Solid State Physics*. U.S.A.: Brooks/Cole, 1976.

[122] Y. J. Uemura, T. Yamazaki, D. R. Harshman, M. Senba, and E. J. Ansaldo, "Muon-spin relaxation in AuFe and CuMn spin glasses," *Physical Review B*, vol. 31, pp. 546–563, 1985.

[123] C. R. Wiebe, J. E. Greedan, P. P. Kyriakou, G. M. Luke, J. S. Gardner, A. Fukaya, I. M. Gat-Malureanu, P. L. Russo, A. T. Savici, and Y. J. Uemura, "Frustration-driven spin freezing in the $S = \frac{1}{2}$ fcc perovskite Sr_2MgReO_6," *Physical Review B*, vol. 68, p. 134410, 2003.

[124] A. S. Wills, G. S. Oakley, D. Visser, J. Frunzke, A. Harrison, and K. H. Andersen, "Short-range order in the topological spin glass $D_3OFe_3(SO_4)_2(OD)_6$ using xyz polarized neutron diffraction," *Physical Review B*, vol. 64, p. 094436, 2001.

[125] D. Schmitt and B. Ouladdiaf, "Absorption Correction for Annular Cylindrical Samples in Powder Neutron Diffraction," *Journal of Applied Crystallography*, vol. 31, pp. 620–624, 1998.

[126] C. W. Dwiggins, Jnr, "Rapid calculation of X-ray absorption correction factors for cylinders to an accuracy of 0.1 %," *Acta Crystallographica Section A*, vol. 31, pp. 146–148, 1975.

[127] G. J. Nilsen, F. C. Coomer, M. A. de Vries, J. R. Stewart, P. P. Deen, A. Harrison, and H. M. Rønnow, "Pair correlations, short-range order, and dispersive excitations in the quasi-kagome quantum magnet volborthite," *Physical Review B*, vol. 84, p. 172401, 2011.

[128] R. D. Shannon, "Revised effective ionic radii and systematic studies of interatomic distances in halides and chalcogenides," *Acta Crystallographica Section A*, vol. 32, pp. 751–767, 1976.

[129] D. P. Shoemaker, A. Llobet, M. Tachibana, and R. Seshadri, "Reverse Monte Carlo neutron scattering study of the ordered-ice oxide pyrochlore $Pb_2Ru_2O_{6.5}$," *Journal of Physics: Condensed Matter*, vol. 23, p. 315404, 2011.

[130] B. J. Kennedy and T. Vogt, "Structural and Bonding Trends in Ruthenium Pyrochlores," *Journal of Solid State Chemistry*, vol. 126, pp. 261–270, 1996.

[131] D. R. Pederzolli and J. P. Attfield, "$Nd_4Cu_2O_7$: A Copper(I) Oxide with a Novel Cooperatively Distorted T Type Structure," *Journal of Solid State Chemistry*, vol. 136, pp. 137 – 140, 1998.

[132] J. P. Attfield and G. Férey, "Preparation and crystal structures of $La_2Cu_{1-x}Li_xO_4$ solid solutions and evidence for a new oxide with a defect K_2NiF_4 structure: $La_4Li_2O_7$,"

[133] M. Yang, J. Oró-Solé, A. Fuertes, and J. P. Attfield, "Topochemical Synthesis of Europium Molybdenum Oxynitride Pyrochlores," *Chemistry of Materials*, vol. 22, pp. 4132–4134, 2010.

[134] I. Kennedy, B. J. Kennedy, B. A. Hunter, and T. Vogt, "Bonding and Structural Variations in Doped $Bi_2Sn_2O_7$," *Journal of Solid State Chemistry*, vol. 131, pp. 317 – 325, 1997.

[135] M. Tachibana, T. Tojo, H. Kawaji, T. Atake, H. Ikuta, Y. Uchimoto, and M. Wakihara, "Influence of oxygen stoichiometry on the spin-glass behavior of $LiCrMnO_{4-\delta}$ spinels," *Physical Review B*, vol. 66, p. 092406, 2002.

[136] S. R. Dunsiger, R. F. Kiefl, K. H. Chow, B. D. Gaulin, M. J. P. Gingras, J. E. Greedan, A. Keren, K. Kojima, G. M. Luke, W. A. MacFarlane, N. P. Raju, J. E. Sonier, Y. J. Uemura, and W. D. Wu, "Muon spin relaxation investigation of the spin dynamics of geometrically frustrated antiferromagnets $Y_2Mo_2O_7$ and $Tb_2Mo_2O_7$," *Physical Review B*, vol. 54, pp. 9019–9022, 1996.

[137] G. Ehlers, J. E. Greedan, J. R. Stewart, K. C. Rule, P. Fouquet, A. L. Cornelius, C. Adriano, P. G. Pagliuso, Y. Qiu, and J. S. Gardner, "High-resolution neutron scattering study of $Tb_2Mo_2O_7$: A geometrically frustrated spin glass," *Physical Review B*, vol. 81, p. 224405, 2010.

[138] K. Miyoshi, Y. Nishimura, K. Honda, K. Fujiwara, and J. Takeuchi, "Magnetic ordering of pyrochlore oxides $R_2Mo_2O_7$ (R = Er - Nd, Y) by AC and DC magnetic measurements," *Physica B: Condensed Matter*, vol. 284-288, pp. 1463 – 1464, 2000.

[139] J. A. Hodges, P. Bonville, A. Forget, J. P. Sanchez, P. Vulliet, M. Rams, and K. Królas, "Magnetic properties of $Yb_2Mo_2O_7$ and $Gd_2Mo_2O_7$ from rare earth Mössbauer measurements," *European Physics Journal B*, vol. 33, pp. 173–181, 2003.

[140] Y. Moritomo, S. Xu, A. Machida, T. Katsufuji, E. Nishibori, M. Takata, M. Sakata, and S.-W. Cheong, "Chemical pressure control of exchange interaction in Mo pyrochlore," *Physical Review B*, vol. 63, p. 144425, 2001.

[141] J. B. Goodenough, "Theory of the Role of Covalence in the Perovskite-Type Manganites [La,M(II)]MnO_3," *Physical Review*, vol. 100, pp. 564–573, 1955.

[142] J. Kanamori, "Superexchange interaction and symmetry properties of electron orbitals," *Journal of Physics and Chemistry of Solids*, vol. 10, pp. 87 – 98, 1959.

[143] A. P. Ramirez, G. P. Espinosa, and A. S. Cooper, "Strong frustration and dilution-enhanced order in a quasi-2D spin glass," *Physical Review Letters*, vol. 64, pp. 2070–2073, 1990.

[144] M. Ivanov, V. Mitrofanov, L. Falkovskaya, and A. Fishman, "Random fields in disordered magnetics with Jahn-Teller ions," *Journal of Magnetism and Magnetic Materials*, vol. 36, pp. 26 – 38, 1983.

[145] R. Fichtl, V. Tsurkan, P. Lunkenheimer, J. Hemberger, V. Fritsch, H.-A. K. von Nidda, E.-W. Scheidt, and A. Loidl, "Orbital Freezing and Orbital Glass State in $FeCr_2S_4$," *Physical Review Letters*, vol. 94, p. 027601, 2005.

[146] G. M. Veith, M. Greenblatt, M. Croft, and J. B. Goodenough, "Synthesis and characterization of the oxynitride pyrochlore - $Sm_2Mo_2O_{3.83}N_{3.17}$," *Materials Research Bulletin*, vol. 36, pp. 1521 – 1530, 2001.

[147] M. J. Martinez-Lope, M. T. Casais, and J. A. Alonso, "Synthesis and characterization of the oxynitride $Y_2Mo_2O_{4.5}N_{2.5}$ pyrochlore: A neutron diffraction and magnetic study," *Zeitschrift fur Naturforschung B*, vol. 61, pp. 164–169, 2006.

[148] B. D. Gaulin and J. S. Gardner, *Frustrated Spin Systems*, ch. Experimental Studies of Frustrated Pyrochlore Antiferromagnets. Singapore: World Scientific, 2004.

[149] M. Lafontaine, A. L. Bail, and G. Férey, "Copper-containing mineralsI. $Cu_3V_2O_7(OH)_22H_2O$: The synthetichomolog of volborthite; crystal structure determination from X-ray and neutron data; structural correlations," *Journal of Solid State Chemistry*, vol. 85, pp. 220 – 227, 1990.

[150] M. P. Shores, E. A. Nytko, B. M. Bartlett, and D. G. Nocera, "A structurally perfect $S = \frac{1}{2}$ kagome antiferromagnet," *Journal of the American Chemical Society*, vol. 127, pp. 13462–13463, 2005.

[151] R. H. Colman, C. Ritter, and A. S. Wills, "Toward perfection: Kapellasite, $Cu_3Zn(OH)_6Cl_2$, a new model $S = \frac{1}{2}$ kagome antiferromagnet," *Chemistry of Materials*, vol. 20, pp. 6897–6899, 2008.

[152] Y. Okamoto, H. Yoshida, and Z. Hiroi, "Vesignieite $BaCu_3V_2O_8(OH)_2$ as a candidate spin-$\frac{1}{2}$ kagome antiferromagnet," *Journal of the Physical Society of Japan*, vol. 78, p. 033701, 2009.

[153] H. Yoshida, J. Yamaura, M. Isobe, Y. Okamoto, G. J. Nilsen, and Z. Hiroi, "Orbital switching in a frustrated magnet," *Nature Communications*, vol. 3:860, 2012.

[154] F. Bert, S. Nakamae, F. Ladieu, D. L'Hôte, P. Bonville, F. Duc, J.-C. Trombe, and P. Mendels, "Low temperature magnetization of the $S = \frac{1}{2}$ kagome antiferromagnet $ZnCu_3(OH)_6Cl_2$," *Physical Review B*, vol. 76, p. 132411, 2007.

[155] E. Kermarrec, P. Mendels, F. Bert, R. H. Colman, A. S. Wills, P. Strobel, P. Bonville, A. Hillier, and A. Amato, "Spin-liquid ground state in the frustrated kagome antiferromagnet $MgCu_3(OH)_6Cl_2$," *Physical Review B*, vol. 84, p. 100401, 2011.

[156] B. N. Figgis and M. A. Hitchman, *Ligand Field Theory and its Applications*. U.S.A: Wiley-VCH, 2000.

[157] Z. Ropka and R. J. Radwanski, "Electronic structure and crystal-field states in V_2O_3," *Physica B: Condensed Matter*, vol. 378380, pp. 301 – 303, 2006.

[158] E. M. Wheeler, B. Lake, A. T. M. N. Islam, M. Reehuis, P. Steffens, T. Guidi, and A. H. Hill, "Spin and orbital order in the vanadium spinel MgV_2O_4," *Physical Review B*, vol. 82, p. 140406, 2010.

[159] J.-S. Zhou, Y. Ren, J.-Q. Yan, J. F. Mitchell, and J. B. Goodenough, "Frustrated Superexchange Interaction Versus Orbital Order in a $LaVO_3$ Crystal," *Physical Review Letters*, vol. 100, p. 046401, 2008.

[160] A. P. Ramirez, S.-W. Cheong, and M. L. Kaplan, "Specific heat of defects in the haldane systems Y_2BaNiO_5 and NENP - absence of free $S = \frac{1}{2}$ excitations," *Physical Review Letters*, vol. 72, pp. 3108–3111, 1994.

[161] M. A. de Vries, K. V. Kamenev, W. A. Kockelmann, J. Sanchez-Benitez, and A. Harrison, "Magnetic Ground State of an Experimental $S = 1/2$ Kagome Antiferromagnet," *Physical Review Letters*, vol. 100, p. 157205, 2008.

[162] J. H. Brewer, S. R. Kreitzman, D. R. Noakes, E. J. Ansaldo, D. R. Harshman, and R. Keitel, "Observation of muon-fluorine "hydrogen bonding" in ionic crystals," *Physical Review B*, vol. 33, pp. 7813–7816, 1986.

[163] T. Lancaster, S. J. Blundell, P. J. Baker, M. L. Brooks, W. Hayes, F. L. Pratt, J. L. Manson, M. M. Conner, and J. A. Schlueter, "Muon-Fluorine Entangled States in Molecular Magnets," *Physical Review Letters*, vol. 99, p. 267601, 2007.

[164] A. P. Ramirez, "Strongly Geometrically Frustrated Magnets," *Annual Review of Materials Science*, vol. 24, pp. 453–480, 1994.

[165] M. Yamashita, N. Nakata, Y. Senshu, M. Nagata, H. M. Yamamoto, R. Kato, T. Shibauchi, and Y. Matsuda, "Highly Mobile Gapless Excitations in a Two-Dimensional Candidate Quantum Spin Liquid," *Science*, vol. 328, no. 5983, pp. 1246–1248, 2010.

[166] S. Yamashita, Y. Nakazawa, M. Oguni, Y. Oshima, H. Nojiri, Y. Shimizu, K. Miyagawa, and K. Kanoda, "Thermodynamic properties of a spin-$\frac{1}{2}$ spin-liquid state in a κ-type organic salt," *Nature Physics*, vol. 4, pp. 459–462, 2008.

[167] J. S. Helton, K. Matan, M. P. Shores, E. A. Nytko, B. M. Bartlett, Y. Yoshida, Y. Takano, A. Suslov, Y. Qiu, J.-H. Chung, D. G. Nocera, and Y. S. Lee, "Spin Dynamics of the Spin-1/2 Kagome Lattice Antiferromagnet $ZnCu_3(OH)_6Cl_2$," *Physical Review Letters*, vol. 98, p. 107204, 2007.

[168] I. A. Campbell, A. Amato, F. N. Gygax, D. Herlach, A. Schenck, R. Cywinski, and S. H. Kilcoyne, "Dynamics in canonical spin glasses

observed by muon spin depolarization," *Physical Review Letters.*, vol. 72, pp. 1291–1294, 1994.

[169] P. Mendels, F. Bert, M. A. de Vries, A. Olariu, A. Harrison, F. Duc, J. C. Trombe, J. S. Lord, A. Amato, and C. Baines, "Quantum Magnetism in the Paratacamite Family: Towards an Ideal Kagomé Lattice," *Physical Review Letters*, vol. 98, p. 077204, 2007.

[170] B. Fåk, E. Kermarrec, L. Messio, B. Bernu, C. Lhuillier, F. Bert, P. Mendels, B. Koteswararao, F. Bouquet, J. Ollivier, A. D. Hillier, A. Amato, R. H. Colman, and A. S. Wills, "Kapellasite: A Kagome Quantum Spin Liquid with Competing Interactions," *Physical Review Letters*, vol. 109, p. 037208, 2012.

[171] A. Olariu, P. Mendels, F. Bert, F. Duc, J. C. Trombe, M. A. de Vries, and A. Harrison, "^{17}O NMR Study of the Intrinsic Magnetic Susceptibility and Spin Dynamics of the Quantum Kagome Antiferromagnet $ZnCu_3(OH)_6Cl_2$," *Physical Review Letters*, vol. 100, p. 087202, 2008.

[172] M. Yamashita, T. Shibauchi, and Y. Matsuda, "Thermal-Transport Studies on Two-Dimensional Quantum Spin Liquids," *Chemical Physics and Physical Chemistry*, vol. 13, pp. 74–78, 2012.

[173] R. H. Mitchell, *Perovskites Modern and Ancient*. Ontario, Canada: Almaz Press Inc., 2002.

[174] V. M. Goldschmidt, "Die Gesetze der Krystallochemie," *Naturwissenschaften*, vol. 14, 1926.

[175] M. A. de Vries, A. C. Mclaughlin, and J.-W. G. Bos, "Valence Bond Glass on an fcc Lattice in the Double Perovskite Ba_2YMoO_6," *Physical Review Letters*, vol. 104, p. 177202, 2010.

[176] S. J. Clarke, K. A. Hardstone, C. W. Michie, and M. J. Rosseinsky, "High-Temperature Synthesis and Structures of Perovskite and $n = 1$ Ruddlesden Popper Tantalum Oxynitrides," *Chemistry of Materials*, vol. 14, pp. 2664–2669, 2002.

[177] A. M. Glazer, "The classification of tilted octahedra in perovskites," *Acta Crystallographica Section B*, vol. 28, pp. 3384–3392, 1972.

[178] A. M. Glazer, "Simple ways of determining perovskite structures," *Acta Crystallographica Section A*, vol. 31, pp. 756–762, 1975.

[179] C. J. Howard and H. T. Stokes, "Group-Theoretical Analysis of Octahedral Tilting in Perovskites," *Acta Crystallographica Section B*, vol. 54, pp. 782–789, 1998.

[180] H. D. Megaw, "A note on the structure of lithium niobate, $LiNbO_3$," *Acta Crystallographica Section A*, vol. 24, pp. 583–588, 1968.

[181] M. Jansen and H. P. Letschert, "Inorganic yellow-red pigments without toxic metals," *Nature*, vol. 404, pp. 980–982, 2000.

[182] Y. Kim, P. M. Woodward, K. Z. Baba-Kishi, and C. W. Tai, "Characterization of the Structural, Optical, and Dielectric Properties of Oxynitride Perovskites AMO_2N (A = Ba, Sr, Ca; M = Ta, Nb)," *Chemistry of Materials*, vol. 16, pp. 1267–1276, 2004.

[183] M. Yang, J. Oró-Solé, A. Kusmartseva, A. Fuertes, and J. P. Attfield, "Electronic Tuning of Two Metals and Colossal Magnetoresistances in $EuWO_{1+x}N_{2-x}$ Perovskites," *Journal of the American Chemical Society*, vol. 132, pp. 4822–4829, 2010.

[184] M. Yang, J. Oró-Solé, J. A. Rodgers, A. B. Jorge, A. Fuertes, and J. P. Attfield, "Anion order in perovskite oxynitrides," *Nature Chemistry*, vol. 3, pp. 47–52, 2011.

[185] V. F. Sears, "Neutron Scattering Lengths and Cross Sections," *Neutron News*, vol. 3, pp. 26–37, 1992.

[186] N. Madras, "End Patterns of Self Avoilding Walks," *Journal of Statistical Physics*, vol. 53, pp. 689–701, 1988.

[187] P. J. Camp, A. Fuertes, and J. P. Attfield, "Subextensive Entropies and Open Order in Perovskite Oxynitrides," *Journal of the American Chemical Society*, vol. 134, pp. 6762–6766, 2012.

[188] J. Oró-Solé, L. Clark, W. Bonin, J. P. Attfield, and A. Fuertes, "Anion-ordered chains in a d^1 perovskite oxynitride: $NdVO_2N$," *Chemical Communications*, vol. 49, pp. 2430–2432, 2013.

[189] K. Tatsumi and R. Hoffmann, "Bent cis d^0 MoO_2^{2+} vs. linear trans d^0f^0 UO_2^{2+}: a significant role for nonvalence $6p$ orbitals in uranyl," *Inorganic Chemistry*, vol. 19, pp. 2656–2658, 1980.

[190] M. H. Sage, G. R. Blake, C. Marquina, and T. T. M. Palstra, "Competing orbital ordering in RVO_3 compounds: High-resolution X-ray diffraction and thermal expansion," *Physical Review B*, vol. 76, p. 195102, 2007.

[191] P. Antoine, R. Assaba, P. L'Harridon, R. Marchand, Y. Laurent, C. Michel, and R. C. B., "Transport properties of the new perovskite-type $LaVO_{3-x}N_x$ oxynitrides," *Materials Science and Engineering*, vol. B5, pp. 43–46, 1989.

[192] S. M. Selbach, J. R. Tolchard, A. Fossdal, and T. Grande, "Non-linear thermal evolution of the crystal structure and phase transitions of LaFeO3 investigated by high temperature X-ray diffraction," *Journal of Solid State Chemistry*, vol. 196, pp. 249–254, 2012.

[193] E. Iturbe-Zabalo, O. Fabelo, M. Gateshki, and J. M. Igartua, "Mode-crystallography analysis and magnetic structures of $SrLnFeRuO_6$ (Ln = La,

Pr, Nd) disordered perovskites," *Acta Crystallographica Section B*, vol. 68, pp. 590–601, 2012.

[194] K. Page, M. W. Stoltzfus, Y.-I. Kim, T. Proffen, P. M. Woodward, A. K. Cheetham, and R. Seshadri, "Local Atomic Ordering in $BaTaO_2N$ Studied by Neutron Pair Distribution Function Analysis and Density Functional Theory," *Chemistry of Materials*, vol. 19, pp. 4037–4042, 2007.

[195] L. Clark, C. Ritter, A. Harrison, and J. P. Attfield, "Oxygen miscibility gap and spin glass formation in the pyrochlore $Lu_2Mo_2O_7$," *Journal of Solid State Chemistry*, vol. 203, pp. 199 – 203, 2013.

[196] L. Clark, J. C. Orain, F. Bert, M. A. De Vries, F. H. Aidoudi, R. E. Morris, P. Lightfoot, J. S. Lord, M. T. F. Telling, P. Bonville, J. P. Attfield, P. Mendels, and A. Harrison, "Gapless Spin Liquid Ground State in the S=1/2 Vanadium Oxyfluoride Kagome Antiferromagnet $[NH_4]_2[C_7H_{14}N][V_7O_6F_{18}]$," *Physical Review Letters*, vol. 110, p. 207208, 2013.